



UNIVERSITY OF HAMBURG
DEPARTMENT OF PHYSICS



Imaging nanomaterials in solution –
A multimodal approach
using in situ X-ray ptychography,
spectroscopy and scattering

Dissertation

zur Erlangung des Doktorgrades
an der Fakultät für Mathematik,
Informatik und Naturwissenschaften
Fachbereich Physik
der Universität Hamburg

vorgelegt von

Lukas Grote

Hamburg

2022

Gutachter/innen der Dissertation:

Prof. Dr. Dorota Koziej
Prof. Dr. Christian Schroer

Zusammensetzung der Prüfungskommission:

Prof. Dr. Dorota Koziej
Prof. Dr. Christian Schroer
Prof. Dr. Arwen Pearson
Prof. Dr. Gabriel Bester
PD Dr. Thomas Keller

Vorsitzende der Prüfungskommission:

Prof. Dr. Arwen Pearson

Datum der Disputation:

16.08.2022

Vorsitzender Fach-Promotionsausschuss PHYSIK:

Prof. Dr. Wolfgang J. Parak

Leiter des Fachbereichs PHYSIK:

Prof. Dr. Günter H. W. Sigl

Dekan der Fakultät MIN:

Prof. Dr. Heinrich Graener

Abstract

Nonclassical nucleation and growth pathways of nanomaterials in solution often involve the emergence of pre-crystalline precursor states and the assembly of building blocks into superstructures, yielding nanomaterials with complex morphologies. Within the scope of nonclassical pathways, the formation of unoriented nanoparticle assemblies from amorphous precursors represents a particularly unexplored process. Nevertheless, a deep understanding of the underlying mechanisms is required to arrive at rational control over the synthesis. Within this thesis, in situ X-ray spectroscopic, scattering, and microscopic methods are utilized to follow chemical and structural changes during complex nanomaterial syntheses in solution.

A combination of high energy-resolution fluorescence-detected X-ray absorption near edge structure (HERFD-XANES) and X-ray scattering is used to disentangle the nonclassical nucleation and growth mechanism of unoriented CoO nanoassemblies. The spectroscopy is sensitive to changes in the local chemical environment of the absorber. It reveals that initially, the precursor Co(III) acetylacetonate is reduced to Co(II) acetylacetonate. At the same time, the complex rearranges from an octahedral to a square planar conformation and additionally coordinates to oxygen atoms of solvent molecules. A pair distribution function (PDF) analysis of total scattering data provides complementary structural information at pre-crystalline reaction stages and during crystallization. The PDFs allow to identify a lengthening of the Co-O bond during the rearrangement of the precursor complex and the subsequent crystallization into CoO. With small-angle scattering (SAXS), it becomes evident that CoO crystallites as small as 3 nm assemble into spherical superstructures of 20 nm. The individual crystallites and the assemblies continue to grow at a similar pace. The combination of complementary X-ray spectroscopy and scattering methods thus provides a detailed perspective on the formation of CoO nanoassemblies.

The morphology of nanomaterials can be modified via secondary chemical reactions after the growth stage. Several pathways exist yielding hollow nanoparticles, but the exact mechanisms via which the hollowing occurs are often difficult to probe, since the applicability of transmission electron microscopy (TEM) in solution is limited. X-ray microscopy overcomes the limitations of TEM due to the high penetration power of X-rays and enables visual in situ studies on the morphological evolution of nanomaterials in a thick chemical reactor. Ptychography is a lensless coherent imaging technique in which the object is reconstructed computationally from a set of far-field diffraction patterns. To enable in situ imaging with X-ray ptychography, a reactor with high mechanical and thermal stability is designed.

The applicability of X-ray ptychography for in-solution imaging is demonstrated on the example of Cu₂O nanocubes growing on the windows of the reactor. The method allows to reconstruct separate images of nanocubes growing on the entrance and the exit windows of the reactor with the multi-slicing approach. Since the distance between the reactor windows exceeds the depth of field of the imaging experiment, multi-slicing additionally allows for an optimal lateral resolution of the images. A series of in situ images is recorded to track the growth and subsequent hollowing of the nanocubes with a spatial resolution of 66 nm and a time resolution of 21.6 min. The nanocubes reach an average size of 450 nm. The hot solution or free floating particles in the beam path induce background artefacts, however they do not compromise the image interpretation. Knowing the composition of the nanocubes, the quantitative phase shift in the images allows to calculate the particle thickness along the beam direction. This reveals that the nanocubes have in fact the shape of cuboids with one shorter edge perpendicular to

the substrate. Hollowing sets in when the Cu_2O nanocuboids are reduced to metallic copper in the solid state. The void formation starts close to the particle-substrate interface.

With an extended setup, scanning X-ray diffraction (XRD) is measured alongside the ptychographic images during the growth of Cu_2O nanocuboids. This multimodal approach allows to link the shape of the particles with their crystallographic orientation, indicating the presence of (100) crystallographic planes at the facets of the nanocuboids. In a subsequent galvanic replacement reaction, the Cu_2O is replaced with gold. The material contrast in the X-ray images enables to clearly distinguish the newly formed shell of gold particles from the Cu_2O template. As the reaction progresses, porous gold nanocages form.

The experiments indicate that radiation damage is a recurring problem for in situ imaging of nanochemical processes in solution. The interaction of the X-ray beam with reagents or with the solvent induces side reactions which can make the composition and morphology of the nanoparticles deviate from the usual reaction product. Taking images at a photon energy of 15 keV greatly reduces this effect in the case of Cu_2O nanocuboids compared to imaging at 8.98 keV. Furthermore, the comparison of images measured in the X-ray focus with such measured out of focus shows that distributing the radiation dose to a large area reduces the damage when imaging the galvanic replacement with gold. Near-field ptychography can be used with a larger X-ray probe compared to the far-field ptychographic measurements in this work. In future experiments, the near-field method may thus allow to further reduce radiation damage.

Zusammenfassung

Nicht-klassische Nukleations- und Wachstumsprozesse von Nanomaterialien in Lösung beinhalten oft die Entstehung von prä-kristallinen Vorstufen und die Assemblierung von Bausteinen zu Überstrukturen, wobei Nanomaterialien mit komplexer Morphologie entstehen. Im Rahmen nicht-klassischer Prozesse stellt die Bildung von unorientierten Nanopartikel-Assemblaten aus amorphen Vorstufen einen besonders wenig erforschten Prozess dar. Dennoch ist ein tiefes Verständnis der zugrundeliegenden Mechanismen erforderlich, um eine gezielte Kontrolle über die Synthese zu erreichen. In dieser Arbeit werden röntgenbasierte in situ Spektroskopie-, Streuungs-, und Mikroskopie-Methoden eingesetzt, um chemische und strukturelle Veränderungen während der komplexen Synthesen von Nanomaterialien in Lösung zu verfolgen.

Eine Kombination von hochaufgelöster, fluoreszenzdetektierter Röntgen-Nahkanten-Absorptionsspektroskopie (engl. high energy-resolution fluorescence-detected X-ray absorption near edge structure, HERFD-XANES) mit Röntgenstreuung wird verwendet, um den nicht-klassischen Nukleations- und Wachstumsmechanismus von unorientierten CoO-Nanoassemblaten zu entschlüsseln. Die Spektroskopie ist empfindlich auf Veränderungen in der direkten chemischen Umgebung des absorbierenden Atoms. Sie zeigt, dass zunächst das Edukt Cobalt(III)-acetylacetonat zu Cobalt(II)-acetylacetonat reduziert wird. Gleichzeitig lagert sich der Komplex von einer oktaedrischen zu einer quadratisch-planaren Konformation um und koordiniert zusätzlich zwei Sauerstoffatome von Lösungsmittelmolekülen. Eine Analyse von Totalstreuungsdaten (engl. total scattering) mittels Paarverteilungsfunktionen (engl. pair distribution function, PDF) bietet komplementäre strukturelle Informationen über die Reaktionsstadien vor und während der Kristallisation. Die Paarverteilungsfunktionen ermöglichen es, eine Vergrößerung der Co-O Bindungslänge während der Umstrukturierung des Komplexes und der anschließenden Kristallisation von CoO zu bestimmen. Eine Untersuchung mittels Kleinwinkelstreuung (engl. small-angle X-ray scattering, SAXS) zeigt, dass CoO-Kristallite mit einer Größe von nur 3 nm zu 20 nm großen, sphärischen Überstrukturen assemblieren. Die einzelnen Kristallite und die Assemblate wachsen mit ähnlichen Geschwindigkeiten weiter. So bietet die Kombination von komplementären Methoden der Röntgenspektroskopie und -streuung einen detaillierten Einblick in die Entstehung von CoO-Nanoassemblaten.

Die Morphologie von Nanomaterialien kann durch sekundäre chemische Reaktionen nach der Wachstumsphase verändert werden. Es existieren verschiedene Wege, die zu hohlen Nanopartikeln führen, doch die exakten Mechanismen der Hohlraumbildung sind oft schwer zu untersuchen, da die Anwendbarkeit von Transmissionselektronenmikroskopie (engl. transmission electron microscopy, TEM) in Lösung begrenzt ist. Röntgenmikroskopie überwindet diese Einschränkung von TEM aufgrund des großen Durchdringungsvermögens von Röntgenstrahlung, und ermöglicht visuelle in-situ-Untersuchungen der morphologischen Entwicklung von Nanomaterialien in einem ausgedehnten chemischen Reaktor. Ptychographie ist eine linsenlose, kohärente Bildgebungstechnik, die einen rechnergestützten Algorithmus zur Rekonstruktion eines Objektes aus einem Satz von Fernfeld-Beugungsmustern verwendet. Um die in-situ-Bildgebung mit Röntgenptychographie zu ermöglichen, wird ein Reaktor mit hoher mechanischer und thermischer Stabilität konstruiert.

Die Anwendbarkeit von Ptychographie für die Bildgebung in Lösung wird am Beispiel von Cu₂O-Nanowürfeln demonstriert, die auf den Fenstern des Reaktors wachsen. Die Methode erlaubt es, mithilfe von Mehrschichtptychographie (engl. multi-slicing) separate Bilder von Nanowürfeln auf dem Eintritts-

und dem Austrittsfenster des Reaktors zu rekonstruieren. Da der Abstand zwischen den Fenstern die Schärfentiefe des bildgebenden Experiments übersteigt, führt die Mehrschichtptychographie zudem zu einer optimalen lateralen Auflösung der Bilder. Eine Serie von in-situ-Bildern wird aufgenommen, um das Wachstum und die darauffolgende Hohlraumbildung in den Nanowürfeln mit einer räumlichen Auflösung von 66 nm und einer Zeitauflösung von 21,6 min zu verfolgen. Die Nanowürfel erreichen eine durchschnittliche Größe von 450 nm. Die geheizte Lösung oder frei bewegliche Partikel im Strahlengang verursachen Hintergrundartefakte, die jedoch nicht die Interpretierbarkeit der Bilder beeinträchtigen. Da die Zusammensetzung der Nanowürfel bekannt ist, erlaubt es der quantitative Phasenschub in den Ptychogrammen, die Dicke der Partikel entlang der Strahlrichtung zu berechnen. Dies zeigt, dass die Nanowürfel eigentlich die Form flacher Quader haben, bei denen die Seite rechtwinklig zum Substrat kürzer ausfällt. Die Hohlraumbildung setzt ein, wenn die Cu_2O -Nanoquader im festen Zustand zu metallischem Kupfer reduziert werden. Der Hohlraum entsteht nahe der Grenzfläche zwischen Partikeln und Substrat.

Mit einem erweiterten Aufbau wird zusätzlich zur Ptychographie orts aufgelöste Röntgenbeugung (engl. X-ray diffraction, XRD) während des Wachstums der Cu_2O -Nanoquader gemessen. Dieser multimodale Ansatz erlaubt es, die Form der Partikel mit ihrer kristallographischen Orientierung in Verbindung zu setzen. Dies zeigt, dass an den Oberflächen der Nanoquader (100) Kristallebenen vorhanden sind. In einer anschließenden galvanischen Austauschreaktion wird Cu_2O mit Gold ersetzt. Der Materialkontrast in den Röntgenbildern ermöglicht es, die neu gebildete Schicht von Goldpartikeln von dem Cu_2O -Vorläufer klar zu unterscheiden. Die Reaktion bildet schließlich poröse Gold-Nanokäfige.

Die Experimente machen deutlich, dass das Auftreten von Strahlenschaden ein wiederkehrendes Problem bei der in-situ-Bildgebung von nanochemischen Prozessen in Lösung ist. Die Wechselwirkung des Röntgenstrahls mit Reagenzien oder mit dem Lösungsmittel induziert Nebenreaktionen, die zu einer Abweichung in der Zusammensetzung oder der Morphologie der Nanopartikel vom erwarteten Reaktionsprodukt führen können. Im Fall von Cu_2O -Nanoquadern reduziert das Messen bei einer Photonenenergie von 15 keV diesen Effekt deutlich gegenüber einer Messung bei 8,98 keV. Weiterhin zeigt ein Vergleich von Bildern, die im Fokus des Röntgenstrahls aufgenommen wurden mit solchen außerhalb des Fokus, dass eine Verteilung der Strahlendosis auf eine große Fläche den Strahlenschaden bei der Abbildung der galvanischen Austauschreaktion mit Gold reduziert. Im Vergleich zu der in dieser Arbeit angewendeten Fernfeld-Ptychographie kann Nahfeld-Ptychographie mit einer größeren Röntgenbeleuchtung verwendet werden. In zukünftigen Experimenten kann die Nahfeld-Methode daher helfen, den Strahlenschaden weiter zu reduzieren.

Contents

Abstract	3
Zusammenfassung	5
1 Introduction	11
1.1 Scope of this thesis	12
2 Growth of complex nanomaterials	15
2.1 The classical nucleation theory.....	15
2.2 Nonclassical nucleation and growth.....	16
2.2.1 Oriented aggregation.....	17
2.2.2 Unoriented assemblies	17
2.3 Void formation mechanisms.....	17
2.3.1 Ostwald ripening.....	18
2.3.2 The nanoscale Kirkendall effect	19
2.3.3 Surface-protected conversion.....	20
2.3.4 Galvanic replacement reaction.....	20
2.4 Summary.....	21
3 Fundamentals of X-ray based methods utilized to study nanomaterials	23
3.1 X-ray analytical techniques	23
3.1.1 X-ray absorption spectroscopy	23
3.1.1.1 HERFD-XANES.....	25
3.1.1.2 Following chemical reactions in solution	26
3.1.2 X-ray scattering methods.....	26
3.1.2.1 Atomic pair distribution function.....	28
3.1.2.2 Small-angle X-ray scattering	29
3.1.2.3 X-ray diffraction	29
3.2 X-ray microscopy	30
3.2.1 X-ray microscopy for materials science.....	30
3.2.2 Ptychography	31
3.2.2.1 The basic ptychographic model	32
3.2.2.2 Extension of the model to thick objects.....	33
3.2.2.3 Data acquisition and sampling requirements	33
3.2.2.4 The 3PIE reconstruction algorithm	34
3.2.2.5 Spatial resolution	36

3.3	Summary.....	38
4	X-ray studies bridge the molecular and macro length scales during the emergence of CoO assemblies	39
4.1	Abstract.....	39
4.2	Introduction	39
4.3	Results	40
4.3.1	Tracking chemical changes of the reactants via in situ X-ray absorption spectroscopy...	41
4.3.2	Pinning down nucleation and growth of nanoparticles with in situ PDF.....	44
4.3.3	Tracking the assembly with SAXS	47
4.4	Discussion.....	49
4.5	Experimental section	51
4.6	Acknowledgements	53
4.7	Author contributions.....	53
4.8	Additional information	54
4.9	Supplementary information	54
5	In situ reactor for imaging	77
5.1	Experimental requirements.....	77
5.2	Mechanical design.....	77
5.2.1	Shape of the reactor	77
5.2.2	Choice of materials	80
5.3	Heating and temperature stability.....	80
5.4	Thermal simulation.....	81
6	Multi-slice ptychography enables high-resolution measurements in extended chemical reactors	83
6.1	Abstract.....	83
6.2	Introduction	83
6.3	Results	85
6.4	Discussion.....	91
6.5	Experimental section	91
6.6	Acknowledgments	95
6.7	Author contributions.....	95
6.8	Additional information	95
7	Imaging Cu₂O nanocube hollowing in solution by quantitative in situ X-ray ptychography	97
7.1	Abstract.....	97
7.2	Introduction	97
7.3	Results	98
7.3.1	Quality of ptychographic images in solution	99

7.3.2	Nucleation and growth of Cu ₂ O nanocubes in 2D.....	101
7.3.3	From 2D to 3D: Differentiating hollow nanocubes and -cuboids.....	102
7.3.4	Photon energy dependent radiation damage in X-ray imaging.....	105
7.4	Discussion.....	106
7.5	Experimental section.....	107
7.6	Acknowledgements.....	109
7.7	Author Contributions.....	110
7.8	Additional information.....	110
7.9	Supplementary Information.....	110
8	Multimodal imaging of cubic Cu₂O@Au nanocage and CuPd alloy nanosphere formation using X-ray ptychography and nano diffraction	125
8.1	Abstract.....	125
8.2	Introduction.....	125
8.3	Results and Discussion.....	127
8.3.1	Linking crystallization and shape during growth of nanocubes.....	127
8.3.2	Cu ₂ O@Au nanocages: Phase imaging differentiates materials and their respective morphologies.....	129
8.3.3	Quantification of radiation damage by dose calculation and phase analysis.....	131
8.4	Conclusion.....	133
8.5	Experimental section.....	134
8.6	Acknowledgements.....	137
8.7	Author Contributions.....	137
8.8	Supplementary Information.....	137
8.9	Imaging the formation of CuPd alloy nanospheres.....	147
9	Conclusion and outlook	151
	Bibliography	155
	List of abbreviations	171
	List of figures	173
	List of publications	176
	Curriculum vitae	177
	Acknowledgements	179
	Eidesstattliche Versicherung / Declaration on oath	182

1 Introduction

The properties of materials often change drastically when they are structured on the nanometer scale. This effect is known since the pioneering experiment by Faraday back in 1857, demonstrating that the color of colloidal gold nanoparticles changes when modifying the particle size.¹ We attribute the dependence of the material properties on the particle size to the large surface-to-volume ratio of nanoparticles. In consequence, the surface dominates their function. For gold, the surface makes up more than 30% of all the atoms in the particle when the size drops below 3 nm.²

Only in the 1970s, nanoparticles became visible by the use of electron microscopy.^{3,4} This development represents a milestone on the way to understanding the nanoscopic properties of materials. In combination with spectroscopic methods, visual observations on the nanoscale significantly facilitate studying the relation between the fundamental physical properties of nanoparticles and their morphology.⁵ Staying with the example of colloidal gold, experiments pointed out that a changing particle size influences the resonance frequency of surface plasmons, which in turn results in the absorption of different parts of the visible light spectrum.⁴ Another major step forward in nanomaterials research followed in the 1990s, when the first semiconductor nanoparticles were realized. It was found that nanostructured semiconductors exhibit a size-dependent electronic band gap due to spatial confinement.^{6,7} Furthermore, the catalytic activity of crystalline nanoparticles can be improved by tuning their morphology. Highest catalytic activity is often reached with a morphology that leads to the preferential exposure of the most active crystallographic facets at the surface of the nanocrystals. Today, nanostructured materials are utilized in a wide range of applications such as optical devices,^{8,9} energy conversion and storage,¹⁰ as well as sensors.¹¹

Tailoring the properties of nanomaterials for specific applications requires rational control over their morphology and composition during the chemical synthesis in solution. To this end, the classical nucleation theory (c.f. Section 2.1) is a commonly utilized model.¹² It describes the formation of nanocrystals in a supersaturated solution via the addition of monomeric species onto a primary nucleus. Although the classical model holds for the growth of single-crystalline nanoparticles, it fails to explain more complex growth processes involving the assembly of primary building blocks into distinct superstructures. Such processes are therefore summarized under the term nonclassical nucleation and growth (c.f. Section 2.2).¹³ The CoO nanoassemblies shown in Figure 1.1a can serve as an example here. In a previous work, nanoassemblies of different cobalt oxides have been synthesized using a solvothermal route.¹⁴ High-resolution transmission electron microscopy (HR-TEM) revealed that the nanoassemblies consist of smaller CoO nanocrystals with no common crystallographic orientation. This observation suggests a nonclassical formation pathway. However, due to the lack of models that can accurately describe the nonclassical formation of unoriented nanoassemblies, the exact mechanism underlying the assembly process remained unclear.

Moreover, changing the material composition via secondary chemical reactions after the growth stage can be used to modify the morphology. Here, the formation of voids yielding hollow nanoparticles represents a major pathway. Owing to their large surface area and at the same time low density, hollow nanostructures are an attractive class of material for practical applications. They can serve in drug delivery,¹⁵ as catalysts¹⁶ as well as nanoreactors by encapsulating active agents.¹⁷ However, even though different void formation mechanisms are known (c.f. Section 2.3), it is not always clear which of them

applies to a particular reaction, and combinations of the mechanisms are possible. The bowl-shaped copper nanocubes shown in Figure 1.1b form during the solvothermal reduction of substrate-bound Cu_2O nanocubes.¹⁸ They have an average size of 450 nm. However, the underlying hollowing mechanism is difficult to probe using TEM, since this method requires thin samples and cannot penetrate the bulky liquid environment necessary for the solvothermal reaction.

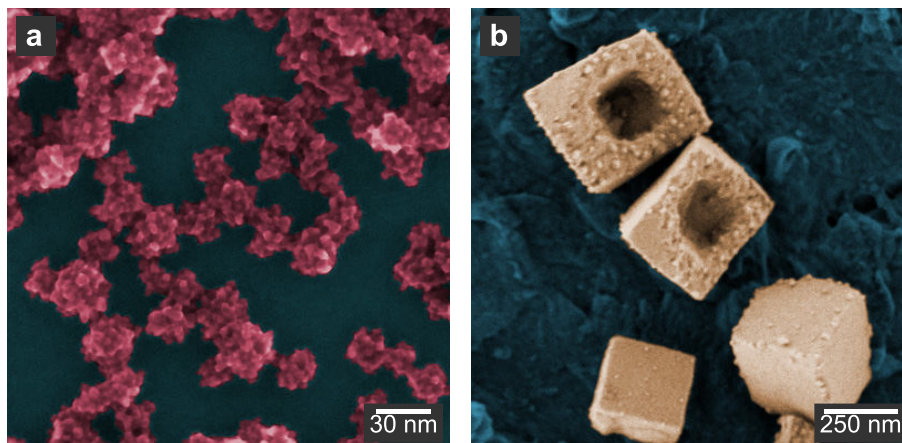


Figure 1.1. False-colored scanning electron microscopy (SEM) images of materials showing nonclassical crystallization and shape transformation. **a** Unoriented CoO nanoassemblies. **b** Bowl-shaped Cu nanocuboids formed via hollowing of substrate-based Cu_2O nanocuboids.

The limited knowledge on CoO nanoassembly formation and Cu_2O nanocube hollowing underline the fact that understanding nonclassical nucleation and growth phenomena as well as secondary shape transformations continues to be a major challenge. Synchrotron-based X-ray methods (Chapter 3) are effective tools to overcome this problem. Since X-rays have the power to penetrate thick chemical reactors, they can be utilized to study the formation of nanomaterials in situ. This way, X-ray methods can help to elucidate the mechanisms underlying complex nanomaterial morphologies, which is a key requirement for rationally controlled syntheses and consequently, for highly efficient functional nanomaterials.

1.1 Scope of this thesis

After this general introduction, the classical nucleation theory is explained, followed by a comparison of different nonclassical nucleation and growth pathways as well as an overview of self-templating void formation mechanisms in nanoparticles (Chapter 2). Fundamentals of different X-ray based methods utilized to study nanomaterials are discussed in Chapter 3, pointing out their respective strengths and weaknesses to characterize chemical, structural, and morphological aspects of a material synthesis.

The aims of the subsequent chapters are two-fold: First, in situ X-ray spectroscopy and scattering methods (c.f. Section 3.1) are utilized to disentangle the formation of the unoriented CoO nanoassemblies shown in Figure 1.1a (Chapter 4). The combination of different X-ray techniques allows to bridge the length scales from dissolved precursor molecules to the final nanoassemblies, elucidating all steps of the nonclassical formation mechanism. The in situ studies point out a rearrangement of the organo-metallic precursor complex at the pre-nucleation stage, followed by the growth of individual CoO crystallites and their concomitant assembly into a polycrystalline superstructure.

Similar excitement as it was caused decades ago by the first electron microscopy observations of nanoparticles may arise today from visualizing in real time their formation and transformation in

solution using X-rays. Thus, the second aim of this thesis is to employ in situ X-ray ptychography (c.f. Section 3.2.2) to enable the visualization of growth and subsequent shape transformation processes of nanoparticles inside a chemical reactor. A novel reactor is designed to enable imaging experiments in solution with position stability in the nanometer range (Chapter 5). First ex situ experiments help to optimize the experimental procedure for imaging inside the reactor (Chapter 6). Since the nanoparticles can grow on both the entrance, and the exit windows of the reactor, it is necessary to apply the multi-slicing model in ptychography (c.f. Section 3.2.2.2) and reconstruct separate images of particles on either of the windows. Subsequently, an in situ microscopic experiment showcases the applicability of X-ray ptychography for in-solution imaging on the example of substrate-based Cu₂O nanocubes (Chapter 7). The growth of the nanocubes is followed by a hollowing process, yielding the bowl-shaped copper nanocubes shown in Figure 1.1b. Ptychography can even access the thickness of nanocubes, allowing to model their three-dimensional (3D) morphology and to uncover the hollowing mechanism. A multimodal approach rounds off the in situ microscopic study of Cu₂O nanocubes (Chapter 8). The simultaneous measurement of X-ray ptychography and diffraction permits to link the shape of the nanocubes with their crystallographic orientation. Furthermore, a galvanic replacement of nanocube templates with gold is visualized. The thesis concludes by giving an outlook on future developments in the field of X-ray microscopy for in situ observations of nanomaterials (Chapter 9).

Comment on the use of the term *we* in this thesis: In chapters explaining experimental methods and instrumentation, the term *we* refers to the reader and the author of the thesis and is used to guide the reader through the text. In chapters presenting the results of individual research studies, *we* means all authors of the respective work.

2 Growth of complex nanomaterials

2.1 The classical nucleation theory

We have seen in the previous chapter that the demand for nanoparticles with tailored sizes steadily increased since their discovery. To this end, rational control over the chemical synthesis and the ability to predict the size of the final particles were required. In 1950, LaMer and Dinegar had proposed a theory about the nucleation of a solid phase from a supersaturated solution.¹⁹ Since the mid-eighties, this theory was commonly adopted to model the formation of nanoparticles.¹² When the supersaturation of a solution exceeds a critical level, a crystalline nucleus can form either via homogeneous nucleation as a result of random collisions of monomeric species, or via heterogeneous nucleation, that is from the interaction of monomer with a seed. The nucleation step is followed by layer-by-layer growth of a crystalline nanoparticle via the addition of more monomer from the solution onto the nucleus. This simple model is nowadays referred to as the classical nucleation theory.

Consulting the Gibbs free energy of the nucleation process ΔG_{nuc} (Equation 2.1) allows to quantify the size of a stable nucleus.²⁰

$$\Delta G_{\text{nuc}} = -\frac{4}{3}\pi r^3 \cdot \Delta G_V + 4\pi r^2 \gamma, \quad (2.1)$$

where ΔG_V is the free energy per unit volume of the solid phase, γ refers to the surface energy per unit area of the nanoparticle and r is the particle radius. The first term denotes a decrease of the bulk free energy upon the formation of chemical bonds in the solid phase, while the second term represents an increase of the free energy due to the newly formed surface. As the surface-to-volume ratio decreases with r , we directly see that there must be a critical radius r^* below which a nucleus is not stable and tends to re-dissolve. For $r > r^*$, the nucleus is stable and further growth is energetically favorable.² This behavior is illustrated in Figure 2.1a. In the classical model, the crystal shape is governed by the difference in surface energy of the crystallographic facets. The area of high-energy surfaces decreases during crystal growth, while low-energy surfaces are preferentially expressed.²¹

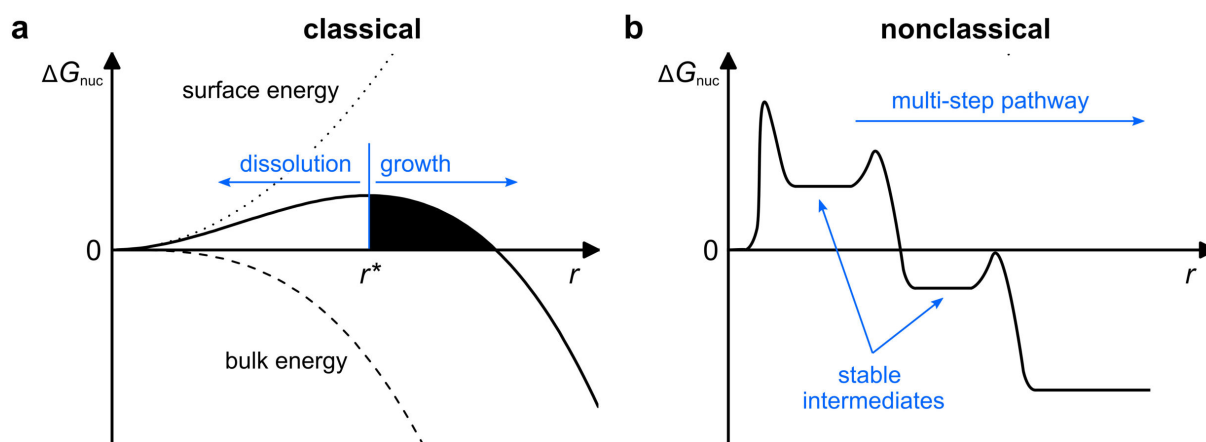


Figure 2.1. Plots of the Gibbs free energy for **a** classical and **b** nonclassical nucleation and growth. The classical model predicts a critical radius r^* below which a nucleus is unstable and tends to dissolve. Above r^* , growth is energetically favorable. Nonclassical pathways exhibit one or more stable intermediate structures within a multi-step growth pathway.^{22, 23}

In response to the ever-growing demand for nanomaterials tailored for specific applications, nanostructures of various morphologies and compositions have been synthesized in recent years. It became evident that many of the newly synthesized materials do not follow the formation pathway outlined by LaMer, challenging the universal validity of the established classical theory. Therefore, we shall review nonclassical formation pathways in the next section.

2.2 Nonclassical nucleation and growth

In the classical model, the growth of nanoparticles is solely described by the addition of atoms, ions, or molecules onto a crystalline nucleus. Nonclassical nucleation and growth is a general term to describe crystallization processes that do not follow the classical model, but involve the formation of distinct pre-crystalline entities and the aggregation of primary building blocks into superstructures. Consequently, γ and ΔG_V in Equation 2.1 become functions of the particle size as well as particle-particle interactions, resulting in stable intermediate structures and multi-step material formation pathways (Figure 2.1b).²² Recent review articles^{13, 24} present elaborate overviews of nonclassical crystallization and categorize known pathways. This section summarizes major aspects by means of the schematic illustrations shown in Figure 2.2.

The nonclassical concept of nucleation is fundamentally different from the classical theory. Initially, stable aggregations of precursor species emerge, generally referred to as pre-nucleation clusters, which are of amorphous nature (top left of Figure 2.2).²⁵ From the pre-nucleation clusters, the pathways in Figure 2.2 split into two major branches, crystal growth (Figure 2.2a-c) and the formation of liquid droplets or amorphous precursors (Figure 2.2d). In the following, we shall discuss the two branches individually.

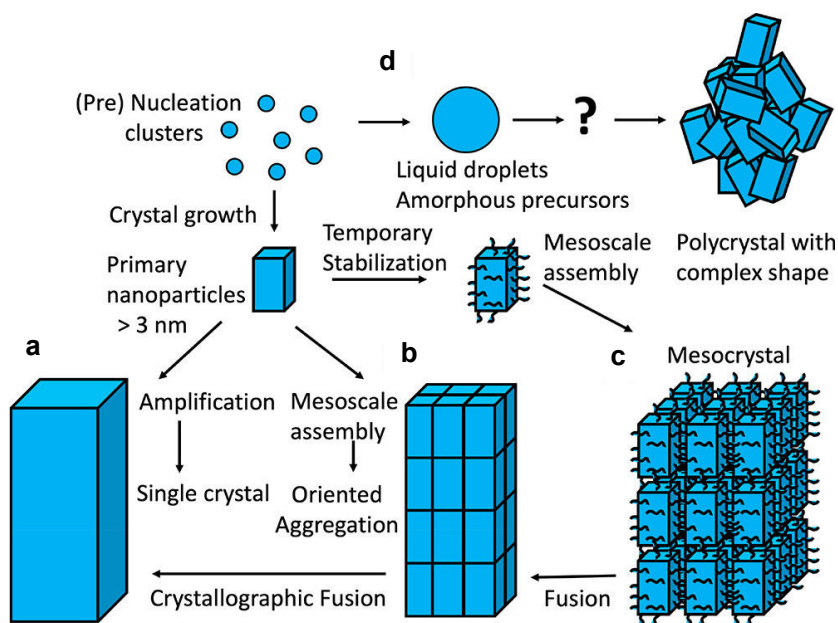


Figure 2.2. Schematic illustration of classical and nonclassical crystallization pathways. **a** Classical crystallization from a stable nucleus to a single crystal by monomer addition. **b** Oriented aggregation of nanoparticles which can be followed by fusion into a single crystal. **c** Oriented aggregation of nanoparticles stabilized by organic ligands into a mesocrystal. Also the mesocrystal can fuse into a single crystal. **d** Formation of an unoriented assembly of nanoparticles via liquid droplets or an amorphous precursor phase. Adapted with permission from¹³. Copyright 2019, American Chemical Society.

2.2.1 Oriented aggregation

As shown in the top left of Figure 2.2, primary nanoparticles can crystallize from the pre-nucleation clusters. If the primary nanocrystals continue to grow (Figure 2.2a), the product is simply a single crystal as we know it from the classical model. However, the primary nanocrystals can also aggregate in a common crystallographic orientation, forming an ordered assembly of iso-oriented nanoparticles (Figure 2.2b). The driving force of the attachment is the overall reduction of surface energy. Fusion of individual particles into a single crystal may follow, resulting in the same product as a classical nucleation and growth scenario. Furthermore, the interaction of organic ligands bound to the surface of the primary nanocrystals can mediate the aggregation process (Figure 2.2c). The ligands temporarily stabilize the primary nanocrystals and act as spacers in the final assemblies. An oriented assembly stabilized in such way is called a mesocrystal.

2.2.2 Unoriented assemblies

Starting from pre-nucleation clusters, crystallization can also occur via liquid droplets or amorphous precursors (Figure 2.2d). This pathway does not involve well-defined primary nanocrystals. It yields polycrystalline assemblies with complex shapes and no common crystallographic orientation of the building units. Some bio-inspired materials²⁶ and biominerals are known to follow this mechanism,^{23, 27} such as the formation of calcite structures in sea urchin spine via a granular phase of amorphous mineral particles.²⁸ However, the emergence of unoriented nanoparticle assemblies, also referred to as nonoriented assemblies,²⁹ is a multifaceted but rather unexplored branch as indicated by the question mark in Figure 2.2d. No generalized theory yet exists that could unequivocally explain the mechanisms leading from distinct, pre-crystalline entities to unoriented nanoassemblies. Thus, it is required to study the underlying mechanisms in more detail. In situ X-ray spectroscopic and scattering methods (c.f. Section 3.1) are effective tools to this end.

Note that polycrystalline assemblies can also form via unoriented aggregation of primary crystalline particles,³⁰ which is however not covered in this thesis.

2.3 Void formation mechanisms

Following the nucleation and growth stages, secondary transformations in solution can modify the composition and morphology of a nanomaterial. Void formation, or hollowing, is a major process in this regard. Hollowing mechanisms that directly follow the growth step are referred to as self-templating mechanisms. Here, the template defines the shape of the final structure while at the same time, it is involved in the chemical reaction that forms the final compound. We can distinguish four major self-templating mechanisms: Ostwald ripening, the nanoscale Kirkendall effect, surface-protected conversion and electroless galvanic replacement.³¹ Figure 2.3 shows an overview of the self-templating hollowing mechanisms. Each mechanism is described in more detail in the following sections.

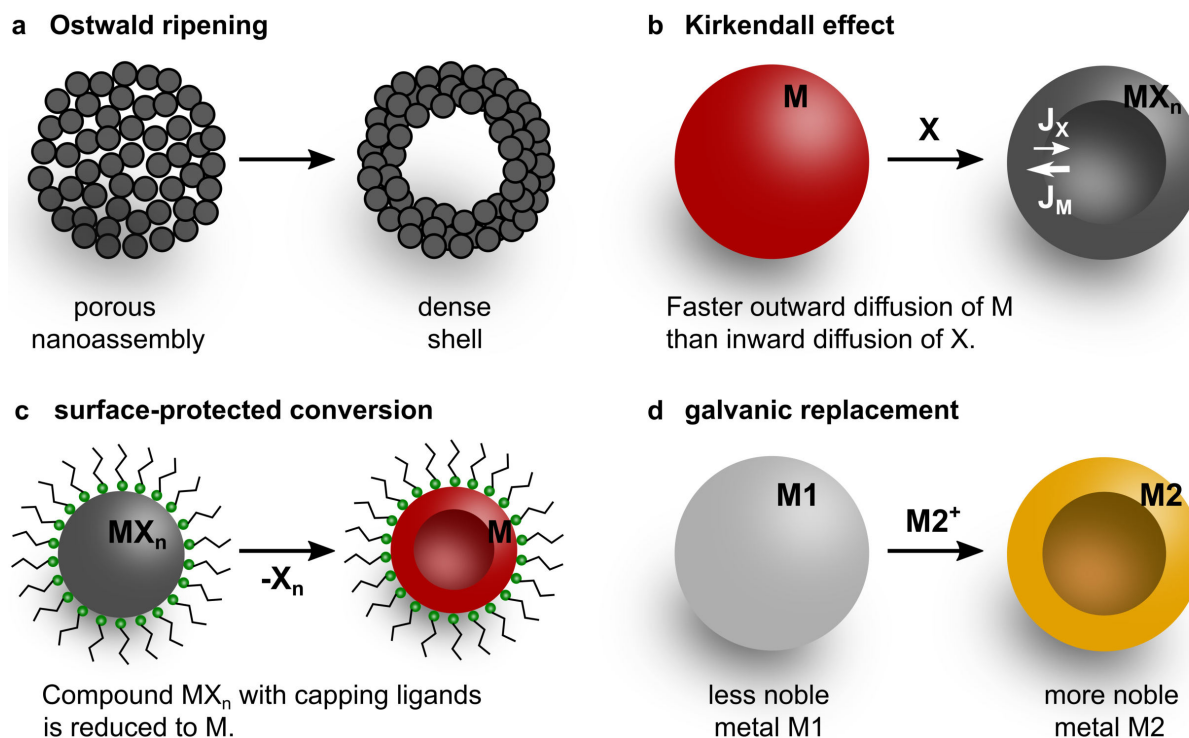


Figure 2.3. Overview of self-templating hollowing mechanisms of nanoparticles. **a** Ostwald ripening. **b** The nanoscale Kirkendall effect. **c** Surface-protected conversion. **d** Galvanic replacement reaction

2.3.1 Ostwald ripening

Ostwald ripening is a well-established phenomenon in crystal growth driven by the difference in surface energy for nanoparticles with different sizes. As we have seen earlier in Equation 2.1 and Figure 2.1a, the free energy of small particles is reduced when they decrease in size, that is when they dissolve. For large particles, the contribution of the bulk free energy dominates, and growth is energetically favorable.³² When the concentration of dissolved species is low at the end of a nanoparticle synthesis, the critical radius shifts to higher values compared to the nucleation stage. At this time, small crystals begin to re-dissolve, while the released material is taken up by large crystals which continue to grow.

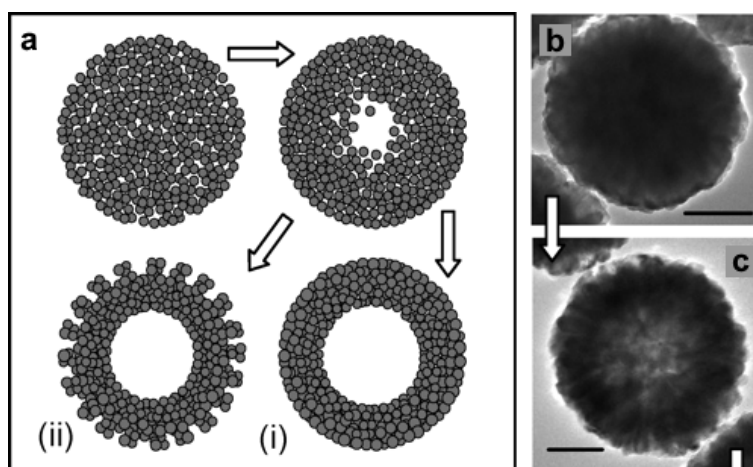


Figure 2.4. Hollowing of TiO_2 spheres via Ostwald ripening. **a** Schematic illustration of the ripening process. **b** TEM image of the TiO_2 spheres before ripening and **c** after 20 h of ripening. Scale bars: 200 nm. Adapted with permission from ³³. Copyright 2004, American Chemical Society.

In an assembly of nanoparticles composed of smaller or less densely packed crystallites in the center and larger or more compact crystallites in the shell, Ostwald ripening hence causes hollowing of the assembly.³⁴ This behavior was first demonstrated for hollow TiO_2 spheres composed of small crystalline nanoparticles synthesized from TiF_4 under hydrothermal conditions at $180\text{ }^\circ\text{C}$ (Figure 2.4).³³ Varying the precursor concentration furthermore resulted in different surface morphologies. While a low precursor concentration led to hollow spheres with smooth surfaces (type (i) in Figure 2.4a), a high concentration caused rough surfaces (type (ii)). Void formation by Ostwald ripening also occurred in mesocrystals assembled from CaTiO_3 nanocubes.³⁵

2.3.2 The nanoscale Kirkendall effect

In classical metallurgy, the Kirkendall effect occurs in the case of unequibrated inter-diffusion of atoms at an interface of two metals. In his first experiment in 1942,^{36, 37} Kirkendall studied the interface between copper and brass. He observed a shift of the interface due to the faster diffusive flux of zinc into copper (J_A) than copper into brass (J_B), resulting in a net directional flow of mass. In consequence, a net diffusive flux of vacancies (J_V) towards the faster diffusion component sets in. The vacancies accumulate and coalesce, giving rise to void formation close to the interface. This process is illustrated in Figure 2.5a. Kirkendall voids at metal interfaces are usually not desired, as they can cause for example cracks at solder joints or failures of integrated circuits.³⁸

However, scientists have turned this destructive effect into an advantage, using it to synthesize hollow nanoparticles.³⁹ When a nanoparticle consisting of a metal M is oxidized by a nonmetal X , the reaction starts at the surface forming a shell of compound MX_n . For most metal oxides, sulfides, nitrides and phosphides, the metal cations of the respective diffusion pairs have significantly higher diffusion coefficients.⁴⁰ Thus, the outward diffusion of M towards the surface is faster than the inwards diffusion of X , and the resulting net inward flux of vacancies leads to the formation of voids.⁴¹

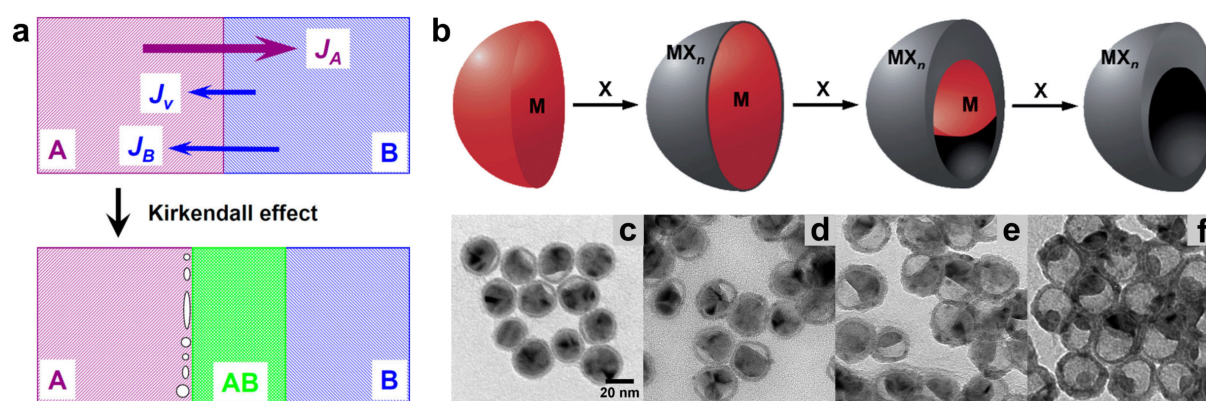


Figure 2.5. Following through the nanoscale Kirkendall effect. **a** Illustration of the Kirkendall effect at the interface between two metals A and B with diffusive fluxes J_A and J_B . If J_A is larger than J_B , a net flux of vacancies (J_V) causes void formation in metal A. **b** Illustration of the Kirkendall effect on the nanoscale, yielding a hollow particle of compound MX_n from the reaction of a solid particle of metal M with a nonmetal X . **c-f** Formation of hollow NiO nanoparticles from solid Ni templates. Panel **a** reprinted with permission from ⁴¹. Copyright 2013, American Chemical Society. Panel **b** reprinted with permission from ⁴². Copyright 2014, Royal Society of Chemistry. Panels **c-f** adapted with permission from ⁴³. Copyright 2010, American Chemical Society.

The vacancies accumulate close to the interface between M and MX_n , initially causing a separation of the core from the shell. The resulting yolk-shell structure is a composite material consisting of an M yolk surrounded by an MX_n shell. At full conversion, the reaction yields a hollow MX_n nanoparticle

(Figure 2.5b).^{38, 41} Figure 2.5c-f exemplarily show this effect for the formation of hollow NiO nanoparticles from solid Ni templates.⁴³

2.3.3 Surface-protected conversion

The Kirkendall effect leads to hollow structures in the special case of oxidation reactions of a metal M to form a compounds MX_n . However, voids can also form during other chemical conversions if those involve a phase change leading to a volume shrinkage upon mass loss from the crystal lattice or upon densification. In such a scenario, it is key to protect the surface of the nanoparticles with strongly interacting capping ligands to stabilize it against a morphological deformation. Then, it is energetically favorable to compensate the volume reduction by the formation of voids in the interior of the nanoparticle instead of decreasing its outer dimension and therefore its passivated surface area (Figure 2.6).³¹

First experiments demonstrated the hollowing of TiO_2 spheres associated with surface protection by poly(acrylic acid) ligands. When part of the material was etched with diethylene glycol, the outer shells of the spheres remained intact while the cores preferentially dissolved.⁴⁴ Later, the conversion of solid $\beta\text{-FeOOH}$ nanorods into hollow Fe_3O_4 structures pointed out that this effect could not only take place during an etching step, but also upon chemical reduction of a metal compound in the solid state. Again, the surface was passivated with poly(acrylic acid). When the loss of oxygen and hydrogen ions from the lattice during the phase change caused a volume shrinkage, hollowing occurred rather than deformation of the nanorod surface.⁴⁵

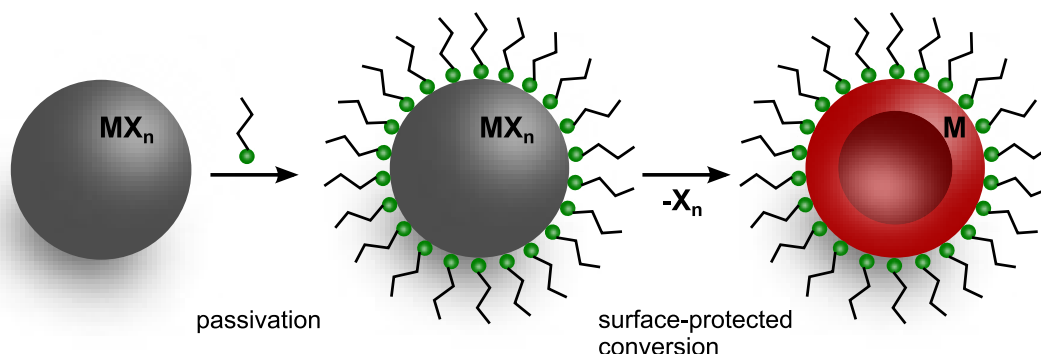


Figure 2.6. Schematic illustration of the surface protected conversion mechanism. After passivating the surface with strongly bound ligands, compound MX_n is reduced to metal M. The mass loss is compensated by void formation.

Similarly, porous MnO nanoplates formed during the reduction of $\text{Mn}(\text{OH})_2$ nanoplates,⁴⁵ and solid CoO nanoparticles transformed into hollow Co nanoboxes.⁴⁶ For the latter, oleylamine at the same time acted as solvent, passivating ligand and reducing agent in a simple one-pot route.

2.3.4 Galvanic replacement reaction

A galvanic replacement reaction (GRR) is a reaction between two metals, one of them contained in a sacrificial solid template particle, the other one dissolved in an aqueous solution. The driving force is the difference in the electrochemical reduction potentials of the metals, resulting in a favorable redox reaction. When a metal ion from in the solution gets in contact with the surface of the template, it reacts with an atom or ion in the template and thereby deposits onto the surface of the template, while the template itself dissolves. This way, a shell of new material forms around the template.³¹

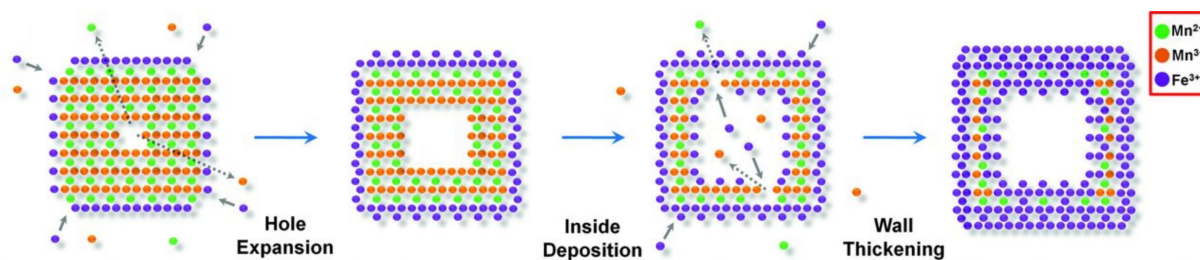


Figure 2.7. Schematic illustration of the GRR of Mn_3O_4 with Fe^{2+} via the pinhole corrosion mechanism. From ⁴⁷. Reprinted with permission from the AAAS.

The coverage of the template with the initial shell increases, the dissolution of the template becomes more pronounced in the weakly covered areas, which causes the formation of pinholes. Experiments on the replacement of manganese(II, III) oxide nanocubes with iron(II) perchlorate indicate that the pores then act as transport paths for the dissolution of the core material.⁴⁷ Finally, the inner surfaces of the template get covered as well, resulting in a thickening of the walls. The process is called pinhole corrosion mechanism and is illustrated on the example of Mn_3O_4 nanocubes in Figure 2.7. Due to the shell formation, the final hollow structures usually possess larger outer dimensions compared to the template.

The GRR represents a versatile method to prepare hollow nanostructures, and combinations with other void formation mechanisms are possible.⁴⁸ As the pinhole corrosion mechanism may leave layers of the template material within the shell of the hollow particles (last step in Figure 2.7), Kirkendall diffusion between the two materials can occur subsequently. This way, using repeated processing, multi-walled and multi-material hollow nanostructures can emerge.⁴⁹

2.4 Summary

In the scope of the classical nucleation theory (c.f. Section 2.1), a crystalline nucleus forms in a supersaturated solution of atomic, ionic, or molecular monomers. If the size of the nucleus exceeds a critical radius, growth is energetically favorable. Nonclassical nucleation and growth phenomena (c.f. Section 2.2) deviate from the classical model. They involve the formation of pre-nucleation clusters and the aggregation of building blocks into superstructures. We distinguish oriented aggregation from the formation of unoriented assemblies. Oriented aggregation (c.f. Section 2.2.1) describes the formation of a superstructure of nanocrystals with a common crystallographic orientation from primary, crystalline building blocks. Unoriented, polycrystalline assemblies (c.f. Section 2.2.2) can form without the crystallization of primary particles, but via amorphous intermediates or liquid droplets. The emergence of unoriented assemblies from amorphous intermediates in a rather unexplored pathway.

We furthermore distinguished four self-templating void formation mechanisms that can follow the growth of nanoparticles: Ostwald ripening, the nanoscale Kirkendall effect, surface-protected conversion and electroless galvanic replacement. Ostwald ripening (c.f. Section 2.3.1) does not involve a chemical change of the material. If a nanoassembly consists of smaller particles in the center, the higher free energy of the central particles induces their dissolution, while particles at the surface grow and densify. The Kirkendall effect (c.f. Section 2.3.2) occurs when a nanoparticle consisting of a metal M is oxidized by a nonmetal X . The faster diffusion of M towards the surface compared to the inwards diffusion of X results in void formation. Hollowing via surface-protected conversion (c.f. Section 2.3.3) takes place when the surface of a nanoparticle is stabilized by strongly interacting ligands while the particle undergoes a phase change that leads to a volume shrinkage. A GRR (c.f. Section 2.3.4) yields

hollow structures if the more noble reactant forms a shell around a less noble template while the template dissolves.

3 Fundamentals of X-ray based methods utilized to study nanomaterials

Material properties, chemical and structural ones, can be deduced from the interaction of the material with X-rays. This chapter introduces X-ray analytical and microscopy techniques and points out their respective strengths and weaknesses to observe different stages of nanomaterials formation and transformation. We shall see that the methods are often complementary to each other and combining them in multimodal experiments leads to the most complete picture of a synthesis.

The most basic phenomenon is the interaction of an X-ray wave with an electron. In a classical picture, the incident electromagnetic wave accelerates the electron which in turn emits radiation of the same frequency. This effect is known as Thomson scattering. For the ensemble of electrons in an atom, we describe the scattering by means of the atomic form factor $f^0(\mathbf{q})$, which is a function of the scattering vector $\mathbf{q} = \mathbf{k}_i - \mathbf{k}_f$, with \mathbf{k}_i and \mathbf{k}_f being the incident and outgoing wavevectors, respectively.

When electrons are bound to an atomic nucleus, they are not entirely free to follow the incident electromagnetic wave. In our classical picture, we could think of such a bound electron interacting with the wave as a forced damped oscillator. A corresponding derivation is presented in ⁵⁰, chapter 8. In essence, the scattering length of the atom is reduced, which is described by an additional term $f'(\omega)$ in the atomic form factor. Furthermore, we need to add an imaginary term $if''(\omega)$, which accounts for dissipation in the oscillator and describes the absorption of X-rays. The complete atomic form factor is thus given by

$$f(\mathbf{q}, \omega) = f^0(\mathbf{q}) + f'(\omega) - if''(\omega). \quad (3.1)$$

The scattering term $f^0(\mathbf{q})$ is dominated by loosely bound electrons in high energy levels. The behavior of the two correction terms $f'(\omega)$ and $f''(\omega)$, however, is governed by core level electrons with binding energies comparable to typical photon energies of X-rays. The correction terms are therefore functions of the frequency ω of the incident X-rays but independent of \mathbf{q} . They reach extremal values if the photon energy equals the binding energy of a core-level electron.

We shall see in the course of this chapter, that from the interactions between X-rays and matter described with $f(\mathbf{q}, \omega)$, we can arrive at several analytical and microscopy techniques. In favor of a concise overview of these methods, we skip detailed derivations. The following descriptions are based on textbooks by Als-Nielsen and McMorrow,⁵⁰ Egami and Billinge,⁵¹ and Jacobsen⁵², and readers who seek for a more fundamental approach are referred to the respective chapters there.

3.1 X-ray analytical techniques

3.1.1 X-ray absorption spectroscopy

In X-ray absorption spectroscopy (XAS), we make use of the frequency dependence of the absorption term f'' in the atomic form factor (Equation 3.1). The method provides element-specific chemical information on the absorbing atom, such as the oxidation state, and on ligands in the local chemical environment. XAS spectra also encode short-range structural information.

The simple model of the forced damped oscillator is thus insufficient to properly describe the absorption of X-rays by bound electrons, but a quantum mechanical treatment of electronic transitions would be required, and the chemical environment of the absorber would need to be considered in the calculation. However, it is not the goal of this section to model f'' from first principles. Instead, we will approach the topic from an experimental perspective, where we describe the absorption of X-rays with the Lambert-Beer law,⁵³

$$I = I_0 \cdot e^{-\mu d} \quad (3.2)$$

where I_0 and I are the incident and transmitted intensities, respectively, d is the thickness of the sample and μ denotes the linear absorption coefficient. The absorption coefficient μ relates to f'' by

$$\mu = 2\rho_{\text{at}}r_0\lambda f'' \quad (3.3)$$

where ρ_{at} is the average atomic number density, r_0 is the Thomson scattering length and λ is the X-ray wavelength. An absorption spectrum results from measuring the dependence of μ on the incident photon energy E .

If E passes the binding energy of a core-level electron, we observe a jump in μ due to photo-absorption of an incident photon upon excitation of the electron. This jump is called an absorption edge. In the nomenclature of absorption edges, capital letters K, L, M, ... denote the primary atomic quantum number n of the initial state, indexes are used both to denote the azimuthal quantum number l as well as to differentiate the high spin-orbit split of the core states. Thus, the excitation of a 1s electron gives rise to a single K edge, while the excitation of a 2s electron is assigned to the L_1 edge, and excitations from the $2p_{1/2}$ and $2p_{3/2}$ levels to the L_2 and L_3 edges, respectively. The position of the edge additionally depends on the oxidation state of the absorber. The binding energy of core-level electrons slightly increases in higher oxidation states, and the edge shifts towards higher incident energies.⁵³

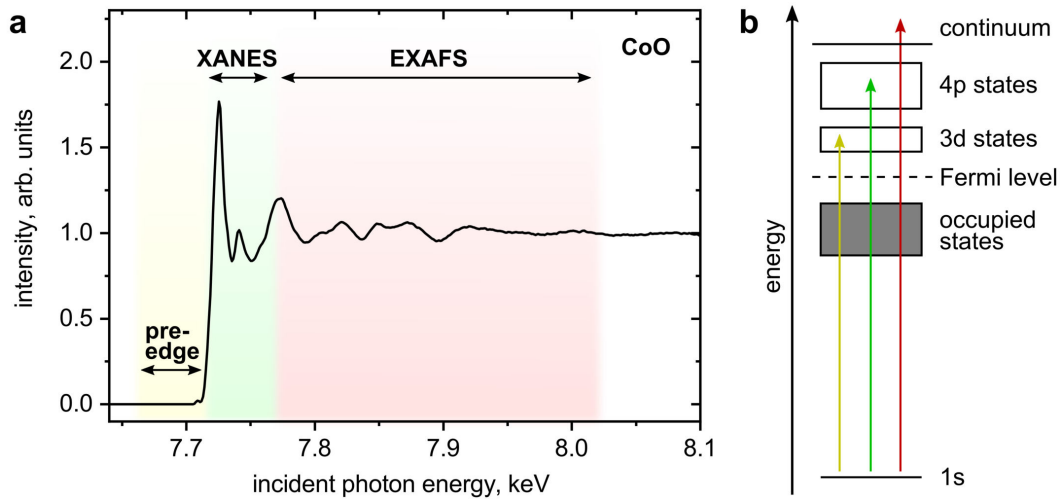


Figure 3.1. **a** X-ray absorption spectrum of CoO at the K edge of Co measured with high energy-resolution fluorescence-detection (HERFD, c.f. Section 3.1.1.1). **b** Energy diagram illustrating the excitations that contribute to the respective parts of the spectrum.

During the following explanations, we will use cobalt as an example, since this element will play a major role in Chapter 4. Figure 3.1a shows the spectrum across the Co K edge in CoO measured in HERFD mode (c.f. Section 3.1.1.1). We can separate a typical absorption spectrum into three regions: pre-edge, X-ray absorption near edge structure (XANES) and extended X-ray absorption fine structure (EXAFS). The excitations contributing to the respective regions in the spectrum are shown in the energy diagram in Figure 3.1b.

In the vicinity of the edge, within the XANES region, $\mu(E)$ is approximately proportional to a symmetry-selected unoccupied density of states (DOS), since the conservation of angular momentum during photoabsorption implies the dipole selection rule. At the Co K edge, the main contribution to XANES therefore results from the excitation of a 1s electron into unoccupied p states, while excitations into unoccupied s, d or f states are excluded.⁵⁴ However, we observe an exception to this rule when p and d states mix upon breaking of the inversion symmetry around the metal center. In that case, weak symmetry-forbidden quadrupole transitions of 1s into unoccupied d states give rise to small features in the pre-edge region. Such pre-edge features occur, among others, in the absorption spectra of transition metals.⁵⁵ From roughly 50 eV above the edge, the spectral features are governed by the interference between photoelectrons excited into the continuum and those backscattered from surrounding atoms. This EXAFS region encodes the structure of the atomic arrangement around the absorber.⁵⁴

3.1.1.1 HERFD-XANES

The end state of a conventional XAS experiment in transmission is an intermediate excited state with a finite lifetime τ_n . During the subsequent relaxation to the final state, an X-ray fluorescence photon is created. Even though we denote the state after this secondary process as the final state, further relaxation steps follow before reaching again the ground state. In turn, also the final state after photon emission has a finite lifetime τ_f . Figure 3.2a illustrates an energy diagram of a corresponding photon-in/photon-out process at the Co K edge with a $1s \rightarrow 4p$ dipole transition and a weak $1s \rightarrow 3d$ quadrupole transition.⁵⁶ Multiple decay pathways usually exist that translate into the emission of fluorescence photons with different energies. At the Co K edge, the $2p \rightarrow 1s$ relaxation leads to the emission of the K_α lines and the weak K_β lines correspond to the $3p \rightarrow 1s$ decay channel. The full landscape of excitations and relaxations provides detailed information on the electronic structure and is probed by varying both the incident and the detected emission energies, resulting in a resonant inelastic X-ray scattering (RIXS) map (Figure 3.2b).

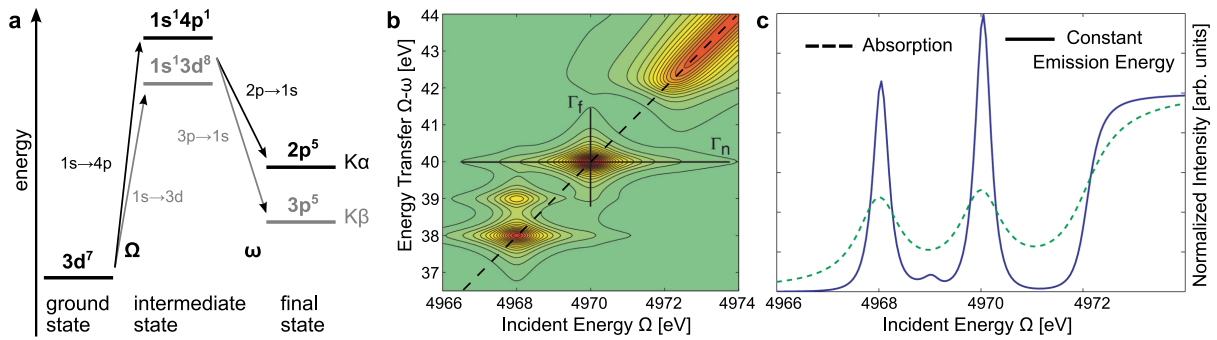


Figure 3.2. Illustration of the photon-in/photon-out process and HERFD-XAS. **a** Energy diagram of the $1s \rightarrow 4p$ excitation in Co. **b** Example RIXS plane of a similar system. Solid lines indicate the lifetime broadening. The dashed line illustrates a HERFD-XAS measurement. **c** Comparison of a conventional XAS (dashed line) and HERFD-XAS (solid line). Panels **b** and **c** adapted by permission from Springer Nature Customer Service Centre GmbH: Springer, The European Physical Journal,⁵⁸ Copyright 2009.

In conventional XAS, the finite lifetime of the intermediate state results in a core-hole lifetime broadening of the spectral features according to the Heisenberg uncertainty relation, limiting the energy resolution. Photon-in/photon-out spectroscopy provides the means to overcome this limitation. As we can see in Figure 3.2b, the broadening Γ_n along the incident energy (here Ω) due to the lifetime of the intermediate state τ_n is strong. The lifetime of the final state τ_f causes a weaker broadening Γ_f along the axis of energy transfer ($\Omega - \omega$). Moving diagonally through the RIXS plane (dashed line) gives a spectrum that resembles the conventional absorption spectrum but has a broadening smaller than Γ_n and Γ_f . This method is called high energy-resolution fluorescence-detected (HERFD) XAS (solid line in

Figure 3.2c).^{58, 59} Of course, to take advantage of bypassing the lifetime broadening, the energy resolution of the experimental setup must also fall below it. To measure HERFD-XAS, the fluorescence is detected at a specific emission line while varying the incident energy. We must note that, since only one of all possible relaxation channels is observed, HERFD-XAS spectra represent an approximation of $\mu(E)$ and some features may be different from conventional XAS (feature at 4969 eV in Figure 3.2c).⁵⁹

3.1.1.2 Following chemical reactions in solution

In Chapter 1, we have seen that the increasing complexity of nanomaterials syntheses results in a high demand for advanced methods to probe the pathways in situ. With the high brilliance of modern synchrotron sources, XANES has become a powerful method to this end. The development of dedicated beamlines for photon-in/photon-out spectroscopy enables high quality data acquisition from dilute reaction mixtures at high time resolution. Moreover, recording XANES in fluorescence mode facilitates measurements in chemical reactors, since photons are emitted from the same spot where the incident beam interacts. Thus, the reactor only needs one X-ray transparent window. Furthermore, XAS does not require a specific aggregation state of the sample, but it can probe dissolved precursors, amorphous intermediates, and crystalline nanoparticles in a reaction mixture.

Using the absorption spectrum as a fingerprint for a specific chemical compound is a common approach to track chemical reactions. A time-resolved set of spectra then allows to detect which compounds are present at all steps of a synthesis. To this end, the high energy resolution of HERFD-XANES means a strong advantage when distinguishing similar chemical species with only slightly different spectral features, such as organo-metallic complexes exchanging individual ligands.⁶⁰

However, the method can go beyond fingerprinting chemical compounds.⁶¹ As we have seen in Section 3.1.1, the post-edge features result from excitations into delocalized unoccupied states and are dominated by interference upon multiple-scattering at neighboring atoms. Thus, they encode information on ligands in the chemical environment of the absorber. Excitations into unoccupied localized states raise pre-edge features which additionally reflect the precise geometry within the first coordination shell around the absorber. The link between the chemical environment of the absorber and the spectral features becomes more easily accessible by comparing measured data with calculated absorption spectra. To this end, the FEFF code is a powerful implementation of the real-space multiple-scattering theory and allows for precise calculations of XANES and EXAFS spectra.⁶² The calculations enable us to identify species which are not easily measurable *ex situ*, like intermediate organo-metallic complexes that only exist for a limited time during a nanoparticle synthesis.

3.1.2 X-ray scattering methods

X-ray scattering complements the chemical information accessible with XAS. It probes the structure of matter by means of the scattered intensity $I(\mathbf{q})$. From a historical perspective, this topic is often introduced in the context of X-ray diffraction from crystalline solids, which denotes the special case of X-ray waves scattered from a *periodic* structure interfering into a *periodic* diffraction pattern. However, non-crystalline forms of matter are of considerable importance not only due to their technological significance, but also since they often denote intermediate states during the formation of crystalline solids (c.f. Section 2.2). Thus, in this section, we will start with the general relation between scattered X-rays and the structure of matter, and cover crystals later on.

A recurring observation in the following sections is that the amplitude $A(\mathbf{q})$ of scattered X-rays encodes the structure of matter in reciprocal space, which relates to the real-space structure by a Fourier transform. However, due to the missing phase information in the measurement of $I(\mathbf{q}) \propto |A(\mathbf{q})|^2$, the

absolute positions of scatterers cannot easily be reconstructed.⁶³ The most straightforward goal of a scattering experiment is thus to resolve their relative positions, i.e. the distances between scatterers, which are readily accessible.^a

In order to describe an elastic X-ray scattering experiment, we can disregard the frequency-dependent contributions to the atomic form factor in Equation 3.1 and focus on $f^0(\mathbf{q})$, which yields the amplitude $A(\mathbf{q})$ of X-rays scattered from a single atom in units of the Thomson scattering length r_0 . We assume that the scattering plane spanned by \mathbf{k}_i and \mathbf{k}_f is perpendicular to the polarization of the incident X-rays. If this is not the case, a polarization factor needs to be considered. In the so-called Born approximation, we furthermore disregard multiple scattering, which is valid for most scattering experiments. $f^0(\mathbf{q})$ results from integrating the electron number density $\rho_e(\mathbf{r})$ over the volume of the atom. Each volume element $d\mathbf{r}$ at a given \mathbf{r} carries a phase factor $e^{i\mathbf{q}\mathbf{r}}$.

$$A(\mathbf{q}) = -r_0 f^0(\mathbf{q}) = -r_0 \int \rho_e(\mathbf{r}) e^{i\mathbf{q}\mathbf{r}} d\mathbf{r} \quad (3.4)$$

$f^0(\mathbf{q})$ is the Fourier transform of the real-space electron density of the atom. It is equal to the atomic number Z in the case of forward scattering ($q = |\mathbf{q}| = 0$) and decreases with increasing q . The precise scattering behavior depends on the shape of the atomic orbitals and is tabulated for all elements.⁶⁴ From $f^0(\mathbf{q})$, we can directly formulate the scattering intensity from a disordered arrangement of N atoms of the same element. Conventionally, we stay in units of $-r_0$.

$$I(\mathbf{q}) = \frac{AA^*}{r_0^2} = f^{02} \sum_n e^{i\mathbf{q}\mathbf{r}_n} \sum_m e^{-i\mathbf{q}\mathbf{r}_m} = Nf^{02} + f^{02} \sum_n \sum_{m \neq n} e^{i\mathbf{q}(\mathbf{r}_n - \mathbf{r}_m)} \quad (3.5)$$

Similar to the integral over the atomic volume in Equation 3.4, we can integrate over the volume V of the atomic arrangement to replace the sum over $m \neq n$.

$$I(\mathbf{q}) = Nf^{02} + f^{02} \sum_n \int_V \rho_n(\mathbf{r}_{nm}) e^{i\mathbf{q}(\mathbf{r}_n - \mathbf{r}_m)} dV_m \quad (3.6)$$

Here, $\rho_n(\mathbf{r}_{nm})$ is the local atomic number density at the position $\mathbf{r}_n - \mathbf{r}_m$. Since the scattering signal arises from deviations of the local atomic density from the average density ρ_{at} , subtracting and adding a term proportional to ρ_{at} allows us to separate two important contributions.

$$I(\mathbf{q}) = \underbrace{Nf^{02} + f^{02} \sum_n \int_V (\rho_n(\mathbf{r}_{nm}) - \rho_{\text{at}}) e^{i\mathbf{q}(\mathbf{r}_n - \mathbf{r}_m)} dV_m}_{I^{\text{SR0}}(\mathbf{q})} + \underbrace{f^{02} \rho_{\text{at}} \sum_n \int_V e^{i\mathbf{q}(\mathbf{r}_n - \mathbf{r}_m)} dV_m}_{I^{\text{SAXS}}(\mathbf{q})} \quad (3.7)$$

Averaging $\rho_n(\mathbf{r}_{nm})$ in Equation 3.7 over different choices of origin leads to a simplified expression for $I(\mathbf{q})$.

$$I(\mathbf{q}) = \underbrace{Nf^{02} \left[1 + \int_V (\rho(\mathbf{r}) - \rho_{\text{at}}) e^{i\mathbf{q}\mathbf{r}} dV \right]}_{I^{\text{SR0}}(\mathbf{q})} + \underbrace{f^{02} \left| \int_V \rho_{\text{at}} e^{i\mathbf{q}\mathbf{r}} dV \right|^2}_{I^{\text{SAXS}}(\mathbf{q})} \quad (3.8)$$

^a Resolving the full real-space structure of an object by recovering the phase information is a rich discipline. One example is resolving the periodic atomic structure of a single crystal from several diffraction experiments (c.f. Section 3.1.2.3) at multiple rotation angles. Here it can help to label specific sites in the structure composed of e.g., complex biomolecules, with heavily scattering atoms. Furthermore, using coherent X-rays, it is possible to reconstruct even non-periodic objects via an appropriate phase retrieval strategy (c.f. Section 3.2.2).

The first term is sensitive to local fluctuations in $\rho(\mathbf{r}) - \rho_{\text{at}}$ in the range of a few interatomic distances. The scattering described by $I^{\text{SRO}}(\mathbf{q})$ therefore contains information on short range order. The second term $I^{\text{SAXS}}(\mathbf{q})$ only contributes if $q \rightarrow 0$, i. e. at small scattering angles, and encodes structural information on size scales much larger than interatomic distances. We shall in the following discuss the two terms individually, as they correspond to different experimental methods.⁵⁰

3.1.2.1 Atomic pair distribution function

We can rearrange the term $I^{\text{SRO}}(\mathbf{q})$ to yield the atomic pair distribution function (PDF). By averaging over all possible orientations of \mathbf{r} , the phase factor $e^{i\mathbf{q}\cdot\mathbf{r}}$ becomes $\sin(qr)/qr$. Also, if we assume an isotropic arrangement of atoms, which is usually true in amorphous matter, we can replace $\rho(\mathbf{r})$ with $\rho(r)$. Then, by applying an inverse Fourier transform to $I^{\text{SRO}}(q)$ in Equation 3.8, we arrive at the PDF $g(r)$.

$$g(r) = \frac{\rho(r)}{\rho_{\text{at}}} = 1 + \frac{1}{2\pi^2 r \rho_{\text{at}}} \int_0^\infty q \left[\frac{I^{\text{SRO}}(q)}{N f_0^2} - 1 \right] \sin(qr) dq \quad (3.9)$$

Equation 3.9 allows to convert the intensities $I^{\text{SRO}}(q)$ into a PDF, which represents a histogram of interatomic distances (Figure 3.3).^b A peak in $g(r)$ means that two atoms in the sample often have this particular distance r .⁵⁰ In a real experiment, the Fourier transform is very sensitive to any background scattering from the sample matrix, thus one needs to carefully subtract the background before generating the PDF from measured scattering intensities. A second prerequisite results from the integral in Equation 3.9. To avoid artefacts from the Fourier transform, one needs to record $I(q)$ within a wide q -range and at high resolution.⁵¹

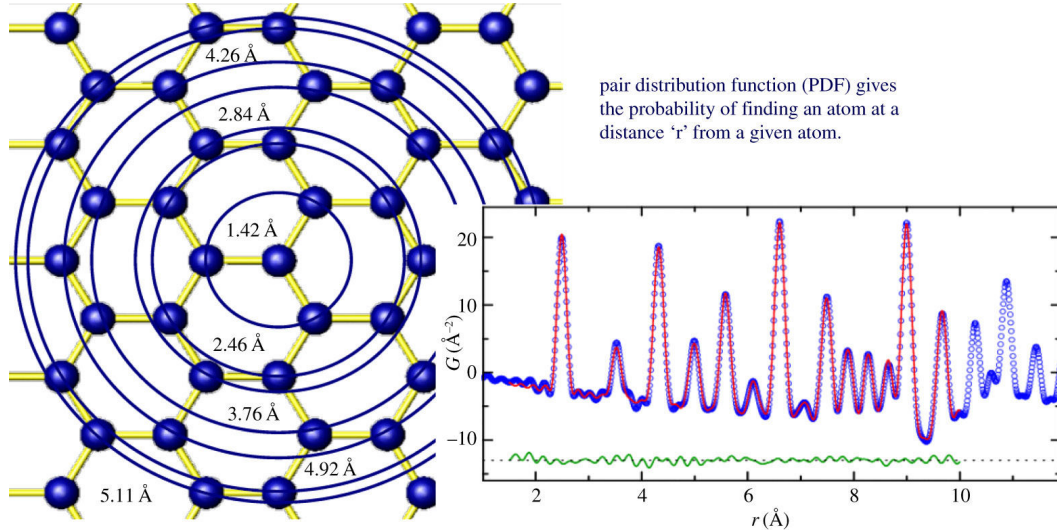


Figure 3.3. Illustration of the pair distribution function. Reprinted with permission from ⁶⁵. Copyright 2019, The Royal Society.

The PDF enables studying the atomic arrangement in liquids, dissolved molecules and complexes, as well as in amorphous solids, where standard X-ray diffraction cannot be applied. In these compounds, one often encounters short range order at interatomic distances in the size range of a single molecule, but the PDF becomes flat at larger correlation lengths where no order exists. The method means a great advantage for in situ measurements of nonclassical nucleation and growth phenomena. It complements the chemical information available from HERFD-XANES (c.f. Section 3.1.1.1) with structural insights,

^b The figure shows $G(r) = 4\pi r \rho_{\text{at}}(g(r) - 1)$, which can be obtained from $I^{\text{SRO}}(q)$ without knowledge of ρ_{at} .

such as monitoring small changes in bond distances while molecules or complexes rearrange and transform into crystalline nanoparticles. As the nanoparticles grow and the atoms develop medium to long range order, refining the measurements with calculated PDFs⁶⁶ further allows to estimate the strain of the unit cell and the size of crystalline domains.

3.1.2.2 Small-angle X-ray scattering

In this section, we discuss the second term on the right hand side of Equation 3.8, which only contributes at small scattering angles and therefore encodes structures which are large compared to interatomic distances. By introducing the single-particle form factor,

$$F(\mathbf{q}) = \frac{1}{V_p} \int_{V_p} e^{i\mathbf{q}\cdot\mathbf{r}} dV_p, \quad (3.10)$$

we can model the small-angle X-ray scattering (SAXS) intensity scattered from a single nanoparticle.

$$I_{\text{particle}}^{\text{SAXS}}(\mathbf{q}) = \Delta\rho^2 V_p^2 |F(\mathbf{q})|^2 \quad (3.11)$$

Here, $\Delta\rho$ is the difference in the scattering length densities of the particle and its surroundings, and V_p is the volume of the particle. For simple shapes like spheres, discs, and rods, analytical solutions for $|F(\mathbf{q})|^2$ exist, which allow to directly obtain the particle size, shape, and polydispersity from the SAXS intensities by fitting the data with the respective form factor. More complicated shapes require numerical calculations of the form factor.⁵⁰ SAXS is commonly used to study the emergence of nanoparticles in situ, and it can furthermore track the formation of mesocrystals as well as unoriented assemblies (c.f. Section 4.3.3).

3.1.2.3 X-ray diffraction

The diffuse scattering obtained from amorphous solids transforms into a periodic arrangement of spots with high intensity when the atoms crystallize into a periodic structure. The resulting X-ray diffraction^c (XRD) pattern encodes the crystal structure. To understand this behavior by means of the scattering amplitude introduced in Equation 3.4, we first need a mathematical description of the crystal structure. We can decompose every crystal structure into the convolution of a periodic lattice with an atomic basis, which is usually an arrangement of a few atoms. The set of vectors \mathbf{R}_n with

$$\mathbf{R}_n = n_1 \mathbf{a}_1 + n_2 \mathbf{a}_2 + n_3 \mathbf{a}_3 \quad (3.12)$$

specifies every lattice point. Here, \mathbf{a}_i are the primitive translations of the lattice and n_i are integers. Given the positions \mathbf{r}_i of the atoms in the basis, we can reach every atom in the structure with the set of vectors $\mathbf{R}_n + \mathbf{r}_i$. Similarly, we describe the reciprocal lattice, which is the Fourier transform of the crystal structure, by means of the reciprocal lattice vectors

$$\mathbf{G}_{hkl} = h\mathbf{b}_1 + k\mathbf{b}_2 + l\mathbf{b}_3. \quad (3.13)$$

The vectors \mathbf{b}_j are the primitive translations of the reciprocal lattice derived from the condition $\mathbf{a}_i \cdot \mathbf{b}_j = 2\pi\delta_{ij}$. Here, δ is the Kronecker delta. The integers h, k and l are denoted Miller indices.

Since we describe the crystal structure as the convolution of a lattice with a basis, it makes sense to also decompose the scattering amplitude into two contributions accordingly:

^c In a broader sense, the term diffraction can also refer to the interference of waves scattered at any obstacle.

$$F^{\text{crystal}}(\mathbf{q}) = \sum_{\mathbf{R}_n + \mathbf{r}_j} f_j^0 e^{i\mathbf{q}(\mathbf{R}_n + \mathbf{r}_j)} = \underbrace{\sum_n e^{i\mathbf{q}\mathbf{R}_n}}_{F^{\text{lattice}}(\mathbf{q})} \underbrace{\sum_i f_i^0 e^{i\mathbf{q}\mathbf{r}_i}}_{F^{\text{basis}}(\mathbf{q})} \quad (3.14)$$

The scattering amplitude corresponds to the Fourier transform of the real-space crystal structure. From evaluating the first factor on the right hand side of Equation 3.14, $F^{\text{lattice}}(\mathbf{q})$, it becomes clear why the scattering amplitude of a crystal is a set of discrete spots. The sum runs over all lattice points, which is a very large number. The phase factors $e^{i\mathbf{q}\mathbf{R}_n}$ will always cancel out, unless the phases $\mathbf{q}\mathbf{R}_n$ are multiples of 2π . From Equations 3.12 and 3.13, it is clear that the reciprocal lattice vectors \mathbf{G} meet this condition, since

$$\mathbf{G}\mathbf{R}_n = 2\pi(hn_1 + kn_2 + ln_3). \quad (3.15)$$

Thus, high scattering intensities can only be measured if $\mathbf{q} = \mathbf{G}$, which we refer to as the Laue condition. The spots of high scattering intensity at $\mathbf{q} = \mathbf{G}$ are called reflections following the concept of Bragg reflection. In this alternative approach, a set of equivalent lattice planes is identified based on a unique set of (h, k, l) with a distance d between the planes. A high scattered intensity is measured when the angle θ between the incident X-rays and the lattice planes fulfills the Bragg condition

$$n\lambda = 2d \sin(\theta) \quad (3.16)$$

which is equivalent to the Laue condition. Here, n is an integer and λ is the X-ray wavelength.⁵⁰ The full width at half maximum $\Delta(2\theta_{(hkl)})$ of a Bragg reflection encodes the size L of the crystal in the direction perpendicular to the lattice planes $(h k l)$.

$$L_{(hkl)} = \frac{K\lambda}{\Delta(2\theta_{(hkl)}) \cos(\theta_{(hkl)})} \quad (3.17)$$

Equation 3.17 is known as the Scherrer equation where $K \approx 0.9$ is the Scherrer form factor.⁶⁷

XRD rounds off the portfolio of X-ray scattering techniques. In addition to characterizing the crystal structure, it allows to determine the size, anisotropy, and orientation of crystalline domains. It is commonly used to study the growth of crystalline nanoparticles.

3.2 X-ray microscopy

3.2.1 X-ray microscopy for materials science

We have seen so far that analytical X-ray spectroscopy and scattering methods allow to track chemical and structural changes at the atomic level. In the small-angle regime, the scattering signal also contains structural information at the size scale of entire nanoparticles. SAXS, however, has the drawback that it requires a model to interpret the data and extract insights on the morphology. Therefore, it can be difficult to arrive at an unequivocal understanding of shape transformation processes such as void formation. Also, the X-ray analytical methods usually average over a given sample volume and do not allow to observe single nano-objects individually. Hence, the ultimate tool for probing the mechanisms underlying various nanoparticle morphologies is a direct visualization at the micro-to-nanometer scale using X-ray microscopy. The method denotes a paradigm shift in the way we study nanostructures in situ, away from ensemble-averaging and model-based analyses towards real-time visual observations.

Indeed, X-ray microscopy has proven to enable this novel, direct way of observing nanostructures in different modern fields of materials research. Here, in situ studies in gas atmospheres and at high

temperatures compose a major group of experiments. After an early demonstration on lithium zirconate nanoparticles studied at 600 °C in a CO₂ atmosphere,⁶⁸ in situ X-ray microscopy visualized the annealing of Au nanoparticles in different gas atmospheres⁶⁹⁻⁷¹ and revealed a phase transition during the melting of Sn-Bi alloy particles with a spatial resolution of 25 nm.⁷² Operando measurements denote another promising class of experiments, tracking the effect of real operating conditions on particle morphology. Recent gas-phase experiments revealed morphological changes of a porous Ni/Al₂O₃ gel catalyst during the methanation of CO₂ with H₂ at 400 °C.⁷³ Also, by exploiting magnetic contrast obtained with a circularly polarized X-ray beam, the magnetization of GdCo microdiscs was visualized in 3D during repetitive magnetization.⁷⁴ X-ray microscopy using a free electron laser furthermore showed the formation of cracks in micrometer-sized Ge particles within a lithium ion battery anode during cycling.⁷⁵

To date, however, examples of X-ray microscopy experiments on nanoparticle syntheses are very rare, despite the great potential that comes from this method. This may be due to the fact that the vast majority of nanoparticle growth and transformation processes takes place in solution at elevated temperatures, which requires imaging in a more challenging liquid environment compared to the aforementioned examples.

In this thesis, we extend the capabilities of in situ X-ray microscopy to samples in solution (Chapter 6), visualizing nanoparticle growth and shape transformation (Chapter 7). We make use of the latest developments in hard X-ray ptychography, which provides access to time-resolved morphological information at the required spatial resolution. Ptychography is a scanning microscopy technique based on coherent diffraction (c.f. Section 3.2.2). It is possible to combine ptychography with analytical methods in a multimodal imaging experiment. In combination with XAS, resonant ptychography revealed the chemical state of Au nanoparticles with high spatial resolution.⁷⁶ In Chapter 8, we combine ptychographic imaging with XRD to track the crystallographic orientation of nanoparticles while we image them in situ.

3.2.2 Ptychography

Ptychography allows to reconstruct an aperiodic object from diffraction patterns that result from the interaction of the object with a coherent X-ray wavefield.^{77, 78} This task requires to recover the phase information lost during the measurement of the diffraction patterns. As we will see, the phase retrieval is achieved by propagating the X-ray wave back and forth iteratively between the detector plane and the object. The method was conceived already in the late 1960s,^{79, 80} however, it became computationally feasible only in the last two decades.⁸¹⁻⁸⁶

To describe the interaction of the coherent wavefield with the object, we recall the atomic form factor introduced in Equation 3.1. Any material consisting of an ensemble of scattering atoms induces a phase shift to an X-ray wave as it propagates through the material, as well as reduces its amplitude due to absorption. We can express these two effects by means of the complex-valued refractive index $n(\omega)$.

$$n(\omega) = 1 - \frac{\rho_{at} r_0 \lambda^2}{2\pi} f(q = 0) \quad (3.18)$$

Here, $f(q = 0)$ is the atomic form factor for forward scattering. We can rewrite $n(\omega)$ in a way that the phase shift induced when X-rays travel through a material is expressed in a refractive index decrement δ , and the absorption is given by an imaginary part $i\beta$:

$$n(\omega) = 1 - \delta + i\beta, \quad \text{with} \quad \delta = \frac{\rho_{at} r_0 \lambda^2}{2\pi} (Z + f'(\omega)) \quad \text{and} \quad \beta = \frac{\rho_{at} r_0 \lambda^2}{2\pi} f''(\omega) \quad (3.19)$$

3.2.2.1 The basic ptychographic model

The most essential components of the ptychographic model are two functions modeling the illuminating X-ray wavefield (probe) $P(\mathbf{r})$ and the object to be visualized, $O(\mathbf{r})$. Both functions are defined in two dimensions, thus $\mathbf{r} = (r_x, r_y)$. The beam axis defines the z direction. Standard ptychography, like other coherent imaging techniques, relies on the fact that $P(\mathbf{r})$ is a single mode given by its amplitude $A_P(\mathbf{r})$ and phase $\phi(\mathbf{r})$:

$$P(\mathbf{r}) = A_P(\mathbf{r}) e^{i\phi(\mathbf{r})} \quad (3.20)$$

The coherent illumination is incident on the object transmission function $O(\mathbf{r})$ that models the phase shift and the absorption induced by the object:

$$O(\mathbf{r}) = \underbrace{\exp\left(ik \int \delta(\mathbf{r}, r_z) dr_z\right)}_{\text{phase shift}} \cdot \underbrace{\exp\left(-k \int \beta(\mathbf{r}, r_z) dr_z\right)}_{\text{absorption}} \quad (3.21)$$

where $k = \frac{2\pi}{\lambda}$ is the wave number of the probing X-rays. Since for ptychography the object should be two-dimensional (2D), $O(\mathbf{r})$ is defined as the projection of the phase shift and absorption induced by the object along the beam direction. As we will see in the next section, this is an approximation neglecting changes of the illumination along the thickness of a real object.

From Equations 3.19 and 3.21, it follows that the phase shift in $O(\mathbf{r})$ directly relates to the atomic density and the atomic form factor. Thus, ptychographic phase images allow to determine the thickness of a reconstructed object quantitatively given that its chemical composition is known. If the X-ray energy is not close to an electronic binding energy, we can utilize tabulated values of the atomic form factors of the elements present in the sample to calculate δ .⁶⁴ We make use of this property in Chapter 7, when we derive a 3D growth model of nanoparticles from ptychographic projections and in Chapter 8, we estimate the amount of material in selected image areas.

After the probe interacted with the object, the exit wavefield $\psi(\mathbf{r})$ directly behind the object is simply given by the multiplication of the two:

$$\psi(\mathbf{r}) = P(\mathbf{r}) O(\mathbf{r}) \quad (3.22)$$

From here, the exit wavefield propagates to the detector. The fact that the wavefield consists of a single coherent mode allows to calculate its amplitude and phase in any plane along the r_z direction. The actual mathematical operation to be performed depends on the propagation distance. In the near field, we use the Fresnel propagator \mathcal{N} while in the far field (Fraunhofer regime), the propagator is equivalent to the Fourier transform \mathcal{F} .⁵² To arrive at the detector, which is positioned in the far field, we thus calculate

$$\Psi(\mathbf{q}) = \mathcal{F}(\psi(\mathbf{r})) \quad (3.23)$$

If the detector was capable of measuring amplitude and phase of the complex-valued $\Psi(\mathbf{q})$, we could propagate this back to the object plane and, with knowledge of $P(\mathbf{r})$, calculate the object function. Unfortunately, the detector only measures $I(\mathbf{q}) = |\Psi(\mathbf{q})|^2$, thereby losing the phase information. The phases need to be recovered to calculate $O(\mathbf{r})$ and $P(\mathbf{r})$, which in ptychography is achieved on the basis of j discrete measurements of $I_j(\mathbf{q})$ at different relative shifts $\Delta\mathbf{r}_j$ between the object and the probe. Phasing is then handled by an iterative reconstruction algorithm.

Before we discuss the data acquisition and the reconstruction algorithm, however, we need to lay out a way to handle real-world samples which are often not at all two-dimensional. To model the interaction

of the probe with such a thick object, we need to take into account the propagation of the wavefield within the sample.

3.2.2.2 Extension of the model to thick objects

We have seen that in the basic ptychographic model, the object function is a projection of the phase-shifting and absorbing properties of the sample, and that its interaction with the probe is modeled by a multiplication. This thin sample approximation only holds if the illumination does not change significantly as it propagates inside the sample. A first estimation of the maximum propagation distance that we can tolerate within the sample is given by the depth of field (DOF) of the imaging geometry (c.f. Section 3.2.2.5). If the extension of the sample along the beam direction falls below the DOF, we can consider it optically thin.

If this is not the case, we need to model the object as consisting of several layers, each of which fulfills the thin sample approximation. We furthermore introduce additional propagation steps between the layers. This approach is called the multi-slice model.⁸⁷ At every object slice $O_i(\mathbf{r})$, the probe $P_i(\mathbf{r})$ interacts and forms the respective exit wave $\psi_i(\mathbf{r})$ just as it was the case in the basic model (c.f. Equation 3.22).

$$\psi_i(\mathbf{r}) = P_i(\mathbf{r}) O_i(\mathbf{r}) \quad (3.24)$$

The exit wave then propagates a distance d_i to the next slice, where it acts as the new probe $P_{i+1}(\mathbf{r})$.

$$P_{i+1}(\mathbf{r}) = \mathcal{N}_{i,i+1}(\psi_i(\mathbf{r})) \quad (3.25)$$

Here, $\mathcal{N}_{i,i+1}$ denotes the near-field propagator along the distance from slice i to slice $i + 1$. To model the propagation correctly, the distances between the slices must be known with an accuracy smaller than the DOF. The procedure is repeated until the wavefield interacted with all n slices of the sample. Then, the propagation to the detector takes place in accordance with the basic model (c.f. Equation 3.23).

$$\Psi(\mathbf{q}) = \mathcal{F}(\psi_{i=n}(\mathbf{r})) \quad (3.26)$$

The multi-slice model has the great advantage not only to enable imaging of thick samples, but also to achieve depth resolution within the sample, thereby partially revealing its internal structure in 3D. Having elaborated the ptychographic model for the general case of thick samples, we will continue with the experimental procedure to record a ptychographic data set.

3.2.2.3 Data acquisition and sampling requirements

We already stated that it is not possible to calculate $O_i(\mathbf{r})$ and $P(\mathbf{r})$ from a single measurement of $I(\mathbf{q}) = |\Psi(\mathbf{q})|^2$ at the detector due to the missing phase information. To overcome this problem, we take a number of measurements $I_j(\mathbf{q})$ while scanning the object in the (r_x, r_y) plane with respect to the probe position. This way, each measurement of $I_j(\mathbf{q})$ is recorded at a different offset Δr_j between the object and the probe (Figure 3.4). For the reconstruction, all diffraction patterns and the respective measured offsets are combined into one ptychographic data set. However, scanning is only one part of the solution and by itself, it does not increase the amount of information contained in the diffraction patterns. The key to making the ptychographic problem solvable is an overlap of the probe between adjacent scan points, thereby creating redundant information in $I_j(\mathbf{q})$. Usually, with an overlap of 60 % to 70 %, the redundancy reaches a level that allows to perform phase retrieval and recover $O_i(\mathbf{r})$ and $P(\mathbf{r})$. When a thick sample is imaged with a divergent beam, one needs to pay attention that this overlap condition is fulfilled in all slices $O_i(\mathbf{r})$.

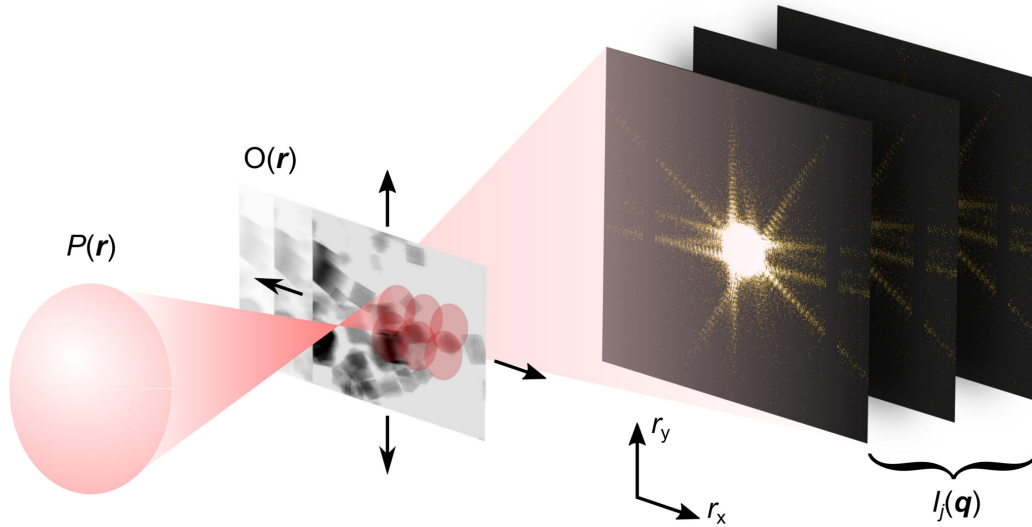


Figure 3.4. Acquisition scheme of a ptychographic data set. $O(\mathbf{r})$ is illustrated on the example of Cu_2O nanocubes (c.f. Chapters 6-8). The object is scanned in the (r_x, r_y) plane near the focus of the coherent illumination. At each position, a diffraction pattern is recorded in the far field.

It is important to note that the ptychographic model expects background-free diffraction patterns in which the intensity results purely from the coherent interaction between the probe and the object in forward direction. No other scattering effects, inside or outside the sample, such as scattering from the sample matrix or from air, are modeled. Those will contribute to an incoherent background in the diffraction patterns, potentially concealing the coherent signal towards higher q and limiting the spatial resolution of the reconstructions.

In addition to the overlap of the probe and the reduction of incoherent background, we must also ensure proper sampling of the speckles in the diffraction patterns. Sufficient sampling is achieved when the pixel size of the detector p_{det} is smaller than half the speckle size. Given that the speckle size scales inversely to the size of the illumination P , we can restrict the illumination size below to a certain limit to keep the speckles resolvable.

$$P < \frac{\lambda d_{\text{SD}}}{2p_{\text{det}}} \quad (3.27)$$

Here, d_{SD} is the distance between the sample and the detector. When using a focused X-ray beam, the sample is positioned at a certain defocus to adjust the illumination size.

Having recorded a ptychographic data set with sufficient overlap of the probe and properly sampled speckles in ideally low-background diffraction patterns, we can move on to the image reconstruction.

3.2.2.4 The 3PIE reconstruction algorithm

In order to recover the object slices $O_i(\mathbf{r})$ and the probe $P(\mathbf{r})$ from the measurements $I_j(\mathbf{q})$ at their respective offset Δr_j , it is necessary to solve the inverse problem posed by the ptychographic model. We can achieve this task by means of the three-dimensional ptychographic iterative engine (3PIE) algorithm.⁸⁷ It represents a generalization of the originally developed extended iterative ptychographic engine (ePIE) algorithm that was only capable of reconstructing objects consisting of a single slice.⁸³ The working principle is based on an iterative propagation of the wavefield from the object to the detector and back to the object, while updating the object and probe functions using the measured intensities. The algorithm is outlined in Figure 3.5. We can separate the algorithm into the forward direction (left side in Figure 3.5) and the backward direction (right side).

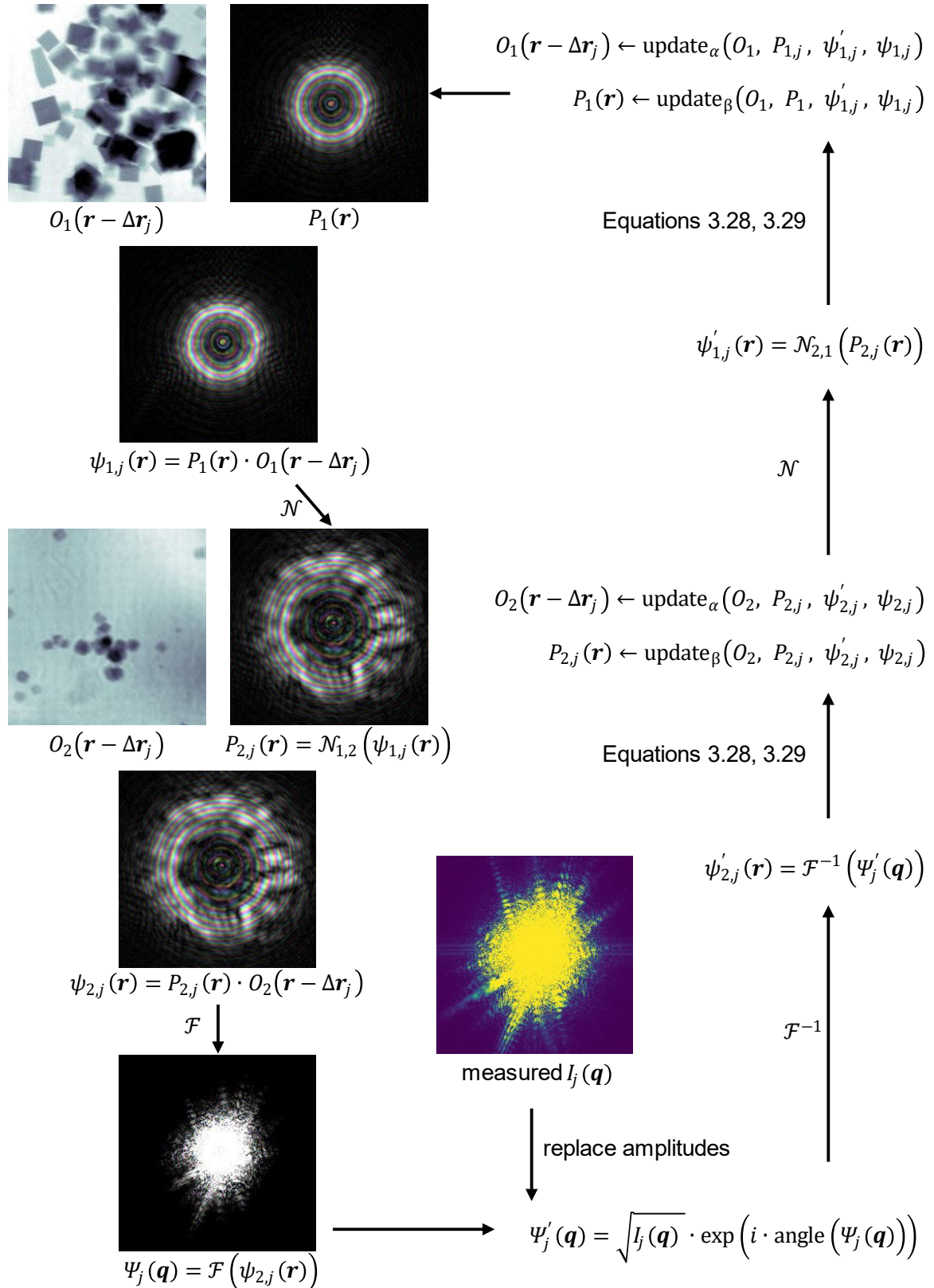


Figure 3.5. The 3PIE reconstruction algorithm on the example of a 2-sliced object. In the forward direction (left side), the algorithm calculates the Ptychographic model until arriving at the detector plane. These steps are illustrated with a simulated wavefield. The brightness represents the amplitude of the wave, and the color encodes its phase. The scattering power of the object was enhanced for a good visibility of the scattering signal. At the detector, the amplitudes are replaced using the measured signal. In the backward direction, an update step is performed at each object slice. $O(\mathbf{r})$ is illustrated on the example of Cu_2O nanocubes (c.f. Chapters 6-8).

In the forward direction, the algorithm calculates the ptychographic model of a thick object as described above. It is advantageous that in the first iteration, no information needs to be a priori known about the object besides the number of slices and their spacing. Usually, the slices $O_i(\mathbf{r})$ are initialized to be non-phase-shifting and non-absorbing. However, making an educated guess on $P_1(\mathbf{r})$ can help to direct the algorithm towards a good solution. In this thesis, we either use a Gaussian illumination profile according to the parameters of the focussing optics, or a previously reconstructed illumination to initialize $P_1(\mathbf{r})$. In the detector plane, the amplitudes of $\Psi_j(\mathbf{q})$ are replaced by $\sqrt{I_j(\mathbf{q})}$ obtained in the measurement, yielding an updated $\Psi'_j(\mathbf{q})$. The phases, which were not measured, are left unchanged.

In the backward direction, the wavefield is first propagated back from the far field via an inverse Fourier transform \mathcal{F}^{-1} , so that it arrives at the exit wavefield $\psi'_{i=n}(\mathbf{r})$ the object slice which is closest to the detector. There, the object slice and probe functions are updated according to Equations 3.28 and 3.29.

$$O_i(\mathbf{r} - \Delta\mathbf{r}_j) \leftarrow O_i(\mathbf{r} - \Delta\mathbf{r}_j) + \alpha \frac{P_i^*(\mathbf{r})}{|P_i(\mathbf{r})|_{max}^2} (\psi'_{i,j}(\mathbf{r}) - \psi_{i,j}(\mathbf{r})) \quad (3.28)$$

$$P_i(\mathbf{r}) \leftarrow P_i(\mathbf{r}) + \beta \frac{O_i^*(\mathbf{r} - \Delta\mathbf{r}_j)}{|O_i(\mathbf{r} - \Delta\mathbf{r}_j)|_{max}^2} (\psi'_{i,j}(\mathbf{r}) - \psi_{i,j}(\mathbf{r})) \quad (3.29)$$

The parameters α and β denote the update strength per step. From there, the probe $P_{i=n}(\mathbf{r})$ is back-propagated with $\mathcal{N}_{i,i-1}$ to the next object slice, yielding the exit wavefield $\psi'_{i=n-1}(\mathbf{r})$ of that slice. Alternating update and back-propagation steps are repeated until arriving back at $P_1(\mathbf{r})$. Performing this procedure for all j measurements in random order completes one iteration of the algorithm. The algorithm usually runs for several hundred iterations until it converges. We can follow this process by means of the error measure

$$R = \sum_j \left| \sqrt{I_j(\mathbf{q})} - |\Psi_j(\mathbf{q})| \right|^2. \quad (3.30)$$

3.2.2.5 Spatial resolution

The spatial resolution is an important measure to determine the quality of a microscopic measurement. It specifies how close two structural features in the sample can be to still be recognized as separate features in the image. We differentiate the lateral resolution in the (r_x, r_y) plane from the depth resolution in r_z direction.

Lateral resolution

The best achievable lateral resolution (δr) in a coherent imaging experiment, that is the smallest distance at which two features can be resolved as separate, is given by the Abbe resolution limit^{52, 88}

$$(\delta r) \geq \frac{\lambda}{\text{NA}} \quad \text{where} \quad \text{NA} = n \sin\left(\frac{\Omega}{2}\right). \quad (3.31)$$

Here, NA denotes the numerical aperture and Ω is the opening angle of the objective lens. In ptychography, the objective lens of a conventional imaging setup is replaced by the propagation to the far-field detector and the subsequent phase retrieval. We could thus use the opening angle covered by this virtual objective lens in Equation 3.31. Consequently, the resolution in ptychography can exceed that of X-ray optics which usually have a small NA. Moreover, as opposed to conventional scanning

transmission X-ray microscopy (STXM), the lateral resolution is not limited by the beam size on the sample.

In practice, however, the opening angle to be used for calculating the resolution limit is usually smaller than the full opening angle covered by the detector, since the scattering intensity from the sample becomes weaker at higher q and eventually is indistinguishable from the background. Thus, even though we use the same imaging geometry, the resolution limit varies between experiments. It depends on the scattering power of the sample and the statistics of the measurement.

The measurement of the diffraction patterns with a pixel detector furthermore results in a discrete pixel size p_{rec} of the reconstructed object given by

$$p_{\text{rec}} = \frac{\lambda d_{\text{SD}}}{N_{\text{det}} p_{\text{det}}} = \frac{(\delta r)_{\text{det}}}{2} \quad (3.32)$$

where d_{SD} is the distance between the sample and the detector, p_{det} is the detector pixel size, and N_{det} is the size of the diffraction patterns in pixels. Restricting N_{det} to that area of the detector containing coherent scattering signal by cropping the diffraction patterns results in a reconstructed pixel size that reflects the best achievable resolution of the imaging experiment.

The actually achieved resolution in a ptychographic reconstruction can be worse than the resolution limit calculated so far due to experimental imperfections, especially when doing in situ measurements in a heated solution:

- The X-ray probe can change due to inhomogeneities in the reaction medium while propagating through the reactor. Such changes are not covered by the ptychographic model.
- The thermal expansion of the setup during heating leads to an unknown displacement of the sample. This reduces the accuracy in the measurement of the offset Δr_j . We can mitigate this problem with an extension of the reconstruction algorithm called position refinement,⁸⁹ which corrects the measured positions in a way that leads to a better agreement between the measured and calculated diffraction patterns.
- An intrinsic problem of in situ ptychography is that the sample changes during the acquisition of a single data set. This is not modeled in the ptychographic algorithm. Thus, the experimenter needs to find a compromise between a fast measurement to keep the changes of the sample per image acquisition small, and sufficient statistics in the measurement of the diffraction patterns.

Depth resolution

When we introduced the multi-slice model to cover thick objects in ptychography, we said that each slice must be thinner than the DOF in order not to violate the thin sample approximation. Similarly, the DOF sets the minimal distance at which two slices in the object can be spaced in order to reconstruct them separately. The theoretical DOF in ptychography can be estimated from Ewald sphere constructions:⁹⁰

$$\text{DOF} = \frac{2(\delta r)^2}{\lambda}. \quad (3.33)$$

However, empirical studies^{91, 92} indicated that the real DOF in ptychography is by a factor of 2.6 larger than predicted by Equation 3.33. In either case, the DOF is related to the actually achieved lateral resolution of the reconstructions. Therefore, we need to evaluate for each data set whether multiple object slices can be separated. We shall cover this topic in more detail in Chapter 6 by means of actual measurements on multiple layers of nanoparticles inside a chemical reactor, in preparation of in situ experiments presented in later chapters.

3.3 Summary

The portfolio of X-ray methods outlined in this chapter provides the means for detailed investigations at all stages of nanomaterials formation in solution. Within the XANES region of an X-ray absorption spectrum measured with high energy resolution in fluorescence mode, we can track the oxidation state of metals and identify ligands in their close chemical environment (c.f. Section 3.1.1). X-ray scattering techniques provide complementary structural information. The PDF analysis of total scattering data is particularly useful to study amorphous materials and molecules in solution (c.f. Section 3.1.2.1), while XRD probes the structure, size, and orientation of crystals (c.f. Section 3.1.2.3). Scattering at small angles within the SAXS range models the structure of materials at the scale of individual nanoparticles and their assemblies (c.f. Section 3.1.2.2). We shall see in Chapter 4 that a combination of the analytical techniques is most effective to study a nonclassical nanomaterial synthesis, following chemical reactions and the associated structural changes on the molecular and mesoscopic length scales.

Microscopy complements the analytical X-ray techniques by directly visualizing nanomaterials during their growth. This way, we can overcome the model-based interpretation of analytical measurements and obtain an immediate proof of the growth and shape transformation mechanisms that we observe. Ptychography is a microscopy technique that combines coherent diffraction imaging with a scanning scheme (c.f. Section 3.2.2). It reconstructs the object under study and the illuminating probe without a priori knowledge, and at a spatial resolution which is not limited by the beam size. The absorption and phase shift of the object are related to its atomic density and form factor. This allows to quantitatively assess the thickness of the object or the amount of material in the sample from the ptychographic projections, given that its chemical composition is known. As we shall see in Chapter 6, the depth resolution that comes in with the multi-slice model (c.f. Section 3.2.2.2) is particularly useful to image nanoparticles inside a bulky chemical reactor.

4 X-ray studies bridge the molecular and macro length scales during the emergence of CoO assemblies

The content of this chapter was published in Nature Communications 12, 4429 (2021) by Lukas Grote, Cecilia A. Zito, Kilian Frank, Ann-Christin Dippel, Patrick Reisbeck, Krzysztof Pitala, Kristina O. Kvashnina, Stephen Bauters, Blanka Detlefs, Oleh Ivashko, Pallavi Pandit, Matthias Rebber, Sani Y. Harouna-Mayer, Bert Nickel, and Dorota Koziej as corresponding author.

These authors contributed equally: Lukas Grote, Cecilia A. Zito, Kilian Frank

My contribution to this work comprises the synthesis of CoO nanoassemblies, the measurement and analysis of in situ HERFD-XANES, the FEFF simulations, the measurement of in situ total scattering, and the TEM characterization.

4.1 Abstract

The key to fabricating complex, hierarchical materials is the control of chemical reactions at various length scales. To this end, the classical model of nucleation and growth fails to provide sufficient information. Here, we illustrate how modern X-ray spectroscopic and scattering in situ studies bridge the molecular- and macro- length scales for assemblies of polyhedrally shaped CoO nanocrystals. Utilizing high energy-resolution fluorescence-detected X-ray absorption spectroscopy, we directly access the molecular level of the nanomaterial synthesis. We reveal that initially $\text{Co}(\text{acac})_3$ rapidly reduces to square-planar $\text{Co}(\text{acac})_2$ and coordinates to two solvent molecules. Combining atomic pair distribution functions and small-angle X-ray scattering, we observe that, unlike a classical nucleation and growth mechanism, nuclei as small as 2 nm assemble into superstructures of 20 nm. The individual nanoparticles and assemblies continue growing at a similar pace. The final spherical assemblies are smaller than 100 nm, while the nanoparticles reach a size of 6 nm and adopt various polyhedral, edgy shapes. Our work thus provides a comprehensive perspective on the emergence of nanoassemblies in solution.

4.2 Introduction

With the emerging demand for materials with complex morphological and structural properties, understanding their formation in solution continues to be a major challenge. Most syntheses of colloidal nanoparticles rely on classical crystallization and growth by monomer addition from supersaturated media, which enables the rational synthesis of nanocrystals.^{19, 93-98} The recently discovered nonclassical formation pathways involving the assembly of building blocks into distinctive superstructures have opened up completely new ways of complex nanomaterials design.^{13, 22, 99, 100} Different mechanisms exist within the scope of these nonclassical pathways.^{13, 24, 29} Besides the oriented assembly of nanocrystals into mesocrystals,^{22, 101, 102} the formation of polycrystalline, unoriented assemblies from distinct primary structures^{23, 26, 99, 103-105} is a major yet rather unexplored branch (see Cölfen et al. 2019¹³, Figure 1d). To date, nonclassical nucleation is still far from reaching the level of control established for classical growth pathways. This is by no means a surprise, since the fundamental phenomena cannot be easily generalized, and the existing theory merely provides an overview of possible pathways.^{13, 106, 107} The

major experimental difficulties to provide a unique description arise from the fact that we need to study the complex chemical and structural changes on multiple length scales.

To date, synchrotron-based methods such as X-ray absorption spectroscopy (XAS) and powder X-ray diffraction (PXRD)^{14, 18, 108-114} are routinely combined to study colloidal reactions. However, to follow chemical and electronic changes in complex reactions in solution with high sensitivity and at low concentrations,¹¹⁵⁻¹¹⁸ more advanced spectroscopic techniques such as high energy-resolution fluorescence-detected X-ray absorption near edge structure (HERFD-XANES) are needed. Compared to conventional XAS, the higher energy resolution of HERFD-XANES makes it sensitive to subtle changes in the local chemical environment of the absorbing atom. Complementary structural information can be obtained from the pair distribution function (PDF) analysis of high energy in situ X-ray total scattering. This method takes into account both the Bragg scattering from crystalline and the diffuse scattering from amorphous phases. It results in a real space representation of the interatomic distances of all constituents in a reaction mixture. In this manner, local ordering during the formation of nuclei, the initial growth of nanocrystals as well as the restructuring of solvent molecules at the surface of nanoparticles were revealed.¹¹⁹⁻¹²² Self-assembly of building blocks into superstructures can be probed with small-angle X-ray scattering (SAXS).¹²³⁻¹²⁵ This way, length scales all the way from atomic to macroscopic are accessible via X-ray techniques.

Here, we uniquely combine HERFD-XANES, PDF and SAXS to study the emergence of CoO nanoassemblies, a noticeable example for a nonclassically crystallized nanostructure. In general, cobalt oxide has applications in lithium ion^{126, 127} and lithium oxygen batteries,¹²⁸ as a catalyst for electrochemical^{129, 130} and for solar water splitting.¹³¹⁻¹³⁵ Cobalt precursors under solvothermal conditions¹³⁶ show a complex redox behavior that can lead to CoO, but also to Co₃O₄, and to metallic Co particles. Interestingly, the crystal structure of individual CoO nanoparticles determines the growth mechanism. CoO nanoparticles with rock salt structure have the tendency to form polycrystalline assemblies, while wurtzite CoO preferentially grows into single crystals.^{106, 134, 137} The specific mechanism in solution, however, favoring crystallization into one or the other phase, and the interdependence of crystallite growth and their assembly into superstructures remain unsolved. Here, starting from Co(III) acetylacetonate (acac), we synthesize phase pure CoO assemblies with an average size of 58 nm composed out of smaller, polyhedrally shaped, edgy 5-7 nm large particles. We show that HERFD-XANES enables us to track the rearrangement of the organo-metallic precursor complex accompanying the initial reduction of Co³⁺ to Co²⁺ in solution. PDF reveals the transition from the dissolved Co²⁺ complex to rock salt CoO nanocrystals by monitoring the changes in bond length between the metal ion and the surrounding oxygen atoms. The combination of PDF and SAXS finally elucidates the interdependence of crystallite growth and assembly that results in the final morphology.

4.3 Results

The reaction of Co(acac)₃ with benzyl alcohol (BnOH) yields spherical CoO assemblies. They are composed of polyhedrally shaped, edgy nanocrystallites as shown in scanning electron microscopy (SEM) and high-resolution transmission electron microscopy (HR-TEM) images in Figure 4.1. From TEM images recorded at different reaction times, we estimate that both the smaller crystallites and the assemblies grow with reaction time (Supplementary Figure 4.2-4.4). Distinct particles are first visible in TEM after 20 min (Supplementary Figure 4.5). The crystallites reach an average size of 6 nm and the assemblies have a final size between 20 and 45 nm. The HR-TEM image of a single assembly in Figure 4.1c reveals an arbitrary orientation of the crystallites, since different crystallographic planes are exhibited within the same assembly. This can be more easily seen in Figure 4.1d and f where we Fourier-filter the HR-TEM image of a single assembly, highlighting crystallites exhibiting the (111) planes in

violet and those exhibiting the (200) planes in blue. The assembly of polyhedrally shaped particles into spherical structures implies a nonclassical multi-step reaction pathway. To access the complexity of the reaction mechanism, we utilize complementary in situ X-ray spectroscopic and scattering methods.

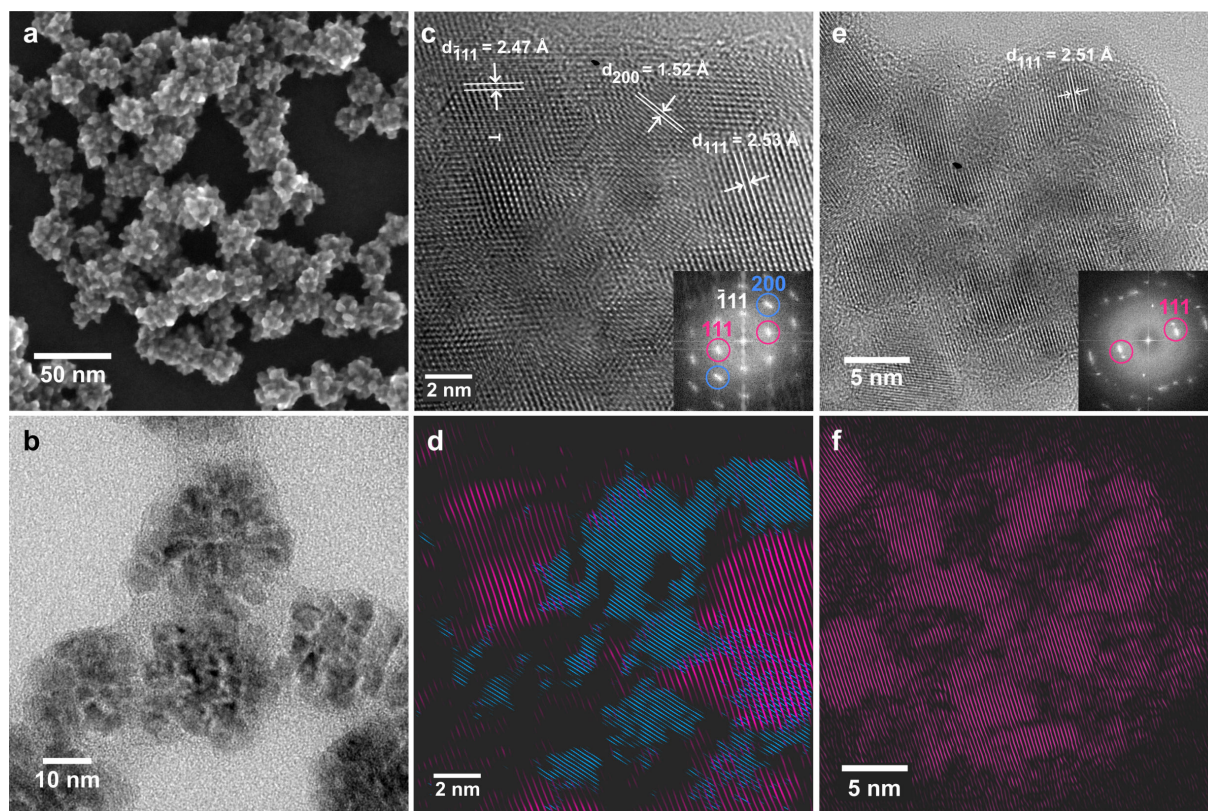


Figure 4.1. SEM and TEM images of CoO assemblies at the end of the reaction. Different magnifications highlight their hierarchical structure. **a** Probe-corrected SEM image of spherical assemblies built of irregularly shaped crystallites. **b** TEM image of assemblies grown after 90 min reaction time. **c** HR-TEM image and corresponding Fourier transformation (FT) (inset) reveal that an assembly exhibits different crystallite orientations. A dislocation in the $(\bar{1}11)$ plane is marked with a white T. **d** Filtered image of **c** by inverse FT of the frequency components highlighted by circles in **c** selectively showing the (111) orientation in violet and the (200) orientation in blue. **e** HR-TEM image of a different assembly and its corresponding FT, and **f** filtered inverse FT of **e** highlighting only the (111) orientation. Individual crystallites do not align to each other in a common crystallographic orientation.

4.3.1 Tracking chemical changes of the reactants via in situ X-ray absorption spectroscopy

To elucidate the chemical reactions in solution, we recorded in situ HERFD-XANES spectra of the CoO assembly synthesis at 160°C. The full time series is shown in Supplementary Figure 4.6. There we notice that, immediately after the reaction temperature is reached, the absorption edge shifts by 3.4 eV towards lower energies, indicating the reduction of the Co^{3+} precursor. Figure 4.2a depicts four representative stages of the time series in more detail. The multiple features in the pre-edge (second row in Figure 4.2a) at 7709.5, 7712.5 and 7716 eV that are present at the beginning of the reaction, reduce to a single feature at 7708.5 eV. These pre-edge features originate from hybridization of 3d and 4p unoccupied states in Co^{2+} and Co^{3+} , allowing quadrupole transitions of a 1s core electron into unoccupied 3d states.¹³⁸⁻¹⁴⁰ Towards the end of the reaction, we observe an increase of the intensity of the white line at 7726 eV that corresponds to 1s→4p transitions in CoO, confirming the formation of the final product.¹³⁹⁻¹⁴¹

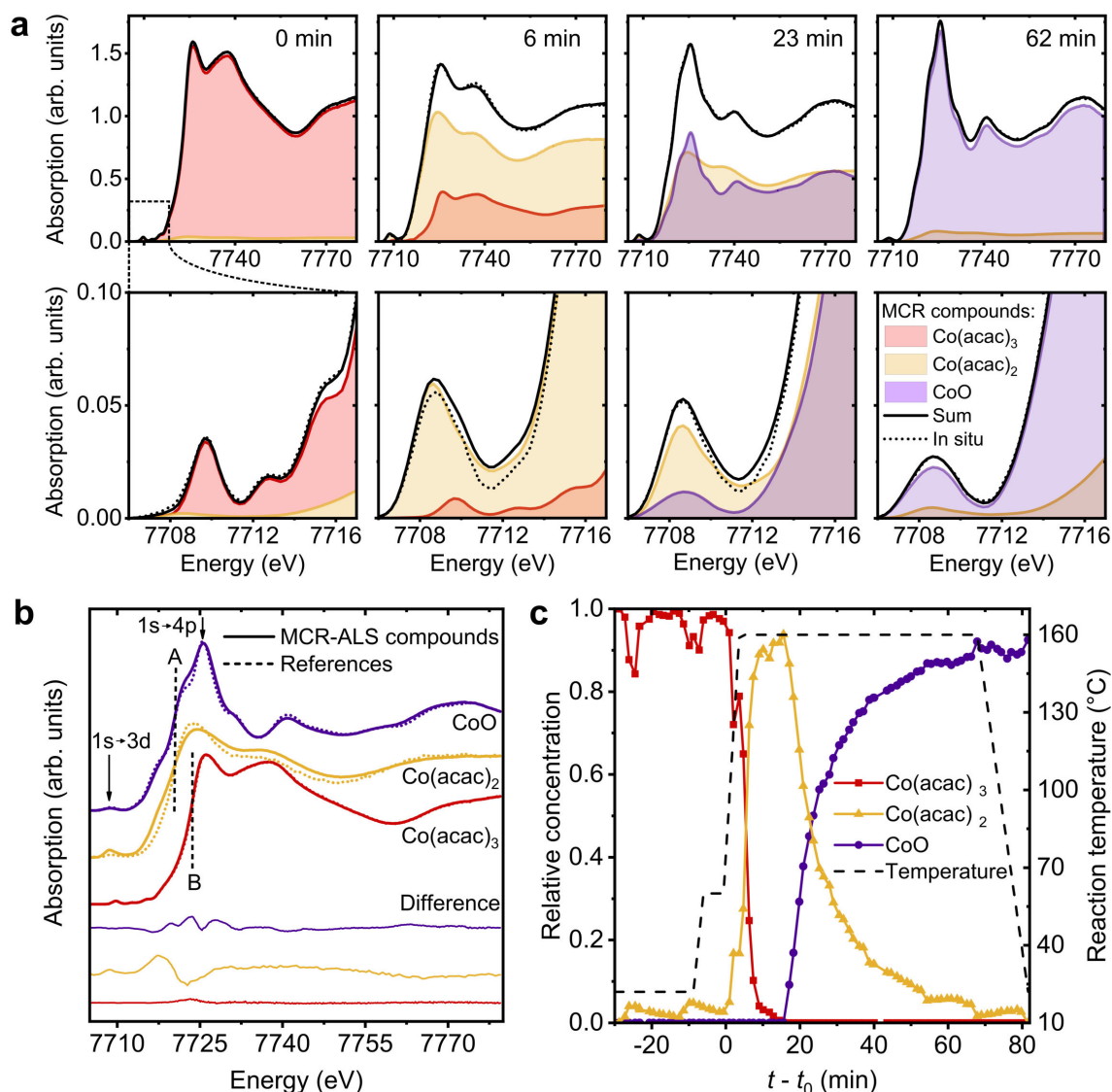


Figure 4.2. Determination of chemical constituents from the in situ HERFD-XANES study and the MCR-ALS analysis. **a** Selected HERFD-XANES spectra of the time series with the main edge shown in the first and the pre-edge in the second row. The spectra are plotted together with the multivariate curve resolution by alternating least squares (MCR-ALS) compounds recovered at the respective times. Linear combinations of the recovered spectra (black solid lines) match the in situ data (dotted lines). **b** Spectra of recovered MCR-ALS compounds compared to measured reference spectra of Co(acac)₃ dissolved in BnOH (red), Co(acac)₂ (orange) and CoO (violet). Dashed vertical lines emphasize the edge positions of Co²⁺ (“A” at 7720.2 eV) and Co³⁺ (“B” at 7723.6 eV). **c** Relative concentrations of the MCR-ALS compounds over reaction time. The dashed line indicates the temperature set point. We set t_0 (beginning of reaction time) to the point when we start heating to 160 °C.

We use a multivariate curve resolution by alternating least squares (MCR-ALS) analysis to recover the number and spectra of independent compounds in the reaction mixture and follow changes of their concentration over time.^{142, 143} This way, we determine the presence of three independent compounds in the in situ data. Further details on the MCR-ALS analysis are given in Supplementary Notes 4.1 and Supplementary Figure 4.7. By comparing linear combinations of the three recovered spectra to the in situ data at different reaction stages (Figure 4.2a), we conclude that these compounds accurately describe both the overall spectral features including the position of the absorption edge and the post-edge fluctuations as well as the pre-edge region. The residual portion of the experimental data not described by the three compounds is 2.1%.

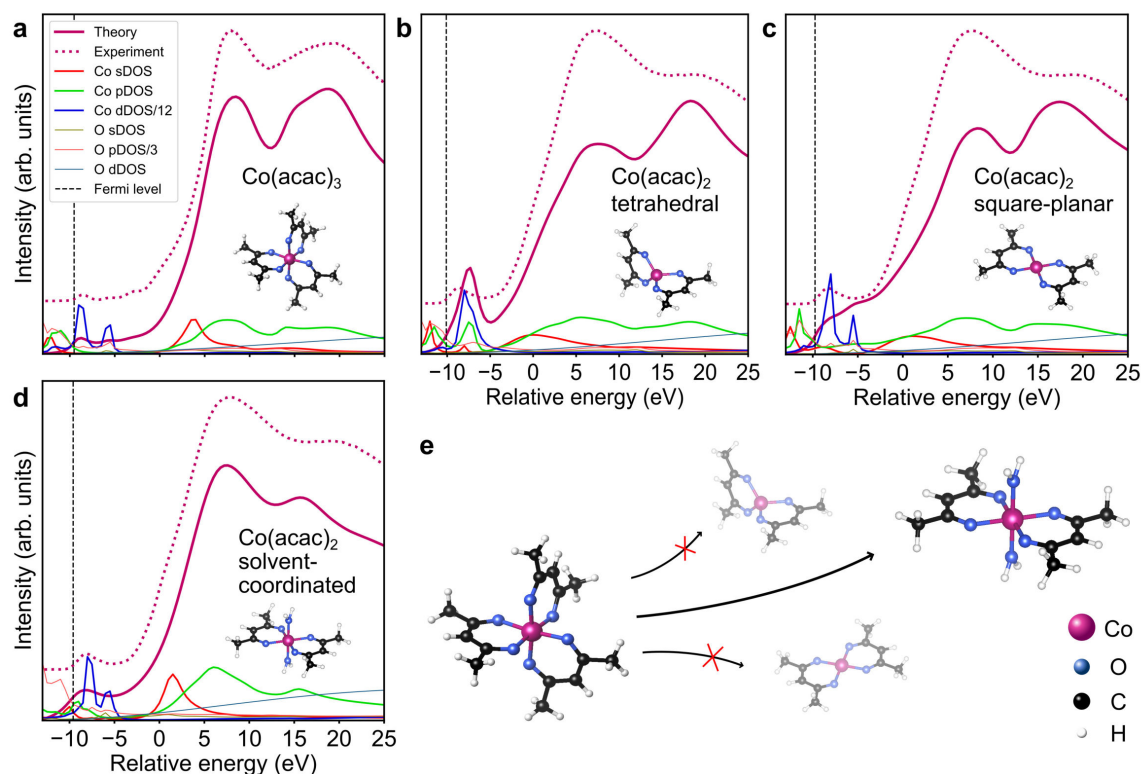


Figure 4.3. Structure determination of the reaction intermediate $\text{Co}(\text{acac})_2$. The structure is determined by means of theoretical XANES spectra calculated using the FEFF code.⁶² The spectrum of $\text{Co}(\text{acac})_3$ is shown in **a** for comparison. Examined structures include **b** tetrahedral, **c** square-planar and **d** solvent-coordinated with water as a model solvent, since the precise coordination geometry of BnOH is unknown. The recovered spectra from the MCR-ALS analysis corresponding to $\text{Co}(\text{acac})_3$ and $\text{Co}(\text{acac})_2$ are shown as dotted lines for reference in parts **a** and **b-d**, respectively. Spectra are plotted together with the local density of states (DOS) for s, p and d states of cobalt and oxygen atoms. The energy scale is relative to the absorption edge E_0 . The position of the Fermi level is indicated for each structure as a vertical dashed line. No instrumental broadening was necessary for the energy resolution of FEFF calculations to be in good agreement with the experimental HERFD-XANES spectra (for details, see Supplementary Notes 4.4). **e** Structural models of the proposed reaction pathway. The atomic positions in square-planar and tetrahedral $\text{Co}(\text{acac})_2$ were taken from reference¹⁴⁴ and the structure of $\text{Co}(\text{acac})_3$ was adopted from reference¹⁴⁵.

In Figure 4.2b we compare the recovered compound spectra to references. We find that the compound mostly present at the beginning of the reaction (shown in red) is in very good agreement with the reference spectrum of $\text{Co}(\text{acac})_3$ dissolved in BnOH . We determine the edge position at 7723.6 eV (labeled B in Figure 4.2b) confirming the valency of the precursor.^{146, 147} For the other compounds the edge is observed at 7720.2 eV (labeled A in Figure 4.2b) indicating that both are in the oxidation state Co^{2+} .¹⁴⁸⁻¹⁵⁰ At the end of the reaction, the predominant compound (violet) reproduces all features of the CoO reference that was measured as a dry powder and corrected for self-absorption¹⁵¹ (for details, see Supplementary Notes 4.2 and Supplementary Figure 4.8).

Most importantly, the compound shown in orange in Figure 4.2 compares well to the $\text{Co}(\text{acac})_2$ reference, which we identify as a reaction intermediate. This is affirmed by the simulation of XANES spectra of $\text{Co}(\text{acac})_2$ using the FEFF code⁶² as shown in Figure 4.3, Supplementary Figure 4.10-4.11 (refer to the Supplementary Notes 4.4 and Supplementary Table 4.3 for details on the FEFF calculations). Furthermore, FEFF calculations allow deeper insight into the conformation of the reaction intermediate, since the spectral features are very sensitive to the local chemical environment around the absorbing Co^{2+} ion. Tetrahedral and square-planar conformations have been suggested for the isolated $\text{Co}(\text{acac})_2$ molecule,¹⁴⁴ however, only the calculated XANES spectra of an octahedrally coordinated

Co²⁺ ion are in good agreement with the experiment. We thus conclude that in solution, the Co²⁺ ion is additionally coordinated by oxygen atoms of two solvent molecules, forming a bis-adduct of the square-planar Co(acac)₂ with octahedral coordination.¹⁵² Due to the limited solubility of Co(acac)₂ in BnOH at room temperature, the reference for the MCR-ALS analysis was measured as a powder where the complex is known to form the tetramer Co₄(acac)₈ that also exhibits octahedral coordination^{152, 153} (Supplementary Figure 4.11d). Thus we attribute the deviations between the spectrum of the reaction intermediate recovered by MCR-ALS and the Co(acac)₂ reference in Figure 4.2b to slight changes in the coordination geometry and the second-shell chemical environment upon dissolving.

To quantify the portion of each compound in the system, in Figure 4.2c we examine the profiles of relative concentrations over time that result from the MCR-ALS analysis. When the temperature reaches the set point, BnOH reduces Co(acac)₃ to Co(acac)₂ within 10 min, significantly faster than the formation of CoO from Co(acac)₂. Both reaction steps are best described by pseudo first order kinetics^{154, 155} (for details, see Supplementary Notes 4.3 and Supplementary Figure 4.9) with the rate of the initial reduction being significantly higher than that of the formation of the final product. We ascribe the fluctuations in the relative concentrations most notable in the beginning and at the end of the reaction to changes of the position of the X-ray beam on the reaction cell, in combination with no stirring applied. This can be a reason why the relative concentration of Co(acac)₂ never reaches 100%. Precipitation of large particles could be another reason why this is neither the case for CoO. However, it is important to note that the formation of CoO only sets in after the precursor has been completely reduced to Co(acac)₂. We can thus exclude the possibility of parallel reactions such as the precursor reacting to CoO without a stable intermediate.

4.3.2 Pinning down nucleation and growth of nanoparticles with in situ PDF

X-ray spectroscopy provides information about the chemical state of cobalt species. However, it fails to investigate the crystallization and growth of the CoO nanoparticles from a structural perspective. Therefore, we performed in situ total X-ray scattering experiments of the synthesis at 160 °C. Supplementary Figure 4.12 shows the integrated and background-subtracted in situ total X-ray scattering data. The constant broad feature at around 1 Å⁻¹ results from the remaining scattering from the sample environment (glass vessel filled with BnOH) after background subtraction (Supplementary Figure 4.13). Except for the residual background, no reflections are seen either in the initial stages of the reaction or during the step of heating. The crystallization of CoO starts after ca. 20 min reaction time suggested by the appearance of CoO reflections, which persist until the reaction finishes after 90 min.

Total scattering data encodes structural information on chemical constituents independent of their aggregation state and ordering, and thus enables to study precursor molecules in solution, as well as amorphous and crystalline nanoparticles. To access this information, we convert the in situ recorded scattering data into the time-resolved PDFs ($G(r)$), as shown in Figure 4.4a. We obtain a real space representation of the interatomic distance changes of all compounds in the reaction mixture over the course of reaction. At the beginning, the time-resolved PDFs reveal only short-range order within a correlation length r of less than 5 Å, indicating the presence of isolated molecular species. The long-range order suddenly appears after 20 min, pinning down the nucleation of the crystalline CoO phase.

The low r region of the time-resolved PDFs before the crystallization as seen in Figure 4.4b clearly shows a single and intense feature at r ca. 2 Å that is constant until longer-range order appears. This peak represents the nearest neighbor Co-O bond. However, the position of this peak starts shifting to higher r values only 4 min after heating to the final reaction temperature is started, revealing the initial changes of the Co environment in the precursor prior to nucleation. To quantify this behavior, the PDFs corresponding to selected reaction stages are depicted in Figure 4.4c. At early reaction times below 13

min, the PDFs show only local order of the reactant. As the reaction progresses further to 20 min and beyond, the peaks related to the structure of CoO first on the short to medium range and soon also on the long-range emerge and intensify as indicated by the dashed lines. Moreover, small features at around 2.34, 2.76 and 3.14 Å in the initial stage match very well with the C-O and two different Co-C bond distances in the $\text{Co}(\text{acac})_3$ molecule.¹⁴⁵ These peaks change position over time and disappear when the crystalline CoO phase appears, most noticeably when the peak of nearest Co-Co distance at around 3.01 Å emerges. The overall behavior is similar to ex situ reference measurements after selected reaction times, as shown in Supplementary Figure 4.14a,b.

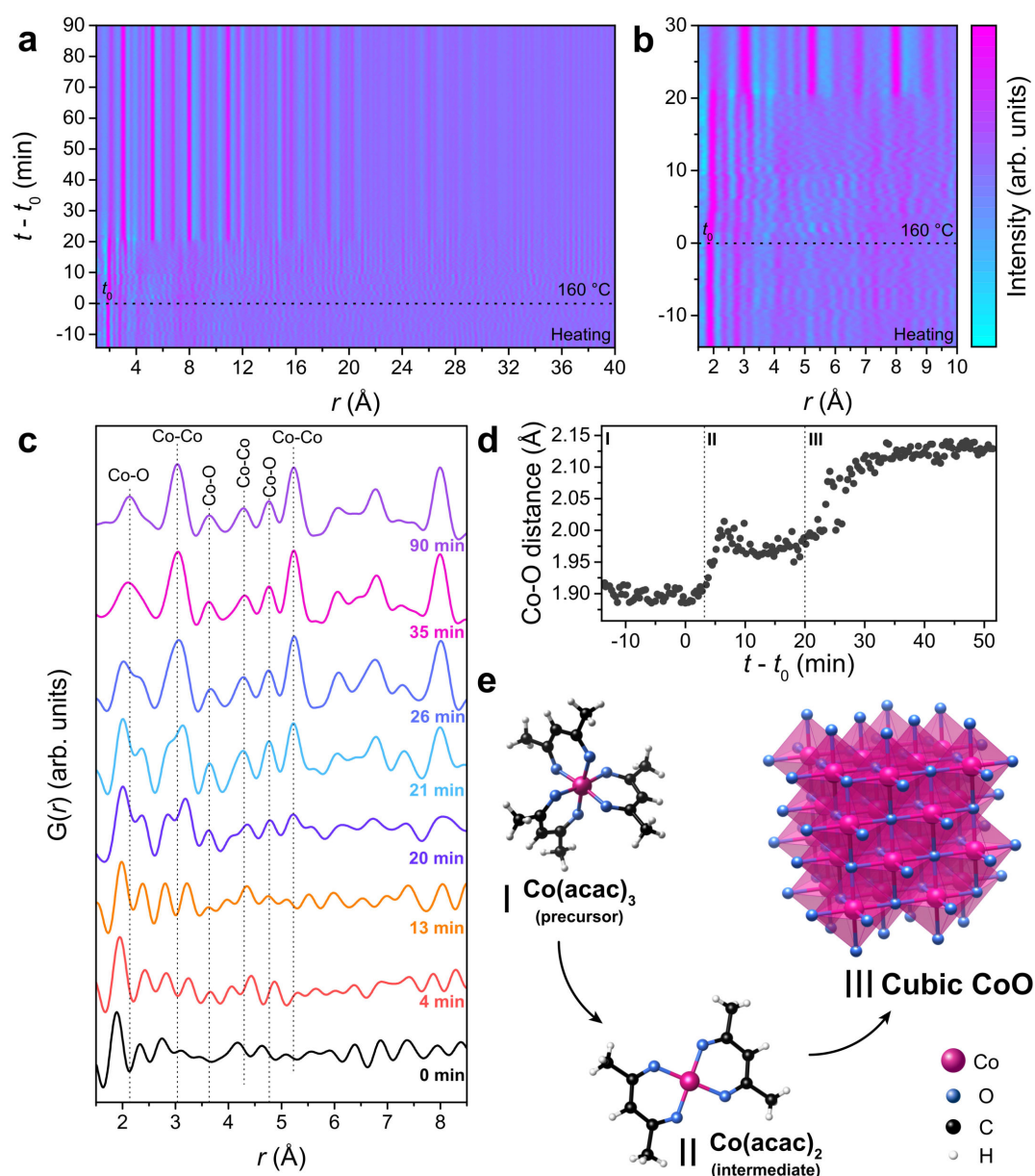


Figure 4.4. Following the structural rearrangement of the Co complex and the crystallization of CoO. **a** In situ time-resolved PDFs $G(r)$ for the CoO synthesis. The heating step includes heating from room temperature to 60 °C, 5 min at 60 °C, and heating from 60 to 160 °C. We set t_0 (beginning of reaction time) to the point when we start heating to 160 °C. **b** Region of **a** illustrating the short range order before the crystallization of CoO. **c** Zoom into the local order region of the PDFs for selected reaction times of the in situ data. Dashed lines show the first coordination shells of CoO. **d** Changes in the shortest Co-O bond over the reaction course, which indicate 3 reaction stages. **e** Structural models for the proposed reaction stages. The structures were obtained from the crystallographic data from references^{145, 156, 157} using the VESTA software.¹⁵⁸

The observed shifts of PDF peaks during the reaction suggest that the effective Co-O distance can act as fingerprint of the nucleation pathway. To test this approach, we depict the changes in the shortest Co-O distance over reaction time in Figure 4.4d. Simple eye inspection reveals three stages for the reaction. At room temperature and during heating, the Co-O distance remains close to ~ 1.90 Å (stage 1), which agrees well with the bond length obtained from our ex situ measurements of the $\text{Co}(\text{acac})_3$ reference (Supplementary Figure 4.15c). After about 4 min, the Co-O bond length rapidly increases and fluctuates around 1.98 Å until 20 min, suggesting an intermediate state (stage 2). Then, the Co-O distance gradually expands further up to 30 min, where it approaches a value of ~ 2.12 Å that remains close to constant (stage 3). It is worth noting that the transformation from stage 1 to 2 occurs much faster than the final changes from stage 2 to 3, matching the reaction rates found by the HERFD-XANES study (Figure 4.c).

The reaction stages can thus be explained as follows. Stage 1 is associated with the precursor $\text{Co}(\text{acac})_3$ without noticeable changes. For stage 2, HERFD-XANES pointed out $\text{Co}(\text{acac})_2$ as the reaction intermediate at comparable reaction times as those inferred from Figure 4.4d. Thus, it is reasonable that the Co-O bond lengthening associated with the lack of long range order corresponds to the reduction of the precursor to $\text{Co}(\text{acac})_2$ during stage 2, although the ex situ measurement of the $\text{Co}(\text{acac})_2$ reference at room temperature provides a slightly longer Co-O bond length of 2.05 Å (Supplementary Figure 4.14c). Finally, stage 3 corresponds to the formation of CoO nanoparticles, as the Co-O distance approaches that of the first coordination shell in rock salt CoO. The proposed reaction course is illustrated in Figure 4.4e.

To track the structural evolution of the CoO particles in the final phase 3, we perform a sequential refinement on the time-resolved PDFs starting from the final product after 90 min, and trace the signal back towards earlier reaction times. In this process, calculated PDFs are fitted to the data in the r range between 1.5 and 40 Å applying the crystal structure of cubic CoO. Besides other structural parameters, we refine the spherical particle (sp) diameter which represents the size of individual crystallites in PDF. Figure 4.5a shows the sp-diameter as a function of the reaction time. The refinement results for the other parameters are depicted in Supplementary Figure 4.15. At 21 min 20 s, the initial value of the sp-diameter is ~ 35 Å, increasing rapidly to ca. 50 Å within additional 10 min. Crystallites gradually continue to grow until the end of the reaction at 90 min and reach a diameter of 64 Å. At the final reaction stage, the crystallite sizes are in good agreement with the size of 6 nm of the small building blocks of the assemblies visible in TEM images as shown in Figure 4.1. The lattice parameter a rapidly decreases as the reaction progresses and fluctuates around 4.28 Å throughout most of the reaction time. It is worth noting that the sequential refinement was also carried out in a higher r range of 1.5–60 Å, comparable to the size of the small building blocks, and similar refinement results are observed as illustrated in Supplementary Figure 4.16.

The fit quality R_w (lower is better) corresponding to the PDF refinement presented in Figure 4.5a and S14 is shown in Figure 4.5b as a function of the reaction time. For the reaction time before 40 min, the co-existence of $\text{Co}(\text{acac})_2$ and CoO induces a misfit in the low r region. The sp-diameter is robust against the misfit in this region and thus the relative changes of crystallite size are reliable. However, the CoO structural model does not well describe the experimental data before 40 min as shown in Supplementary Figure 4.17a. After 40 min and beyond, the PDF data and fit match well, with R_w dropping below 0.3, and improving continuously with reaction time. The modeling of the PDF obtained at 90 min reveals good agreement with the cubic CoO structure in the whole r range, i.e. a low R_w of 0.233, as depicted in Figure 4.5c. Additional refinements of the PDFs at other reaction stages are shown in Supplementary Figure 4.17b-d.

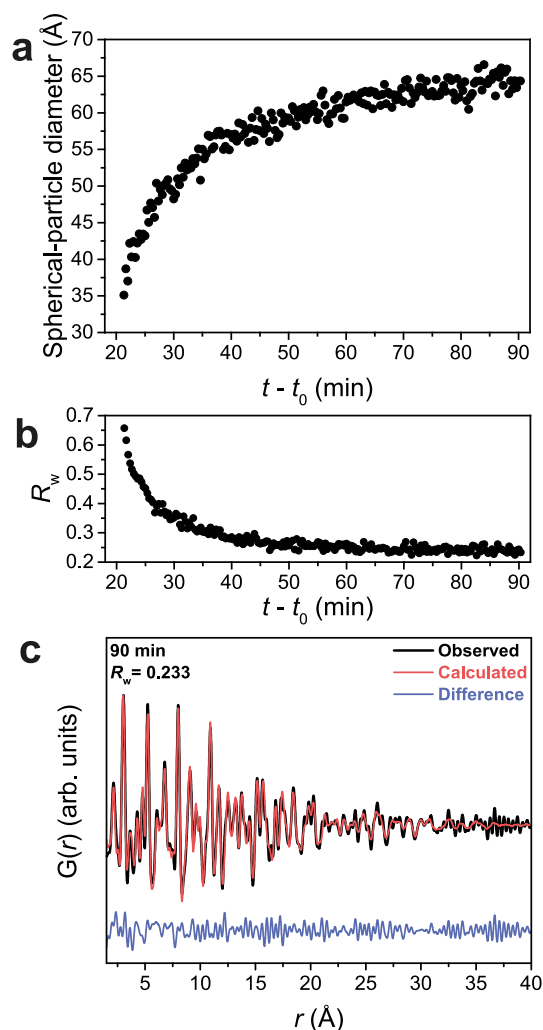


Figure 4.5. Results of the sequential PDF refinement. **a** Evolution of sp-diameter as a function of the reaction time. **b** Fit quality R_w progression as a function of the reaction time. The data in **a** and **b** were obtained from the sequential refinement of time-resolved PDFs. **c** Experimental and calculated PDFs $G(r)$ for the reaction at 160 °C after 90 min. The calculation imposes a rock salt CoO phase.¹⁵⁷

The in situ reaction at a milder temperature of 140 °C compared to the reaction at 160 °C discussed so far presents a similar trend of the formation of the CoO nanoparticles. The kinetics and growth rate are, however, significantly slower than those at 160 °C, as discussed in Supplementary Notes 4.5 and Supplementary Figure 4.18-4.19.

4.3.3 Tracking the assembly with SAXS

So far, we have elucidated the reaction pathway from the dissolved precursor to the product phase. While with PDF analysis we have been able to follow nucleation and growth, information about the process of crystallite assembly into the superstructure is missing. The size and the internal structure of assemblies in solution are accessible from the scattered X-ray intensity at small scattering angles 2θ , here below 4.2° . We show this SAXS data as a function of scattering vector $q = 4\pi/\lambda \sin(\theta)$, where λ is the X-ray wavelength. SAXS intensities $I(q)$, shown in Figure 4.6a, were recorded ex situ from aliquots obtained by ceasing the reaction at five different time points. After 10 minutes reaction time, the SAXS intensity shows a pronounced divergence at low q . The intensity obeys approximately a q^{-4} power law characteristic for scattering contrast from objects with well-defined boundaries.^{159, 160} The slight kink below $q = 0.01 \text{ \AA}^{-1}$ indicates that the characteristic length scale of the scattering objects ($2\pi/q$) is a

few 10 nm. At this reaction stage, the intermediate $\text{Co}(\text{acac})_2$ dominates the reaction mixture according to our HERFD-XANES measurements reported in Figure 4.2c. Since the intermediate is not well soluble in BnOH at room temperature the scattering signal visible in SAXS at this stage may be from precipitates of the intermediate.

From 20 min reaction time onwards, the SAXS signal at low angles, i.e. low values of q , is well described by an intensity plateau region and a subsequent intensity drop. This is clear evidence that well-defined objects have formed. A fit with a model assuming homogeneous spherical assemblies (solid line in Figure 4.6a, see also Supplementary Notes 4.6 and Supplementary Table 4.4) yields an assembly diameter of $D = 21$ nm. Additionally, a size polydispersity of $\Delta D/D = 25\%$ is obtained. For 40, 60, and 90 min reaction time, the assembly diameter gradually increases, i.e. the plateau region narrows. The sphere size obtained from the analysis levels off at a diameter of $D = 58$ nm, $\Delta D/D = 19\%$, as summarized in Figure 4.6b.

For larger diameters, a second intensity oscillation is observed in the data close to the plateau region, as expected for scattering from homogeneous spheres. The homogeneous spherical model, however, only describes the SAXS intensity well up to $q = 0.04 \text{ \AA}^{-1}$. For larger q values, the model strongly underestimates the SAXS intensity, indicating a more complex internal structure.

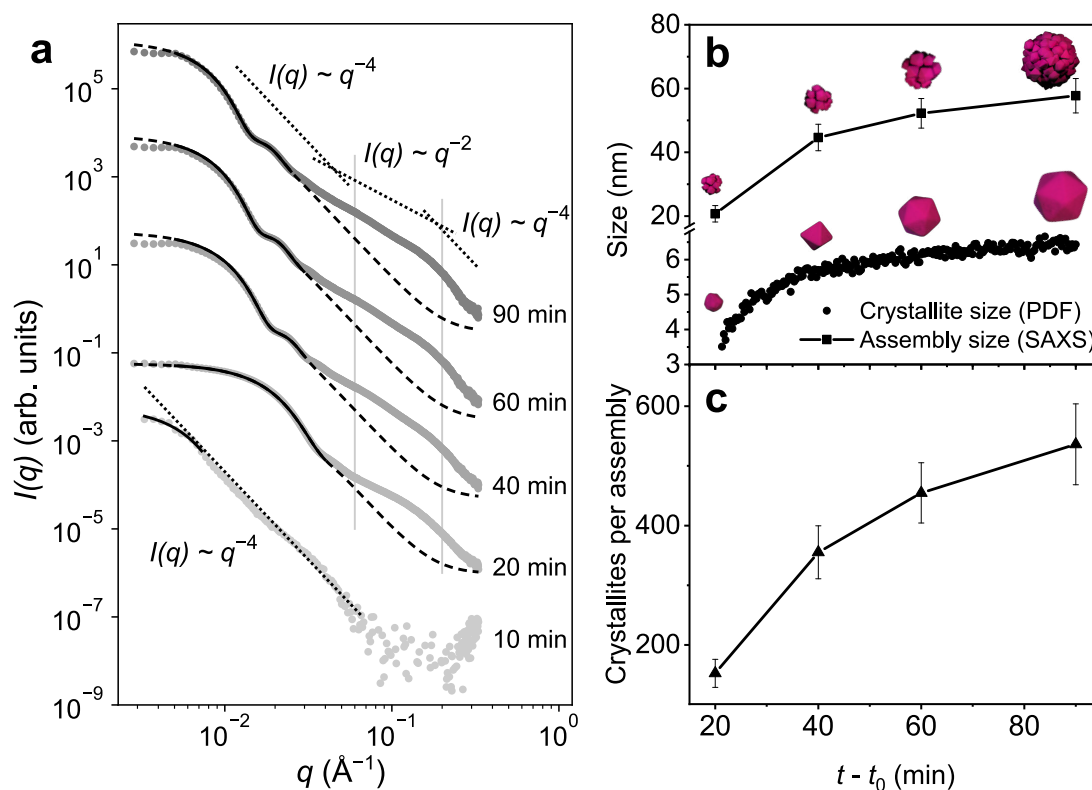


Figure 4.6. SAXS data modelling to follow the assembly of CoO nanocrystals. **a** SAXS intensities $I(q)$ of CoO assemblies for different reaction times. Dashed curves: Calculated intensities for homogeneous spherical assemblies. Superimposed bold curves indicate the least-squares fitting range. Dotted lines: Power laws describing the contributions of compact particle shape (q^{-4}) and corrugated surface (q^{-2}) on the different length scales. An intermediate region is emphasized by vertical grey lines. **b** Comparison of size evolution over time of polyhedra (spherical particle diameter obtained from in situ PDFs and assemblies obtained from SAXS). Here, the error bars indicate the polydispersity of the assemblies. **c** Average number of crystallites per assembly obtained from average assembly size in **b** assuming that they are built from densely packed spherical units with a filled volume fraction of 74%. Here, the error bars result from the error propagation of the average assembly sizes (SAXS) and of the standard deviation of the crystallite sizes (PDF) in **b**.

Particles with pronounced internal structure, such as fractal and porous materials, are known to show a crossover of the power law underlying the SAXS intensity, at the point where q is large enough to resolve these internal structures.¹⁵⁹ Our data suggest that such a crossover from initially q^{-4} to q^{-2} occurs here at ca. $q = 0.06 \text{ \AA}^{-1}$, i.e. for length scales smaller than 10 nm, illustrated by the dotted lines in Figure 4.6a. The region described by q^{-2} extends up to $q = 0.2 \text{ \AA}^{-1}$ (indicated by vertical lines) beyond which the q^{-4} behavior is recovered. Thus, the scattering signal in the intermediate region originates from inhomogeneities at length scales of ca. 3 nm up to 10 nm. This size range is considerably smaller than the full diameter of the assemblies but coincides with the size range of the building units determined with PDF (sp-diameter in Figure 4.5a). On an even smaller scale, i.e. for $q > 0.2 \text{ \AA}^{-1}$, the assemblies scatter like compact objects. In SAXS the dimensional crossover is seen for all reaction times between 20 and 90 min, suggesting that the assemblies are corrugated and porous throughout the reaction. The SEM and TEM images shown in Figure 4.1 and Supplementary Figure 4.2-4.3, 4.22 also display that the compact crystallites form porous assemblies with voids in the interior.

We measured samples after selected reaction times in our laboratory SAXS system. Here, we are able to calibrate the SAXS data on absolute scale, allowing us to determine the volume fraction of the reactant (for details, see Supplementary Notes 4.6). At the end of the reaction, the volume fraction of the assembly is 0.026 %, corresponding to a CoO concentration of 1.65 mg/ml and a reaction yield of ca. 22%. However, since these samples were measured ex situ, precipitation may have led to an underestimation of the concentration and thus the reaction yield. The final assembly size of $D = 58 \text{ nm}$ reported by SAXS is in good agreement with TEM images taken from the same batch used for SAXS analysis (Supplementary Figure 4.22). However, assemblies are about 30 % larger than those from another batch shown in TEM images of Figure 4.1. Even though the absolute values vary between the batches, we observed the similar growth trends independent of the batch. We measured PXRD for the same samples as used for the SAXS analysis, yielding cubic CoO domain sizes of $4.9 \pm 2.8 \text{ nm}$, $5.8 \pm 1.0 \text{ nm}$, and $6.0 \pm 1.2 \text{ nm}$ by Scherrer analysis for 40, 60 and 90 min reaction times, respectively. For details, refer to Supplementary Table 4.4 and Supplementary Figure 4.21. These values are in good agreement with the crystallite sizes found by the in situ PDF analysis.

The average number of crystallites per assembly can now be estimated as a function of reaction time. For this purpose, we compare the assembly size as obtained from SAXS with the diameter of the crystallites, i.e. the sp-diameter as obtained from the PDF refinement (Figure 4.6b). We plot the resulting number of crystallites per assembly in Figure 4.6c, assuming dense packing of spherical units with a filled volume fraction of 74%. From the similarity of the three curves, we conclude that during the entire evolution of the CoO phase, both the attachment of crystallites onto the assemblies and the growth of the individual crystallites contribute similarly to the resulting growth of the assemblies. Moreover, time-resolved TEM images shown in Supplementary Figure 4.2-4.3 support our findings and show that during all reaction stages, crystallites in the center of the assemblies are of the same size as the ones at the surface.

4.4 Discussion

Previous studies of nonclassical crystallization mechanisms suggest that multiple pathways exist involving distinct pre-crystalline entities (see Cölfen et al. 2019¹³, Figure 1d therein and references). Our work provides an experimental complement to this work. Using the example of polycrystalline assemblies of polyhedrally shaped CoO nanoparticles, we illustrate that advanced X-ray spectroscopic and scattering in situ studies are very powerful tools for bridging the molecular- and macro- length scales. Putting together complementary pieces of information, we can pin down the formation of

monomers, nucleation, growth and assembly of the CoO polyhedra as schematically shown in Figure 4.7 and Supplementary Figure 4.23. In summary, HERFD-XANES revealed $\text{Co}(\text{acac})_2$ as a monomer species that quickly forms upon reduction of the precursor in solution. FEFF calculations indicated that the intermediate forms a bis-adduct of square-planar $\text{Co}(\text{acac})_2$ with coordinated solvent molecules. Total scattering and PDF analysis gave insights into local structural changes around the Co^{2+} ion during nucleation and growth of the cubic CoO phase. We assigned the stepwise increase of the Co-O bond length to the rearrangement of the organo-metallic precursor upon reduction, and to the nucleation of the crystalline product phase. SAXS measurements together with crystallite size evolution derived from PDF shed light on the assembly mechanism of the final structure. They indicate that crystallites start assembling soon after nucleation and continue to assemble, while the cavernous nature of the assemblies allows crystallites to grow similarly at the surface and in bulk. During the entire reaction, growth and assembly of particles contribute to the size evolution of the final product. The size evolution of crystallites and assemblies, as well as the average number of crystallites per assembly, follow the kinetics of the formation of the product phase. Our findings do not support a classical crystallization and growth mechanism, in which crystallites nucleate and grow only at the surface of the assemblies until they are covered with the next layer of crystallites. On the contrary, the cavernous structure of the nanoparticle assemblies allows the crystallites to always consume material from the solution and thus to grow both on the surface and in bulk. In addition, no isolated, unassembled crystallites are found in SAXS or TEM, indicating that crystallites, which may nucleate in solution, are soon attached to an assembly, keeping the number of isolated crystallites low.

The simultaneous growth and assembly of crystallites we observe here is a markedly different mechanism from e.g. evaporation-induced assembly of pre-formed nanocrystals in dispersion to mesocrystals, which has been in the focus of recent in situ investigations by X-ray methods.¹⁶¹⁻¹⁶³ Here we find that for the synthesis of CoO nanocrystals under solvothermal conditions, crystallite nucleation and growth are accompanied by unoriented assembly into a polycrystalline superstructure.

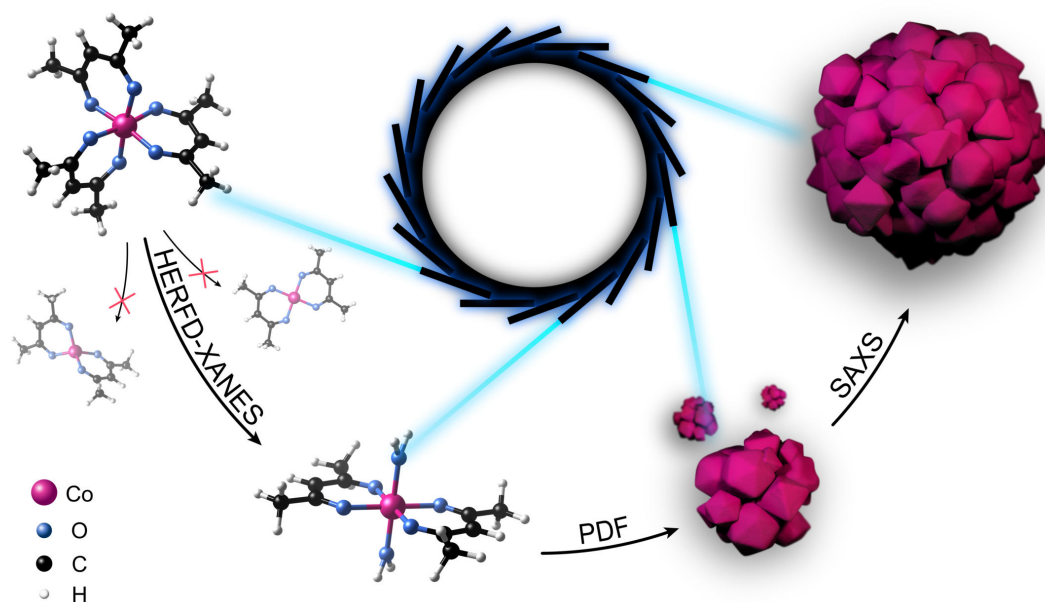


Figure 4.7. Overview of the emergence of nanoassemblies of CoO in BnOH. Complementary X-ray spectroscopic and scattering methods enable the bridging of the studies of reaction mechanism from molecular- to macro- length scales. We combined HERFD-XANES, PDF analysis and SAXS to follow the emergence of CoO nanoassemblies in solution.

More generally, our approach of combining three techniques from the fields of X-ray spectroscopy and scattering made it possible to gain mechanistic insights into all steps of complex nonclassical crystallization. While spectroscopy is focused on the chemistry, scattering in the full range of reciprocal space is essential to follow the structural and morphological evolution at different length scales, both key features when it comes to understanding the complexity of nanomaterials formation. We demonstrate a way to strengthen the use of multimodal in situ X-ray experiments in particular for studying nonclassical crystallization processes. The level of microscopic detail obtained within this study encourages the application of this approach in related fields, which might benefit even more from the combination of structural and spectroscopic synchrotron techniques. Particularly catalysts at functional interfaces, which are notoriously difficult to probe in a coherent chemical and structural way, might be worthwhile to explore.¹⁶⁴

4.5 Experimental section

Synthetic procedure

Chemicals: Benzyl alcohol (>99%), Co(acac)₃ (99.99%), Co(acac)₂ (>99%) were purchased from Sigma Aldrich, and ethanol (absolute) for washing from VWR. All chemicals were used without further purification.

Synthesis: Co(acac)₃ (0.5 mmol) was added to 5 mL of BnOH and stirred for 5 min at room temperature. A quantity of 0.8 mL of the green solution was transferred to the reaction container of the in situ cell (Supplementary Figure 4.1), sealed and heated at an average heating rate of 1 °C/s first to 60 °C for 5 min to homogenize, then at the same rate to 140 °C or 160 °C and stabilized at this temperature during 210 min or 90 min, respectively, for in situ experiments. We define the beginning of the reaction time (t_0) at the point when the heating to the reaction temperature of 140 °C or 160 °C starts. All mentions of reaction time are relative to t_0 . For ex situ SAXS measurements, the reaction was stopped after 20, 40, 60 and 90 min reaction time by quickly cooling down the in situ cell to room temperature with a cold metal block, and the solution was measured without further treatment. For SEM/TEM, the brown precipitate was washed three times with ethanol and dried at 60 °C. For the TEM image in Supplementary Figure 4.22, no washing was applied.

SEM: Scanning electron microscopy images were taken and probe-corrected with a Regulus 8220 (Hitachi High Technologies Corp., Japan) at an acceleration voltage of 10 kV and using the secondary electron signal.

TEM: Transmission electron microscopy images and electron diffraction (ED) measurements were taken with a JEM 1011, High-resolution TEM images with a JEM 2200 FS (JEOL Ltd., Japan) at an acceleration voltage of 100 kV.

In situ reactor

The reactor and measurement cell (Supplementary Figure 4.1) is composed of a polyether ether ketone (PEEK) reaction container inserted into a heated brass housing and surrounded by thermally insulating alumina bricks. The container is sealed by a PEEK cap pressed against the top side of the container. A 0.2 mm thin PEEK wall on one side of the container serves as entrance and exit window for fluorescence-detected XAS. For total scattering measurements, a cylindrical quartz capillary with a diameter of 6.5 mm and a wall thickness of 0.5 mm is held in place by a PEEK support not in contact with the primary X-ray beam in order to avoid background signal from the semi-crystalline PEEK. No stirring is applied to the reaction solution.

X-ray techniques

HERFD-XANES: Spectra were recorded at beamline ID26 at the European Synchrotron Radiation Facility (ESRF), Grenoble, France. Using a Si (111) double crystal monochromator (DCM), the incident energy was varied from 7.70 to 7.78 keV over the Co K edge. The maximum of the Co $K\alpha_1$ (1s2p) fluorescence line was selected with an emission spectrometer in Rowland geometry with five Si (531) analyzer crystals aligned at the Bragg angle of 77° . HERFD-XANES spectra were recorded in continuous scan mode every 80 s with an overall energy resolution of 1.22 eV and average energy steps of 0.05 eV. The position of the beam on the in situ cell was changed after each scan to avoid beam damage. The CoO reference was measured as a dry powder using a Si (311) DCM and the Co(acac)₂ reference was measured at beamline BM14 at ESRF selecting the $K\beta_{1,3}$ (1s3p) emission line with one Ge (444) analyzer crystal aligned at the Bragg angle of 83° .¹⁶⁵ Spectra were later aligned to the absorption edge to account for possibly different energy calibrations.

Total X-ray scattering: Data was taken at beamline P21.1 of PETRA III at Deutsches Elektronen-Synchrotron (DESY), Hamburg, Germany. Diffraction patterns were recorded every 10 s at an X-ray energy of 102.92 keV ($\lambda = 0.121$ Å) using a digital X-ray flat panel detector XRD1621 (Perkin Elmer Inc., USA) with a pixel size of 200×200 μm^2 and a sample-to-detector distance of 0.411 m, obtained from a calibration with a CeO₂ powder standard packed into the quartz capillary of the in situ cell.

SAXS: Data were obtained at beamline P03 at PETRA III.¹⁶⁶ The X-ray energy was 12.9 keV ($\lambda = 0.961$ Å). Samples were loaded in 2 mm quartz glass capillaries (Hilgenberg, Malsfeld, Germany). Data were recorded with a Pilatus 1M detector (Dectris, Baden-Dättwil, Switzerland) for 5×0.1 s at 5.2 m and for 0.5 s at 2.0 m sample-to-detector distance, and combined. Additional SAXS data were recorded at a sealed tube Mo anode microfocus X-ray setup at LMU, Munich.¹⁶⁷ A Pilatus 300K detector (Dectris, Baden-Dättwil, Switzerland) was used at 1.0 m sample-to-detector distance. Samples were loaded in custom-made chambers with Kapton foils (DuPont, USA) as windows and measured for 5x20min and 7x20 min before taking the median, for the samples after 20 min and 90 min reaction time, respectively.

PXRD: Data were recorded using the laboratory molybdenum anode microfocus X-ray setup at LMU, Munich.¹⁶⁷ The X-ray energy was 17.4 keV ($\lambda = 0.71$ Å). Samples were dried for three days on Kapton foils (DuPont, USA) for measurements. A Pilatus 100K detector (Dectris, Baden-Dättwil, Switzerland) was raster-scanned perpendicular to the beam to enlarge the q range. The total exposure time per sample was 18 h. A LaB₆ powder standard was used for calibration of the sample-to-detector distance and the instrumental resolution.

Data analysis

HERFD-XANES: Data reduction of HERFD-XANES spectra in the energy range from 7.705 to 7.780 keV was performed with the software package PyMCA.¹⁶⁸ Binning was applied to reduce the number of data points by a factor of five and the edge step was normalized by fitting a constant to the pre and post edge regions. Edge positions were calculated and spectra were aligned with Athena, part of the Demeter software package.¹⁶⁹ The in situ data set was analyzed with the MCR-ALS method implemented in MATLAB (The MathWorks Inc., USA).^{142, 143, 170} An uncertainty estimation with a noise level of 3% was applied. The number of components was determined by means of singular value decomposition and the initial spectra and concentration profiles were estimated by the Purest Variables detection method. The ALS algorithm was applied with the following constraints: (1) non-negativity of spectra and concentrations, (2) unimodality of concentrations with 20% tolerance and (3) convergence criterion of 0.1.

FEFF: Theoretical XANES spectra were calculated using the FEFF code⁶² in version 9.6.4 with the Hedin-Lundquist energy dependent exchange correlation potential. The settings are listed in Supplementary Table 4.3. For the Co₄(acac)₈ tetramer, calculations with each of the Co ions set as the

absorber were averaged, since their environments are not equivalent. For additional details, refer to Supplementary Notes 4.4. Experimental and theoretical spectra were aligned with Athena.¹⁶⁹

Total scattering: The azimuthal integration of the 2D diffraction patterns was performed with pyFAI.¹⁷¹ CeO₂ powder packed into the quartz capillary was used as a calibrant for the integration parameters and the instrumental parameters in real space. The integrated data were normalized and further processed using the program xPDFsuite¹⁷² with PDFgetX3⁶⁶ to perform the background subtraction, normalization to the atomic form factors, and Fourier transformation (FT) to obtain the PDF ($G(r)$). For the background subtraction, the glass capillary filled with BnOH was measured under the same conditions as for the synthesis. Q_{\min} and Q_{\max} parameters were set to 0.59 Å⁻¹ and 16.5 Å⁻¹, respectively. The resulting PDFs were sequentially refined applying PDFgui.¹⁷³ Q_{damp} and Q_{broad} were determined as 0.0463 and 0.0574 Å⁻¹, respectively, from the CeO₂ calibrant. Structural refinements were performed using crystallographic data of cubic CoO (*Fm-3m* (225) space group) from the Inorganic Crystal Structure Database (ICSD)-9865.¹⁵⁷

SAXS and PXRD: Intensities were azimuthally averaged and binned using the Nika¹⁷⁴ package for Igor Pro (Wavemetrics, Portland OR, USA). A solution of Co(acac)₃ in BnOH was recorded as background and subtracted from all SAXS data of ex situ samples of the synthesis. A Kapton foil background was recorded and subtracted from the PXRD data. For additional details, refer to Supplementary Notes 4.6 and Supplementary Notes 4.7.

4.6 Acknowledgements

This work was supported by the European Research Council within the project LINCHPIN (grant no. 818941), by the Bundesministerium für Bildung und Forschung (BMBF) via project LUCENT (grant no. 05K19WMA), by the Bavarian State Ministry of Science, Research, and Arts through the grant “SolarTechnologies go Hybrid (SolTech)”, by the Cluster of Excellence “The Hamburg Centre for Ultrafast Imaging” of the Deutsche Forschungsgemeinschaft (DFG) - EXC 1074 - project ID 194651731, by the Cluster of Excellence “CUI: Advanced Imaging of Matter” of the DFG - EXC 2056 - project ID 390715994, by the DFG via project ID 201269156-SFB1032, and by the São Paulo Research Foundation (FAPESP, grant no. 2018/08271-7 and 2016/25267-8).

This work benefited from the use of the SasView application (version 4.2.2), originally developed under NSF award DMR-0520547, further developed within the European Union’s Horizon 2020 research and innovation programme under the SINE2020 project (grant no. 654000).

We thank Dr. Lucia Amidani, Dr. Rafal Baran, Dr. Roelof van Silfhout, Dirk Detollenaere, Florian Ledrappier, Martina Ober, and Ludwig Hendl for supporting the X-ray measurements and laboratory experiments, Andreas Kornowski, Andrea Koeppen, Stefan Werner and Susanne Kempfer for TEM imaging, Tarcísio Perfecto for designing Figure 4.7 and ESRF, ID26 for beamtime allocation.

We acknowledge DESY (Hamburg, Germany), a member of the Helmholtz Association HGF, for the provision of experimental facilities. Parts of this research were carried out at PETRA III and we would like to thank Prof. Stephan Roth, Dr. Matthias Schwarzkopf and Dr. Martin Roelsgaard for assistance in using beamlines P03 and P21.1.

4.7 Author contributions

D.K., L.G. and C.A.Z. conceived the project. L.G., C.A.Z., D.K., K.P., K.O.K. and S.B. conducted the X-ray absorption experiments. L.G., C.A.Z., M.R. and S.Y.H.-M. designed and conducted the X-ray

total scattering experiments. K.F., P.R., B.N. and P.P. designed and conducted the SAXS experiments. A.-C.D., B.D. and O.I. supported the synchrotron experiments. L.G. and K.P. analyzed the HERFD-XANES data. C.A.Z. and A.-C.D. analyzed the total scattering data. K.F. and P.R. analyzed the SAXS data. All authors contributed to data interpretation and the preparation of the manuscript.

4.8 Additional information

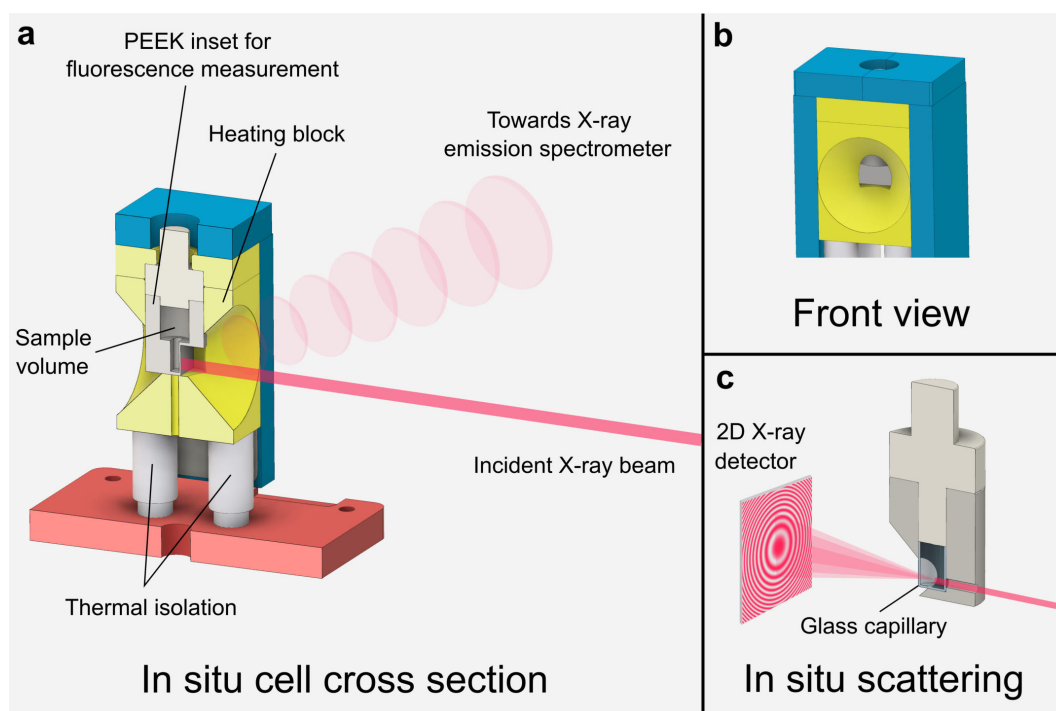
Competing Interests

The authors declare no competing interest.

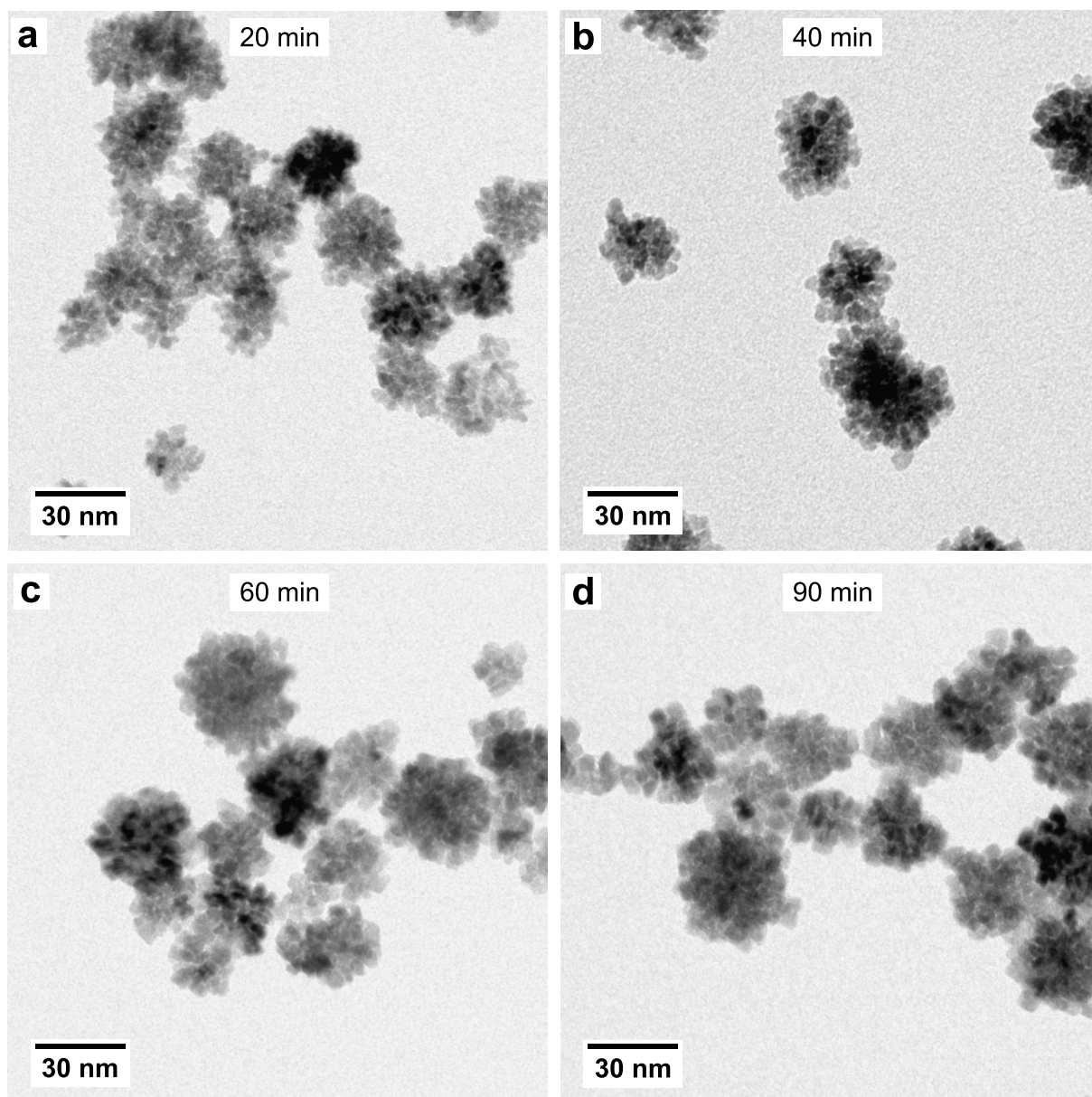
Data Availability

The SEM, TEM, HERFD-XANES, total X-ray scattering, PXRD and SAXS datasets generated and analysed during the current study are available in the zenodo repository, [DOI: 10.5281/zenodo.4746349](https://doi.org/10.5281/zenodo.4746349)¹⁷⁵

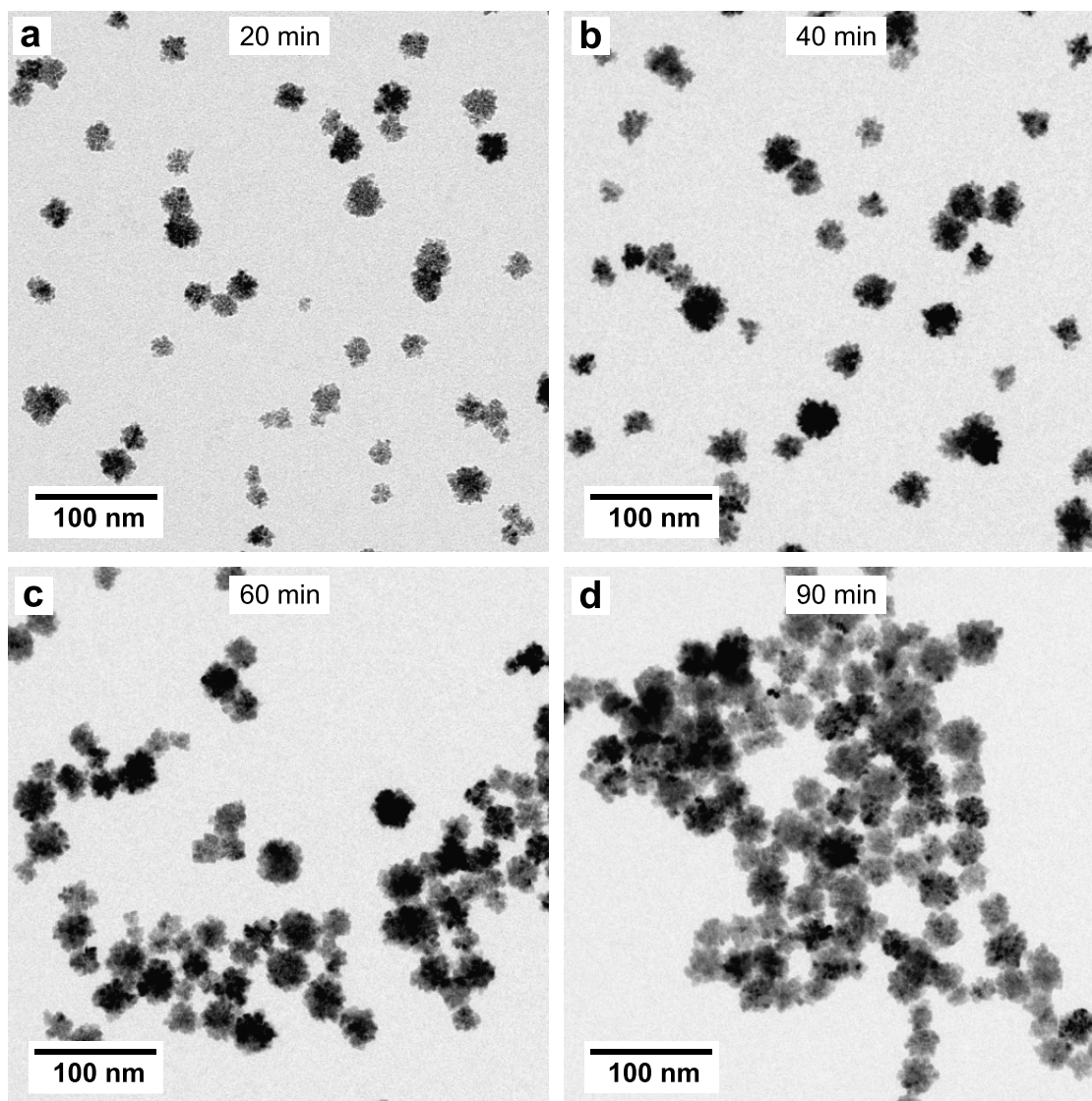
4.9 Supplementary information



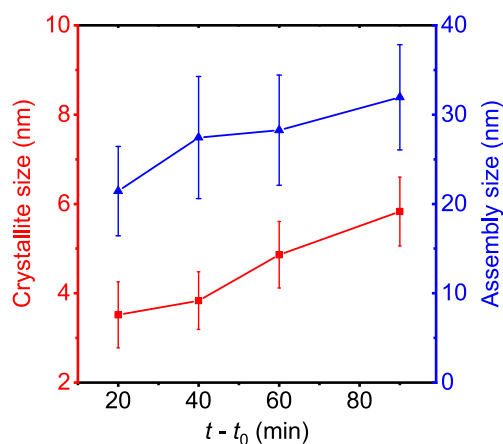
Supplementary Figure 4.1. Schematics of the reaction cell used for in situ HERFD-XANES and total X-ray scattering studies. **a** Cross section of the in situ cell with a PEEK inset suitable for fluorescence-detected XAS. The heating block is made of brass and is heated by proportional–integral–derivative (PID)-controlled heating elements. The PEEK inset is sealed with a PEEK cap that is pressed down by the top brass part. One wall of the PEEK vial has a thickness of 0.2 mm acting as entrance and exit window for the X-rays. Emitted X-rays are detected with a Rowland-circle spectrometer. **b** Front view of the in situ cell with the inset used for fluorescence-detected HERFD-XANES. Additional thermal insulation around the heating block is shown in blue. **c** PEEK inset holding a glass capillary suitable for in situ total X-ray scattering. This inset replaces the one in **a** for total scattering studies. A glass reaction vial is needed here to avoid background diffraction from the semi-crystalline PEEK. A 2D X-ray detector collects the scattered intensities behind the sample. The in situ cell was adopted from reference¹⁴.



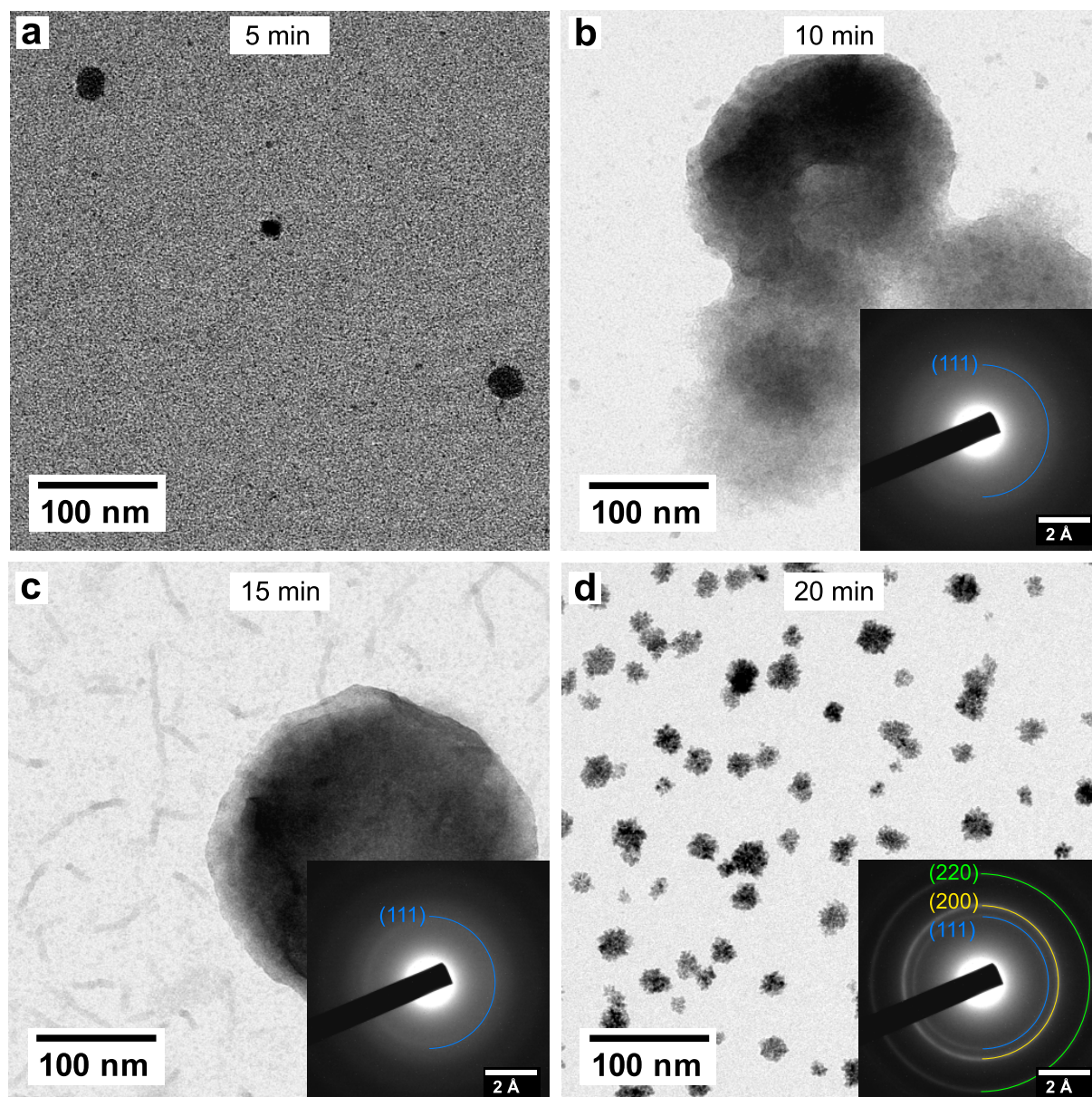
Supplementary Figure 4.2. TEM images of CoO nanocrystallite assemblies at high magnification. The images were obtained after **a** 20 min, **b** 40 min, **c** 60 min and **d** 90 min reaction time. We used these micrographs for the size analysis of crystallites presented in Supplementary Figure 4.4.



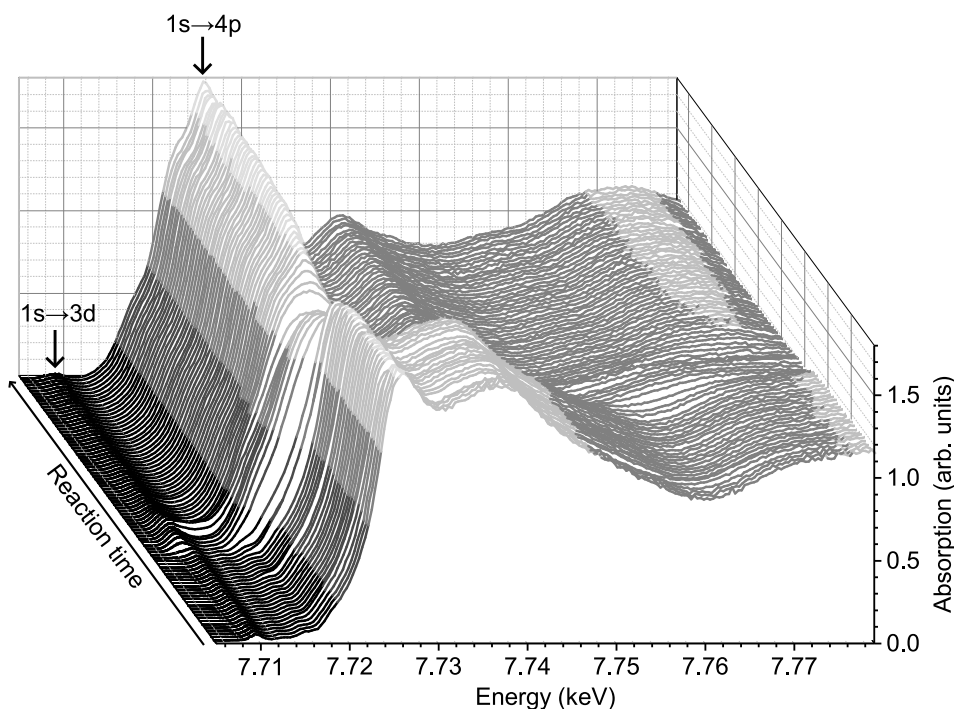
Supplementary Figure 4.3. TEM images of CoO nanocrystallite assemblies at lower magnification compared to Supplementary Figure 4.2. The images were obtained after **a** 20 min, **b** 40 min, **c** 60 min and **d** 90 min reaction time. We used these micrographs for the size analysis of assemblies presented in Supplementary Figure 4.4.



Supplementary Figure 4.4. Size evolution of polyhedral crystallites and assemblies. The values were obtained from the analysis of time-resolved TEM images in Supplementary Figure 4.2 and Supplementary Figure 4.3, respectively. At each reaction time, the size analysis is based on 50 crystallites and assemblies. Error bars correspond to the standard deviation of the size distribution.



Supplementary Figure 4.5. TEM images of early reaction stages before (5 to 15 min) and just after (20 min) the onset of crystallization of CoO assemblies (c.f. Figure 4.2c and Figure 4.4d). The images were obtained after **a** 5 min, **b** 10 min, **c** 15 min and **d** 20 min reaction time. Insets show ED patterns of different, representative sample regions, respectively, with indexed reflections of the rock salt CoO phase.¹⁵⁷ We account the large structures visible between 10 and 15 min to precipitation of unreacted intermediate $\text{Co}(\text{acac})_2$ or precursor $\text{Co}(\text{acac})_3$. Only the sample after 20 min shows distinct CoO assemblies, together with a strong crystalline ED signal. In the sample after 15 min, nanosized precipitate is observed. However, the very weak ED signal excludes the presence of final crystalline nanoparticles.



Supplementary Figure 4.6. Set of Co 1s2p HERFD-XANES spectra measured in situ during the reaction of $\text{Co}(\text{acac})_3$ to CoO in BnOH.

Supplementary Notes 4.1. MCR-ALS method for analysis of in situ HERFD-XANES

The MCR-ALS method^{142, 143, 170} used for extracting the reaction pathway from the in situ HERFD-XANES data is briefly explained, followed by detailed fit results. Generally speaking, MCR-ALS is a factor analysis tool, thus it searches for the number and nature of uncorrelated variables explaining the variance in a set of observed, correlated variables. For this, the observed data set needs to be decomposable in the underlying bilinear model given by

$$\mathbf{D} = \mathbf{C}\mathbf{S}^T + \mathbf{E} \quad (4.1)$$

In Equation 4.1 and for our case of time-resolved HERFD-XANES spectra, \mathbf{D} is the experimental data with each row corresponding to a measured spectrum, rows of \mathbf{S}^T are spectra of uncorrelated variables (we call them components) and columns of \mathbf{C} are the concentration profiles of each component over time. \mathbf{E} represents variance in the data not explained by the model. After an initial guess for \mathbf{C} and \mathbf{S}^T , which we do by means of the purest variables detection method,^{143, 176} a set of linear equations is iteratively solved, alternatingly keeping \mathbf{C} or \mathbf{S}^T constant until the change in the standard deviation of \mathbf{E} falls below a certain convergence criterion. Additional constraints can be imposed on the optimization problem (spectral and/or concentration dimension) to facilitate convergence, one being non-negativity and the other one being unimodality.

Quality estimates of a converged fit arise from the unexplained residuals \mathbf{E} , or the difference between the experimental data and the bilinear model, with the lack of fit given by

$$\text{lack of fit (\%)} = 100 \sqrt{\frac{\sum_{i,j} e_{ij}^2}{\sum_{i,j} d_{ij}^2}} \quad (4.2)$$

where d_{ij} is a data matrix element and e_{ij} is the corresponding element of the residuals matrix \mathbf{E} . Additionally, the variance explained in the model can be estimated from

$$R^2 = \frac{\sum_{i,j} d_{ij}^2 - \sum_{i,j} e_{ij}^2}{\sum_{i,j} d_{ij}^2} \quad (4.3)$$

and the standard deviation of the residuals is given by

$$\sigma = \sqrt{\frac{\sum_{i,j} e_{ij}^2}{n m}} \quad (4.4)$$

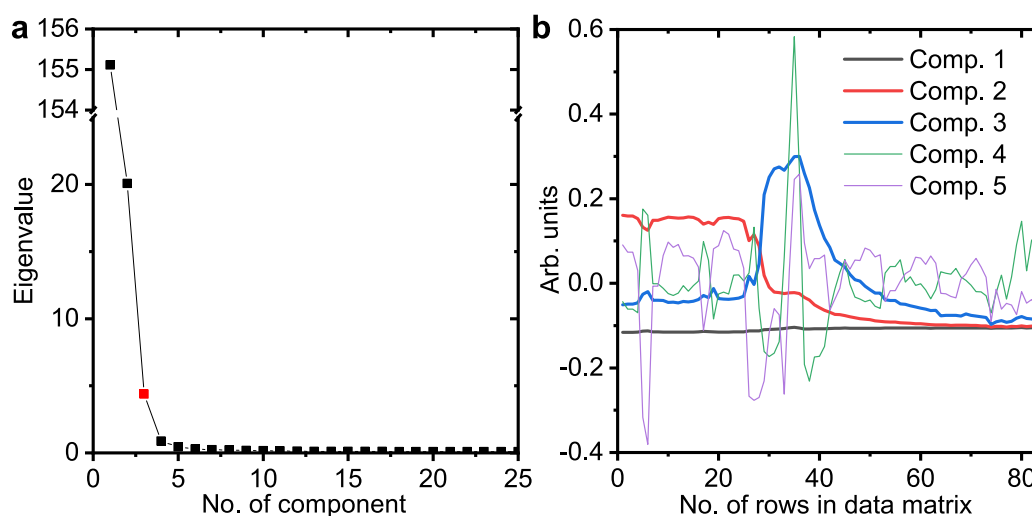
where n, m refer to the dimensions of \mathbf{D} . For the MCR-ALS analysis in the main article, we show the quality estimates in Supplementary Table 4.1.

Supplementary Table 4.1: MCR-ALS fit quality estimates.

fit quality estimate	value
lack of fit (%)	2.088
R^2	99.956
σ	0.017

The MCR-ALS optimization can only start after the dimensions of \mathbf{C} and \mathbf{S}^T have been defined, thus the number of components must be defined beforehand. For this purpose we use singular value decomposition (SVD) which computes a set of eigenvalues and corresponding eigenvectors from the input data set.¹⁴² Both of them contain information to determine the number of components. A higher eigenvalue means that the respective component explains more variance of the data, while the graphical representation of the eigenvector of a meaningful component should display a distinctive profile, independent of its absolute values. Such meaningful components correspond to HERFD-XANES spectra of chemical compounds in the reaction mixture.

We show the results of SVD of the in situ HERFD-XANES data set in Supplementary Figure 4.7. The scree plot of the eigenvalues in Supplementary Figure 4.7a has an elbow starting after component 3. Low eigenvalues after the elbow starting with component 5, which align linearly, correspond to the noise in the data. The exact eigenvalues are given in Supplementary Table 4.2.



Supplementary Figure 4.7 SVD results of the in situ HERFD-XANES data set. **a** Scree plot of eigenvalues with elbow starting at component 3. Small, linearly aligned eigenvalues correspond to noise. **b** Eigenvector representation with components 1 to 3 (bold lines) showing distinctive profiles.

Additionally, looking at the eigenvector representations in Supplementary Figure 4.7b, we see clear profiles only for components 1 to 3, while components 4 and 5 only punctually exceed the noise level, which we assign to fluctuations due to changing positions of the incident beam on the reaction container throughout the collection of the in situ data set. The wall thickness of the reaction container could vary in a certain range, and we have to note that no stirring was applied during the in situ studies. From both measures combined, we conclude that there are 3 independent components in the data set. Additionally, MCR-ALS optimization with 4 and more components would not give physically meaningful results.

Supplementary Table 4.2: The first ten eigenvalues calculated by SVD of the in situ HERFD-XANES data matrix.

no. of component	eigenvalue
1	155.112
2	20.085
3	4.377
4	0.884
5	0.45
6	0.295
7	0.226
8	0.206
9	0.179
10	0.153

Supplementary Notes 4.2. HERFD-XANES self-absorption correction

Self-absorption can affect the intensities of features in fluorescence-detected XAS. In order to correct for this, we apply the method described by Booth and Bridges¹⁵¹ expressed by Equation 4.5:

$$\frac{I_f}{I_0} \equiv I_f^0 = \frac{\varepsilon_a \mu_a}{\mu + g \mu_f} \left[1 - e^{-\left(\frac{\mu}{\sin \varphi} + \frac{\mu_f}{\sin \theta}\right) d} \right] \quad (4.5)$$

Here, I_0 and I_f are the incident and fluorescence intensities, $\varepsilon_a(E)$ is the fluorescence efficiency per unit solid angle, $\mu_a(E)$ is the absorption coefficient due to core hole excitation, $\mu(E)$ is the total absorption coefficient, $\mu_f = \mu(E_f)$ is the absorption coefficient at the detected fluorescence energy, φ and θ are the angles of incident and outgoing X-rays with respect to the sample surface, $g \equiv \sin \varphi / \sin \theta$, and d is the thickness of the sample. Energy dependencies are implicit in all equations. In our case of HERFD-XANES, $\varphi = \theta = 45^\circ$, $\varepsilon_a \approx \text{const.}$ and if we assume a thick sample with respect to the absorption length, we can say that

$$\left[1 - e^{-\left(\frac{\mu}{\sin \varphi} + \frac{\mu_f}{\sin \theta}\right) d} \right] \approx 1$$

and we can additionally assume that $\mu_a(E) \approx \mu(E)$. Thus, Equation 4.5 simplifies to

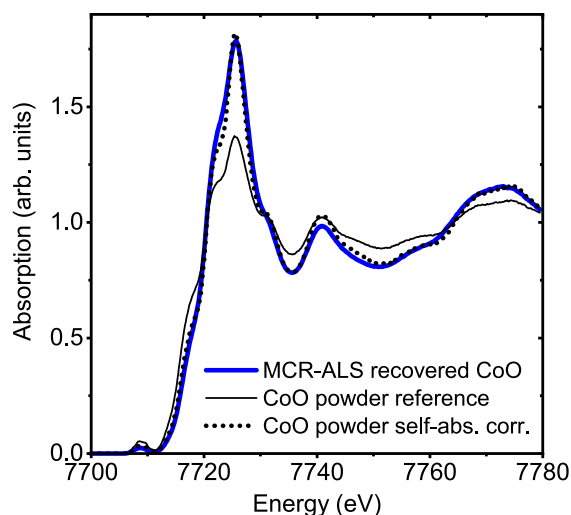
$$I_f^0 \approx \frac{\varepsilon_a \mu}{\mu + \mu_f}$$

which we can rearrange to

$$\mu \approx \frac{\mu_f I_f^0}{\varepsilon_a - I_f^0} \quad (4.6)$$

For the self-absorption corrected fluorescence intensity, $I_{f_{\text{corr}}}^0$, we can say that $I_{f_{\text{corr}}}^0 \sim \mu$ for $I_{f_{\text{corr}}}^0 \ll 1$ and since we are not interested in absolute values for the absorption coefficient, we can use Equation 4.6 to perform self-absorption correction without knowledge of μ_f or ϵ_a .

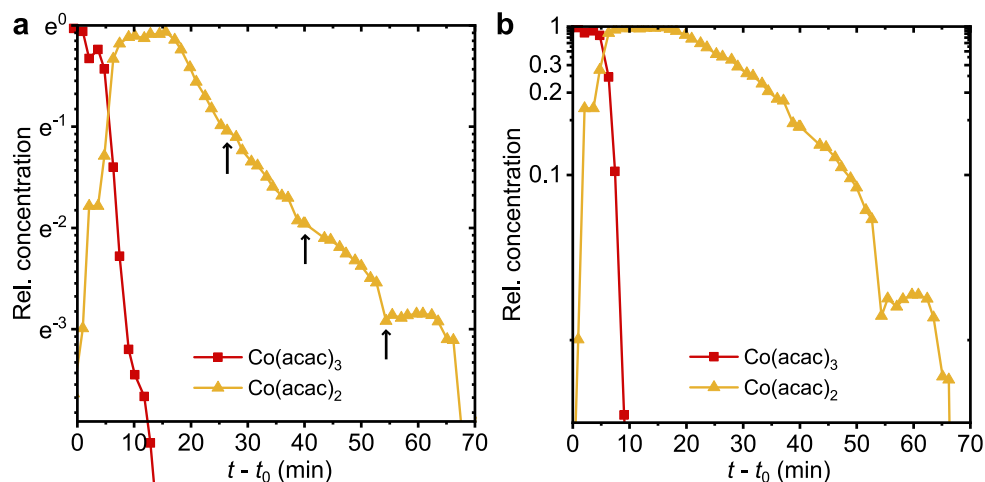
We do the self-absorption correction based on Equation 4.6 for the CoO powder reference in a way that we minimize the difference to the MCR-ALS spectrum of CoO. Due to the relatively low concentration of nanoparticles in the solution, we can assume the MCR-ALS spectrum not to contain any significant self-absorption. The corrected reference spectrum, after re-normalizing the edge step, is shown in Supplementary Figure 4.8 together with the uncorrected MCR-ALS spectrum.



Supplementary Figure 4.8. Co 1s2p HERFD-XANES spectrum of the CoO powder reference before and after self-absorption correction. The spectrum of CoO recovered by MCR-ALS is also shown.

Supplementary Notes 4.3. Kinetic fit of MCR-ALS results

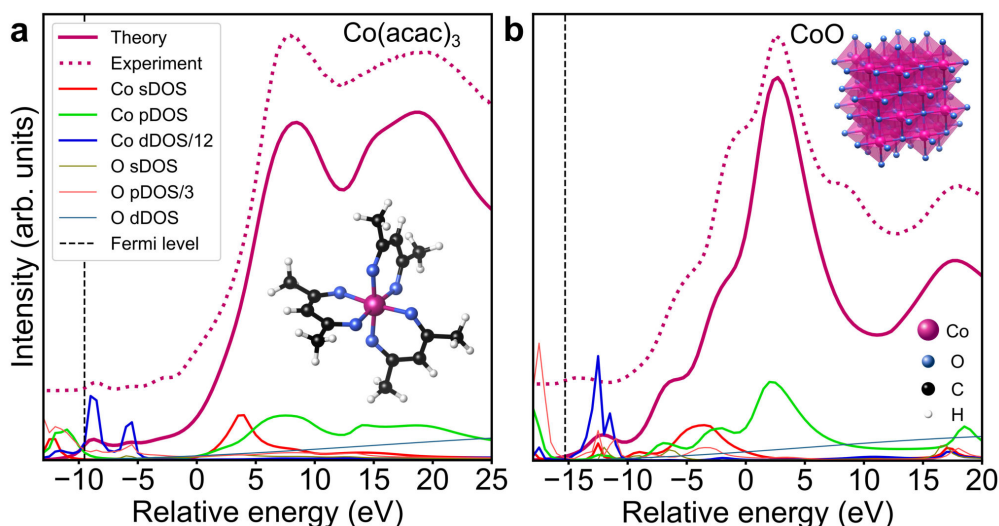
The reaction of $\text{Co}(\text{acac})_3$ with BnOH at 160°C includes two steps, a reduction to $\text{Co}(\text{acac})_2$ followed by the formation of CoO . The concentration profiles obtained from the MCR-ALS analysis give a hint on the kinetics of the reaction steps. Supplementary Figure 4.9 shows plots of the concentrations of the precursor and intermediate in natural logarithmic and reciprocal scale. Arrows in Supplementary Figure 4.9a mark changes in the beam position on the reaction container by a relatively long distance during the collection of the data set. The approximately linear decay in natural logarithmic scale within the intervals between the position changes is a visual indication of pseudo first order kinetics. A previous study on the formation of ZnO nanoparticles from zinc acetate in BnOH reported similar kinetics.^{154, 155}



Supplementary Figure 4.9. Relative concentrations of the precursor and the intermediate. The same values are plotted **a** in natural logarithmic scale and **b** reciprocal scale. Arrows in **a** mark large changes in the position of the X-ray beam on the reaction container. The linear decay in the intervals between the position changes indicates pseudo first order kinetics.

Supplementary Notes 4.4. Calculation of XANES spectra using the FEFF code

In addition to reference measurements, we verify the reaction components identified by MCR-ALS with theoretical calculations of Co K-edge XANES spectra that we obtain using the FEFF code.⁶² From Supplementary Figure 4.10, we see that the calculated spectra of the reaction precursor, $\text{Co}(\text{acac})_3$, and the product, CoO , are in good agreement with the experimentally obtained spectra of these compounds. Additionally, we see that the 3d density of states (DOS) of the cobalt ion mainly determines the shape of the pre-edge transitions. Thus, the pre-edge features arise from hybridization of Co 4p and 3d states, allowing to a certain extent $1s \rightarrow 3d$ quadrupole transitions. The calculated spectrum of CoO is missing a feature ~ 8 eV above the absorption edge compared to the experiment, which we account to a final state effect in the HERFD-XANES measurement not reproducible with FEFF. Standard transmission XANES at the Co K-edge also excludes this feature.¹⁷⁷



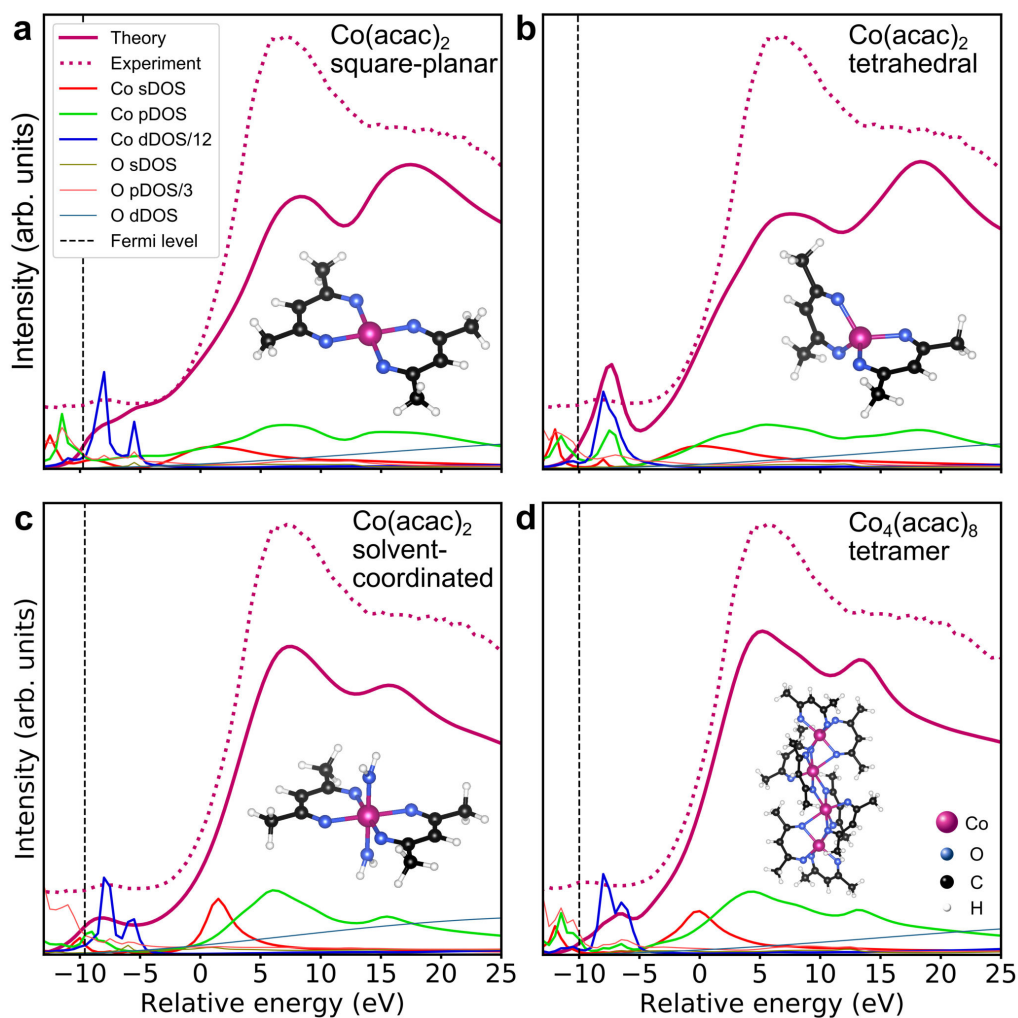
Supplementary Figure 4.10. Theoretical Co K-edge XANES spectra calculated using the FEFF code.⁶² **a** Theoretical spectrum of $\text{Co}(\text{acac})_3$. **b** Theoretical spectrum of CoO . The spectra are plotted together with the local DOS for s, p, and d states. The experimental HERFD-XANES spectrum of the respective compound is shown as dotted line. The energy scale is relative to the absorption edge E_0 . The crystal structure of CoO and the atomic positions in $\text{Co}(\text{acac})_3$ were taken from references^{145, 157}, respectively.

Furthermore, FEFF calculations allow deeper insight into the structure of the reaction intermediate, $\text{Co}(\text{acac})_2$. Previous theoretical and experimental studies revealed a number of conformations of the $\text{Co}(\text{acac})_2$ molecule depending on its aggregate state and environment. Diffraction experiments showed that in the crystalline state, the molecule adopts the tetrameric form $\text{Co}_4(\text{acac})_8$.^{152, 153} Density functional theory (DFT) calculations of the isolated molecule indicate a small energy difference between the square-planar and tetrahedral conformation, thus the interaction with the solvent plays an important role for the actual structure.¹⁴⁴ In Supplementary Figure 4.11, we present FEFF calculations for the possible structures of $\text{Co}(\text{acac})_2$. It is clear that only in the case of an octahedrally coordinated Co^{2+} ion, the theory is in good agreement with the experiment. We conclude that for the reference that was measured as a powder, the molecule forms tetramers with octahedral coordination (c.f. Supplementary Figure 4.11d). In solution, the Co^{2+} ion is additionally coordinated by oxygen atoms of two solvent molecules, forming a bis-adduct with octahedral coordination¹⁵² (c.f. Supplementary Figure 4.11c). Note that since the actual coordination geometry of $\text{Co}(\text{acac})_2$ in BnOH is unknown, we used water as a model coordinating solvent for the FEFF calculations.

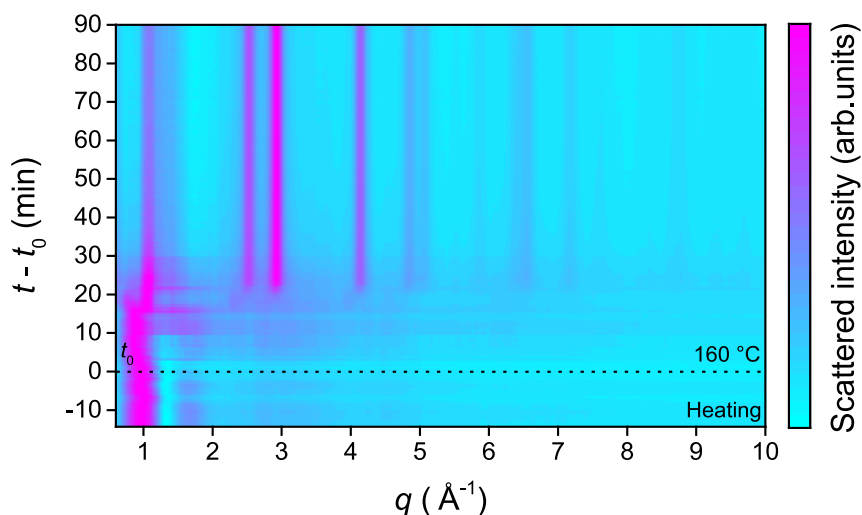
We used the FEFF code⁶² in version 9.6.4 with the Hedin-Lundquist energy dependent exchange correlation potential for all calculations. The settings are listed in Supplementary Table 4.3. Note that no instrumental broadening (EXCHANGE card setting v_i) needed to be applied since the experimental spectra were measured in HERFD mode. For the $\text{Co}_4(\text{acac})_8$ tetramer, we averaged calculations with each of the Co ions set as the absorber, since their environments in the tetramer are not equivalent.

Supplementary Table 4.3: Settings for the FEFF calculations shown in Supplementary Figure 4.10 and Supplementary Figure 4.11.

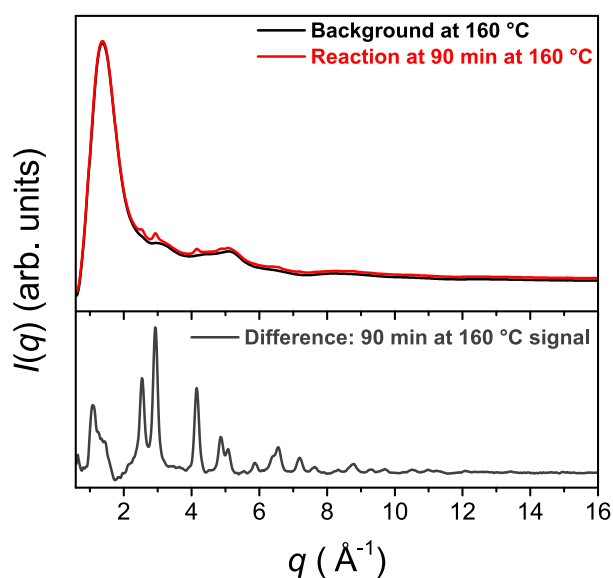
FEFF card	ATOMS	COREHOLE	EXCHANGE		SCF		FMS	
compound	number	type	v_r	v_i	r_{scf}	l_{scf}	r_{fms}	l_{fms}
$\text{Co}(\text{acac})_3$	43	none	3.5	0	6.0	1	6.0	1
$\text{Co}(\text{acac})_2$ tetrahedral	29	none	3.5	0	6.0	1	6.0	1
$\text{Co}(\text{acac})_2$ sq.-planar	29	none	3.5	0	6.0	1	6.0	1
$\text{Co}(\text{acac})_2$ solv. coord.	35	none	3.5	0	6.0	1	6.0	1
$\text{Co}(\text{acac})_2$ tetramer	116	none	3.5	0	6.0	1	6.0	1
CoO	147	none	3.5	0	6.3	0	6.3	0



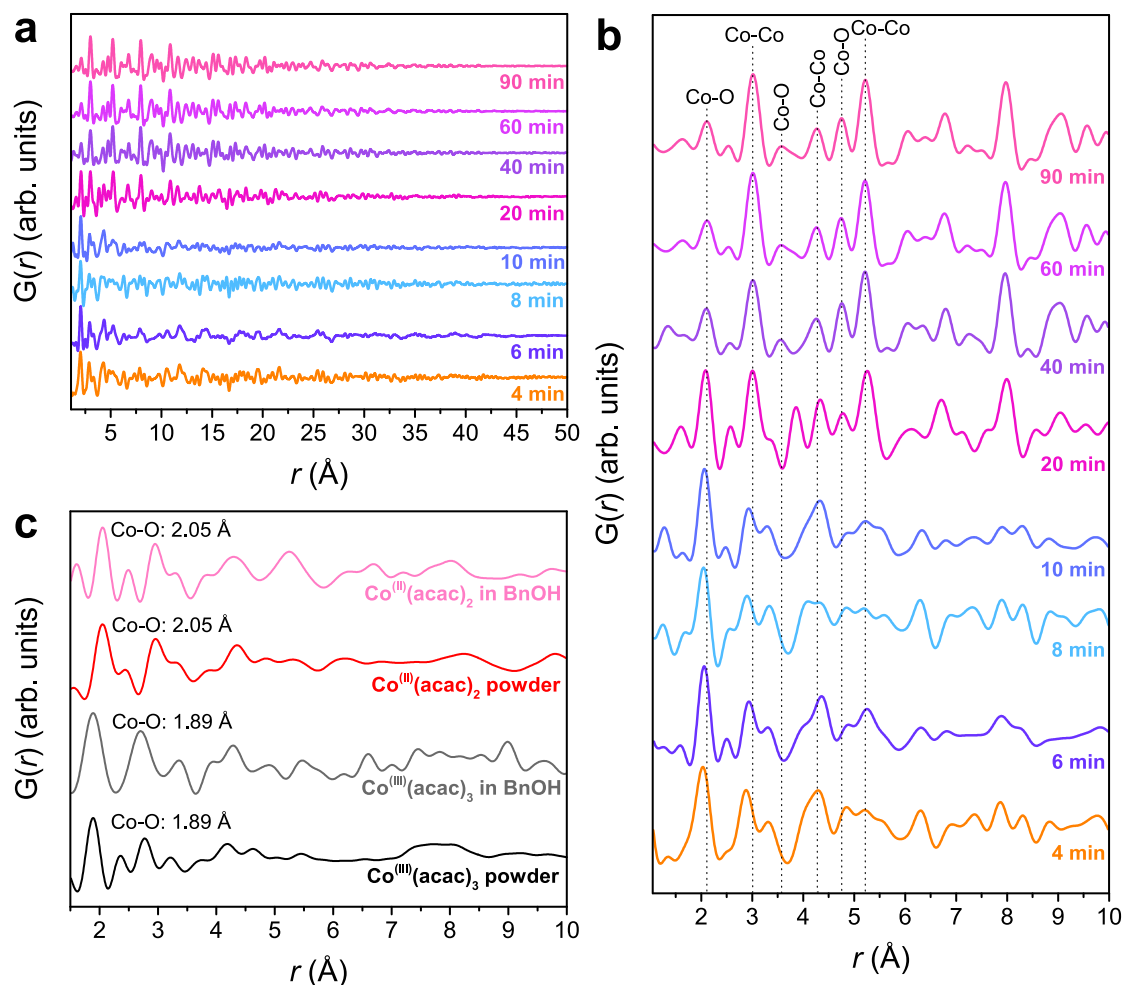
Supplementary Figure 4.11. Theoretical XANES spectra of $\text{Co}(\text{acac})_2$ calculated using the FEFF code.⁶² We compare **a** square-planar, **b** tetrahedral, **c** solvent-coordinated with water as a model solvent and **d** tetrameric geometry. The spectra are plotted together with the local DOS for s, p and d states. The experimental HERFD-XANES spectrum of $\text{Co}(\text{acac})_2$ powder is shown as dotted line. The energy scale is relative to the absorption edge E_0 . Vertical dashed lines indicate the position of the Fermi level. The atomic positions in square-planar and tetrahedral $\text{Co}(\text{acac})_2$ were taken from reference¹⁴⁴ and the structure of the tetramer was adopted from reference¹⁵³.



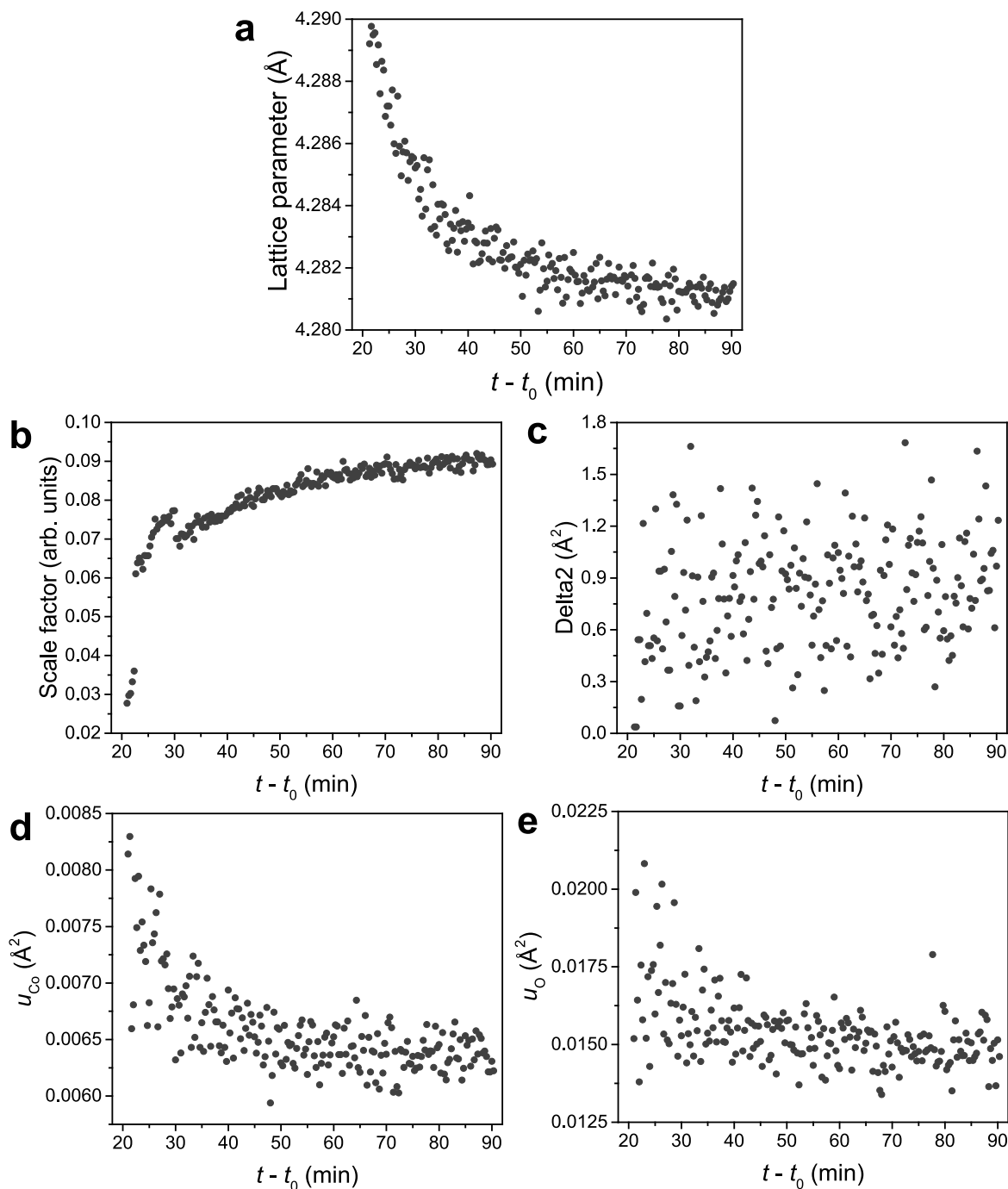
Supplementary Figure 4.12. In situ time-resolved background-subtracted total X-ray scattering measurements for the reaction at 160 °C. The heating step involves heating from room temperature to 60 °C, 5 min at 60 °C, and the heating from 60 to 160 °C. The normalized intensity of the total X-ray scattering data for the final product at 90 min and the background are shown in Supplementary Figure 4.13.



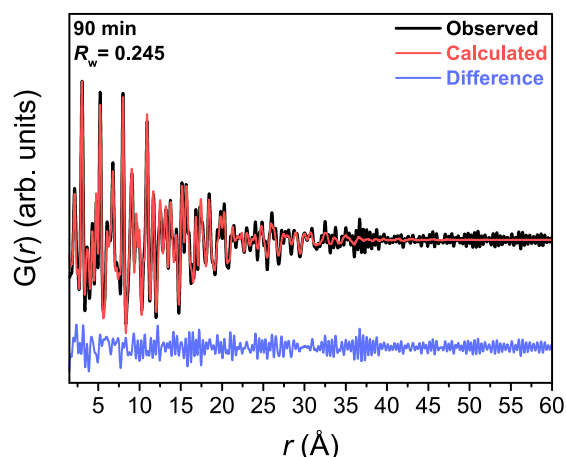
Supplementary Figure 4.13. Normalized total X-ray scattering data for the reaction at 90 min after 160 °C and the background (glass vial filled with BnOH) at 160 °C. The signal to background ratio is very low, mainly due to the low concentration of the precursor. The difference curve reveals the signal of the reaction product after 90 min showing CoO features.



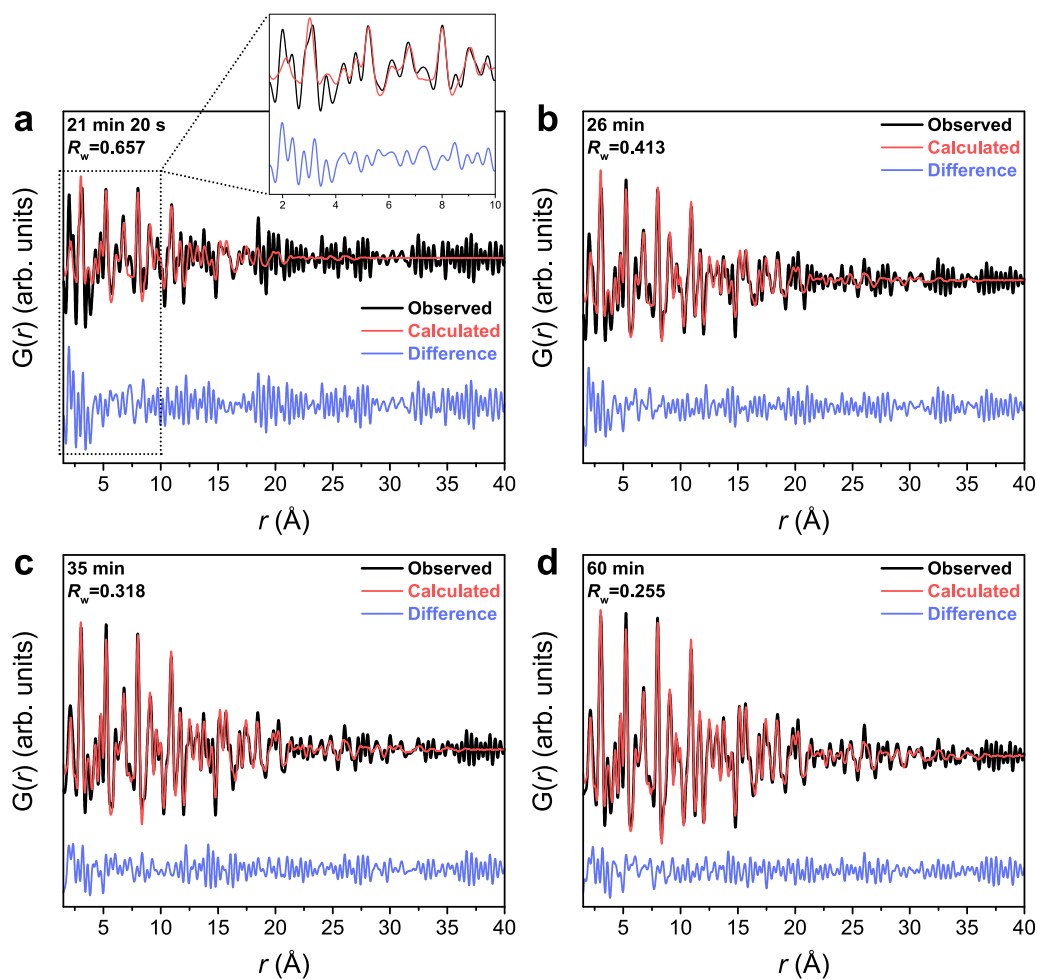
Supplementary Figure 4.14. Ex situ PDFs for the synthesis at 160 °C. **a** PDFs at different reaction times. **b** Zoom of **a** showing the PDFs at the local ordering region. The dashed lines show the first coordination shells of CoO. **c** PDFs of the $\text{Co}(\text{acac})_3$ and $\text{Co}(\text{acac})_2$ references. The measurements were performed for the powders and 0.1 M solutions in BnOH.



Supplementary Figure 4.15. PDF refinement results for the in situ reaction at 160 °C. Evolution of **a** lattice parameter a , **b** scale factor, **c** the quadratic atomic correlation factor δ_2 , **d** isotropic atomic displacement parameter u_{Co} for cobalt, and **e** isotropic atomic displacement parameter u_{O} for oxygen, as a function of the reaction time. The data were obtained from the sequential refinement of time-resolved PDFs. The lattice parameter shown in **a** rapidly decreases as the reaction progresses and fluctuates around 4.28 Å throughout most of the reaction time. However, since the co-existence of $\text{Co}(\text{acac})_2$ and CoO induces a misfit in the low r region before 40 min (Supplementary Figure 4.17a), this strong decrease may not be a real trend.



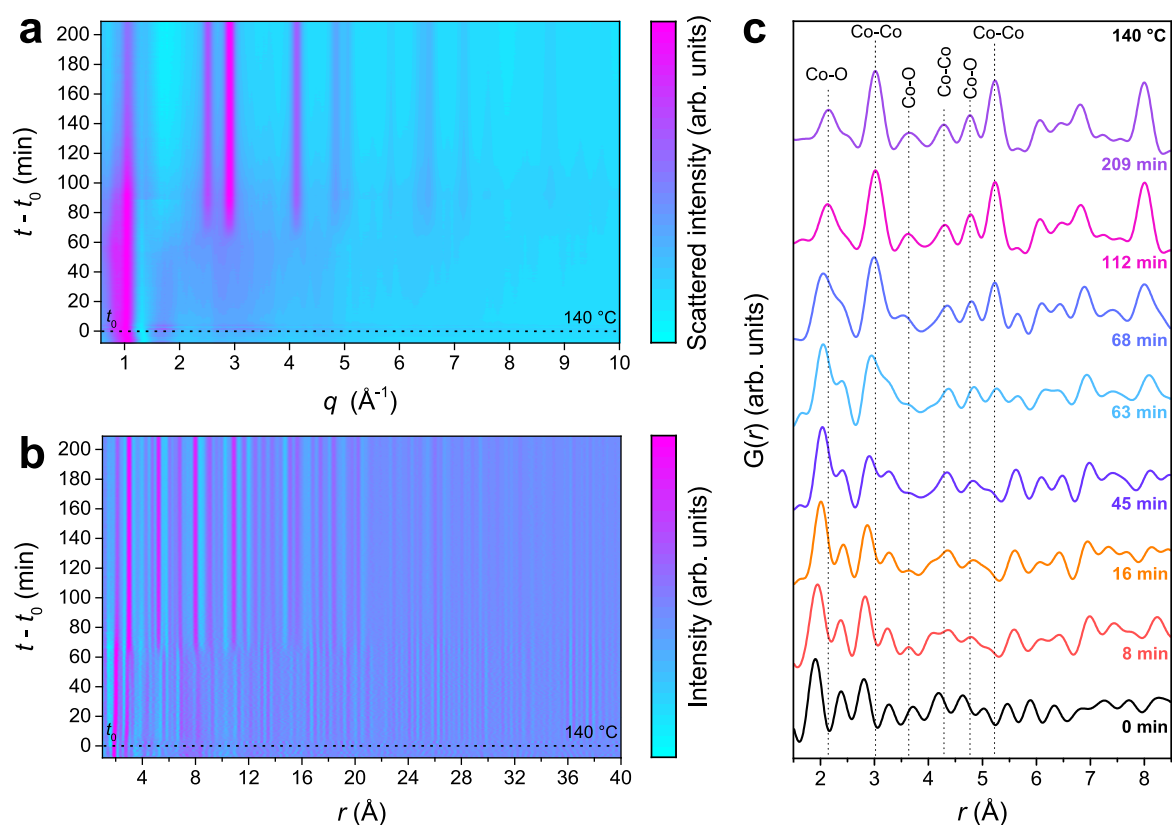
Supplementary Figure 4.16. PDF refinement with higher r range. The plot shows a fit between experimental and calculated $G(r)$ for the PDF obtained at 90 min at 160 °C using a higher r range of 1.5 to 60 Å compared to Figure 4.5c. No correlations are seen beyond 40 Å but noise. Consequently, the R_w value increases compared to the fit up to 40 Å, but no significant changes are observed for the other refined parameters, indicating that the fit up to 40 Å is suitable. The refined value for a is 4.281 Å, for the scale factor is 0.0891, for δ_2 is 1.25 Å², for u_{Co} is 0.0062 Å², for u_{O} is 0.0146 Å², and for the sp-diameter is 64 Å.



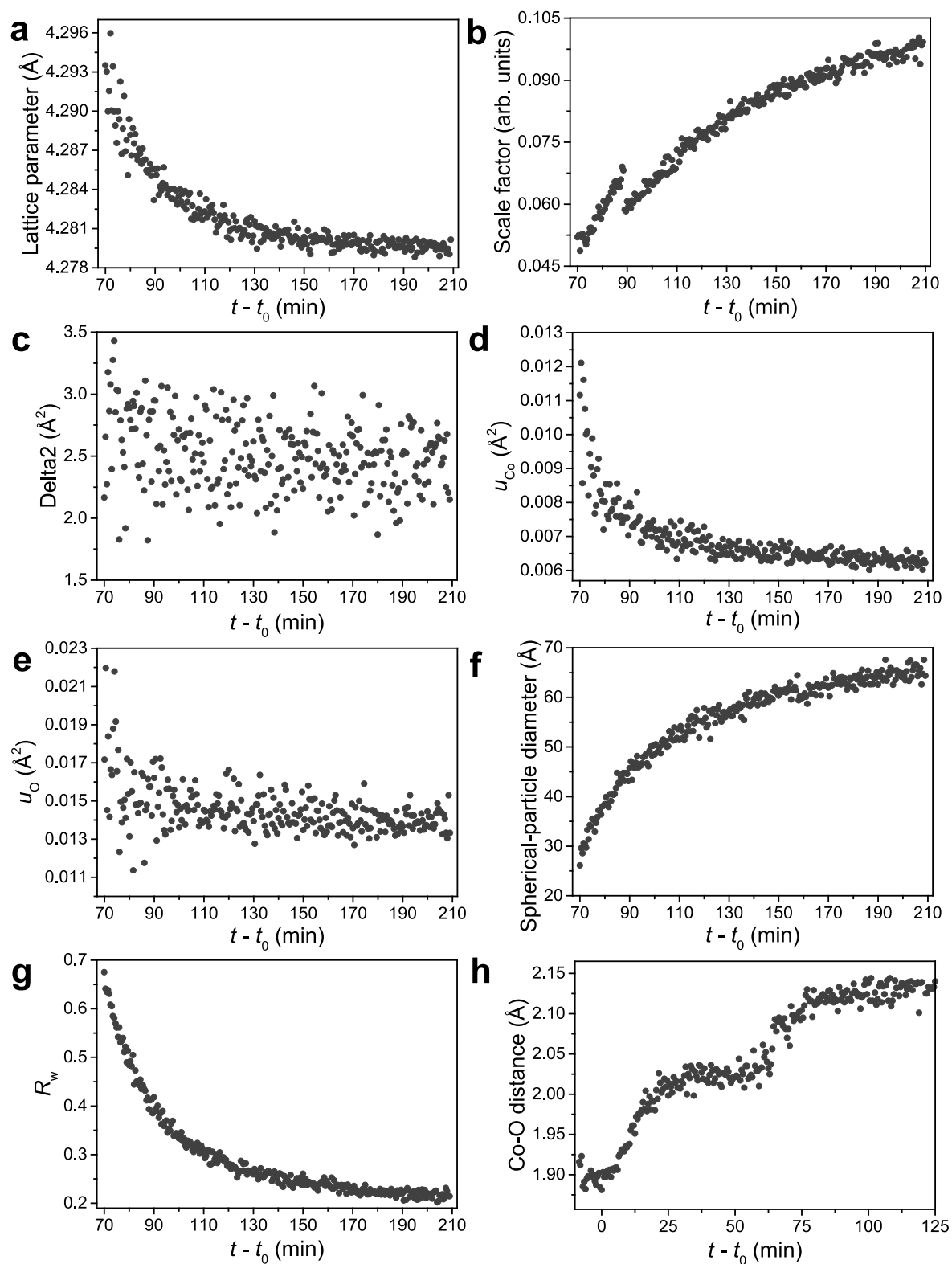
Supplementary Figure 4.17. Fit between experimental and calculated $G(r)$ using the cubic CoO phase. **a** Fit for the in situ reaction at 160 °C at 21 min 20 s reaction time, the inset shows the short range order fit, demonstrating the lack of fit for the first peak probably due to the presence of Co(acac)₂. **b** Fit for 26 min, **c** 35 min, and **d** 60 min reaction time.

Supplementary Notes 4.5. In situ total scattering studies of the reaction at 140 °C

The CoO reflections in time-resolved in situ total scattering data at 140 °C (Supplementary Figure 4.18a) occur after 64 min reaction time, which is 44 min later than at 160 °C. Similarly, the long-range order correlations in the time-resolved PDFs emerge later. (Supplementary Figure 4.18b,c). We evaluate the structural parameters by the same sequential refinement method starting from the final product after 210 min and tracing the signal back towards earlier reaction times. The refinement results are depicted in Supplementary Figure 4.19. The evolution of the sp-diameter over time provides a value of ~26 Å at 70 min, which progressively increases and reaches ~64 Å at 210 min. Therefore, although the reaction at 140 °C yields CoO nanoparticles with a similar particle size as the reaction at 160 °C, the reaction takes ~2.3 times longer.



Supplementary Figure 4.18. In situ total X-ray scattering data for the reaction at 140 °C. **a** In situ time-resolved background-subtracted $I(q)$ data. **b** In situ time-resolved PDFs. The heating steps in **a** and **b** involve the heating from room temperature to 60 °C, 5 min at 60 °C, and the heating from 60 to 140 °C. **c** PDFs at the local ordering region for selected reaction times of the in situ data.



Supplementary Figure 4.19. Additional refined PDF parameters. **a-g** Refinement results for the in situ reaction at 140 °C. Evolution of **a** lattice parameter a , **b** scale factor, **c** the quadratic atomic correlation factor δ_2 , **d** isotropic atomic displacement parameter u_{Co} for cobalt, **e** isotropic atomic displacement parameter u_{O} for oxygen, **f** sp-diameter, and **g** R_w , as a function of the reaction time. The data were obtained from the sequential refinement of time-resolved PDFs. **h** Changes in the shortest Co-O bond over the reaction course at 140 °C.

Supplementary Notes 4.6. SAXS data analysis

Homogeneous spherical model:

The low q regime of the SAXS data was analyzed with a model form factor intensity describing homogeneous spherical particles. The form factor is related to the particle diameter $D = 2R$ by

$$\Psi(q, R) = \frac{3(\sin(qR) - qR\cos(qR))}{(qR)^3} \quad (4.7)$$

The scattering intensity of a particle in a solvent with scattering contrast $\rho_{\text{particle}} - \rho_{\text{solvent}}$ is

$$I(q) = \text{const} \cdot c \cdot V \cdot \left[3(\rho_{\text{particle}} - \rho_{\text{solvent}}) \cdot \frac{\sin(qR) - qR \cos(qR)}{(qR)^3} \right]^2 + \text{background} \quad (4.8)$$

$V = (4\pi/3)R^3$ is the volume of the particle and c is the volume fraction of the particles, which can be determined in absolute units if the instrumental scaling constant (const) and the scattering contrast are determined e.g. by calibration measurements of standard substances.

The model is included in the SasView software package, version 4.2.2. We used the population-based DREAM algorithm with 10^4 samples for fitting. Radii were drawn from a Schulz-Zimm polydispersity distribution.¹⁷⁸ The fitted data range is shown as a solid curve in Figure 4.6. Resulting particle diameter values are given in Supplementary Table 4.4.

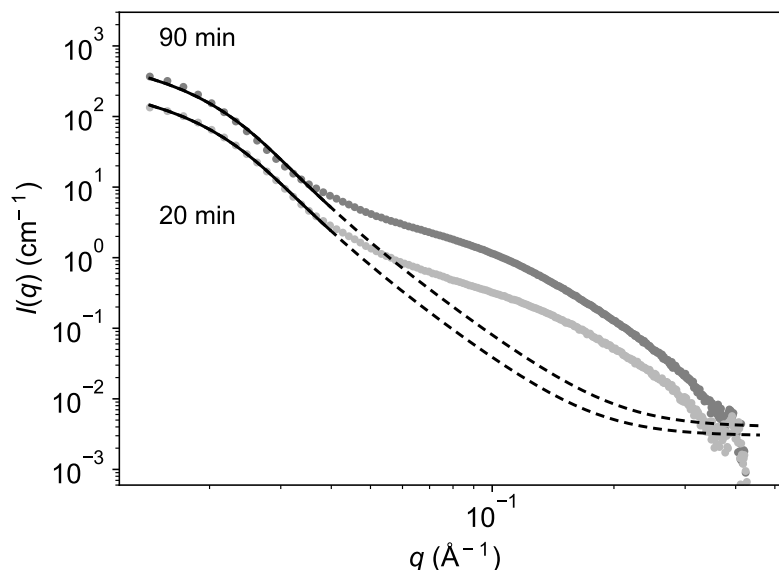
Supplementary Table 4.4: Particle diameters D and polydispersities $\Delta D/D$ obtained from the model.

reaction time	20 min	40 min	60 min	90 min
D	21 nm	45 nm	52 nm	58 nm
$\Delta D/D$	0.25	0.19	0.18	0.19

To quantify the concentration of assemblies obtained at the beginning and end of assembly formation, we recorded SAXS data of aliquots extracted at 20 and 90 min reaction time with our laboratory SAXS setup at LMU. Here, we obtain the scattering intensity on absolute scale (cm^{-1}), by using a high dynamic range, photon counting detector, and normalizing the intensity as

$$I(q) = \frac{I_{\text{raw}}(q)}{I_1 \Omega t_m t} \quad (4.9)$$

$I_{\text{raw}}(q)$ is the integrated SAXS intensity in units of photons. I_1 is the transmitted direct beam intensity through the sample in photons/second. Ω is the solid angle of a detector pixel. t_m is the measurement time in seconds and t the sample thickness in cm. This procedure obviates the need for measuring an intensity standard substance and the instrumental scaling constant (const) equals 1. The data and a least-squares fit with a model of homogeneous spherical particles are shown in Supplementary Figure 4.20. As for the synchrotron SAXS data shown in Figure 4.6a, the deviation between model and data at large q is due to the internal porosity and corrugated surface of the assemblies.



Supplementary Figure 4.20. Laboratory SAXS data of CoO assemblies after 20 and 90 min reaction time, on absolute scale. The dashed lines correspond to a model of homogeneous spherical particles. The solid lines indicate the fitting range of the least-squares model fit.

We assume the reaction product to be composed of CoO assemblies ($\rho_{\text{particle}} = 51.5 \cdot 10^{-6} \text{Å}^{-2}$) in BnOH ($\rho_{\text{solvent}} = 9.47 \cdot 10^{-6} \text{Å}^{-2}$) and use the above Equation 4.9 for fitting. In the case of absolute scale data and scattering contrast the volume fraction of assemblies is obtained from the model fit. Assuming a mass density of CoO of 6.45 g/cm³ and a molecular weight of 74.933 g/mol we calculate the final and initial concentration of CoO. The resulting values are given in Supplementary Table 4.5.

Supplementary Table 4.5: Volume fractions of assemblies and concentrations of CoO obtained from laboratory SAXS data on absolute scale.

reaction time	20 min	90 min
volume fraction	$1.1 \cdot 10^{-4}$	$2.6 \cdot 10^{-4}$
concentration (mass)	0.74 mg/ml	1.65 mg/ml
concentration (amount)	$9.9 \cdot 10^{-3} \text{mol/l}$	$2.2 \cdot 10^{-2} \text{mol/l}$

Given an initial concentration of Co of 0.1 mol/l, the final concentration of $2.2 \cdot 10^{-2} \text{mol/l}$ corresponds to a yield of 22%. The main uncertainty of the concentration measurement is the fit uncertainty of the model, since the data range does not reach the intensity plateau needed to unambiguously determine the particle size distribution. We estimate this uncertainty as 20%, based on a variation of the fitting range.

Supplementary Notes 4.7. PXRD data analysis

In order to probe for crystallinity, PXRD patterns were recorded on the same samples as the SAXS data (Supplementary Figure 4.21). The sample at 20 min reaction time shows some very sharp reflections, which presumably come from a crystallized reaction intermediate, and are not observed in the in situ total scattering experiment (Figure 4.4 and Supplementary Figure 4.12). A crystalline PXRD signal related to CoO was not observed at this reaction time. Starting from 40 min reaction time, Bragg reflections of cubic CoO were seen. A Scherrer analysis of the widths of the reflections yields crystallite sizes of (4.9 ± 2.8) nm, (5.8 ± 1.0) nm, and (6.0 ± 1.2) nm for 40, 60 and 90 min reaction time, respectively. Details of the Scherrer analysis are given below. The PXRD reflections of CoO were fitted with a sum of Lorentzian functions of the scattering angle 2θ . The widths were then analyzed using the Scherrer equation for the crystallite size d :^{179, 180}

$$d = \frac{K\lambda}{\Delta(2\theta) \cos\theta} \quad (4.10)$$

$K = 1$ is a numerical shape factor, $\lambda = 0.71 \text{ \AA}$ is the X-ray wavelength. θ is the Bragg angle in radians of a reflection of width $\Delta(2\theta)$. For $\Delta(2\theta)$, we use the full width at half maximum (FWHM) B of the fitted reflection, corrected by the instrumental resolution $B_1 \approx 3.3 \text{ mrad}$. B_1 is the measured angle-dependent FWHM of a LaB₆ powder standard. In case of a strong Lorentzian broadening $B_2 = \Delta(2\theta)$ due to particle size, and a weak Gaussian instrumental broadening B_1 , the following approximation holds:¹⁸¹

$$\frac{B_2}{B} \approx 1 - \frac{\pi}{2} \left(\frac{B_1}{B}\right)^2$$

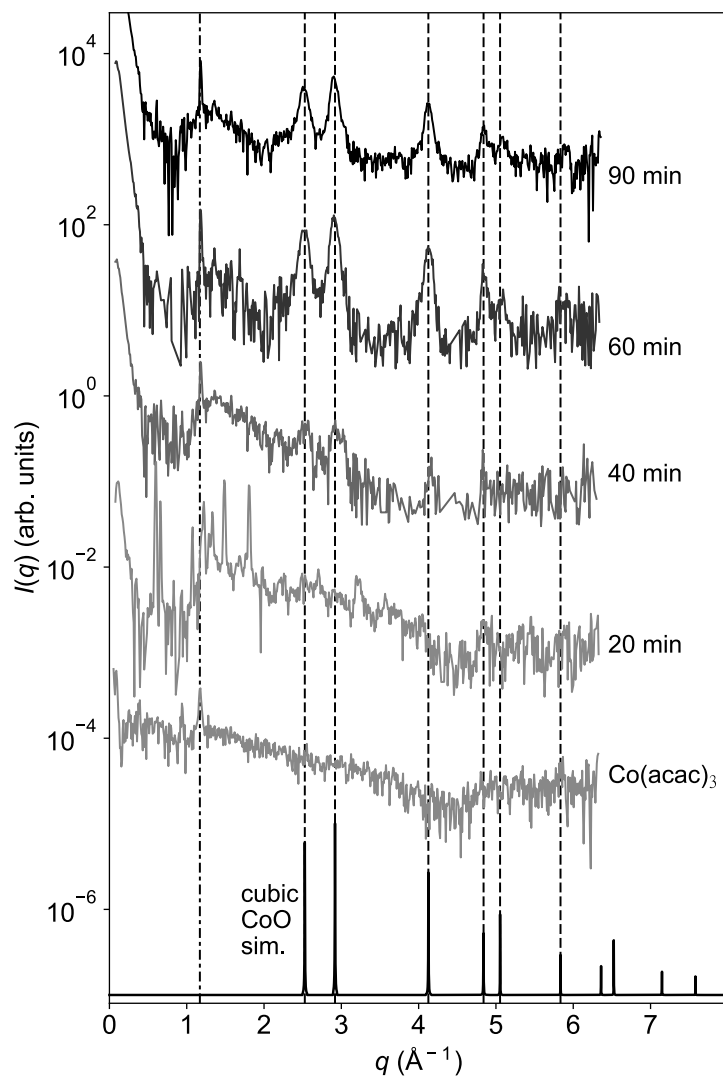
We solve for $B_2 = \Delta(2\theta)$ and obtain

$$\Delta(2\theta) \approx \frac{2B^2 - B_1^2\pi}{2B}. \quad (4.11)$$

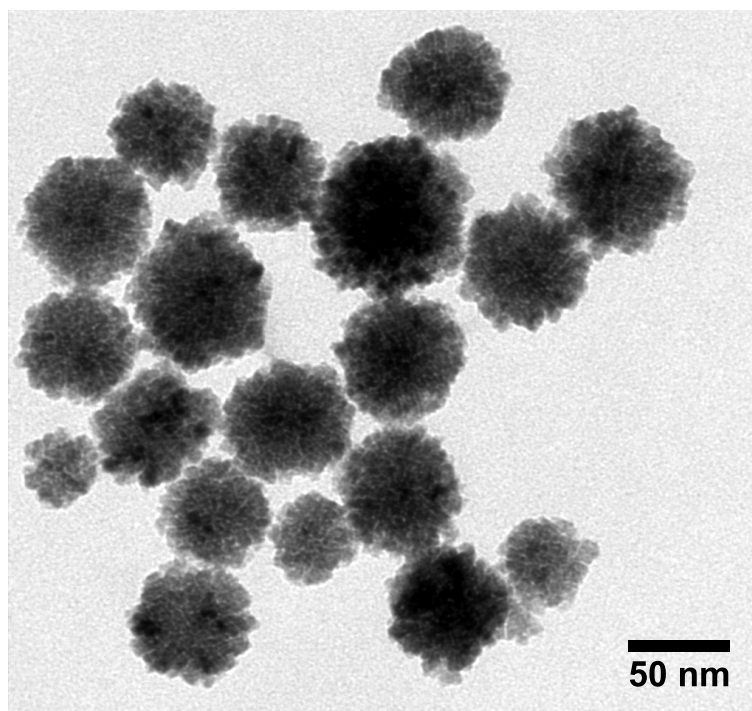
In Supplementary Table 4.6, we report the mean and standard deviation of d obtained from 5 reflections (3 for the 40 min data set). The estimate of the number of crystallites is calculated as $N = 0.74 \cdot D^3/d^3$, with the pre-factor assuming dense packing of spherical crystallites in a spherical particle. This number shows an increasing trend as the values obtained from the combination of assembly sizes from SAXS with crystallite sizes from PDF.

Supplementary Table 4.6: Number of crystallites per particle.

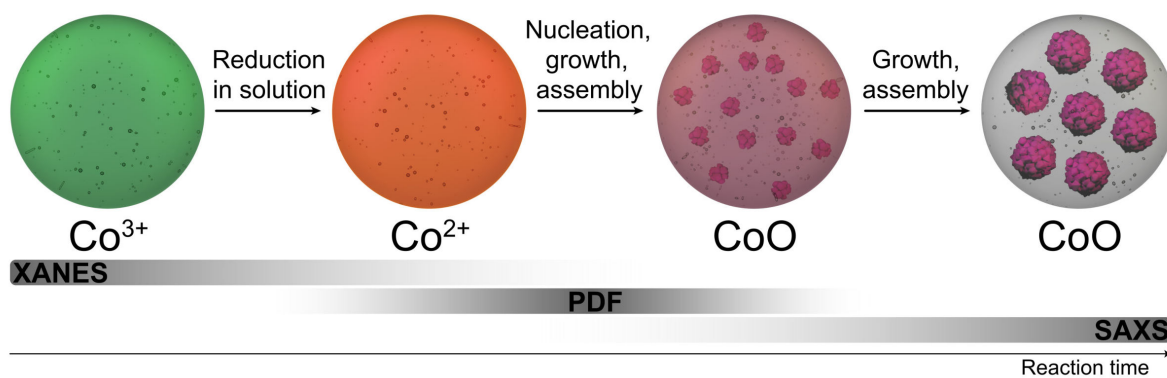
reaction time	40 min	60 min	90 min
<i>D</i> (from SAXS)	45 nm	52 nm	58 nm
<i>d</i> (from PXRD)	(4.9 ± 2.8) nm	(5.8 ± 1.0) nm	(6.0 ± 1.2) nm
<i>N</i>	573	533	668



Supplementary Figure 4.21. PXRD data of dried CoO particles and $\text{Co}(\text{acac})_3$ precursor. Positions of the reflections for 40, 60 and 90 min reaction time match cubic CoO ($a = b = c = 4.31 \text{ \AA}$, $\alpha = \beta = \gamma = 90.00^\circ$, dashed lines). Scherrer analysis of the reflection width shows a crystallite size of 4.9 nm, 5.8 nm, and 6.0 nm, for 40, 60, and 90 min, respectively. The $\text{Co}(\text{acac})_3$ precursor shows only one clear reflection, which is present also in the reacted samples (dash-dotted line). For clarity, only points with intensity above 10^{-5} sr^{-1} after background subtraction are shown.



Supplementary Figure 4.22. TEM image of CoO particles after 90 min reaction time, from the same batch as measured in SAXS. The average particle diameter is 60 nm for the assemblies, and 8-11 nm for the small crystallites.



Supplementary Figure 4.23. Overview of the emergence of nanoassemblies of polyhedrally shaped CoO nanocrystals. We use complementary X-ray spectroscopic and scattering methods to reveal all steps of the nonclassical formation pathway.

5 In situ reactor for imaging

This chapter gives a comprehensive overview of all major aspects of the in situ reactor. Chapters 7-8 present two specific use cases of the reactor, and thus the relevant details of the design are also included in the respective Supplementary Information sections there.

Ralph Döhrmann and Martin Seyrich contributed to the mechanical design of the reactor and Mirko Landmann carried out the thermal simulations.

As we have seen in Section 3.2.1, X-ray microscopy is a promising method for the in situ visualization of nanostructures. In this chapter, we discuss the design of a reactor allowing to image the growth and transformation of substrate-bound nanoparticles in a heated solution. We first identify the experimental requirements that form the basis of the reactor design, followed by a description of the mechanical design of the reactor and the heating equipment. Finally, we apply a thermal simulation to verify the stability of the setup.

5.1 Experimental requirements

X-ray imaging with nanoscale resolution poses high demands on the mechanical stability and position preservation of the entire setup. At the same time, the chemical reactions must not be influenced by the size of the reactor or the choice of materials. We can thus draft the following requirements that need to be considered when designing an in situ reactor for in-solution imaging.

1. The reactor must be thermally and mechanically stable. When heat is applied, residual temperature fluctuations may not cause too large drifts of the reactor so that it is possible to image a selected field of view persistently.
2. The design must be lightweight to ensure the proper function of a piezo-driven nanopositioning stage. At the same time, the body of the reactor must be thin along the beam direction to save space for optical components.
3. A modular design of the reactor is favorable so that the liquid container can be conveniently filled and sealed in an inert gas atmosphere, while the assembly of other reactor components can be done later at the X-ray beamline.
4. The liquid volume to be imaged through must not be too thick along the beam axis to ensure high transmission and low background scattering. The windows must be as thin and X-ray transparent as possible.
5. A relatively large liquid volume is required to ensure reproducible reaction kinetics. If the volume was too small or too thin, the diffusion of reagents could be negatively influenced.^{182, 183}
6. All parts that are in contact with the reaction solution must be made of chemically inert materials.

5.2 Mechanical design

5.2.1 Shape of the reactor

Having identified the above requirements, we continue by discussing a corresponding reactor design. Figure 5.1 shows schematic illustrations of the reactor in exploded and assembled views. The container

for the reaction solution is composed of a polytetrafluorethylene (PTFE) frame stacked between two polyimide windows with a thickness of 125 μm . These are clamped between two frames made of Invar that can be firmly attached to each other with 16 screws. The soft texture of the PTFE ensures the sealing of the container when the polyimide windows are pressed against it. A glass capillary for filling is tightly fit into the PTFE frame at the top and secured with a temperature resistant fluorinated silicone sealant

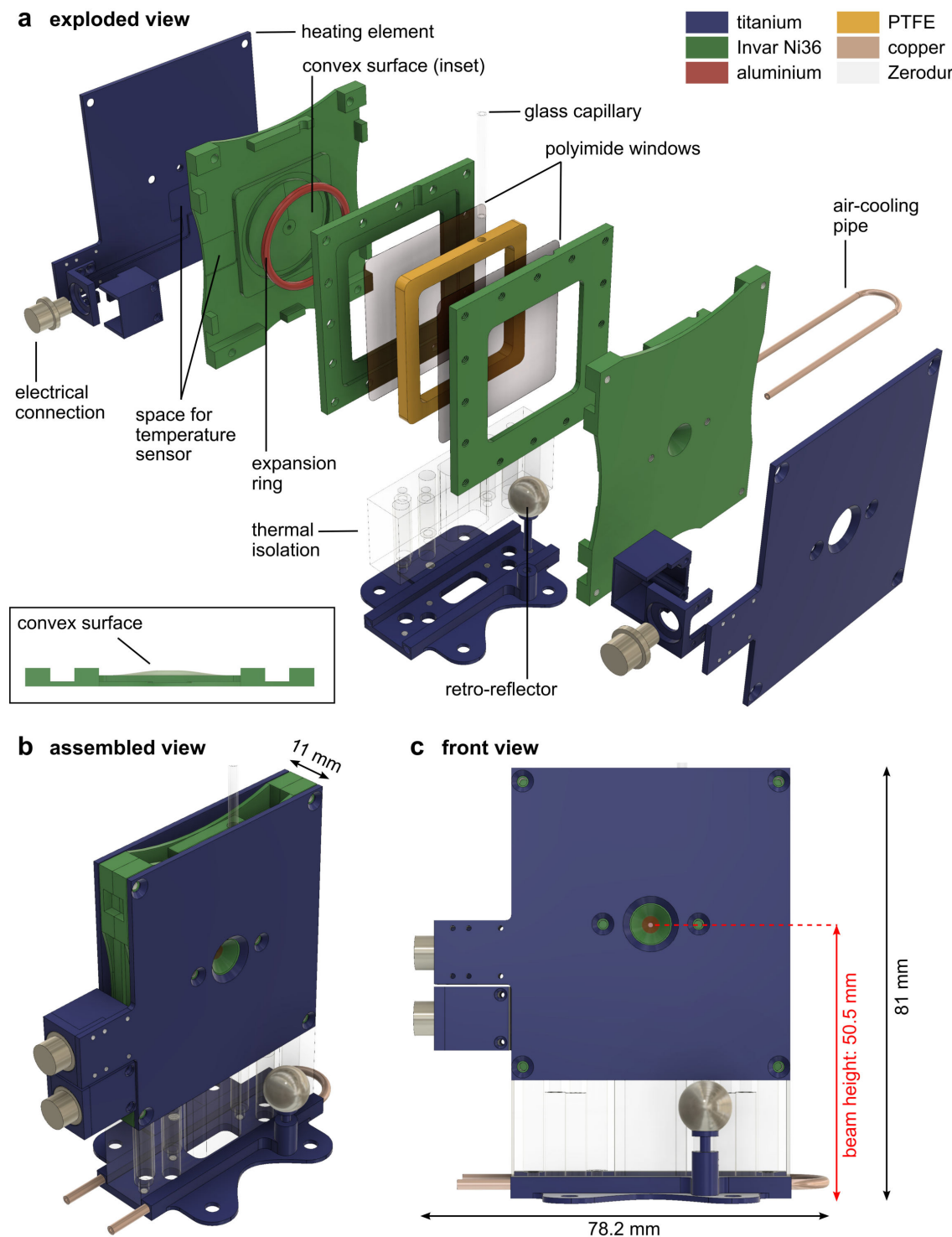


Figure 5.1. Schematic illustration of the in situ reactor. **a** Display of all parts of the reactor in an exploded view. The different materials used for the parts are represented by colors. The inset shows a side view of one of the Invar plates with a convex surface. **b** Display of the assembled reactor. **c** Front view of the reactor indicating the beam position measured from the base plate.

5.2 Mechanical design

(Dowsil 730, Dow Corning, USA). The container can be sealed off by pulling the capillary and transferred to the X-ray beamline, so that the remaining assembly can take place there. Figure 5.2b-c show the assembled and filled container after pulling the capillary.

The container is placed between two plates with a convex surface that push onto the flexible polyimide windows (inset of Figure 5.1a). The liquid volume thereby adapts a concave shape as illustrated in Figure 5.2a. The imprint of the convex plate is also visible in the photograph in Figure 5.2c. This way, the beam path in the solution is reduced to 1 mm at the center of the reactor, while the surrounding liquid volume is thicker and allows for a total of 2.1 mL. With this volume, we can assume reproducible reaction kinetics. When used with benzyl alcohol at 15 keV^d, the transmission of the reactor including the windows is 87%.⁶⁴ At the exit window, scattering up to an angle of 45° can escape from the reactor.

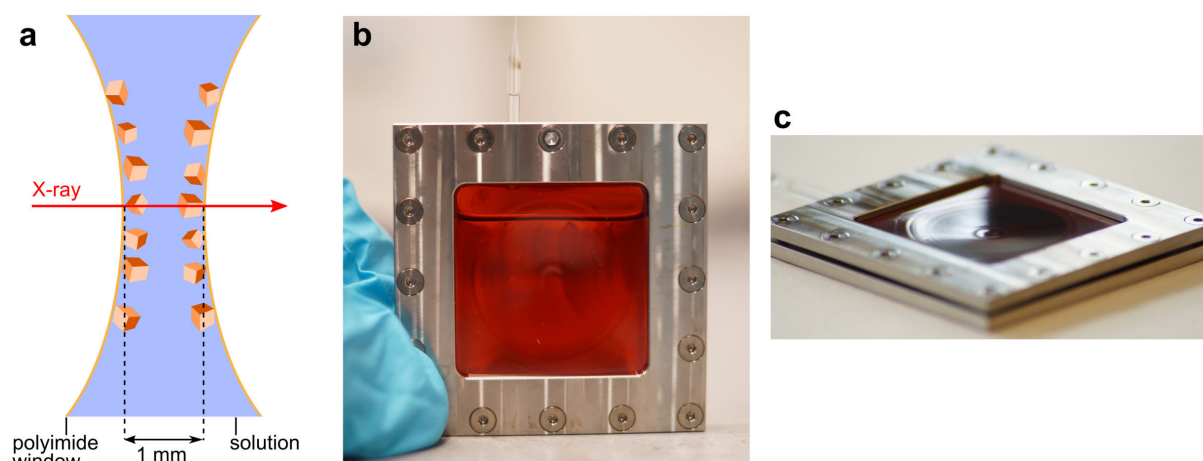


Figure 5.2. Liquid container of the in situ reactor. **a** Illustration of the concave shape of the reaction volume when the container is placed between the outer metal plates. Cubic nanoparticles (enlarged for better visibility) grow on the windows. **b** Front view of the container filled with reaction solution and sealed off at the tip of the capillary. **c** Side view of the container allowing to see the concave imprint of the Invar plate on the shape of polyimide window.

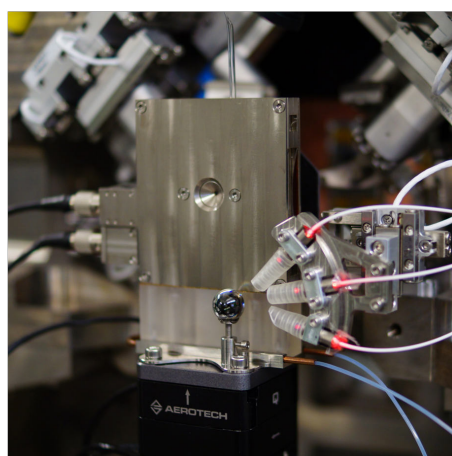


Figure 5.3. Photograph of the in situ reactor mounted at PtyNAMi at beamline P06.

Area heating elements on either side of the reactor provide heat uniformly to the entire body. The heaters are discussed in more detail in Section 5.3. Of course, heating is an optional feature, and the reactor can as well operate at room temperature (c.f. Chapter 8). A thermal isolation is placed between the heated body and the base plate to keep the heat away from the nanopositioning scanner and other motorized

^d Most of the in situ measurements presented in Chapters 7-8 were performed at this energy.

stages beneath it. The base can be air-cooled through a copper pipe to further reduce the amount of heat dissipated to the scanner. The design also includes a retro-reflector to be used for interferometric sample tracking at beamline P06. Figure 5.1b-c show different schematic views of the assembled reactor and Figure 5.3 displays a photograph of the reactor mounted at the Ptychographic Nano-analytical Microscope (PtyNAMi)¹⁸⁴ at beamline P06.¹⁸⁵

5.2.2 Choice of materials

The choice of materials with low thermal expansion is essential for the position stability of the reactor. In Figure 5.1, materials are represented by colors. All components firmly attached to the base require the highest position stability and are made from Ni36 alloy branded under the name Invar. This material has a thermal expansion of -0.04 ppm K^{-1} in a temperature range between $20 \text{ }^\circ\text{C}$ and $100 \text{ }^\circ\text{C}$ ¹⁸⁶ due to the invar effect.¹⁸⁷

During the first in situ imaging experiments (c.f. Chapter 7), it became evident that the polyimide windows slowly deform when continuously heated in the presence of organic solvent. Therefore, in later experiments (c.f. Chapter 8), the convex shaped Invar plates contained an additional expansion ring made from aluminium with a significantly higher expansion coefficient of 23.1 ppm K^{-1} .¹⁸⁸ When the reactor is heated, the ring expands relative to the Invar plate and stretches the polyimide window, resulting in an improved stability of the windows (c.f. Sections 8.3.1 and 8.8).

The main material for the heating elements as well as the base plate is titanium due to its high mechanical toughness and at the same time low density. Titanium has a relatively low thermal expansion coefficient of 8.6 ppm/K .¹⁸⁸ The isolation between the heated body and the base is made from Zerodur, which is a ceramic material produced by Schott (Mainz, Germany). In the intermediate expansion class 2, it has a very low thermal expansion of $0 \pm 0.1 \text{ ppm K}^{-1}$ between $0 \text{ }^\circ\text{C}$ and $50 \text{ }^\circ\text{C}$, and a thermal conductivity of $1.46 \text{ W m}^{-1} \text{ K}^{-1}$.⁷⁰ This combination makes the material an ideal choice to keep heat away from the base and prevent extensive vertical drifts when the heat slowly creeps into the isolation part after the initial heating of the reactor.

5.3 Heating and temperature stability

The heating elements are designed with a flat profile to keep the extension of the reactor along the beam direction small. Figure 5.4a shows a schematic of the heating element. A titanium plate with a thickness of 1.25 mm forms the rigid body. On top of that, a printed circuit board (PCB) on polyimide basis is placed containing a single conductor which acts as resistive heater.

The conductor illustrated in red in the schematics covers almost the entire surface of the heater, ensuring a uniform heat distribution. Only in the vicinity of the beam position where the scattering signal needs to escape, as well as close to the screw positions there is no heating circuit. A flat Pt100 temperature sensor (Ephy Mess GmbH, Wiesbaden, Germany) is placed close to the center of the heating element below the PCB, as it can be dimly seen in the photograph in Figure 5.4b. The resistive sensor has a 4-wire connection to eliminate measurement inaccuracies imposed by the resistance of the cables. A single plug at the side of the heating element connects both the sensor and the heating circuit. Yocto-Pt100 control circuits (Yoctopuce, Cartigny, Switzerland) provide temperature readings from both heating elements. This design of heating elements with built-in sensors was only used in the in situ experiments described in Chapter 8. During in situ experiments presented in Chapter 7, the sensors were positioned into pockets at the edges of the convex Invar plates (Figure 5.1a). The different positions of the sensors resulted in different absolute temperature readings but no apparent difference in temperature stability.

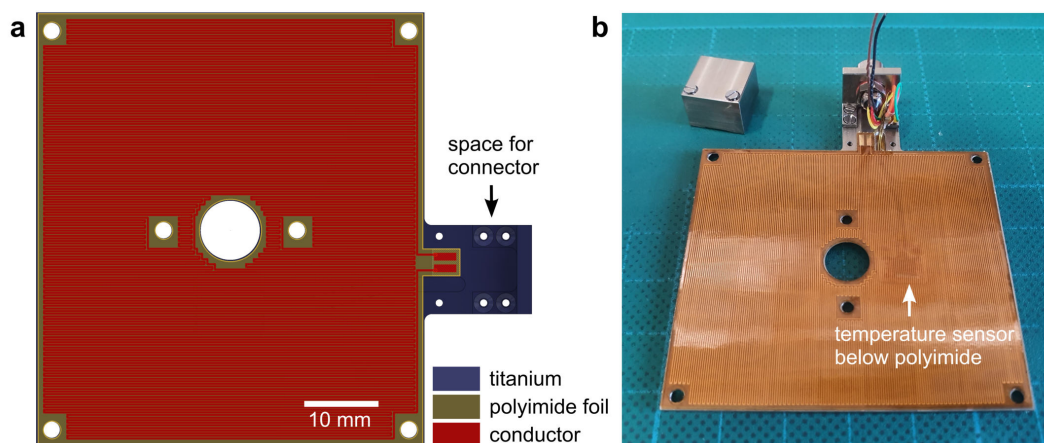


Figure 5.4. Display of a flat heating element. **a** Schematic top view illustration the area covered with the conductor of the resistive heater in red. **b** Photograph of a heating element. The flat Pt100 sensor is located below the polyimide foil. The connection to the sensor and the heating circuit is made with a single plug.

A custom software with a proportional–integral–derivative (PID) controller regulates the resistive heating elements (Figure 5.5a). Heating and cooling rates as well as the setpoint temperature are controlled individually for both heaters. The software uses the temperature reading as feedback to control a DC current through the heaters provided by an external power supply. This procedure avoids switching the heaters on and off repeatedly, which is often found in simple duty-cycle controllers and may introduce vibrations on the nanoscale. The software also provides a feature to auto-tune the PID controllers, which should run after any change to the reactor design or choice of materials. Figure 5.5b shows a typical temperature profile during operation of the reactor measured with one of the built-in sensors. During 1 h of operation, we find peak-to-peak fluctuations of 0.2 °C and a standard deviation of 0.04 °C.

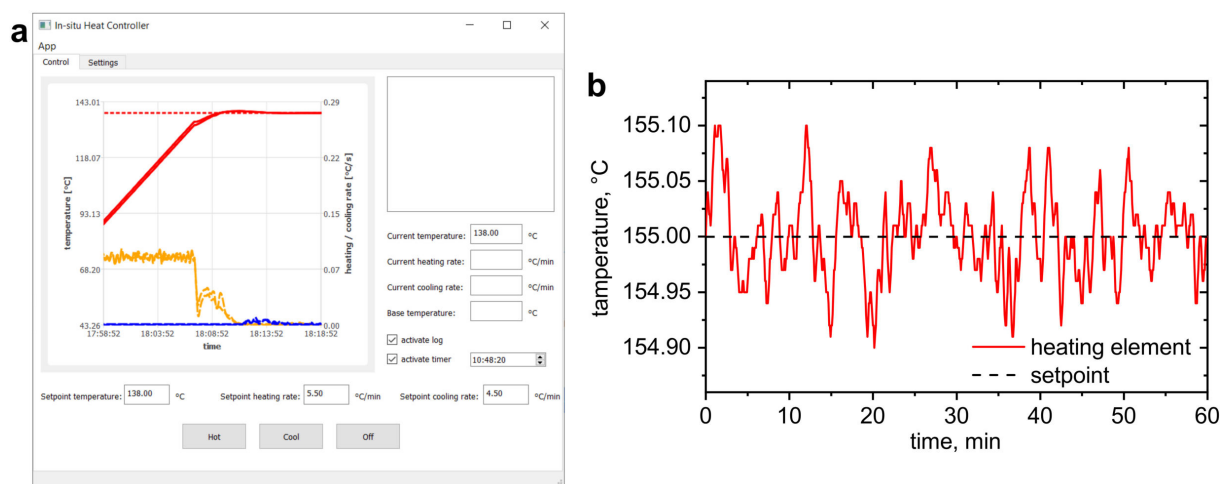


Figure 5.5. Temperature control and stability. **a** Screenshot of the custom software handling the PID controlling of the heating and cooling rates as well as the target temperature. **b** Temperature profile during 1 h of operation at a setpoint of 155 °C measured with the sensor built into the heating element.

5.4 Thermal simulation

Although the materials chosen for the reactor offer very low thermal expansion coefficients, which should result in a high position stability during heating, still some residual drifts were present during the in situ experiments (c.f. Section 7.3.1). We can employ thermal simulations using the finite element

method (FEM) to further characterize the mechanical expansion of the reactor during operation and compare the results to the actually observed drifts. Figure 5.6 gives an overview of the main results of the simulations carried out with the software ANSYS Mechanical, version 17.2 (ANSYS Inc, Canonsburg, USA). The steady-state simulation in Figure 5.6a shows the heat distribution when the reactor reaches an equilibrium state at the setpoint temperature. The heated body (red) is efficiently isolated from base (blue) and positioning stages beneath. During the experiments, we observed a maximum temperature of 42 °C at the top side of the base when the reactor was heated to 155 °C. This observation is in good agreement with the simulation.

Moreover, a transient simulation allows to estimate the residual thermal drifts associated with small temperature fluctuations (Figure 5.6b). An FT of typical temperature fluctuations indicates that the main frequency contribution has period of approximately 6 min. Consequently, the transient simulation uses a sinusoidal temperature profile with the same period and an amplitude of ± 0.05 °C to track the thermal expansion in vertical direction between the base of the reactor and the position of the X-ray beam. As it can be seen from the blue curve in Figure 5.6b, the simulation indicates vertical drifts below 16 nm peak to peak. Due to the symmetry of the reactor, we can expect the horizontal thermal drift to be negligible.

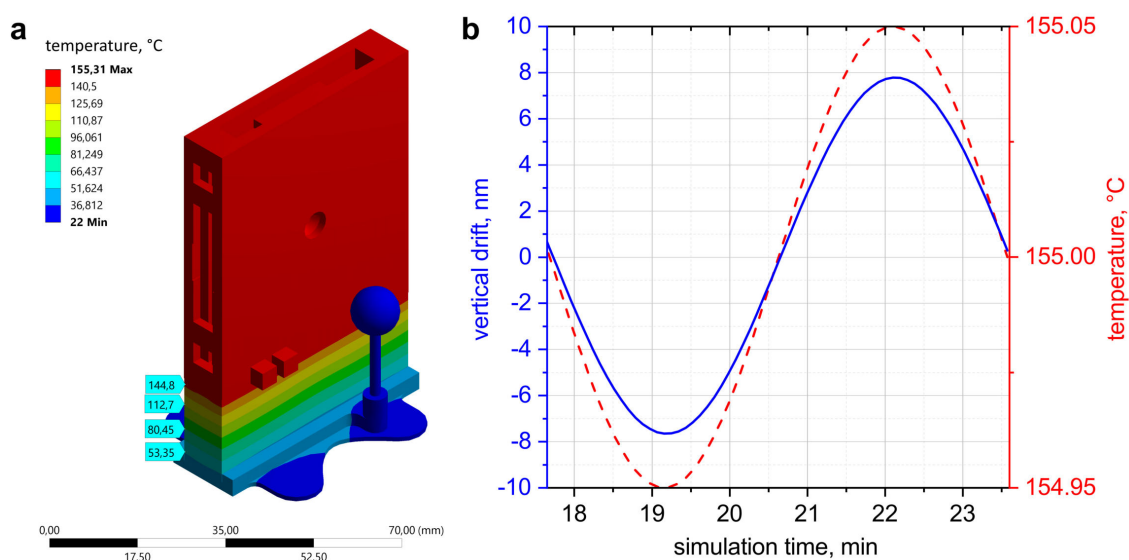


Figure 5.6. Thermal simulation of the reactor. a Stationary simulation of the heat distribution at a setpoint of 155 °C. The body of the reactor is uniformly heated, and the base plate is efficiently isolated. b Transient simulation of the vertical drift between the beam position at the center of the body and the base plate. A sinusoidal temperature profile with a period of approximately 6 min is applied. A vertical drift of 16 nm peak to peak is found.

The actual drifts observed during the experiments were larger, ranging between 100 nm and 1 μm after one image acquisition taking about 22 min. These drifts may thus not result from the thermal expansion of the rigid reactor components, but rather from the polyimide windows which, compared to Invar, have a significantly larger expansion coefficient of 20 ppm K^{-1} .¹⁸⁹ Also, permanent deformations of the window material upon prolonged exposure to organic solvent at an elevated temperature may have played a strong role.

6 Multi-slice ptychography enables high-resolution measurements in extended chemical reactors

The content of this chapter was published in Scientific Reports 11, 1500 (2021) by Maik Kahnt as corresponding author, Lukas Grote, Dennis Brückner, Martin Seyrich, Felix Wittwer, Dorota Koziej, and Christian G. Schroer.

My contribution to this work comprises the synthesis of Cu₂O nanocubes, the SEM characterization, the construction of the reactor, and the acquisition of the ptychographic data set in the reactor.

6.1 Abstract

Ptychographic X-ray microscopy is an ideal tool to observe chemical processes under in situ conditions. Chemical reactors, however, are often thicker than the depth of field, limiting the lateral spatial resolution in projection images. To overcome this limit and reach higher lateral spatial resolution, wave propagation within the sample environment has to be taken into account. Here, we demonstrate this effect recording a ptychographic projection of copper(I) oxide (Cu₂O) nanocubes grown on two sides of a polyimide foil. Reconstructing the nanocubes using the conventional ptychographic model shows the limitation in the achieved resolution due to the thickness of the foil. Whereas, utilizing a multi-slice approach unambiguously separates two sharper reconstructions of nanocubes on both sides of the foil. Moreover, we illustrate how ptychographic multi-slice reconstructions are crucial for high-quality imaging of chemical processes by ex situ studying nanocubes grown on the walls of a liquid cell.

6.2 Introduction

The large penetration depth of hard X-rays in matter makes them an attractive probe to study the inner structures of objects without the need for destructive sample preparation. In particular, X-rays can penetrate sample environments and chemical reactors, making in situ and operando studies of physical and chemical processes feasible.^{68, 190-198} X-ray microscopy is well suited to measure chemical and physical properties with high spatial resolution, even in three dimensions, if it is combined with tomographic techniques.

As a scanning coherent X-ray diffraction imaging technique, X-ray ptychography⁷⁷ takes full advantage of the high brightness of synchrotron radiation sources and greatly benefits from the latest generation of ultra-low emittance sources.¹⁹⁹⁻²⁰¹ Ptychography has revolutionised X-ray microscopy and is routinely used at synchrotron radiation sources around the world.⁷⁷ Compared to conventional X-ray full-field microscopy, X-ray ptychography offers superior resolution, reaching into the single-digit nanometer range.^{202, 203} X-ray ptychography is well suited for in situ and operando measurements and has been utilized to study various physical and chemical processes.^{69, 70, 193, 204} In all cases, the sample is enclosed inside some sample environment that is penetrated by the X-rays during the measurement. For ptychography to work in the thin object approximation, the sample and its surrounding container have to be optically thin. While this can be achieved by using microreactors, the latter are not suited for all types of processes, as some processes cannot be downscaled. For larger reactors, the sample environment may be too thick along the optical axis and exceed the depth of field (DOF) of the

conventional ptychographic model. Such sample environments call for a ptychographic model with extended DOF, the multi-slice model.^{87, 91, 205-212}

A model system to demonstrate the need for multi-slice imaging is a polyimide foil with Cu_2O nanocubes deposited on both of its sides (see Figure 6.1a). To nucleate the Cu_2O on both sides, the foil was immersed in the reaction solution during the non-aqueous nucleation and growth process. The polyimide foil was then removed from the reactor with the nanocubes firmly attached to both its surfaces. For a second demonstration, we mimic an in situ experiment by studying the same Cu_2O nanocubes grown on the two inner surfaces of the polyimide windows of a chemical reactor (see Figure 6.1b).

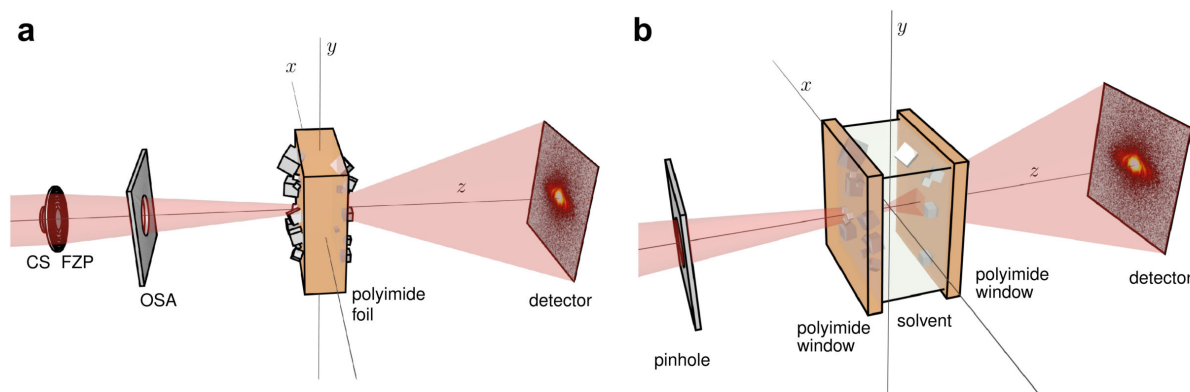


Figure 6.1. Schemes of the two presented experiments: **a** the ptychographic imaging experiment on a single polyimide foil: The central stop (CS), the Fresnel zone plate (FZP) and the order sorting aperture (OSA) are used to focus the coherent X-ray beam (red) on the polyimide foil with Cu_2O nanocubes deposited on both sides. **b** the ptychographic imaging experiment on the chemical reactor: the X-ray beam is focused by a set of two one-dimensional nano-focussing lenses (NFL) (not shown), cleaned up by the pinhole, passes through the extended chemical reactor with particles on the downstream side of the upstream window and the upstream side of the downstream window and is finally measured in the far field by a photon counting pixel detector. In both experiments the sample is scanned perpendicular to the beam (in x and y direction), while diffraction patterns are recorded in the far field downstream of the sample by a photon counting pixel detector. The images were created with blender²¹³ (version 2.83) and were composed using matplotlib²¹⁴ (version 3.1.3).

The Cu_2O nanocubes are formed via a non-aqueous route based on a metal-organic precursor dissolved in benzyl alcohol (BnOH).^{215, 216} The solution is heated, which introduces a heterogeneous nucleation of cubic nanoparticles at solid surfaces in contact with the liquid.¹⁸ Solid surfaces can be the walls of the reaction container or an additional piece of polyimide foil submerged in the solution. The particles nucleate on the surface and grow to a maximum size that depends on several reaction conditions such as the specific precursor, the precursor concentration or the temperature during the growth process. At a reaction temperature of 180 °C, the particles grew to a maximum size of about 500 nm (see Figure 6.2). Like many chemical reactions, this deposition occurs only above a certain process volume due to a disturbance of the reaction kinetics upon downscaling. The slow deposition and growth of the nanocubes is reaction-controlled, meaning that the diffusion of new material towards the particles is fast compared to the consumption of material upon particle growth. Here, the assumption is that above the surface where the particles grow, there is a sufficiently vast continuum of BnOH in which the concentration of the dissolved metal-organic precursor never changes significantly in the vicinity of the particles upon precursor consumption during the reaction. Reducing the size of the reaction chamber even in one dimension along the beam axis would limit the diffusion of precursor material, which could make the process diffusion-controlled and alter the reaction product. The smallest feasible size for reactors that ensure reaction-controlled particle growth is on the order of half a millimetre, well beyond

the DOF for conventional high-resolution X-ray ptychography. To proof the feasibility of an in situ experiment, we first image the Cu_2O nanocubes deposited on the two sides of a polyimide foil (see Figure 6.1a) and then on the polyimide entry and exit windows of the chemical reactor (see Figure 6.1b).

The polyimide foil had a thickness of $\approx 100 \mu\text{m}$, which is already smaller than the minimal extension of the reactor along the optical axis. For high-resolution ptychography, even a thickness on the order of $\approx 100 \mu\text{m}$ exceeds the DOF, demonstrating the need for multi-slice reconstructions for the high-resolution in situ X-ray imaging study of the reaction.

6.3 Results

In the conventional ptychographical model, the sample is assumed to be thin, allowing the sample to be modeled as a two-dimensional complex-valued field $O(\mathbf{r})$ and the interaction with a probing coherent wavefront $P(\mathbf{r})$ can be described by the multiplication of the two.^{83, 84}

There are three thickness regimes to differentiate.

First: the sample is so thick that the X-ray beam changes significantly while propagating through the sample and thus the sample cannot be regarded as optically thin. For the first experiment described here, the DOF of the Fresnel zone plate (FZP) that was used for focusing the X-rays was calculated to be $\text{DOF}_{\text{FZP}} = 143.86 \mu\text{m}$, which is larger than the sample thickness of $100 \mu\text{m}$. Thus the first experiment does not fall into this category. This would change, if the numerical aperture (NA) of the optics was increased, e. g., to reach higher spatial resolution in conventional scanning microscopy, or if the sample would be even thicker, like in the second presented experiment. There the DOF of the nano-focussing lenses (NFL) was estimated to be $\text{DOF}_{\text{NFL}} = 182.95 \mu\text{m}$ (see Section 6.5 for details), which is smaller than the estimated sample thickness of $650 \mu\text{m}$. The chemical reactor can thus not be modeled as a thin sample in the presented experiment.

Second: the sample is thinner than the DOF of the illuminating beam and the latter does not significantly change along the whole thickness of the sample. In ptychographic imaging, however, the largest scattering angle with sufficient scattered signal on the detector defines the effective NA of the virtual objective lens. It often exceeds that of the illuminating beam significantly and thus allows for far higher resolution than the illuminating beam size. Along with this comes a reduced DOF for ptychography that is smaller than that of the illuminating beam and can be smaller than the thickness of the sample. If it really becomes smaller than the thickness of the sample, the sample has to be regarded as optically thick for ptychography. In the presented experiments, the smallest possible DOF for ptychographic imaging is defined by the physical size of the cropped diffraction patterns on the detector. For the experiment on the polyimide foil, it is calculated to be $6.39 \mu\text{m}$ and for the experiment on the chemical reactor it is calculated to be $2.58 \mu\text{m}$ (see Section 6.5 for details). The Cu_2O nanocubes themselves are therefore thin enough to be modeled as thin samples in both experiments. The polyimide foil and the extended chemical reactor however are much thicker than those two numbers respectively. For the latter it was already established that it cannot be modeled as a thin sample. For the experiment on the polyimide foil, this case of being thin for the probing X-ray beam but not being also necessarily thin for the virtual imaging lens, does apply. To determine if the foil can be considered as optically thick or optically thin, the effectively used NA of the detector has to be determined. It can be smaller than the chosen cropping of the diffraction patterns, thus resulting in an effective DOF larger than the minimal achievable DOF calculated above.

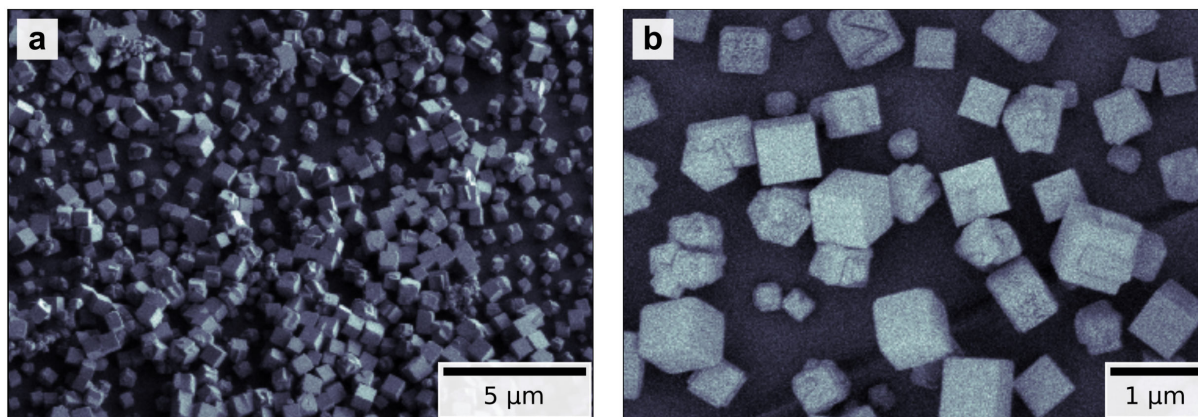


Figure 6.2. Scanning electron microscopy (SEM) overview images of two different regions on the same side of a polyimide foil covered with Cu_2O nanocubes similar to the ones used in the X-ray imaging experiment. **a** Secondary electron image of tilted sample taken at 1 keV accelerating voltage showing mostly smooth nanocubes and varying local covering densities of the surface with nanocubes; **b** Mixed secondary and back scattered electron beam image taken at 0.3 keV accelerating voltage reveal irregularly facets at the surface of some nanocubes and additionally irregularly shaped particles. The images were recorded using a Hitachi Regulus 8200 Series field-emission (FE) SEM, operation on the control software version 3.2. The figure was created using matplotlib²¹⁴ (version 3.1.3).

Third: the sample is thinner than the DOF of the ptychographic imaging geometry. In that case, the sample is optically thin and the conventional ptychographic model can be applied. This would for example hold true for the nanoparticles on one side of the polyimide foil and the particles on one window of the chemical reactor.

To resolve the question if the experimental data taken on the polyimide foil can be regarded as optically thin, the previous arguments can be turned around, asking what spatial resolution can be expected if one assumes a given object to be optically thin. In that case a DOF matching the sample thickness implies a lower limit for the spatial resolution. This has been investigated by Tsai et al.,⁹¹ where this relationship has been determined numerically:

$$T \leq 5.2 \cdot \frac{(\delta r)^2}{\lambda}, \quad (6.1)$$

where T is the thickness of a sample that is treated as thin, δr is the achievable image resolution and λ is the wavelength of the probing X-ray beam. Using the experimental parameters for the experiment on the polyimide foil (see Section 6.5 for details), and the known sample thickness of $T = 100 \mu\text{m}$, Equation 6.1 yields a resolution δr of at best 51.1 nm in thin-sample approximation.

To be able to compare this resolution limit with the actually achieved resolution, the recorded data from the experiment on the polyimide foil needed to be reconstructed using the thin sample approximation. We separated the set of recorded diffraction patterns into two halves and reconstructed both halves with identical reconstruction parameters using the extended ptychographic iterative engine (ePIE) algorithm,⁸³ which is based on the thin-sample approximation (see Section 6.5 for details on the reconstructions). One of the reconstructed objects is shown in Figure 6.3a, showing the Cu_2O nanocubes scattered all over the imaged field of view. We estimated the resolution using Fourier ring correlation (FRC)^{217, 218} between the two reconstructions to be 49.3 nm (see Figure 6.4a). In this experiment the resolution in the ptychographic image thus might have been limited by the DOF as described by Equation 6.1. If that were the case, the object needs to be modeled as optically thick to push the resolution beyond this limit.

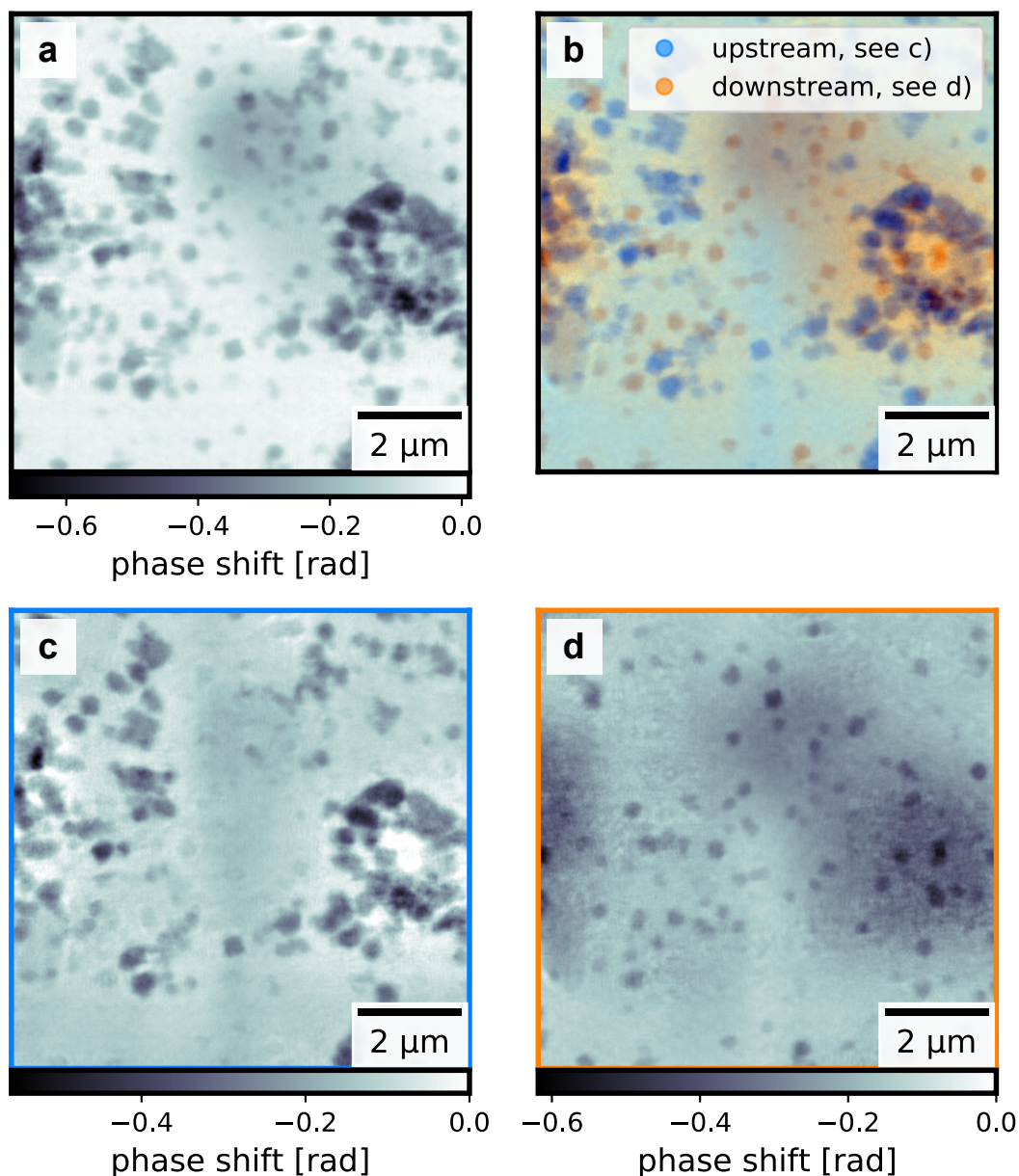


Figure 6.3. Phases of the reconstructed objects from the single polyimide foil experiment in direct comparison: **a** single object slice reconstruction using ePIE. **b** colored overlay of the upstream object slice (blue, **c**) and the downstream object slice (orange, **d**), reconstructed using the three-dimensional Ptychographic Iterative Engine (3PIE). The figure was created using matplotlib²¹⁴ (version 3.1.3).

To test this hypothesis, multi-slice reconstructions of the same dataset were carried out subsequently using the three-dimensional Ptychographic Iterative Engine (3PIE) algorithm,⁸⁷ modeling the sample as two distinct slices separated by the measured 100 μm thickness of the polyimide foil (see Section 6.5 for details on the reconstructions). The reconstructed object slices are shown in Figure 6.3b-d. We estimated a resolution of 36 nm in all reconstructed slices by comparing the reconstructed slices from the two reconstructions using FRC (see Figure 6.4b). The improvement in resolution by accounting for an X-ray optically thick sample confirms the consideration above.

Both the ePIE and the 3PIE algorithm reconstruct the same particles at the same position. Every single Cu_2O nanocube can be found either in the upstream sample slice or the downstream sample slice of the multi-slice reconstruction. None of the Cu_2O nanocubes is reconstructed in both slices. The algorithm unambiguously separated the particles according to which surface they are located on. Long-ranged artefacts (see Figure 6.5g-h) can be seen in the background. As they are the same in the single slice

reconstruction and the multi-slice reconstruction, we can exclude that the introduction of a second object slice and the connected reduced redundancy in the data is the reason for their appearance. The reconstruction of these low spatial frequencies is a known problem of such phase retrieval algorithms in the presence of short-term instabilities.²¹⁹

Looking at the background behind the particles, a vertical stripe can be seen in the center of both multi-slice reconstructed object slices. In the upstream slice (see Figure 6.3c) it appears more phase shifting than its surrounding and in the downstream slice (see Figure 6.3d) it appears less phase shifting than its surrounding. Adding both slices together makes this feature vanish and results in an image very similar to the single slice reconstruction (see Figure 6.3a). There is no way of disproving that those are real features in both the upstream slice and the downstream slice. However, the fact that these two stripes cancel out so perfectly suggest that this is another artefact introduced by the 3PIE reconstruction and not real features of the sample. As the stripe is vertical and thus follows the fast scanning direction, we believe this artefact is the result of instability of the probing X-ray beam, as this is more likely than two features in the two slices aligning and cancelling out perfectly.

The two sides of the polyimide foil show a distinct difference of Cu_2O nanocube coverage. These local differences in covering density of particles have already been observed between different regions on the same side of the polyimide foil using scanning electron microscopy (SEM) (see Figure 6.2). Therefore, the differences in covering density between the two reconstructed slices do not necessarily indicate global differences between the two sides of the polyimide foil, but rather only local differences in the reconstructed field of view. That is why the differences in coverage do not indicate an arbitrary separation of the Cu_2O nanocubes to one of the reconstructed slices. In fact, the multi-slice reconstruction of a second scan resulted in the very same separation of particles.

Changing the order of initialization (see Section 6.5 for details) of the slices in the algorithm resulted in the very same separation of the particles between the two slices (see Figure 6.5). Only the long-range artefacts switched slices, as they always remained in the slice which was initialized first (see Figure 6.5g-h). This strengthens our confidence in the truthfulness of the separation into particles on the upstream surface and particles on the downstream surface of the polyimide foil. However, because of the small size of the scanned area ($10 \times 10 \mu\text{m}^2$) compared to the size of the full sample ($10 \times 10 \text{mm}^2$) it was not possible to independently verify the separation of particles into upstream and downstream surface after the X-ray experiments using SEM imaging.

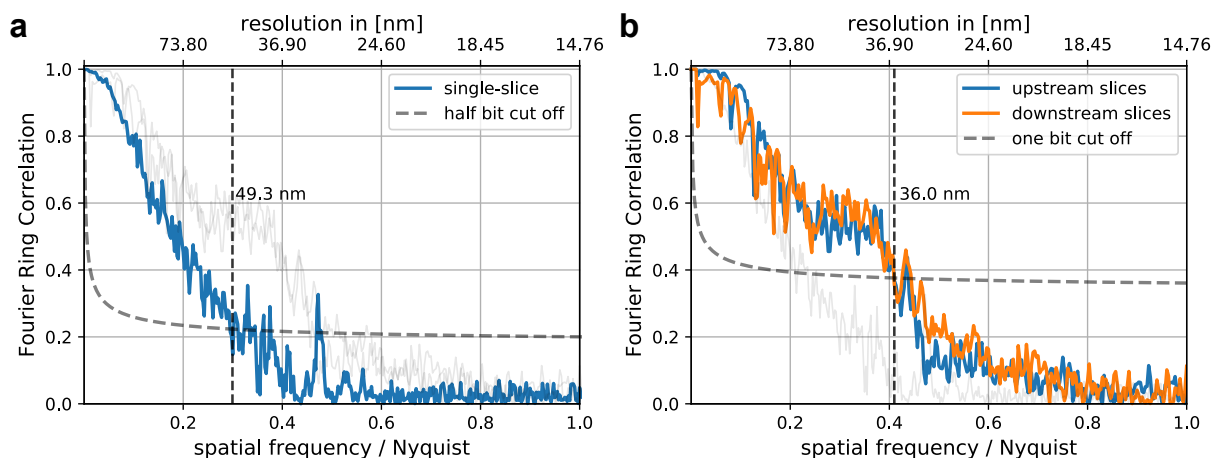


Figure 6.4. Estimated resolutions of the single polyimide foil experiment using FRC: **a** using two single slice reconstructions from halved datasets. **b** using the two multi-slice reconstructions with inverted initialization order. The light gray lines show the FRC of the respective other reconstructions for an easier comparison. The figure was created using matplotlib²¹⁴ (version 3.1.3).

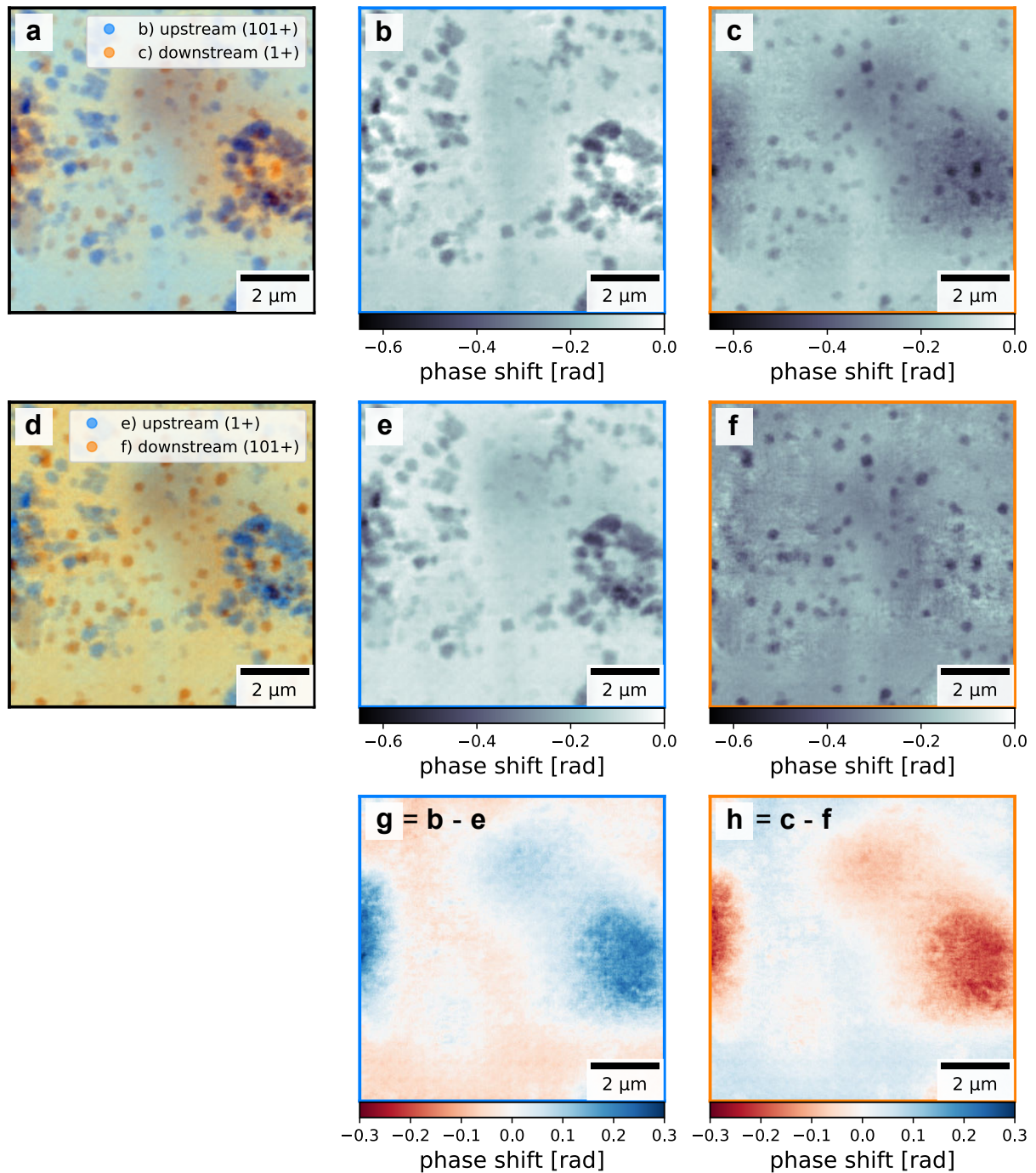


Figure 6.5. Comparison of two multi-slice reconstructions of the same recorded dataset from the single polyimide foil experiment with inversed initialization order of the two object slices: **a-c** reconstructed object slices of the reconstruction where the downstream sample slice was initialized first, **d-f** reconstructed object slices of the reconstruction where the upstream sample slice was initialized first, **g** and **h** difference between the reconstructed up-/downstream slices respectively between the two initialization cases showing the long range cloud like artefacts switching slices depending on the initialization order. The figure was created using matplotlib²¹⁴ (version 3.1.3).

The final step towards an in situ experiment was to image particles inside the reaction chamber they were grown in. A chemical reactor with two polyimide foils as entry and exit windows for the probing X-ray beam was designed and built. In a first test, Cu₂O nanocubes were grown inside the chemical reactor in the lab without a probing X-ray beam. The precursor solution was removed from the chemical reactor, the chemical reactor was disassembled and both the entry and exit windows were imaged by

SEM to verify that nanocubes have indeed grown on both windows. Afterwards the chemical reactor was reassembled using the very same windows and filled with the solvent.

The distance between the inside window surfaces was estimated to be around $650\ \mu\text{m}$, which is significantly more than the previous test based on the $100\ \mu\text{m}$ thick polyimide foil. The reassembled chemical reactor was then ptychographically measured using X-rays without heating it (see Figure 6.6a) to verify that the particles can be imaged in this sample environment (experimental details can be found in the Section 6.5).

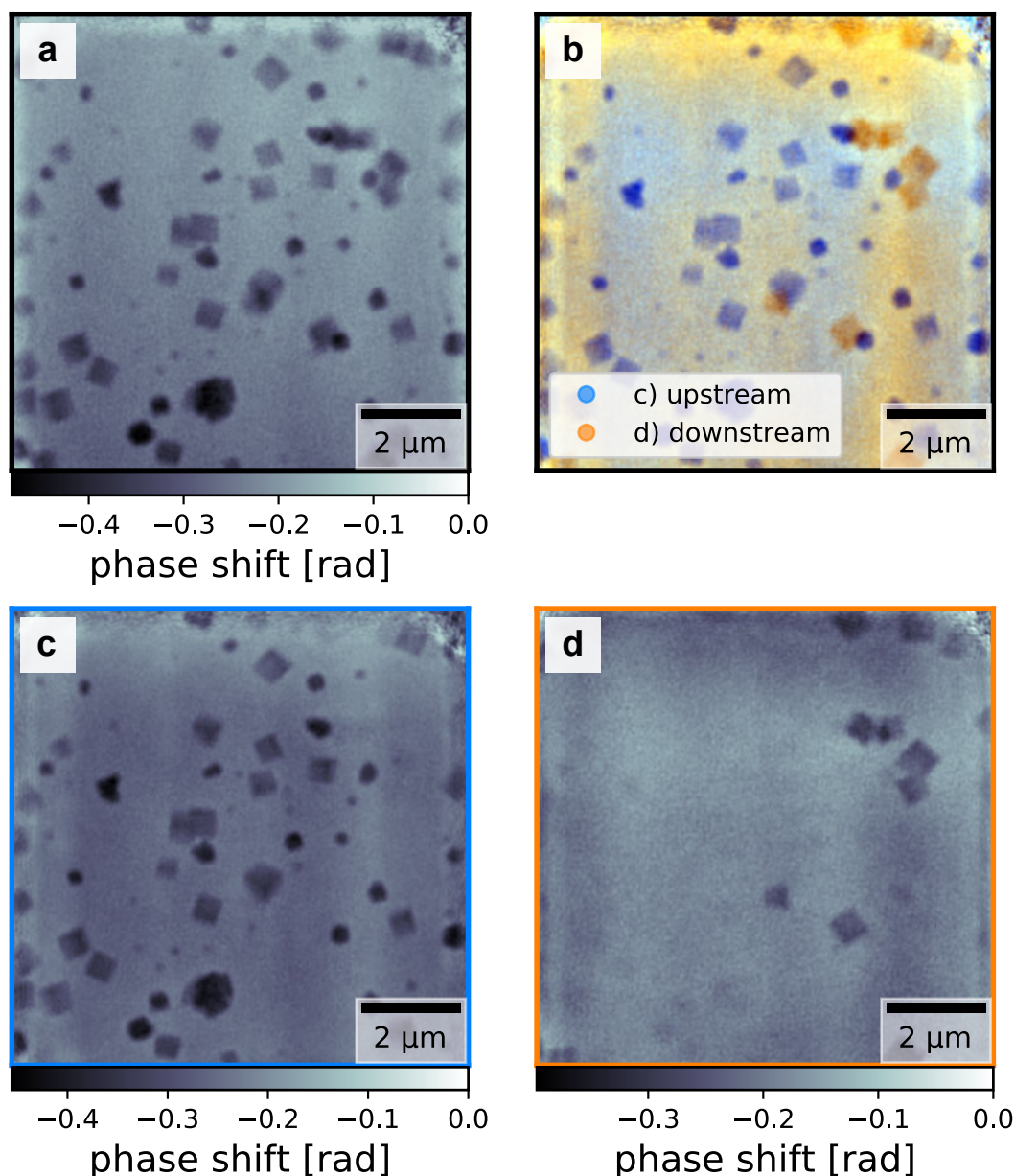


Figure 6.6. Phase reconstructions of the experiment using the chemical reactor: **a** ptychographically reconstructed object phase using the single slice ePIE algorithm. **b** colored overlay of the upstream object slice (blue, **c**) and the downstream object slice (orange, **d**), reconstructed using the multi slice 3PIE algorithm. The figure was created using matplotlib²¹⁴ (version 3.1.3).

The X-ray focus was created by two sets of one-dimensional NFLs²²⁰ and cleaned by a pinhole between the lenses and the sample, resulting in a DOF of approximately $183\ \mu\text{m}$, which is significantly smaller than the separation of the inner surfaces of the entry window and exit windows. Hence, the thin sample approximation was not applicable for this experimental situation as well. As with the single foil, both

the single-slice reconstruction using the ePIE algorithm (see Figure 6.6 a) and the multi-slice reconstruction using the 3PIE algorithm (see Figure 6.6 b-d) succeeded and the Cu₂O nanocubes could be clearly resolved. Again, the multi-slice reconstructions appeared sharper and separated particles on the upstream window and on the downstream window, again revealing difference in local covering density of particles.

6.4 Discussion

We have shown that the Cu₂O nanocubes themselves are thinner than the maximal depth resolution achievable with the given detector size and thus justify a single-slice reconstruction using the ePIE algorithm. However, once they are present on two surfaces, separated by a distance T , a conventional thin-object reconstruction, e. g., by ePIE, is limited in spatial resolution according to Equation 6.1. For the example with the nanocubes grown on the two sides of the foil, this limit is 51.1 nm. In order to reach higher spatial resolution, a multi-slice model of the sample needs to be employed. The reconstruction using a multi-slice algorithm allows to separate the imaged nanocubes reliably according to which surface of the polyimide foil they grew on.

We have furthermore proven that these nanocubes can be imaged inside the (cold) chemical reactor they were grown in, where the separation of the upstream surface and downstream surface covered in particles was even larger than with the previous experiment on the single polyimide foil. Here, the multi-slice reconstruction allowed again to separate the imaged nanocubes reliably according to which polyimide foil window they grew on.

High-resolution in situ X-ray imaging measurements following the presented growth process can not be performed in a way that a thin-sample approximation is applicable. The X-ray beam will always have to pass through at least two container surfaces which are covered with nanocubes. Those two surfaces will have to be spaced far enough apart to accommodate the minimum volume of liquid needed for this reaction to occur in the first place. This distance between the two container surfaces is limiting the achievable resolution in the reconstructions, if a reconstruction algorithm based on the thin sample approximation is used.

Ptychographic multi-slice reconstructions allow to image the growth process of Cu₂O nanocubes as it is and without imposing experimental restrictions on the imaged sample being optically thin. The separation of the nanocubes between the two layers is conclusive, because it does not depend on the chosen initialization order of the slices and is identical over multiple measurements.

6.5 Experimental section

Sample preparation - single polyimide foil

To prepare the sample of Cu₂O nanocubes on a support, 0.25 mmol (65 mg) of copper acetylacetonate (Cu(acac)₂, 98 %, Acros Organics) were mixed with 5 mL of BnOH (puriss., Sigma Aldrich) under ambient conditions and stirred for 15 minutes.¹⁸ A piece of polyimide foil (Kapton HN, DuPont, USA) with a size of approximately 10 mm × 10 mm was cleaned by rinsing with ethanol (abs., Scharlau). 0.8 mL of the Cu(acac)₂ solution were transferred into a specially designed PEEK reaction vial¹⁴ with a total volume of 1 mL and the polyimide foil was placed upright into the vial in a way that both sides were in contact with the precursor solution. After sealing the vial with a PEEK cap and a PTFE sealing ring, it was clamped into a heatable brass chassis. The vial was heated to 180 °C with a rate of 1 °Cmin⁻¹ and kept at that temperature for 60 min, followed by cooling down quickly. The polyimide

foil was cleaned again by rinsing with ethanol and dried at 60 °C overnight. All chemicals were used as purchased without further purification.

Experiment - single polyimide foil

The experiment was performed at the hard X-ray nanoprobe station PtyNAMi of beamline P06 at the synchrotron radiation source PETRA III (Hamburg, Germany).^{185, 221} The polyimide foil with the Cu₂O particles on both sides was glued to a thin silicon frame, covering a hole of 10 mm diameter. The plate with the foil on top was clamped into a sample holder, which was placed inside the PtyNAMi setup.^{184, 222} The X-ray beam coming from the undulator was monochromatized to 9.1 keV using a Si-(111) double crystal monochromator (DCM). Higher harmonics were suppressed by a pair of flat horizontally deflecting mirrors. An FZP with 125 μm diameter and 70 nm outer-most zone width was used to focus the X-ray beam. The focal length of the FZP was 64.2 mm. Therefore, the DOF of the FZP is 143.86 μm.

$$\text{DOF}_{\text{FZP}} = \frac{\lambda}{\text{NA}_{\text{FZP}}^2} = \frac{4 \cdot \lambda f_{\text{FZP}}^2}{D_{\text{FZP}}^2} = \frac{4 \cdot 0.136 \text{ nm} \cdot (64.2 \text{ mm})^2}{(0.125 \text{ mm})^2} = 143.86 \text{ } \mu\text{m} \quad (6.2)$$

The sample was placed approximately 750 μm upstream of the focus, resulting in a full width at half maximum (FWHM) beam diameter of 1.4 μm at the sample position. Piezoelectric motors were used to scan the sample on a rectangular grid with a size of 10 μm × 10 μm in 20 × 20 steps. At each of the 21 × 21 = 441 positions, a far-field diffraction pattern was recorded with 1 s exposure time using an EIGER X 4M detector (DECTRIS, Switzerland, 75 μm pixel size) positioned 4.16 m downstream of the sample. The relative sample positions were measured by three interferometers retro-reflected by a ball-lens located below the sample.²²² The thickness of the polyimide foil was measured after the experiment using calipers to be 100 μm ± 5 μm.

Ptychographic reconstructions - single polyimide foil

The 441 recorded diffraction patterns were cropped to a size of 512 × 512 pixels resulting in a pixel size of 14.75 nm in the sample plane. The ePIE algorithm⁸³ was used for the ptychographic single slice reconstruction. The update strength α for the object and the update strength β for the probe were both set to 1.0 and the regularization parameter was set to 0.002. The initial object was chosen to be non-phase-shifting and non-absorbing. The initial probe was a gaussian with 2 μm FWHM and a phase curvature of −1 mm. The reconstruction was run for 1000 iterations. The phase of the reconstructed object is shown in Figure 6.3a. The resolvable DOF from the detector was calculated to be 6.39 μm:

$$\text{DOF}_{\text{det}} = \frac{\lambda}{\text{NA}_{\text{det}}^2} = \frac{4 \cdot \lambda d_{\text{det}}^2}{D_{\text{det}}^2} = \frac{4 \cdot 0.136 \text{ nm} \cdot (4.16 \text{ m})^2}{(0.0384 \text{ m})^2} = 6.39 \text{ } \mu\text{m} \quad (6.3)$$

where λ is the X-ray photon wavelength, NA_{det} is the numerical aperture covered by the cropped detector images, d_{det} is the propagation distance from the sample to the detector, and D_{det} is the size of the cropped detector images. These 6.39 μm are smaller than the 100 μm separation of the Cu₂O nanocubes on the two sides of the polyimide tape, making the sample optically thick. Therefore, a multi-slice reconstruction was carried out using the 3PIE⁸⁷ algorithm. As for the single slice reconstruction, the update strengths α for the object and β for the probe were both set to 1.0 and the regularization was set to 0.002. Two object slices separated by 100 μm were used to model both sides of the polyimide tape. As there were no other windows in the beam and the polyimide foil itself is believed to be homogeneous, these two slices suffice to model the object. The propagation between these two slices was implemented as a convolution with a Fresnel kernel:

$$\text{Prop}_{\Delta d_z}[\Psi(\mathbf{r})] = \mathcal{F}^{-1}\{\mathcal{F}[\Psi(\mathbf{r})]\exp(i\pi\lambda(q_x^2 + q_y^2) \cdot \Delta d_z)\}, \quad (6.4)$$

where $\Psi(\mathbf{r})$ is the complex-valued wavefield to be propagated by the distance Δd_z along the beam axis, \mathcal{F} denotes the Fourier transform, \mathcal{F}^{-1} denotes the inverse Fourier transform while q_x and q_y are the coordinates in Fourier space. The distance from the downstream object plane to the detector was kept the same. It fulfills the far-field condition, therefore this propagation was implemented as a simple Fourier transform, as in the ePIE algorithm.

The initial probe estimate was the same as for the previous ePIE reconstruction. Both object slices were initialized as non-absorbing and non-phase shifting. For the first 100 iterations, only the downstream sample slice was used, making the first 100 iterations identical to ePIE with particles from both sides in this slice. From the 101st iteration on the upstream slice was included in the update process and the particles on the side of the polyimide facing the source migrated into this slice. After 1000 iterations in total, no further changes in the reconstructed sample slices and the reconstructed probing wavefield could be observed. The reconstructed object slices are shown in Figure 6.3b-d. Introducing a second sample slice and the propagation between the two slices into the algorithm, increased the number of computing tasks by a factor of three. Therefore, this reconstruction took about three times longer than the single-slice ePIE reconstruction.

As a confirmation, the initialization order of the two slices was reversed in an additional reconstruction: using only the upstream slice for the first 100 iterations and switching on the update of the downstream slice from iteration 101 on (see Figure 6.5).

To check if the chosen 100 μm separation of the two object slices was indeed correct, multiple reconstructions with varied distances were performed. We found that decreasing the slice separation resulted in the particles being reconstructed in both slices. Particles from the downstream slices were reconstructed weaker but also in the upstream slice and vice versa. Increasing the slice separation resulted in the over exaggeration in the particles in their respective slice and negative version of them in the other slice. Particles in the downstream slice appeared more phase shifting in the downstream slice and negatively phase shifting in the upstream slice. The same was true for the particles in the upstream slice. Most particles are either in the upstream slice or the downstream slice, and only in a very few cases particles from the two slices overlap in projection. Looking only at the majority of particles that appear only in either one of the slices, we could verify that indeed a slice separation of 100 μm created flat phases in the same position in the respective other slice. As the phase shifts of negative and mirror particles scaled with the change in distance of the object slices, we estimated the exact optical sample thickness to be 100 $\mu\text{m} \pm 10 \mu\text{m}$. Multiple ptychographic algorithms exist, which can estimate the slice separation by themselves.^{91, 223} Future experiments, in which the exact slice separation is unknown, can use those to perform the ptychographic multi-slice reconstructions.

Sample preparation - chemical reactor

The preparation of the precursor solution was identical to the previous sample. Two reactions of particle growth were performed inside the chemical reactor. The chemical reactor was heated to 150 $^{\circ}\text{C}$ and kept at this temperature for 4 h and 12 h respectively. After cooling down and disassembling the chemical reactor, the windows were washed with ethanol prior to the SEM imaging. The SEM imaging proved that particles had grown on the inside surfaces of the windows in both runs. The chemical reactor was reassembled using the downstream window from the 4 h hours reaction in the downstream position and the upstream window from the 12 h reaction in the upstream position. Finally the chemical reactor was filled with BnOH before closing.

Experiment - chemical reactor

The experiment was again performed at the hard X-ray nanoprobe station PtyNAMi of beamline P06 at the synchrotron radiation source PETRA III (Hamburg, Germany).^{185, 221} The whole chemical reactor with all connections needed to potentially operated it, was placed inside the PtyNAMi setup.^{184, 222} In this experiment, the chemical reactor was kept at room temperature. The X-ray beam coming from the undulator was monochromatized to 15.25 keV using a Si-(111) DCM. Higher harmonics were suppressed by a pair of flat horizontally deflecting mirrors. NFLs²²⁰ were used to focus the X-ray beam 30 mm downstream of the most downstream lens exit. The sample was placed 1.5 mm downstream of the X-ray beam focus, resulting in a beam size of about 450 nm (FWHM) on the sample. The DOF was calculated to be:

$$\text{DOF}_{\text{NFL}} = \frac{\lambda}{\text{NA}_{\text{NFL}}^2} = \frac{4 \cdot \lambda f_{\text{NFL}}^2}{D_{\text{NFL}}^2} = \frac{4 \cdot 0.081 \text{ mm} \cdot (30 \text{ mm})^2}{(0.04 \text{ mm})^2} = 182.95 \text{ } \mu\text{m} \quad (6.5)$$

Piezoelectric motors were used to scan the sample on a rectangular grid with a size of $8 \text{ } \mu\text{m} \times 8 \text{ } \mu\text{m}$ in 80×80 steps. At each of the $81 \times 81 = 6561$ positions, a far-field diffraction pattern was recorded with 20 ms exposure time using an EIGER X 4M detector (DECTRIS, Switzerland, $75 \text{ } \mu\text{m}$ pixel size) positioned 3.435 m downstream of the sample. The relative sample positions were measured by three interferometers retro-reflected by a ball-lens located below the sample.²²² Using again a cropping of 512×512 pixels, the minimal possible DOF for this experiment was calculated to be:

$$\text{DOF}_{\text{det}} = \frac{\lambda}{\text{NA}_{\text{det}}^2} = \frac{4 \cdot \lambda d_{\text{det}}^2}{D_{\text{det}}^2} = \frac{4 \cdot 0.085 \text{ nm} \cdot (3.435 \text{ m})^2}{(0.0384 \text{ m})^2} = 2.58 \text{ } \mu\text{m} \quad (6.6)$$

Again the whole sample is much thicker than this, but the nanocubes themselves fulfil the thin sample approximation, even if the signal were to scatter sufficiently over the whole size of the cropped diffraction patterns. The distance between the inside surfaces of the upstream window and the downstream window was estimated to be $650 \text{ } \mu\text{m}$. Both windows had a slight curvature, most likely due to expansion while the chemical reactor was heated during the sample growth. Hence the exact distance would also depend on where the X-ray beam measures and might also change while heating the chemical reactor.

Ptychographic reconstructions - chemical reactor

The 6561 recorded diffraction patterns were cropped to a size of 512×512 pixels resulting in a pixel size of 7.27 nm in the sample plane. The ePIE algorithm⁸³ was used for the ptychographic single slice reconstruction. The update strength α for the object and the update strength β for the probe were both set to 1.0 and the regularization parameter was set to 0.002. The initial object was chosen to be non-phase-shifting and non-absorbing. The initial probe was a gaussian with 500 nm FWHM and a phase curvature of 2 mm. The reconstruction was run for 1000 iterations. The phase of the reconstructed object is shown in Figure 6.6b.

The multi-slice reconstruction using the 3PIE⁸⁷ algorithm was performed as before. The samples was modeled by two slices, separated by $650 \text{ } \mu\text{m}$ of free propagation space. Both object slices were initialized as non-absorbing and non-phase shifting. The initial estimate for the probing beam was the same as for the single slice reconstruction using the ePIE algorithm. For the first 100 iterations, only the upstream sample slice was used, making the first 100 iterations identical to ePIE with particles from windows in this slice. From the 101st iteration on the downstream slice was included in the update process and the particles on the downstream window migrated into this slice. After 1000 iterations in total, no further changes in the reconstructed sample slices and the reconstructed probing wavefield could be observed. The phases of the reconstructed object slices are shown in Figure 6.6b-d.

6.6 Acknowledgments

We acknowledge DESY (Hamburg, Germany), a member of the Helmholtz Association HGF, for the provision of experimental facilities. Parts of this research were carried out at PETRA III and we would like to thank Jan Garrevoet and Kathryn Spiers for assistance in using the P06 beamline.

6.7 Author contributions

M.K., D.K., L.G, M.S. and C.G.S. conceived the experiments. L.G. performed all synthesis of nanocubes and their SEM characterization, and designed the liquid cell. M.K., L.G., D.B., M.S. and F.W. conducted the ptychography experiments. M.K. carried out the reconstructions and analyzed the results. All of the authors contributed to the preparation of the manuscript.

6.8 Additional information

Competing interests

The ptychographic imaging technique described in this paper are the subject of awarded patents owned by Phase Focus Ltd, which is a spin-out company of the University of Sheffield. None of the authors is affiliated to this company. This conflict exists for all the authors.

Data availability

The raw dataset²²⁴ used for the results presented in this article is openly available via zenodo.

7 Imaging Cu₂O nanocube hollowing in solution by quantitative in situ X-ray ptychography

The content of this chapter was accepted for publication in Nature Communications. The manuscript was authored by Lukas Grote, Martin Seyrich, Ralph Döhrmann, Sani Y. Harouna-Mayer, Federica Mancini, Emilis Kaziukenas, Irene Fernandez-Cuesta, Cecilia A. Zito, Olga Vasylieva, Felix Wittwer, Michal Kronenberg, Natnael Mogos, Mirko Landmann, Christian G. Schroer, and Dorota Koziej as corresponding author.

7.1 Abstract

Understanding morphological changes of nanoparticles in solution is essential to tailor the functionality of devices used in energy generation and storage. However, we lack experimental methods that can visualize these processes in solution, or in electrolyte, and provide three-dimensional information. Here, we show how X-ray ptychography enables in situ nano-imaging of the formation and hollowing of nanoparticles in solution at 155°C. We simultaneously image the growth of about 100 nanocubes with a spatial resolution of 66 nm. The quantitative phase images give access to the third dimension, allowing to additionally study particle thickness. We reveal that the substrate hinders their out-of-plane growth, thus the nanocubes are in fact nanocuboids. Moreover, we observe that the reduction of Cu₂O to Cu triggers the hollowing of the nanocuboids. We critically assess the interaction of X-rays with the liquid sample. Our method enables detailed in-solution imaging for a wide range of reaction conditions.

7.2 Introduction

Hollow nanoparticles with sizes in the range of several hundred nanometers comprise a material class with widespread application potential.^{11, 225-229} They are often utilized to form composite materials for high performance electrodes in lithium ion batteries,^{225, 226} for (photo-) catalytic energy production^{227, 228} and as sensors.^{11, 229} Precise control over the structural and morphological evolution during the synthesis of these materials or during their operation in an electrolyte²³⁰ is decisive to reach the desired functionality and high performance. In many cases, however, understanding and manipulating the course of the underlying morphological changes remains a major challenge. This is mainly due to the lack of experimental methods that can observe the dynamics of chemical processes in situ in a bulk solution under relevant conditions, such as high temperature and pressure. Visual insights into the formation dynamics of nanomaterials are thus rare.

Recently, efforts have been made to address this problem by exploiting in situ microscopy techniques. Liquid-cell transmission electron microscopy (TEM) plays an important role in this context,^{184, 189, 231-234} since it can provide spatial resolution down to the atomic scale.¹⁸⁹ In this way, the growth pathways of polyhedrally shaped Au nanoparticles²³⁵ and the temperature-dependent shape evolution of Au-Pd core-shell nanorods²³⁶ have been revealed. The outstanding spatial resolution makes this method a powerful tool to study the growth of nanoparticles, however, the applicability of liquid-cell TEM to solution-based nanoparticle syntheses is limited, since it requires thin reactors with small volumes which can disturb the kinetics of the reaction and thus alter its pathway.

X-ray microscopy using synchrotron radiation overcomes these limitations.^{69-72, 190, 237-240} Hard X-rays have the power to penetrate thick samples in extended environments,²³⁷ while at the same time allowing nano imaging with a spatial resolution as high as 10 nm.^{202, 241} X-ray ptychography, which is a scanning coherent diffraction imaging technique, extends these benefits even further with the possibility of interpreting images quantitatively.^{79, 81, 242-244} The method reconstructs the complex transmission function of the sample from a series of diffraction patterns using a phase retrieval algorithm. In contrast to scanning transmission microscopy, the spatial resolution achievable with X-ray ptychography is not limited by the beam size. The resulting images contain the local phase shift induced by the sample, which gives access to physical parameters such as the area density or, with some additional assumptions, the density or thickness of the material.

Early in situ experiments demonstrated that lithium zirconate nanoparticles could be imaged in different gas atmospheres at elevated temperatures using X-ray ptychography,⁶⁸ and the strain and deformation of a polymer-metal composite under pressure was quantitatively assessed in three dimensions (3D) by in situ X-ray ptychographic tomography.²⁴⁵ Later, a phase transition during the melting of Sn-Bi alloy particles was recently visualized with a spatial resolution of 25 nm⁷² and the annealing of Au nanoparticles was observed in different gas atmospheres.⁶⁹⁻⁷¹ Additionally, X-ray ptychography allows the calculation of the wavefield at each point within the imaging setup. This enables the reconstruction of several individual objects, which are stacked along the beam direction, from a single two-dimensional (2D) scan. This procedure is referred to as multi-slicing.^{87, 91} In combination with the quantitative information contained in each image slice, we can obtain some 3D insights into chemical processes at the nanoscale without the need for tomographic scanning.

In this study, we apply quantitative X-ray ptychography in solution, visualizing the nucleation and growth of cuprous oxide (Cu₂O) nanocubes, and their subsequent transformation into hollow copper structures (Figure 7.1).^{18, 136, 216} Using multi-slicing, we reconstruct separate 2D images of particles growing on the entrance and exit windows of the reactor, tracking the morphological evolution of individual nanocubes over time. We then access the third dimension by calculating the thickness of the particles from the quantitative phase images, allowing us to infer the full growth and transformation process in 3D. This way, we find different morphologies for particles that nucleate heterogeneously on the reactor walls as compared to those nucleating homogeneously. At the end of the growth process, the nanocubes are reduced to metallic copper in a solid-state reaction.¹⁸ At this point, we observe voids forming in the center of the particles and follow their expansion towards the surface, resulting in hollow nanocubes.

7.3 Results

With the example of Cu₂O nanocubes, we show how X-ray ptychography can be used for in situ nano-imaging of the shape evolution of nanomaterials in solution. To this end we developed a liquid reactor that provides the necessary mechanical and thermal stability for long-term imaging (Supplementary Notes 7.1 and Supplementary Figure 7.1). By simulating the thermal expansion of the reactor for small temperature fluctuations during operation, we find that thermal drifts of the reactor itself can be expected below 10 nm. (Supplementary Figure 7.2). While keeping the in-liquid beam path as short as 1 mm, the reactor contains a volume of 2 mL ensuring stable reaction kinetics.

The reaction of copper(II) acetylacetonate (acac) in benzyl alcohol (BnOH) is known to yield copper-based nanostructures with different morphologies,^{108, 216} among those are Cu₂O nanocubes which represent an intermediate product after the initial reduction of the precursor. Even though the subsequent reduction of the material to metallic Cu was observed,¹⁸ tracking the shape of the material at all reaction

stages was never accessible in situ. To image the formation process of the nanocubes with X-ray ptychography, we fill the precursor solution into the in situ reactor and heat it to a reaction temperature of 155 °C. The nanocubes nucleate mostly on the walls of the reactor, which immobilizes them for sequential imaging (Figure 7.1). We image the growth process at a time resolution of 21.6 min over 18 h. Applying the multi-slice model^{87, 91} during the ptychographic reconstruction allows us to display the particles on the entrance and exit windows of the reactor separately. The particles on both windows are similar in size and morphology, we therefore show here only the nanocubes on the entrance window, unless otherwise noted. The respective images taken from the exit window are compiled in Supplementary Figure 7.3.

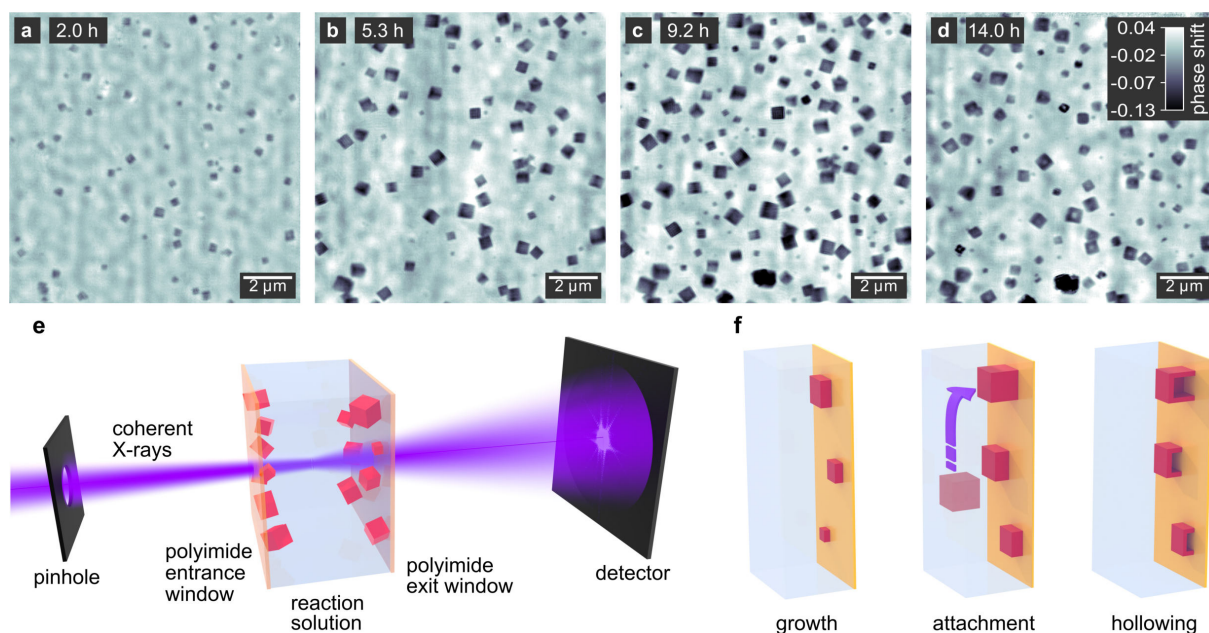


Figure 7.1. Overview of the in situ imaging experiment. a-d Ptychographic reconstructions of nanocubes on the entrance window of the in situ reactor. The gray scale indicates the phase shift in radian. e Schematic illustration of the experimental setup. A section through the reactor is shown for simplicity, including the entrance and exit windows that the nanoparticles grow on as well as the solution. f Illustration of the morphological evolution of the nanocubes as observed during in situ imaging.

7.3.1 Quality of ptychographic images in solution

To determine the influence of the liquid reactor at high temperatures on the quality of the micrographs, we evaluate the spatial resolution, stability, and the occurrence of background artefacts. We select ptychograms at intermediate reaction times to ensure a representative number of particles in the images. In addition, we evaluate the images taken on the entrance and exit windows of the reactor individually (Figure 7.2a-b).

To estimate the spatial resolution, we use Fourier ring correlations²¹⁷ (FRC) displayed in Figure 7.2f, which we obtain by splitting the diffraction patterns of a single ptychogram into two separate sets. We then reconstruct the sets individually and calculate the FRC of the two resulting images (c.f. Supplementary Figure 7.4). We apply the half bit criterion²¹⁸ compensating for the quality loss introduced by splitting the data set and find that the images of the entrance and exit windows have resolutions of 66 nm and 64 nm, respectively. The resolution is mainly limited by the reactor and the beam path of 1 mm in the hot liquid. Ex situ single-digit nanometer resolution images of Cu₂O nanocubes can be achieved when measured in air.^{221, 237}

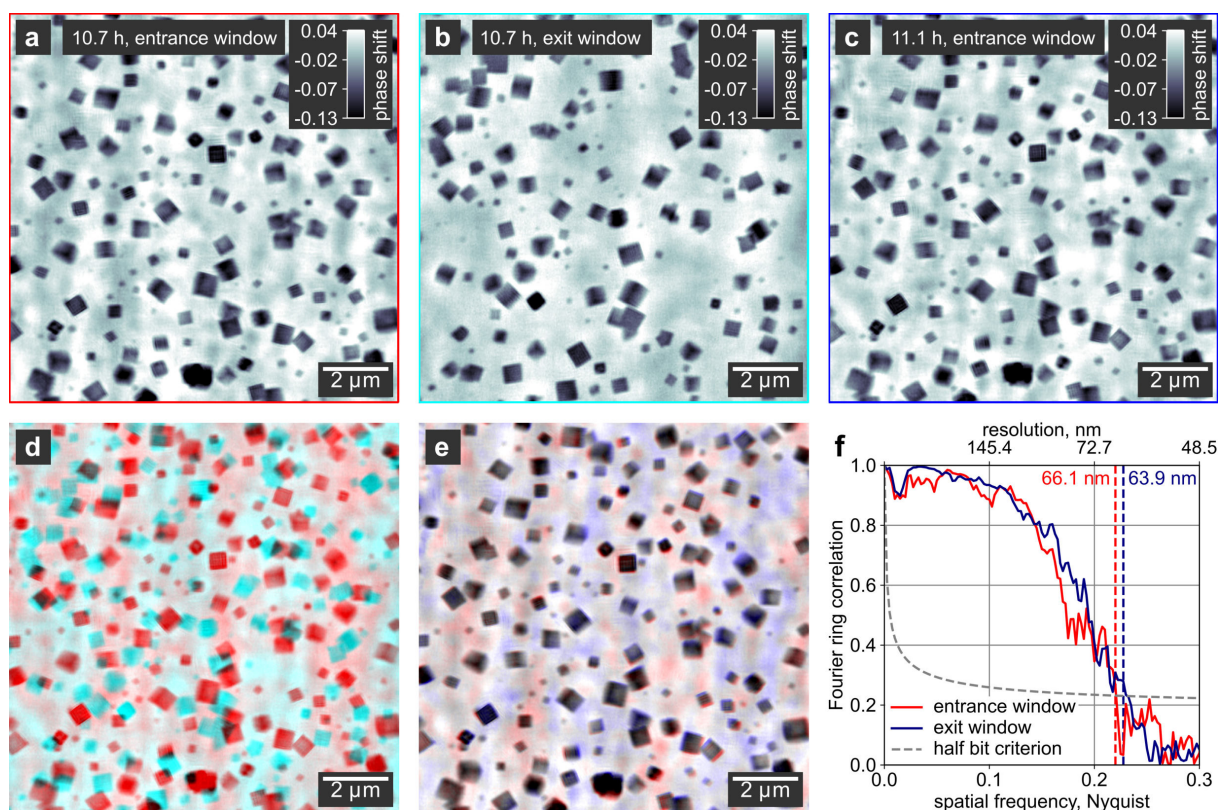


Figure 7.2. Quality estimation of in situ images. **a-b** Ptychographic images of particles growing on the entrance and exit windows, respectively, of the in situ reactor at the same reaction time. In **b**, the background fluctuations are varying on larger scales compared to **a** due to the larger illumination size on the exit window. **c** Ptychographic image of the entrance window at a later reaction time compared to **a-b**. The gray scale indicates the phase shift of the image in radian. **d** False-colored overlay of images of the entrance (red) and exit (cyan) windows taken at the same reaction time. **e** False-colored overlay of aligned images of the entrance window taken at consecutive time steps of 10.7 h (red) and 11.1 h (blue). The background randomly fluctuates between images. **f** FRC plotted for the entrance and exit window slices. We used the half-bit criterion²¹⁸ (dashed line) for resolution estimation to account for the loss in reconstruction quality induced by splitting the data set.

Position stability is another important aspect for nano-imaging of chemical processes. To compensate for thermal drifts of the reactor, we mechanically adjusted its position after each image. At the ptychographic reconstruction step, we applied automated position refinement²⁴⁶ to correct for drifts of the reactor during the acquisition of a single image. Supplementary Figure 7.5 shows a comparison of reconstructions with and without position refinement. After reconstruction, we performed additional image alignment (for details, see Methods section). Figure 7.2e shows a false-colored overlay of two aligned images of the entrance window taken at consecutive time steps (Figure 7.2a and c). Small remaining shifts of the particle positions are visible in the lower right area of the image, which do however not affect the information content or the later quantitative analysis of the images. This confirms that the substrate-bound nanoparticles in a heated solution can be imaged reproducibly and with high stability.

The main differences of the consecutive images are found in the background between the particles. We account the random background fluctuations to free floating particles in solution or to convection of the hot solvent. Since the ptychographic model assumes a steady sample during the acquisition of one image, these non-static portions of the sample cause inconsistencies in the ptychographic data set that result in a non-flat background. However, we can conclude that the inconsistencies do not significantly affect the reconstruction quality of the substrate-bound nanocubes. It is noteworthy that the predominant

size of the background features is smaller in the reconstruction of the entrance window (Figure 7.2a) compared to the exit window (Figure 7.2b). The different feature sizes agree well with the diameter of the illuminating beam on the respective reactor windows (c.f. Supplementary Figure 7.6).

The multi-slice approach allows us to reliably separate images of nanocubes growing on the entrance and exit windows of the reactor. A confirmation of proper slice separation is given by the false color overlay of the two windows at a single time step (Figure 7.2d) showing that each particle appears in either of the two slices, but never in both. Due to a slow deformation of the polyimide windows, the distance between the slices gradually decreased during the reaction from initially 1000 μm to below 300 μm . Since an incorrect slice distance introduces artefacts to the reconstruction and lowers its resolution, we determined the distance several times during the reaction to ensure high image quality throughout the full time series. For more details, see Supplementary Notes 7.2 and Supplementary Figure 7.7. When the distance between the windows reached 400 μm and thus approached the depth of field (DOF) of the imaging experiment of 280 μm , the slice separation started to be incomplete, with particles on the entrance window becoming dimly visible also in the reconstruction of the exit window (Supplementary Figure 7.8). After about 17 h reaction time, the distance dropped below the DOF, and a multi-sliced reconstruction of the respective data sets was no longer possible. We thus treated the sample as a single slice at later reaction times, and reconstructions represent a superposition of the entrance and exit windows.

7.3.2 Nucleation and growth of Cu_2O nanocubes in 2D

Particles are first visible after 2 h reaction time (Figure 7.1a). Initially, with only a few small particles in the field of view, the quality of the reconstructed image is comparatively low, since the data set does not contain enough information for the iterative reconstruction algorithm to converge. After 5.3 h, the number of particles has increased, and they have grown to an average size of 450 nm. The image quality has also increased, and the cubic shape of the particles can be clearly distinguished (Figure 7.1b). Since the ptychographic images represent projections of the electron density, we can recognize the orientation of the nanocubes when they reach their final size after 9.2 h (Figure 7.1c). While some are oriented with one face parallel to the substrate, we can also see nanocubes facing towards the substrate with an edge or corner. There seems to be no preferential orientation. At a later reaction stage after 14 h, the particles develop a cubic central void (Figure 7.1d), which suggests their reduction to metallic copper.

To determine the growth behavior in more detail, we track the size of the nanocubes throughout the in situ image series using image processing functions of the OpenCV library²⁴⁷ (Figure 7.3). Tracked particles are redrawn with a green rectangle in Figure 7.3b, and the changing edge length is plotted for each particle in Figure 7.3c. To ensure reliable results, we select only those nanocubes oriented with one face parallel to the substrate. A set of images with a smaller field of view is shown in Supplementary Figure 7.9 for comparison and details on the image processing steps are given in Supplementary Figure 7.10-7.11. The overall growth rate is fast in the beginning and successively slows down, resembling the pseudo first-order kinetics that one would expect for this reaction of a single precursor with the solvent.

Most importantly, we observe that in addition to the nanocubes that nucleate on the substrate and are thus visible from the beginning of the reaction, new particles successively appear in the images. For example, within the time delay of 23 min between Figure 7.3a and b, the three particles marked with yellow arrows appear. Since the new particles seemingly have similar sizes as those already present on the substrate, we can conclude that they must have nucleated homogeneously in solution and attach to the substrate at some point during their growth process. The fact that we see no particles detaching eliminates the possibility of nanocubes hopping into the field of view from a different area of the

substrate. The free-floating particles are invisible to the in situ imaging, since their motion in solution is faster than the acquisition time of a single image.

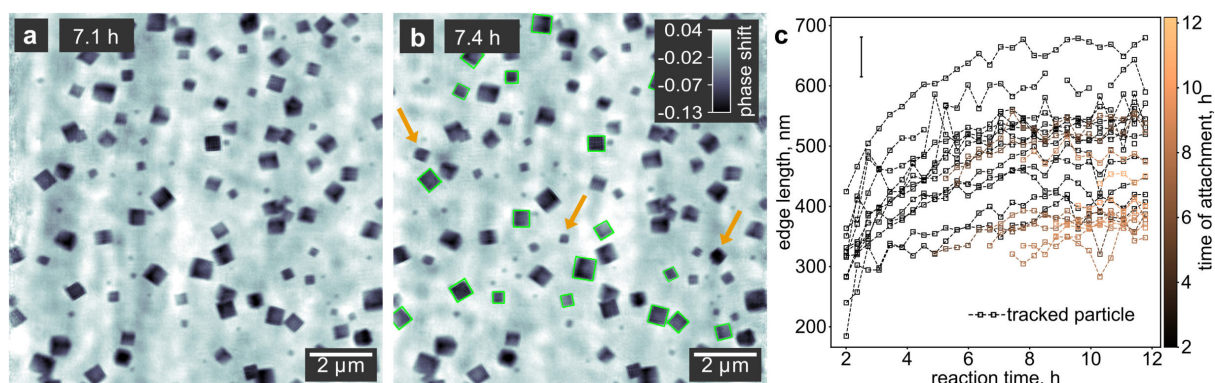


Figure 7.3. Analysis of the growth process from a 2D perspective. **a-b** In situ ptychographic images taken at 7.1 h and 7.4 h, respectively. Particles marked with arrows appear in **b** but are not seen in **a**, indicating that they attached from the solution onto the reactor window. The gray scale indicates the phase shift of the images in radian. We used nanocubes highlighted with green rectangles for size estimation. **c** Evolution of the particle size for all nanocubes in **b** framed with a green rectangle. The color indicates the time when a particle attaches to the substrate. Independent of the attachment time, all particles show a similar growth behavior in the 2D projection. The error bar indicates the spatial resolution of the ptychograms of 66.1 nm.

This interpretation is affirmed by inspecting the size evolution of newly attached particles only. In Figure 7.3c, the time when a nanocube attaches to the substrate is encoded by the color of the respective data points. While the edge length of particles growing on the substrate since the beginning of the reaction is shown in black, yellow color represents late attachment. It turns out that both the size and the growth rate of nanocubes attaching at intermediate and late reaction times integrate well with the overall behavior.

However, from a pure 2D perspective, we cannot differentiate between the morphological evolution of nanocubes attached to the windows of the in situ reactor and those dispersed in the solution. To this end, additional depth information is required.

7.3.3 From 2D to 3D: Differentiating hollow nanocubes and -cuboids

As X-ray waves accumulate phase shift while propagating through matter, the thickness of an object along the beam path, i.e. perpendicular to the image plane, can be calculated from a ptychographic image for known density and composition. This additional information allows us to put together a 3D model of the sample. Given the X-ray wavelength and the electron density of the material, we calculate the thickness of each tracked particle from its phase shift by taking the average of the pixel values across individual particles in the quantitative ptychograms. To account for the finite resolution, we exclude pixels close to the edges of a particle, as it is exemplarily shown for a single time step in Figure 7.4a. Since the sizes of the nanocubes vary, we use the aspect ratio rather than the absolute thickness to describe the 3D shape of each particle. The aspect ratio is calculated as the quotient of the edge length in the image plane and the out-of-plane thickness. The fluctuating background induces an error for the calculation of the aspect ratio at a given time, but it does not change the observed general trends in the evolution of particle shape (c.f. Supplementary Notes 7.3).

In Figure 7.4b, we see that the aspect ratio of individual nanocubes remains nearly constant, however, a systematic trend is visible with regards to the time a particle attaches to the substrate, which is highlighted by color. Those particles that attach when growth has almost finished at late reaction times

(yellow) are cubic. However, the longer a particle grows on the substrate, the more it deviates from an ideal cubic shape with the edge length perpendicular to the substrate being much shorter. Particles that are visible from the beginning of the reaction and thus presumably nucleate on the substrate (black data points in Figure 7.4b) are cuboids with an aspect ratio of about 0.5. For the growth mechanism, this means that the particles grow from only one face in the direction perpendicular to the substrate, while they grow parallel to the substrate equally from all four faces, as illustrated in Figure 7.4c.

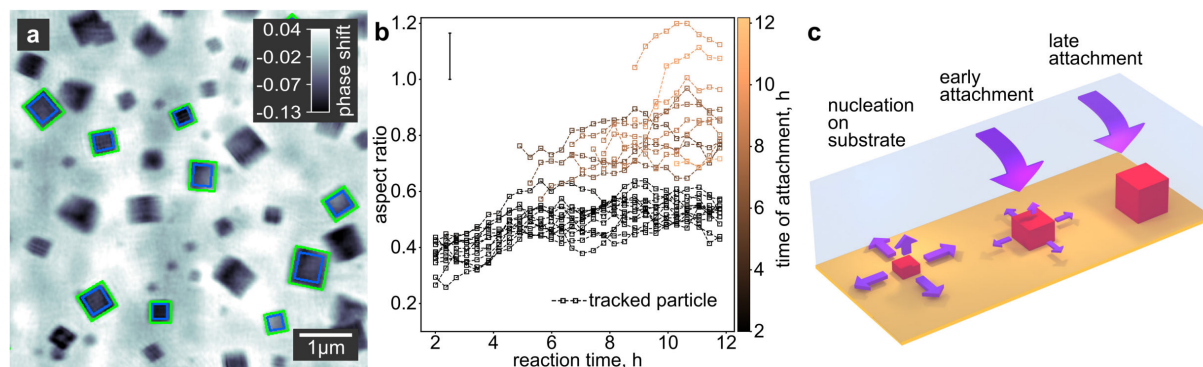


Figure 7.4. Analysis of the growth process from a 3D perspective. **a** In situ ptychographic image highlighting the in-plane dimension of the nanocuboids by green rectangles. The out-of-plane thickness is calculated from the phase shift within the area highlighted by blue rectangles. The gray scale indicates the quantitative phase shift of the image in radian. **b** Evolution of the aspect ratio for all particles highlighted in Figure 7.3b. The aspect ratio is calculated as the quotient of the in-plane dimension and the out-of-plane thickness of the nanocuboids. A moving average window of four time steps is applied. See Supplementary Figure 7.12 for a plot without moving average. Yellow color indicates the time when a particle attaches to the substrate. While the aspect ratio of individual particles does not change significantly with reaction time, it is strongly affected by the time when a particle attaches. The later the attachment takes place during the growth phase, the more cubic the respective particle becomes. This process is illustrated in **c**. For clarity, the error bar in **b** represents the mean error resulting from the error propagation of the in-plane particle size and the out-of-plane thickness of all tracked particles (for details, see Supplementary Notes 7.3).

We account the apparent increase in the aspect ratio from about 0.3 to 0.5 during the first 5 h of reaction time in Figure 7.4b to a systematic error in the calculation of the thickness for these particles. Since the nanocuboids are small at the beginning of the reaction, in combination with the limited resolution, the fading of the phase shift signal at the edges of the nanocuboids leads to an underestimation of the thickness for these early reaction times.

Once we have derived the growth mechanism in 3D from the quantitative phase images, we can begin to understand the hollowing process of the nanocuboids bound to the substrate (Figure 7.5). After ca. 11.8 h, the particles do not grow significantly larger (compare Figure 7.3c) and we can assume that most precursor has been consumed. At this point, cubic voids start to form in the center of the particles and grow towards the surface over the next 3.2 h (Figure 7.5a-f). We confirm that the hollowing process is not due to the X-ray exposure by taking a single ptychographic image at the end of the reaction at a different part of the reactor window, ca. 2 mm away from the previously exposed region (Supplementary Figure 7.13). This image also shows hollow particles.

Even though the reduction of the Cu_2O nanocuboids to metallic Cu was known,^{18, 108} previous in situ measurements never observed hollow particles due to their lack of depth information. X-ray ptychography can now enable us to also probe the internal morphology of the material. When Cu_2O is reduced in the solid state to Cu, there must be an outward flow of oxygen species caused by the reaction with BnOH taking place at the particle surface. Recently, Kirkendall hollowing was found during the fast extraction of phosphorous from PdP_2 nanoparticles.²⁴⁸ In Cu_2O , however, the diffusion coefficient

of Cu^+ cations is much higher than that of O^{2-} anions.⁴¹ This difference in diffusion rates would only cause void formation during oxidation of Cu to Cu_2O , but we observe the hollowing process in the course of reduction. Due to the slow void formation in our nanocuboids during 3 h, it is unlikely that the extraction of oxygen species from the nanocuboids has a significant effect on the diffusion rates. Thus, the diffusion of ionic species and therefore the Kirkendall effect³⁹ are unlikely the cause of void formation in the nanocuboids. Instead, interactions with the solvent and the substrate at the surface of the nanocuboids protect their outer shape during reduction. The binding of the Cu_2O nanocuboids to the polyimide substrate indicates a strong interaction between the two materials, and furthermore, strong adsorption of BnOH at the surface of Cu_2O was observed in a previous in situ spectroscopic study.¹⁰⁸ Due to these surface interactions, the mass reduction upon depletion of oxygen from the crystal lattice and, more importantly, the increase in density from 6.0 g/cm^3 (Cu_2O) to 8.92 g/cm^3 (Cu)¹⁸⁸ are compensated by a central void instead of shrinking of the outer particle dimension.^{31, 249}

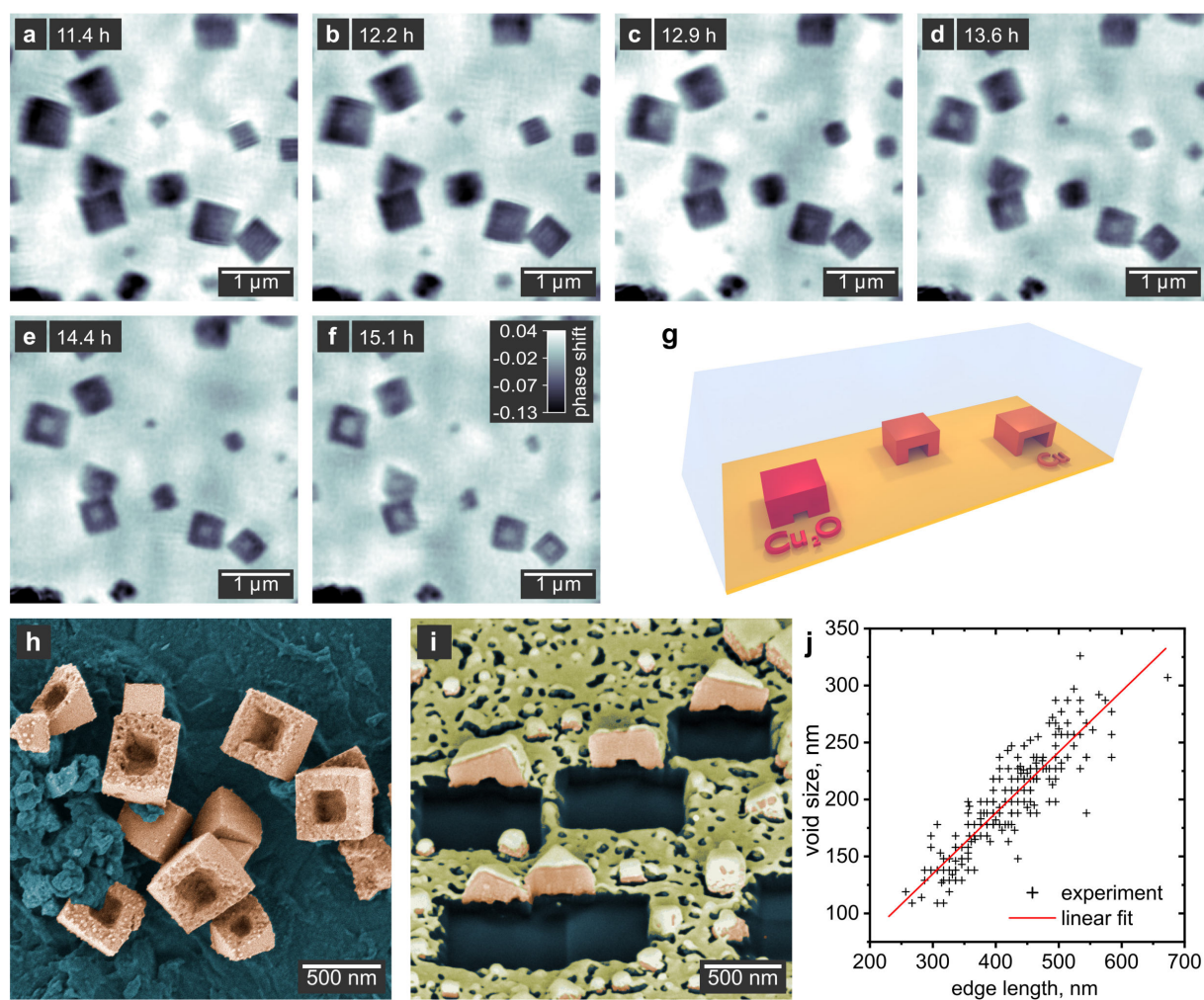


Figure 7.5. Hollowing process of the nanocuboids. **a-f** Ptychographic images of the hollowing process between 11.4 h and 15.1 h reaction time. The gray scale indicates the phase shift of the images in radian. **g** Schematic illustration of the void formation. **h** False-colored scanning electron microscopy (SEM) image of bowl-shaped hollow nanocuboids (orange) taken from the same sample used for the in situ imaging in **a-f**. **i** SEM image of hollow nanocuboids cut in half using a focused ion beam (FIB). These particles were prepared in the in situ reactor but without exposure to X-rays. The sample was sputtered with a thin Au layer (yellow) to minimize charging effects. In the areas cut with the FIB, the substrate can be seen (blue). **j** Scatter plot of the void size versus the outer particle dimension obtained from SEM images of the same sample used for the in situ imaging in **a-f**. The fit indicates a systematic size ratio of 53%.

A similar effect was observed during the reduction of CoO particles to form hollow Co shells in the presence of oleylamine,⁴⁶ as well as for the reduction of β -FeOOH to hollow Fe₃O₄ nanorods with strongly bound capping agents.⁴⁵ Since no more nanocuboids attached to the reactor windows after the beginning of the void formation, we cannot conclude if dispersed particles undergo the same shape transformation.

To further verify our interpretation, we compare the edge length of the cubic voids to the outer edge length of the particles at the end of the reaction (Figure 7.5j and Supplementary Figure 7.14). Independent of the absolute sizes, we find a ratio of approximately 53%, which underpins the void formation to originate from a specific chemical transformation. However, assuming full conversion from Cu₂O to Cu, we would expect a size ratio of 73.8%, indicating the presence of some residual oxide in the final hollow structures.

To verify the role of the substrate in the hollowing process of nanocuboids, we examined the particles grown on the reactor window during the in situ measurements in the scanning electron microscope (SEM). The false-colored image in Figure 7.5h shows that the particles in fact have the shape of rectangular bowls. Due to their flatness, it is reasonable to assume that the hollowing process starts at or close to the particle-substrate interface, and then carves into the particle in the direction away from the substrate. To further test this hypothesis, we use a focused ion beam (FIB) on a fresh sample not exposed to X-rays and cut some nanocuboids in half that are still bound to the substrate (Figure 7.5i). It is clear that the void is located in between the bowl-shaped copper particles (orange) and the substrate (blue). Thus, the particles in Figure 7.5h must have detached from the substrate and turned around before the image was taken. The void formation process is schematically illustrated in Figure 7.5g.

7.3.4 Photon energy dependent radiation damage in X-ray imaging

We have shown that hard X-ray ptychography can reveal the shape evolution of hollow copper nanocuboids with a high level of detail. However, when imaging nanostructures in chemically reactive environments, alterations of the sample induced by the probe beam are a common obstacle in both TEM^{233, 250} and X-ray microscopy.^{251, 252} In our case, the partial absorption of the X-ray beam within the reaction medium leads to a local energy deposition that can cause changes in the reaction pathway. We found that the photon energy has a strong influence on the characteristic of the radiation damage. At an energy of 8.98 keV, which is just above the K edge of copper, the X-ray beam triggered the nucleation and attachment of nanoparticles at the reactor windows. As shown in Supplementary Figure 7.15, almost no particles are found outside the illuminated area after 18 h reaction time. Also, in a different experiment under the same conditions, micrometer-sized spherical structures formed under illumination instead of the expected nanocuboids (Supplementary Figure 7.16). This indicates that the comparably high absorption at 8.98 keV fully reduces the Cu(acac)₂ precursor already in solution, causing a deviation from the usual reaction pathway.

Therefore, we use the higher photon energy of 15.25 keV for all in situ images, reducing the influence of the X-ray beam on the reaction. At this energy, the attenuation coefficient of Cu₂O is about 4 times lower than at 8.98 keV, significantly reducing the amount of energy deposited by the beam.²⁵³ Although the field of view was under repeated exposure for continuous imaging, we neither noticed any influence of the beam on the nucleation or attachment of particles, nor was the shape or size of the nanocuboids affected during growth. We showed that the void formation coming along with the solid-state reduction is also not a beam effect. However, after the void has formed, the particles shrink and finally vanish, starting at 16 h (Supplementary Figure 7.17a-c). This suggests that the metallic copper is less stable under irradiation due to its increased density and lower chemical stability compared to Cu₂O. The metallic particles undergo side reactions with the organic solvent forming soluble copper species. At

20.5 h reaction time, we extended the field of view around the region that was continuously exposed before (Figure 7.6a). The disintegration of metallic copper particles is localized to the exposed region. The SEM image of a region in close vicinity to the exposed area (Figure 7.6b) shows nanocuboids with truncated edges. It is plausible that the ablation sets in at the edges where the higher surface energy facilitates side reactions.

While the absorption of X-rays in matter is significantly weaker compared to that of electrons, the high flux and long acquisition time currently required for scanning-based X-ray microscopy diminish this benefit. Still, by choosing a high photon energy, we prevented radiation damage during all reaction stages until the formation of the final hollow structures and could thereby visualize the full undisturbed shape evolution.

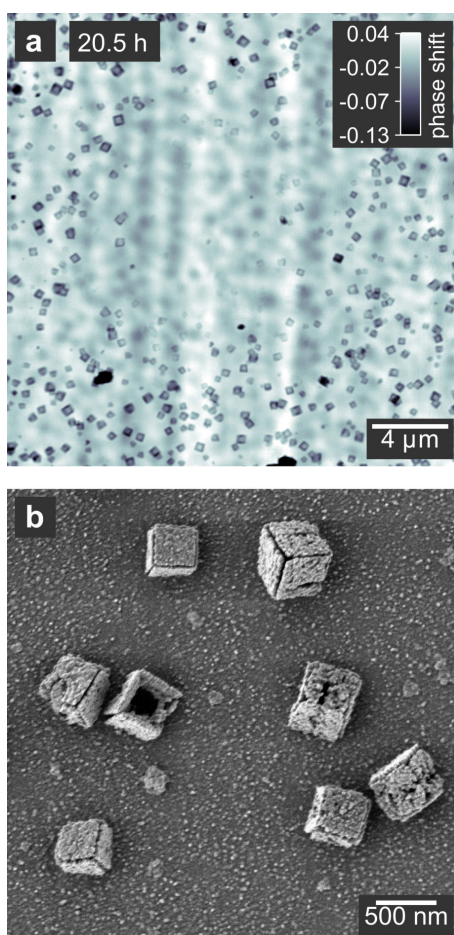


Figure 7.6. Beam-induced damage to the nanocuboids. **a** Ptychographic image taken after 20.5 h with an extended field of view around the region that was continuously exposed for in situ imaging. The beam-induced disintegration of particles is visible in the exposed region in the middle. The image shows an overlay of particles on both reactor windows since multi-slicing could not be applied due to the decreasing distance between the windows. The gray scale indicates the phase shift of the image in radian. **b** SEM image of particles from the same sample as in **a**, taken close to the exposed region. The nanocuboids show the onset of disintegration at the edges.

7.4 Discussion

Recent in situ studies using X-ray spectroscopic and scattering techniques revealed that the nucleation of nanoparticles is followed by complex structural and chemical changes in solution,^{24, 60, 99} including transformations of distinct primary particles,^{22, 254} assembly¹³ and hollowing processes.^{41, 49} These

findings highlight that many pathways exist that lead to complex, hierarchical materials, besides the classical LaMer model of nucleation and growth.¹⁹ However, since X-ray scattering and spectroscopic methods provide information averaged over a given reaction volume, only in situ microscopy gives a proof of these pathways. We demonstrate how in situ imaging in solution with hard X-ray ptychography enables a direct visualization of the complex transformations of shape and size at the nanoscale. The method can be applied to a wide range of materials and reaction conditions, complementing the capabilities of liquid-cell TEM. Such rare visual insights into structural changes in solution are important to deepen our understanding of the origins of nanomaterials morphology, which is a key factor for the future design of highly active catalysts and functional devices.

In summary, we revealed the full morphological growth of Cu₂O nanocuboids and their subsequent transformation into hollow Cu structures by directly visualizing them in situ inside our chemical reactor with an in-liquid beam path of 1 mm. Making full use of the quantitative phase images, we found that the 3D shape of the nanocuboids is strongly influenced by their interaction with the walls of the reactor. When attached to the substrate, the out-of-plane growth is hindered, and the particles grow into flat cuboids with an aspect ratio of 0.5. Particles nucleating in solution and attaching to the substrate at a later growth stage take a more cubic profile. The hollowing process, which we assign to the solid-state reduction of Cu₂O to Cu, originates close to the particle-substrate interface. The voids grow towards those faces that are in contact with the solution, i.e., where the reducing reaction with the solvent takes place, and leave the particles with a bowl-like shape. Finally, we identified the influence of the beam on the reaction at different photon energies and minimized the beam damage by choosing a high photon energy with correspondingly low energy deposition. Under these conditions, only the hollow metallic structures that denote the end of the reaction are sensitive to the beam, but no deviations are observed along the reaction path.

According to our observation of reduced beam damage at the higher photon energy of 15.25 keV, we expect that beam damage will be further reduced with the emergence of fourth generation synchrotron sources providing highly coherent X-rays at even higher energies than 15.25 keV. At the same time, the high coherent flux of these new sources can significantly increase imaging speed and spatial resolution. Already now, the high level of microscopic detail obtained within our in situ X-ray microscopy experiment encourages the application of this approach to explore shape evolution and transformation processes in related fields, such as the formation of hollow metal oxide nanospheres composited with graphite or sulfur for lithium ion batteries,^{225, 226} or with noble metal particles for (photo-) catalytic energy production.^{227, 228} Also, biomineralization processes²⁵⁵⁻²⁵⁷ or syntheses of bio-inspired nanomaterials^{258, 259} may be worth visualizing.

7.5 Experimental section

Synthetic procedure

Chemicals: BnOH (>99.8%, anhydrous) and Cu(acac)₂ (99.99%) were purchased from Sigma-Aldrich, and ethanol (absolute) for washing from VWR. All chemicals were used without further purification.

Synthesis: 1.72 mL of BnOH was added to 0.03 mmol Cu(acac)₂ and stirred for 10 min at room temperature in a glove box under argon atmosphere. The blue solution was transferred to the reaction container of the in situ reactor, sealed, and heated at a rate of 4.5 °C/min to 155 °C. The reaction was stabilized at this temperature for a maximum of 30 h for in situ imaging, and for FIB experiments the reactor was cooled to room temperature after 14.5 h at a cooling rate of 5.5 °C/min. All mentioned reaction times are relative to the point when we start heating. For SEM and FIB, the polyimide windows of the reactor were rinsed thoroughly with ethanol and dried at 60 °C overnight.

Ex situ characterization

SEM: Scanning electron microscopy images were taken with a Regulus 8220 (Hitachi High Technologies Corp., Japan) at an acceleration voltage of 3.6 kV and under the application of a deceleration voltage of 3.5 kV, resulting in a maximum electron energy at the sample surface of 0.1 keV. Secondary and backscattered electron signals were mixed.

FIB: Focused ion beam milling and subsequent SEM imaging was conducted with a Crossbeam 550L (Carl Zeiss AG, Germany) using a Ga ion beam at 30 kV and 50 pA, and an electron probe at 5 kV.

In situ reactor

Detailed information about the in situ reactor including a schematic are given in Supplementary Notes 7.1. The container for the reaction solution is made of polytetrafluoroethylene (PTFE) and two polyimide windows with a thickness of 125 μm . The container has a volume of 2 mL and, when assembled, the beam path through the liquid is 1 mm. The container is clamped into a heatable body made of invar and titanium for low thermal expansion. A PID controller is used to keep the reactor at the reaction temperature with a stability of ± 0.05 $^{\circ}\text{C}$.

X-ray ptychography

Beamline setup and data acquisition: Measurements were performed at the Ptychographic Nanoanalytical Microscope PtyNAMi¹⁸⁴ at the nanoprobe endstation of beamline P06²⁶⁰ at PETRA III at DESY in Hamburg, Germany. A coherent X-ray beam at a photon energy of 15.25 keV was focused using stacks of nanofocusing refractive lenses. An Eiger X 4M (Dectris AG, Baden-Daettwil, Switzerland) photon counting area detector with a pixel size of 75 x 75 μm^2 was placed at the end of an evacuated flight tube 3.435 m behind the sample. For a ptychographic image within a time series, the in situ reactor was raster scanned perpendicular to the beam within a field of view of 12 x 12 μm^2 with a step size of 300 nm. Coherent far-field diffraction patterns were measured with an exposure time of 0.5 s. Thermal drifts of the reactor were compensated by adjusting its position between image acquisitions. Each scan took 21.6 min. For the larger image in Figure 7.6a, a field of view of 24 x 24 μm^2 was scanned. For the images shown in Supplementary Figure 7.15-7.16, measurements were taken at the cSAXS beamline at the SLS at PSI, Villigen, Switzerland. A photon energy of 8.98 keV was used and the beam was focused with a Fresnel zone plate in combination with an order-sorting aperture. At the end of an evacuated flight tube, a Dectris Pilatus 2M detector with a pixel size of 172 x 172 μm^2 was placed 7.35 m behind the sample. The field of view was 10 x 10 μm^2 for an in situ image series, and 30 x 30 μm^2 for the larger image shown in Supplementary Figure 7.15.

Image reconstruction: For reconstruction, the diffraction patterns were cropped to 256 x 256 px, resulting in a pixel size in the reconstructed images of 14.54 nm and 23.06 nm for the measurements at P06 and cSAXS beamlines, respectively. The image reconstruction of data taken at beamline P06 was carried out using the extended ptychographic iterative engine (ePIE)⁸³, and for the data from cSAXS, the difference map algorithm in combination with a maximum likelihood approach was used.^{261, 262} For data taken at P06, the object was initialized to be non-absorbing and non-phase-shifting, and a Gaussian probe with a full width at half maximum of 1 μm and a phase curvature of 2.2 mm was used as the initial probe. For images containing few particles early in the time series before 3.5 h, the illumination was initialized with the reconstructed illumination of the image after 3.83 h. For data measured at the cSAXS beamline, a reconstructed illumination from an ex situ sample was always used as initial probe. Multi-slice reconstructions were carried out for the P06 data. Here, the object slice corresponding to the entrance window was initialized first, and the exit window slice was activated after 20 iterations. From iteration 250, position refinement was performed every 100 iterations with a maximum displacement of 44 nm.²⁴⁶ Reconstructions were run for 1000 iterations. The distance between the slices was initially set to 1 mm and gradually reduced, adapting to the shrinking distance between the windows of the in situ

reactor (for details, see Supplementary Notes 7.2). The Fresnel nearfield propagator²⁶³ was used for wave propagation between slices.

Image analysis

Alignment: To compensate for thermal drifts of the in situ reactor, in addition to the mechanical compensation described above, we aligned the image series using an implementation of the scale-invariant feature transform (SIFT) method²⁶⁴ within the image analysis software ImageJ²⁶⁵ (version 1.53k).

Fourier ring correlation: To calculate FRCs^{217,218}, the diffraction patterns of the image were split into two data sets with equidistant scan points and reconstructed individually, with the refined positions from the full data set. The FRC was calculated from the resulting two images. We used the half bit criterion for resolution estimation in order to account for the lower resolution introduced by splitting the data set.

Depth of field: In the multi-slice model, the DOF can be considered as the maximum thickness that an object may have to be imaged within one slice at a given lateral spatial resolution Δd and wavelength λ . We calculated the DOF using the empirical relation⁹¹ given by

$$\text{DOF} = 5.2 \frac{(\delta r)^2}{\lambda} \quad (7.1)$$

where δr is the lateral resolution and λ is the X-ray wavelength. Here, we calculate a DOF of 280 μm .

Quantitative image analysis: To track and measure the dimension of cubic particles within the image plane, several image processing steps were applied using Python and the PyOpenCV library²⁴⁷ (version 4.5.1.48). First, images were converted to binary (black and white) by applying adaptive thresholding with a Gaussian kernel with a size of 1/8 of the image dimension. Closing (dilation followed by erosion) with a kernel of size (2x2) was used to reduce image noise, and contours (borders between black and white areas) were identified. The smallest rectangle containing all points of a closed contour was taken as the outer dimension of the respective particle. Only particles visibly oriented with one face parallel to the substrate and with an in-plane aspect ratio between 0.7 and 1.3 were tracked. An example image after each of these steps is shown in Supplementary Figure 7.10.

For calculating the thickness of a particle from a quantitative phase image, first the average background phase shift ϕ_{bkg} of the image was calculated by applying a threshold of -0.02 rad to separate particles and background (Supplementary Figure 7.11), and by then averaging the background. Only for particles with one face visibly oriented parallel to the substrate, the average phase shift ϕ_{particle} was calculated within an area covering 70% of the full particle dimension to account for the not perfectly sharp edges (blue rectangles in Figure 7.4a). The thickness d was then calculated using Equation 7.2

$$d = \frac{-(\phi_{\text{particle}} - \phi_{\text{bkg}})\lambda}{2\pi\delta}, \quad (7.2)$$

where λ is the X-ray wavelength and $1 - \delta$ is the real part of the complex refractive index. We used the difference of the refractive index decrement of Cu_2O and the surrounding solvent, resulting in $\delta = 3.98 \cdot 10^{-6}$.⁶⁴

7.6 Acknowledgements

This work was supported by the Bundesministerium für Bildung und Forschung (BMBF) within the Röntgen-Ångström-Cluster via the project 05K2020 - 2019-06104 XStereoVision (grant no. 05K20GUA, L.G., D.K., C.G.S.), by the European Research Council within the project LINCHPIN (grant no. 818941, C.A.Z, D.K.), and by the Cluster of Excellence “CUI: Advanced Imaging of Matter”

of the Deutsche Forschungsgemeinschaft (DFG) – (EXC 2056 – project ID 390715994, S.Y.H.-M., I.F.-C., D.K.).

We thank Dr. Maik Kahnt and Stephan Botta for supporting the X-ray measurements and Prof. Robert H. Blick for providing access to the FIB-SEM device. We also thank Prof. Marcin Sikora and Krzysztof Pitala for EM imaging.

We acknowledge DESY (Hamburg, Germany), a member of the Helmholtz Association HGF, for the provision of experimental facilities. Parts of this research were carried out at PETRA III and at the DESY NanoLab. We would like to thank Dr. Gerald Falkenberg and Dr. Jan Garrevoet for assistance in using beamline P06, and Dr Thomas Keller, Satishkumar Kulkarni and Arno Jeromin for laboratory support.

We acknowledge the Paul Scherrer Institut, Villigen, Switzerland for provision of synchrotron radiation beamtime at the cSAXS beamline of the SLS and would like to thank Dr. Andreas Menzel, Dr. Ana Diaz and Xavier Donath for assistance.

7.7 Author Contributions

D.K., C.G.S. and L.G. conceived the project. L.G. and R.D. designed the in situ reactor. M.L. conducted the thermal simulations of the in situ reactor. L.G., N.M., S.Y.H.-M. and F.M. prepared the synthetic procedure. L.G., M.S., S.Y.H.-M., C.A.Z., O.V., F.W. and M.K. conducted the X-ray ptychography experiments. L.G., E.K., F.M., and I.F.-C. conducted the FIB milling and SEM imaging, and analysed the images. L.G. and M.S. reconstructed the ptychographic images. L.G. conducted the quantitative image analysis. All authors contributed to the data interpretation and the preparation of the manuscript.

7.8 Additional information

Competing Interests

The ptychographic imaging technique used in this paper is the subject of awarded patents owned by Phase Focus Ltd., which is a spin-out company of the University of Sheffield. None of the authors is affiliated to this company. This conflict exists for all the authors.

Data Availability

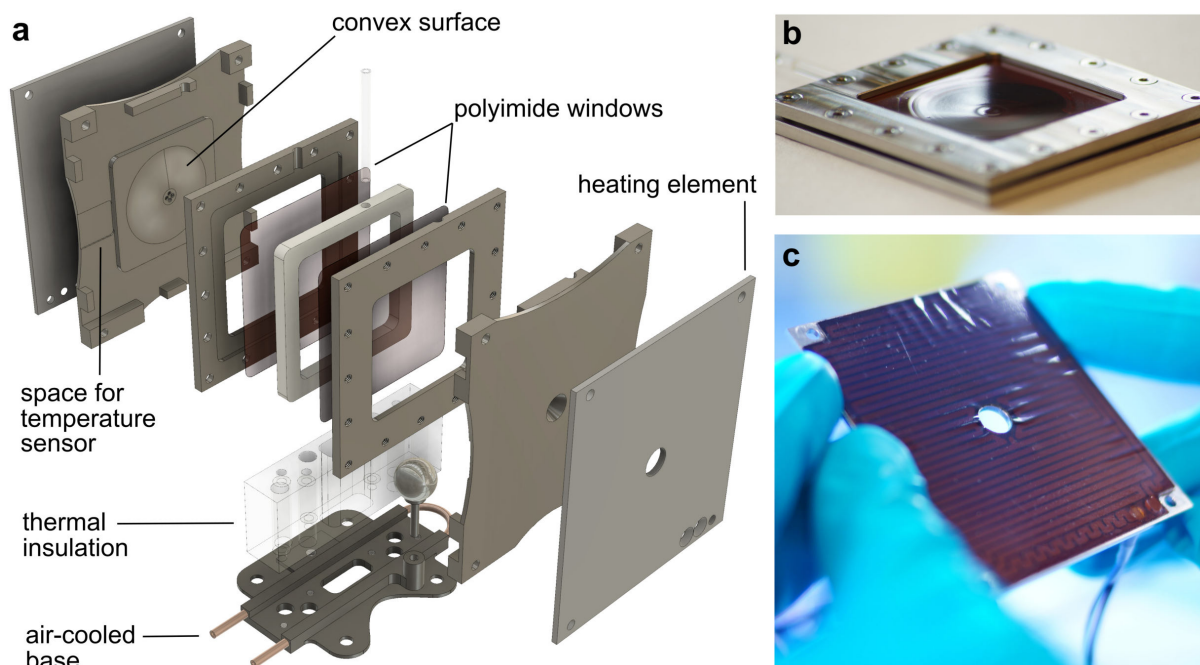
The X-ray ptychography and SEM data sets generated and analysed during the current study are available in the zenodo repository, DOI: 10.5281/zenodo.6675817.²⁶⁶

7.9 Supplementary Information

Supplementary Notes 7.1. Technical information on the in situ reactor

A schematic representation of our in situ reactor in the form of an exploded view is shown in Supplementary Figure 7.1. The liquid container of the reactor is a PTFE autoclave with two 125 µm thin polyimide windows on opposite sides for high X-ray transparency. The autoclave has a volume of 2 mL to ensure undisturbed reaction kinetics as compared to laboratory vials. The autoclave is placed between flat heating elements with a curved surface, pushing onto the flexible polyimide windows at the center of the container which takes a concave shape. This way, the beam path through the liquid measures only 1 mm for low attenuation and background, while at the same time a large liquid volume is provided. To

ensure position stability within the single-digit nanometer range, the heatable body is made of Invar and titanium for low thermal expansion. The body is thermally isolated from the base attached to the nano-positioning stage by a Zerodur (Schott AG, Mainz, Germany) part with almost no thermal expansion and low thermal conductivity. The base is actively cooled with an air flow through a copper pipe. The heating elements are current-regulated and operated with DC to avoid vibrations induced by switching. A proportional–integral–derivative (PID) controller provides high temperature stability of ± 0.05 °C.

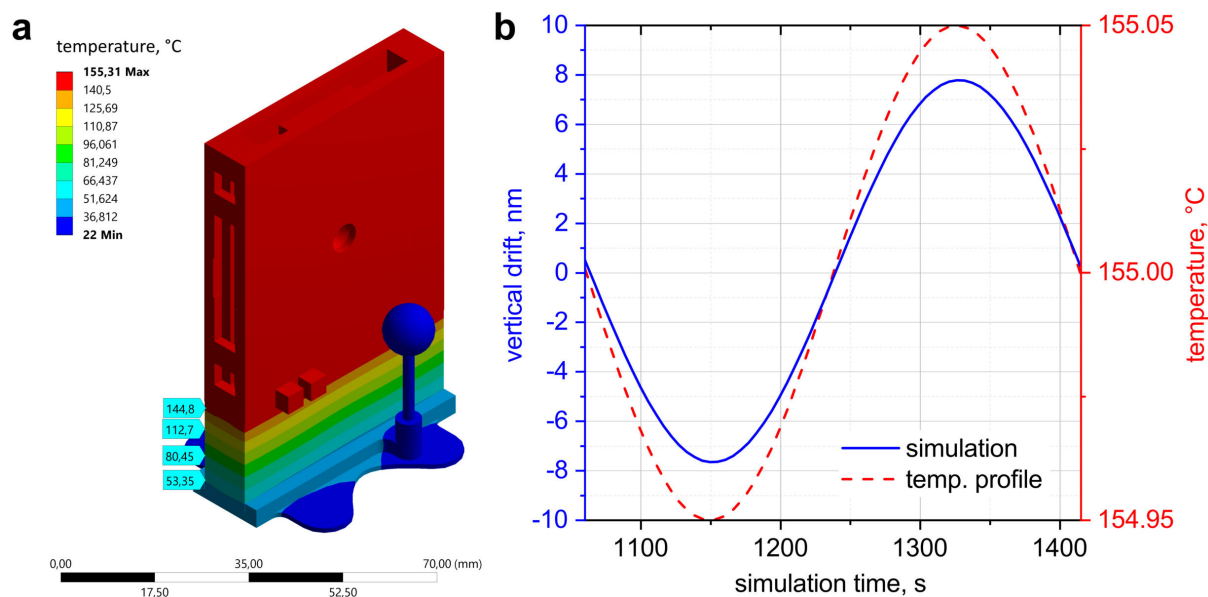


Supplementary Figure 7.1 Schematic representation of the in situ reactor. **a** The exploded view of the in situ reactor shows all components individually. The liquid container is made of a PTFE frame covered with two polyimide windows and clamped between two Invar frames. The container is placed between two Invar heating covers with a convex surface. Flat heating elements provide uniform heat from two sides. A thermal insulation made of Zerodur is placed between the heated body and the air-cooled base. **b** Photograph of the liquid container after a reaction at 155 °C. The concave shape results in a window distance of 1 mm at the center of the container. **c** Photograph of a resistive heating element made of titanium and flexible circuits printed on polyimide.

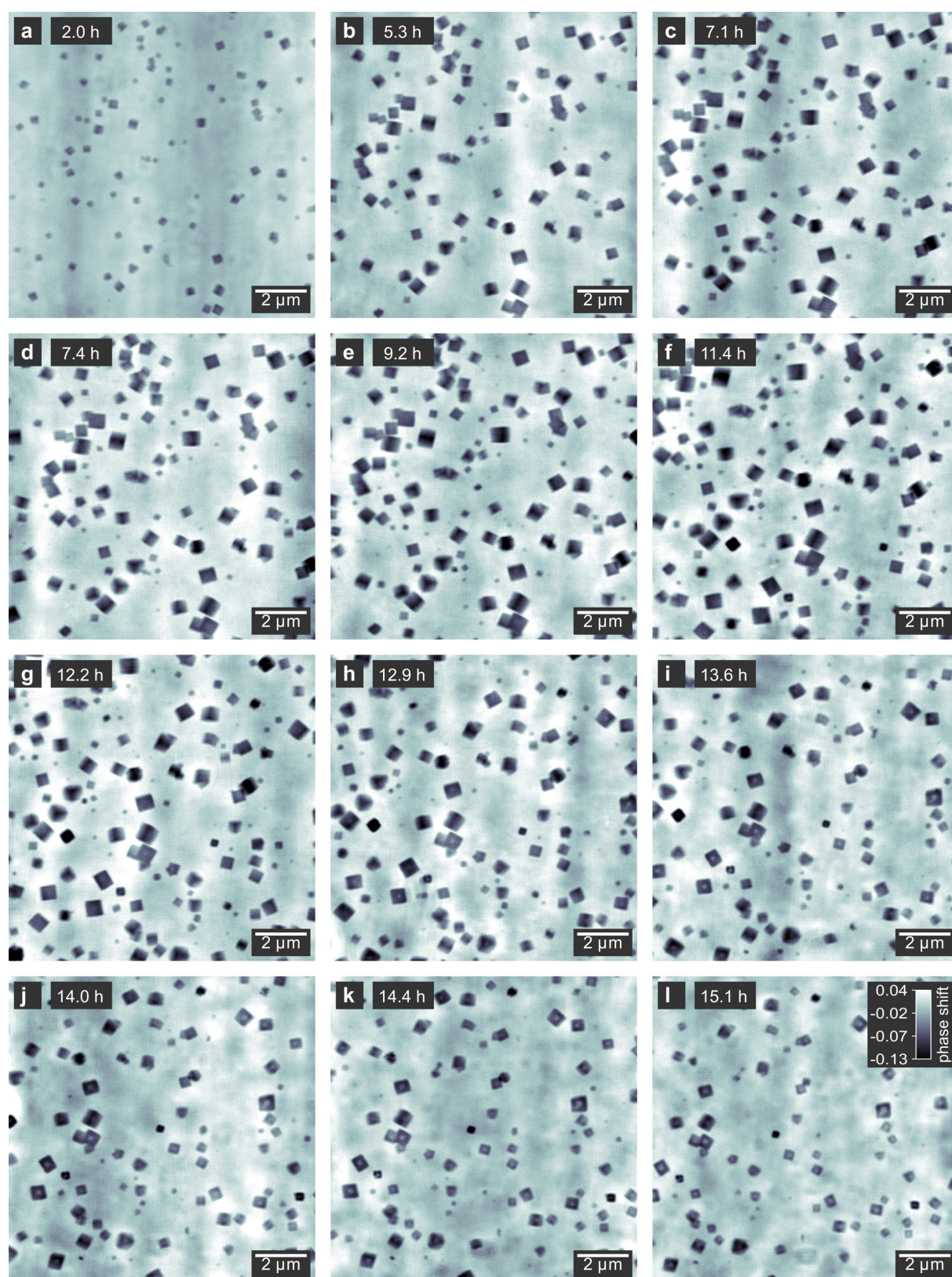
To verify the position stability, we conducted thermal simulations of the reactor applying the finite-element method using the software ANSYS Mechanical version 17.2 (ANSYS Inc, Canonsburg, USA). The results are summarized in Supplementary Figure 7.2. Part a of the figure shows the temperature field in the steady state across the reactor when the reaction temperature of 155 °C is reached. We find that the squared upper body is evenly heated (red), while the thermal insulation efficiently keeps the heat away from the base (blue). Due to the large temperature gradient across the insulation, it is important that we used Zerodur with extremely low thermal expansion for this part.

We also simulated the expected residual thermal drifts of the imaged region of the reactor given a temperature instability of ± 0.05 °C. By Fourier-transforming a measured temperature profile of the reactor at the target temperature, we identified that the main frequency component of the residual temperature fluctuations has a period of 353 s. We used a sinusoidal temperature profile with this period for a transient simulation, tracking the variation in the vertical distance from the base to the beam position on the reactor. Due to the symmetric design of the reactor, we expect no significant thermal drift in the horizontal direction. Supplementary Figure 7.2b shows the thermal expansion as obtained from the transient simulation. We find a residual vertical drift below ± 8 nm. The actual drifts during

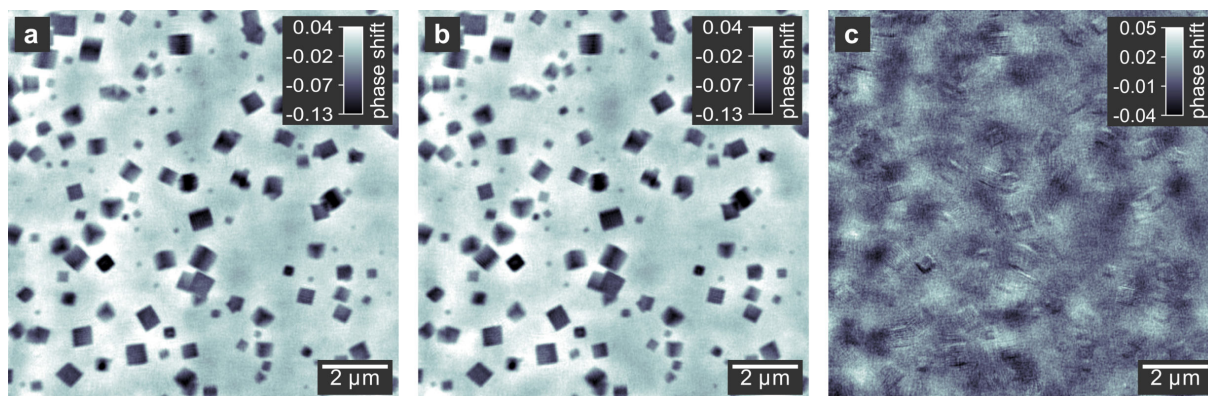
data acquisition may have been larger due to thermal movement of the polyimide windows not covered by the simulation.



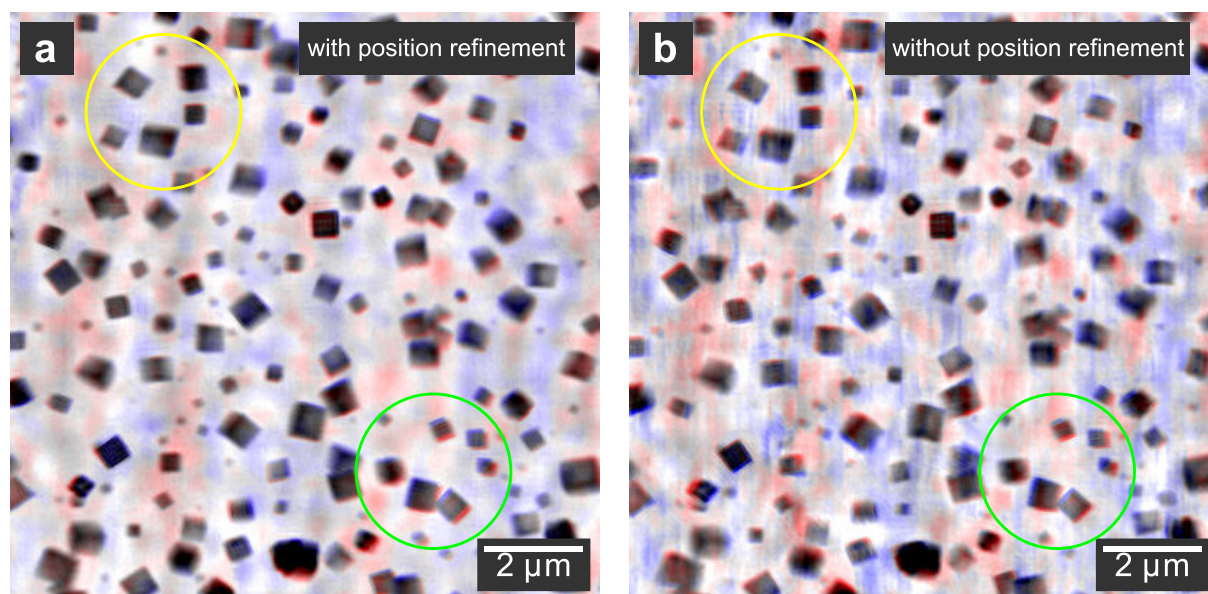
Supplementary Figure 7.2. Thermal simulations on the in situ reactor. **a** Simulation of the heat distribution over the assembled reactor in the stationary case at 155 °C. The upper squared body of the reactor containing the reaction solution is evenly heated. The temperature drops off across the thermal insulation, keeping the base at a low temperature between 30 and 50 °C. **b** Transient simulation of the vertical expansion between the base and the beam position. A sinusoidal temperature profile with a period of 353 s was applied. The residual drift is below ± 8 nm.



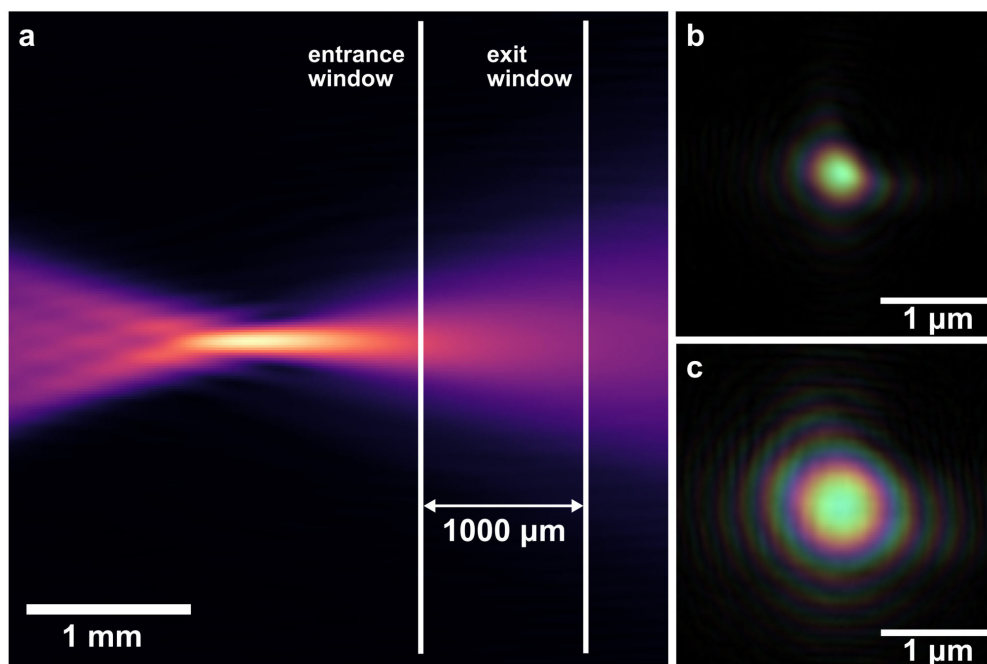
Supplementary Figure 7.3. Overview of the reaction on the exit window. **a-l** Ptychographic reconstructions of nanocubes on the exit window of the in situ reactor. The gray scale indicates the phase shift of the images. At all reaction times, the particles are similar in size and morphology the those on the entrance window.



Supplementary Figure 7.4. Reconstructions from split data set. **a-b** Example of ptychographic reconstructions of nanocubes on the exit window of the reactor, each reconstructed with the data from half of the scan points compared to the full data set. These reconstructions were used to calculate the FRC of the exit window shown in Figure 7.2f. **c** Difference between the reconstructions in **a** and **b**. The gray scale indicates the phase shift of the images.



Supplementary Figure 7.5. Effect of position refinement during reconstruction. False-colored overlay of two consecutive ptychographic reconstructions from the entrance window of the reactor, reconstructed **a** with and **b** without position refinement⁸⁹ enabled during iterative phase retrieval. The overall quality of the reconstruction without position refinement is significantly worse due to thermal movements of the reactor during scanning not being corrected for. Blue and red shadows at particle edges indicate an instability in the position of the respective particles between consecutive images, even though the images have been aligned to each other using the Scale-invariant Feature Transform (SIFT) method²⁶⁴ implemented within the image analysis software ImageJ²⁶⁵ (version 1.53k). From the particles highlighted with a yellow circle, it is visible that the position refinement stabilized their location, since more pronounced red and blue edges can be seen in **b** compared to **a**. Still, for other particles such as those highlighted with the green circle, a displacement remains irrespective of position refinement.



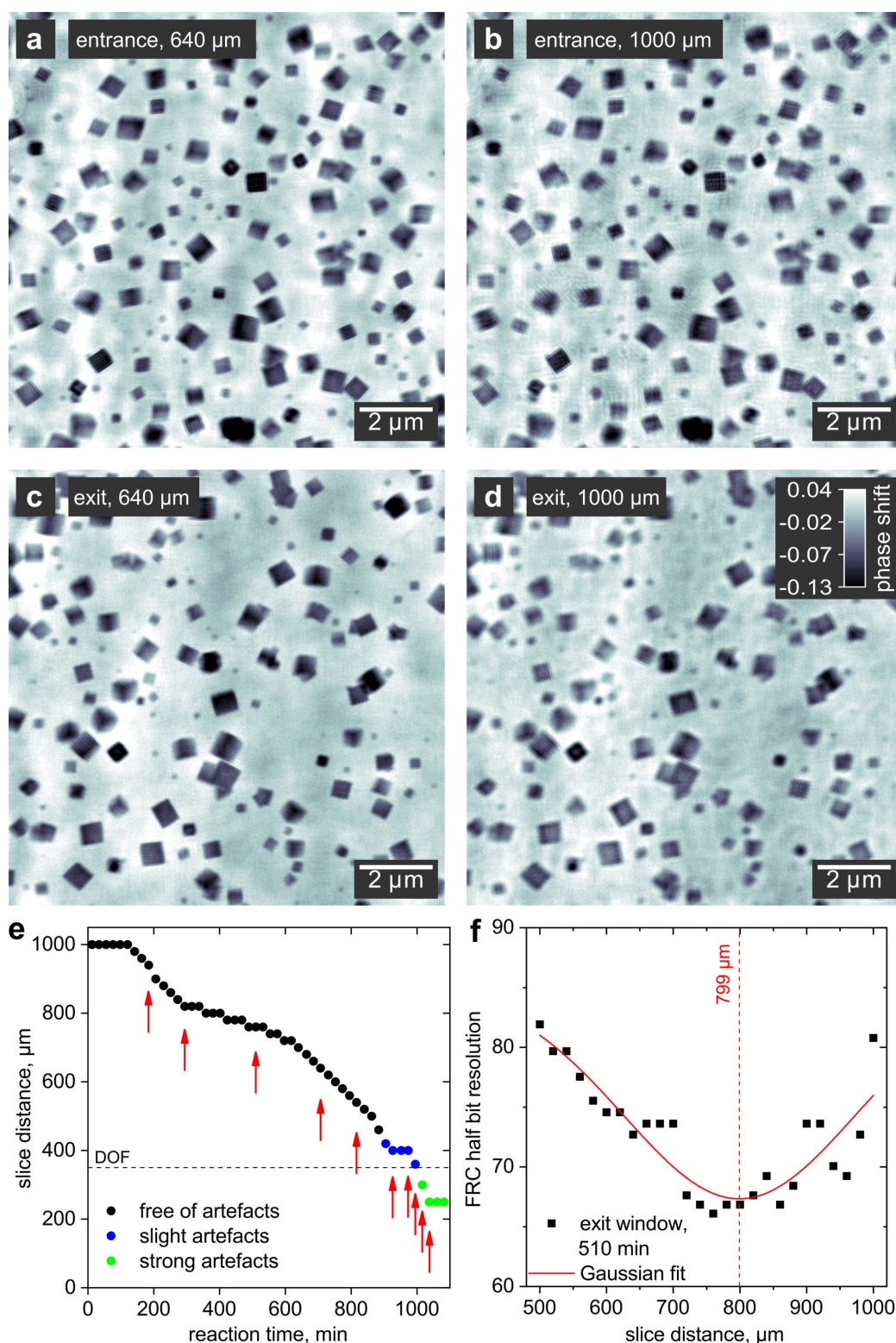
Supplementary Figure 7.6. Reactor position and illumination profiles. **a** Positions of the reactor windows along the caustic of the focused beam, displayed as the horizontal intensity. **b-c** Display of the illuminations on the entrance and exit windows, respectively. Here, brightness represents the amplitude and color represents the phase of the wavefield.

Supplementary Notes 7.2. Distance between reactor windows

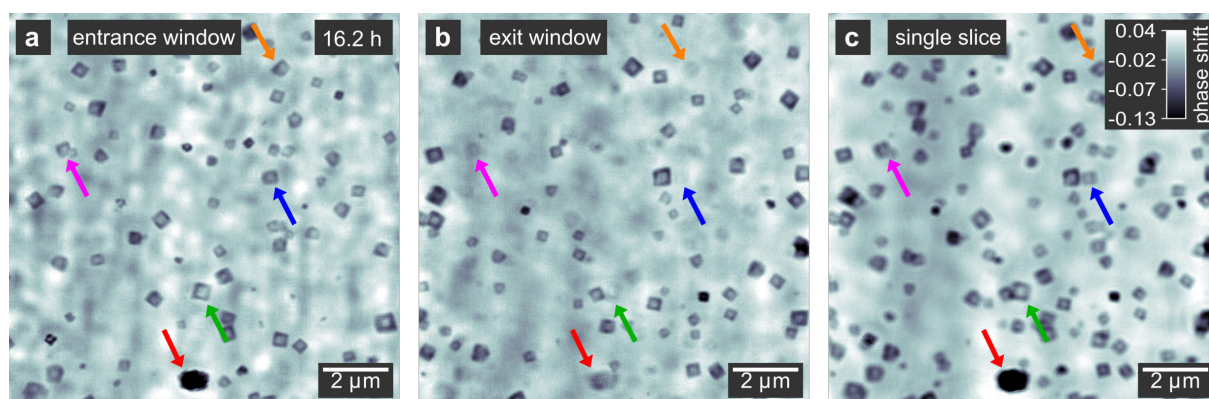
The multi-slice model^{87, 91} allows to separately reconstruct several objects stacked along the beam direction from a single ptychographic data set. To this end, the distance between the layers must be known. In Supplementary Figure 7.7, we exemplarily show the effect of a wrong distance applied to the multi-slice model during reconstruction. Parts a and c of the figure show reconstructions with the correct distance set for the entrance and exit windows, respectively, while parts b and d show reconstructions with a wrong distance setting. We note that for the entrance window, the wrong distance results in artefacts in the form of fringes and additional background fluctuations. The exit window is the second layer in the multi-slice model and its reconstruction is initialized after 20 iterations. Here, a wrong distance leads to a loss in resolution and thus to a blurred image.

Directly after the assembly of the reactor, the distance between the polyimide windows is 1 mm, however, we observed that at 155 °C and in contact with the solvent, the windows deform over time and the distance between them shrinks. Therefore, we track the distance during the in situ imaging (Supplementary Figure 7.7e). By visual inspection of reconstructions using different possible distances, we evaluate the correct distance several times, as indicated by red arrows in Supplementary Figure 7.7e. Between the evaluations, we interpolate the distance. To confirm that the visual inspection results in an accurate determination of the window distance, we exemplarily evaluate the resolution of the exit window reconstruction at many possible distances for the image taken after 510 min reaction time (Supplementary Figure 7.7f). This procedure indicates an optimal distance of 799 μm , which is in good agreement with the distance of 760 μm found by visual inspection.

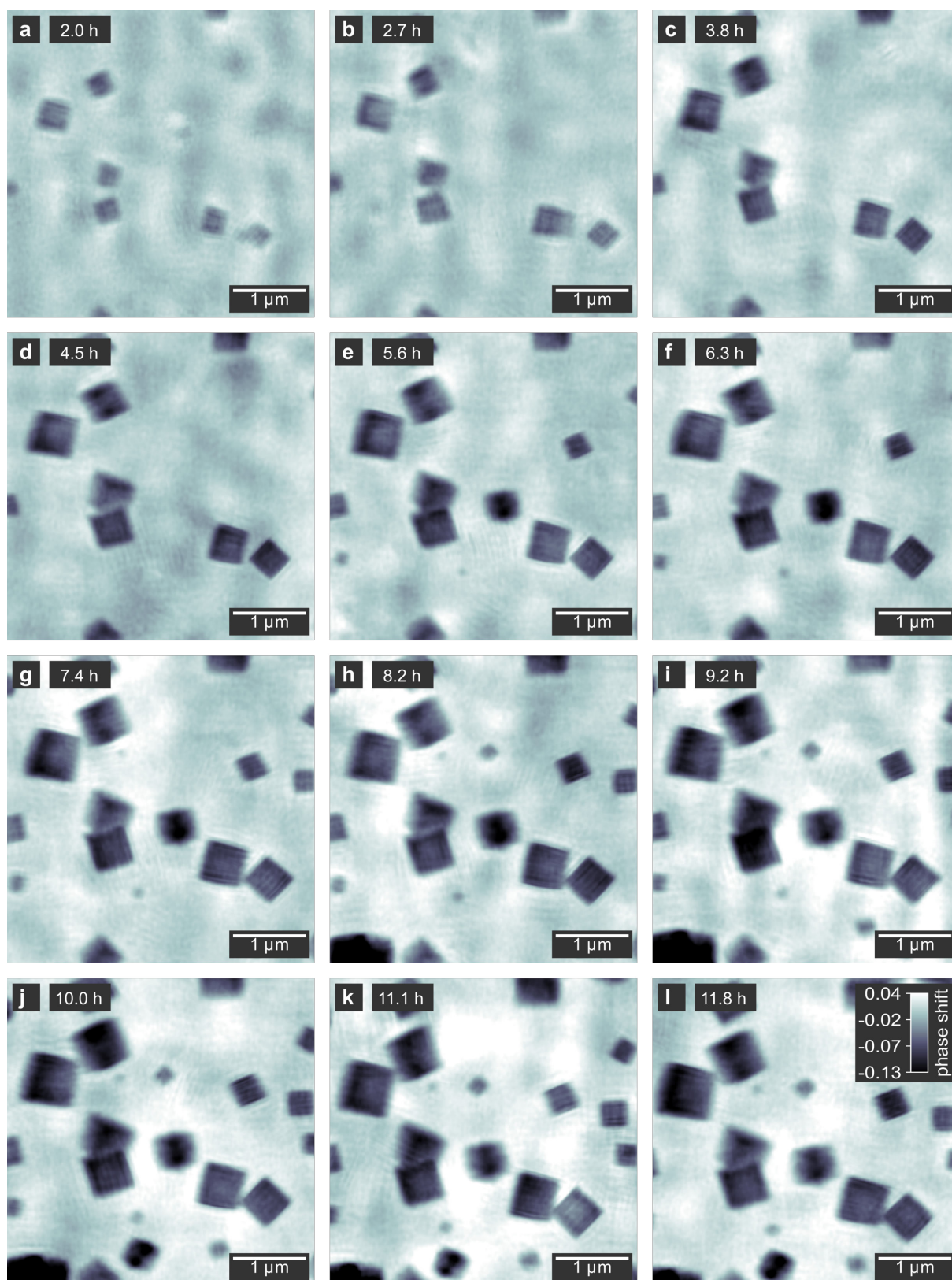
The separation of objects using the multi-slice model only works as long as their distance is larger than the DOF of the imaging setup, in this case 280 μm according to Equation 7.1. This is why starting at 15 h reaction time, when the window distance gets close to the DOF, the layer separation starts to produce artefacts and it fails after 16.7 h reaction time. From this time on, we can only reconstruct an overlay of nanocubes on both windows.



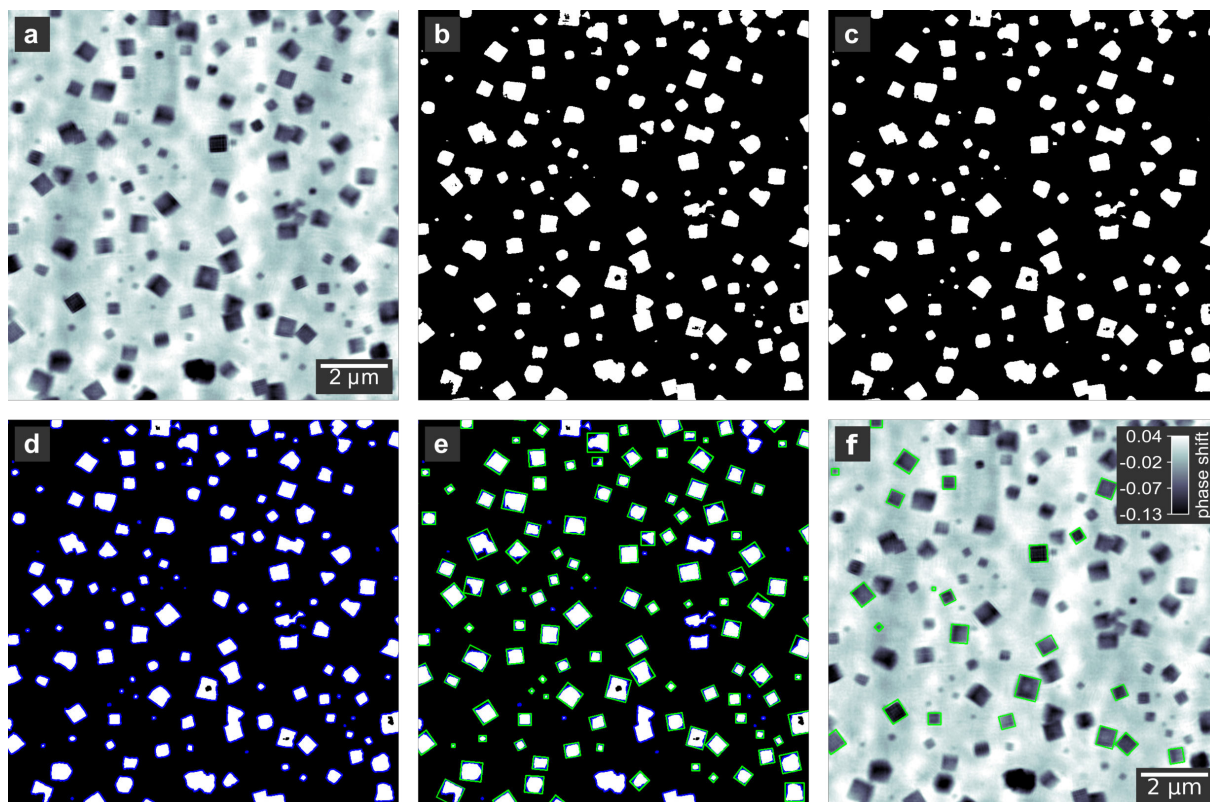
Supplementary Figure 7.7. Finding distance between reactor windows. **a-b** Example ptychographic reconstructions of nanocubes on the entrance window of the reactor applying the correct distance of 640 μm and a wrong distance of 1000 μm , respectively. **c-d** Ptychographic reconstructions from the exit window in accordance to **a-b**. The gray scale indicates the phase shift of the images. **e** Distances between the reactor windows for all time steps of the in situ experiment. Red arrows mark the times for which the distance was determined by eye inspection. **f** Slice distance determined by examining the FRC^{217, 218} resolution of the exit window reconstructions, exemplarily performed for 510 min reaction time. The Gaussian fit indicates that the best resolution is obtained for a distance of 799 μm , which agrees with the distance found by visual inspection in **e**.



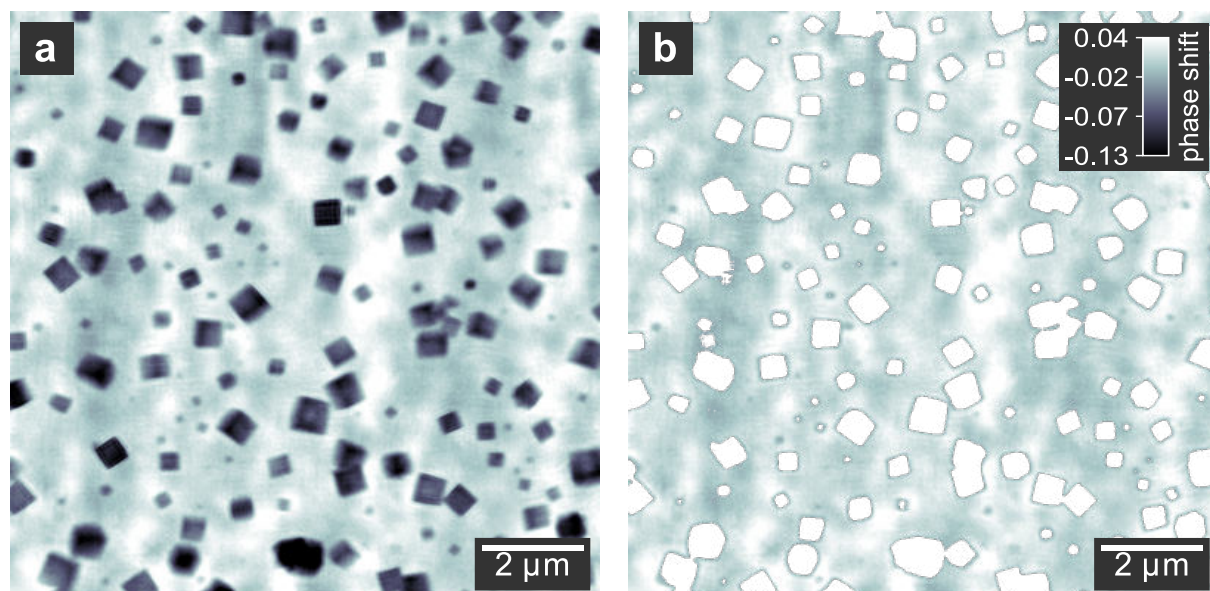
Supplementary Figure 7.8. Effect of incomplete slice separation. **a-b** Ptychographic image slices corresponding to the entrance and exit windows of the reactor, respectively, obtained from a multi-slice reconstruction. The images were obtained after 16.2 h reaction time, when the distance between the two windows had decreased to 400 μm due to deformation of the polyimide foils. Since this distance is not much larger than the DOF of 280 μm of the imaging experiment (see Supplementary Notes 7.2), the slice separation is incomplete. Colored arrows indicate particles in the entrance window slice (**a**) which are also dimly visible in the exit window slice (**b**). For comparison, **c** shows the corresponding reconstruction with only one object layer (single-slice). The gray scale indicates the phase shift of the images.



Supplementary Figure 7.9. Detailed view of the growth phase of Cu_2O nanocubes. **a-l** Ptychographic reconstructions of the entrance window of the reactor with a reduced field of view. The gray scale indicates the phase shift of the images.



Supplementary Figure 7.10. Overview of the image processing steps for tracking nanocubes with the OpenCV library.²⁴⁷ **a** Original ptychographic phase image. **b** Image after applying an adaptive threshold. **c** Image after applying a closing step. **d** Contours in the binary image highlighted in blue. **e** For each contour, the smallest rectangle that contains all points of the contour is drawn in green. **f** From the image in **e**, only squared shapes are selected and overlaid with the original phase image. The identified particle dimension match well. The gray scale indicates the phase shift of the image.



Supplementary Figure 7.11. Background selection. **a** Original ptychographic phase image. **b** Image after applying a phase threshold of -0.02 to select only the background. The gray scale indicates the phase shift of the images.

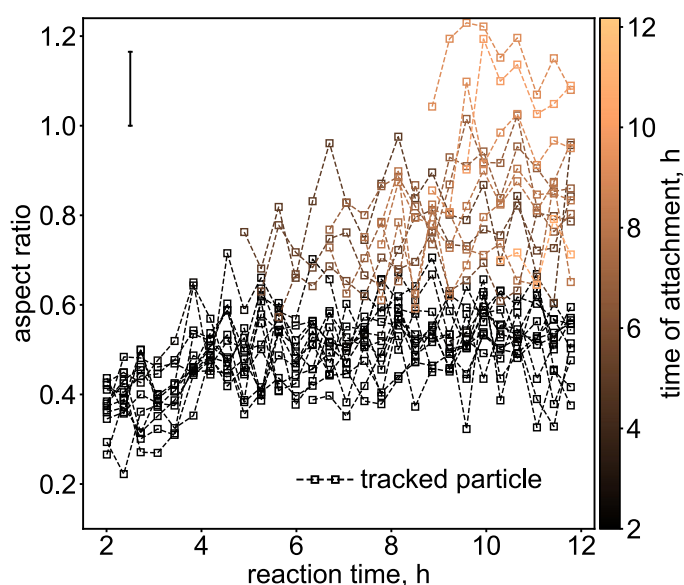
Supplementary Notes 7.3. Error calculation for the aspect ratio of the nanocuboids

The error Δa of the aspect ratio results from the error propagation of the in-plane particle size and the out-of-plane thickness. We calculate Δa according to

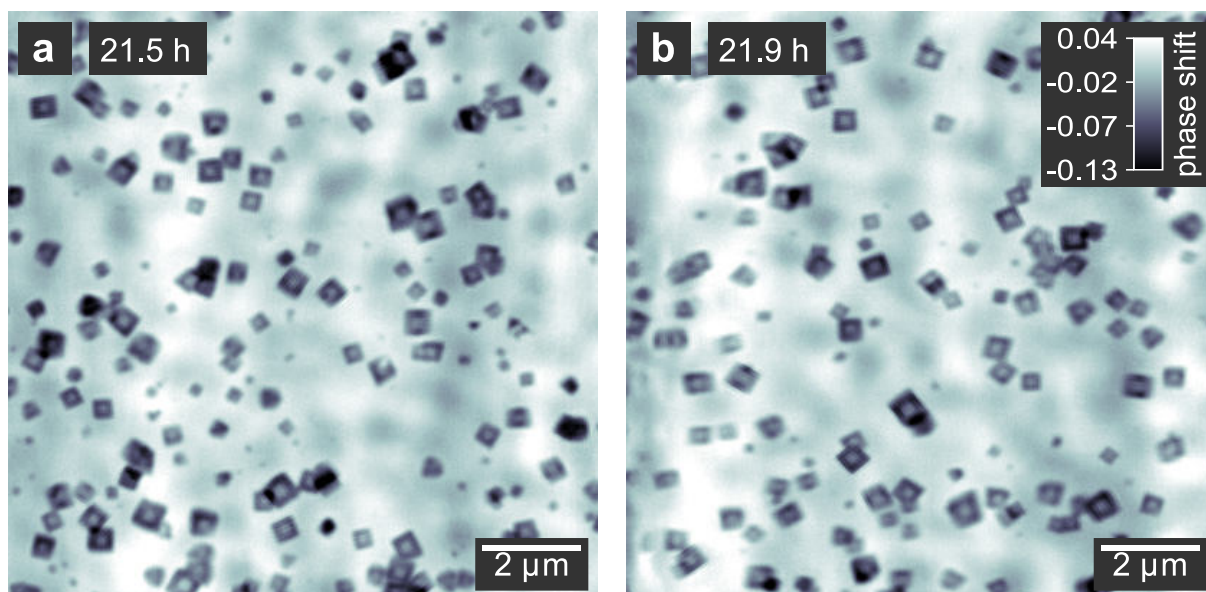
$$\Delta a = a \left(\frac{\Delta \phi}{\phi} + \frac{\Delta d}{d} \right) \quad (7.3)$$

where d and a are the edge length and the aspect ratio of a nanocuboid, respectively, ϕ is the mean absolute phase shift measured for a specific nanocuboid, Δd is the error of the edge length given by the spatial resolution of the ptychographic reconstructions, and $\Delta \phi$ is the error of the phase shift given by the standard deviation of all pixel values within an area covering 70% of the full particle dimension (blue rectangles in Figure 7.4a).

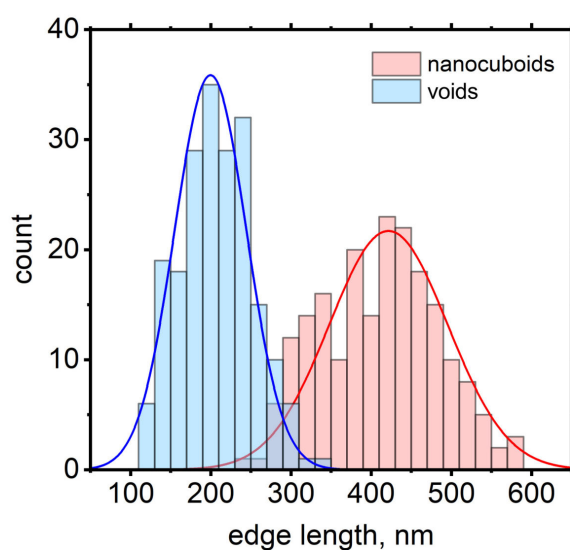
We calculate the error of the aspect ratio individually for each tracked nanocuboids in each image. For clarity, in Figure 7.4b and Supplementary Figure 7.12 the error bar indicates the mean of all calculated errors, equaling 0.165. For all tracked particles at all reaction times, the highest individual error equals 0.3.



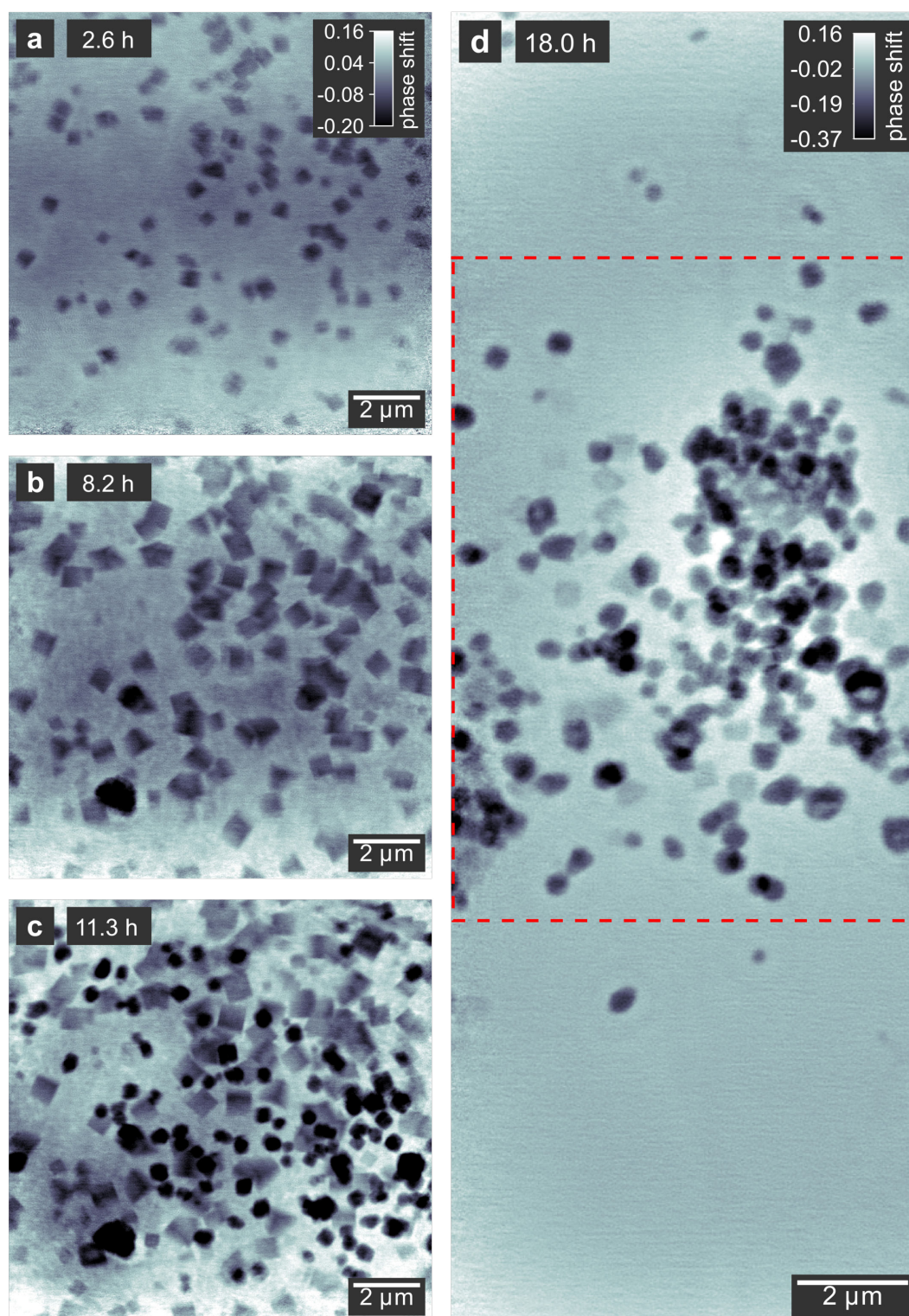
Supplementary Figure 7.12. Evolution of the aspect ratio for all tracked particles highlighted in Figure 7.4a. The aspect ratio is calculated as the quotient of the in-plane dimension and the out-of-plane thickness of the nanocuboids. Yellow color indicates the time when a particle attaches to the substrate. No moving average is applied to this data. The later the attachment takes place during the growth phase, the more cubic the respective particle is. The error bar represents the mean error resulting from the error propagation of the in-plane particle size and the out-of-plane thickness of all tracked particles.



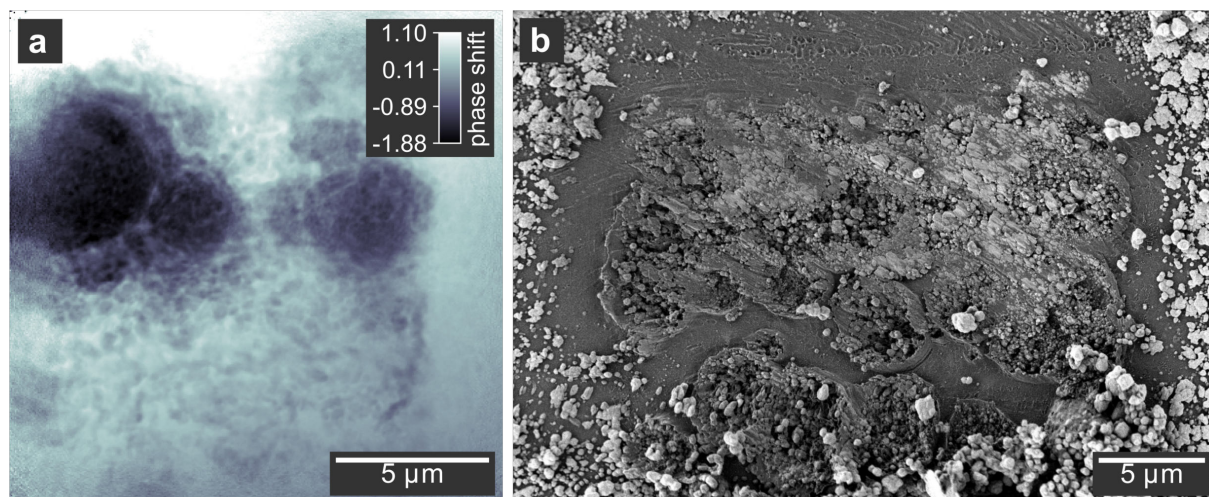
Supplementary Figure 7.13. Confirmation of void formation without beam. Ptychographic reconstructions of nanocubes at the end of the void formation. The images in **a** and **b** were taken at a different part of the reactor window, ca. 2 mm away from the previously exposed region, confirming that the hollowing process is not triggered by the X-ray beam. The images show overlays of particles on both reactor windows since multi-slicing could not be applied due to the decreasing distance between the windows. The gray scale indicates the phase shift of the images.



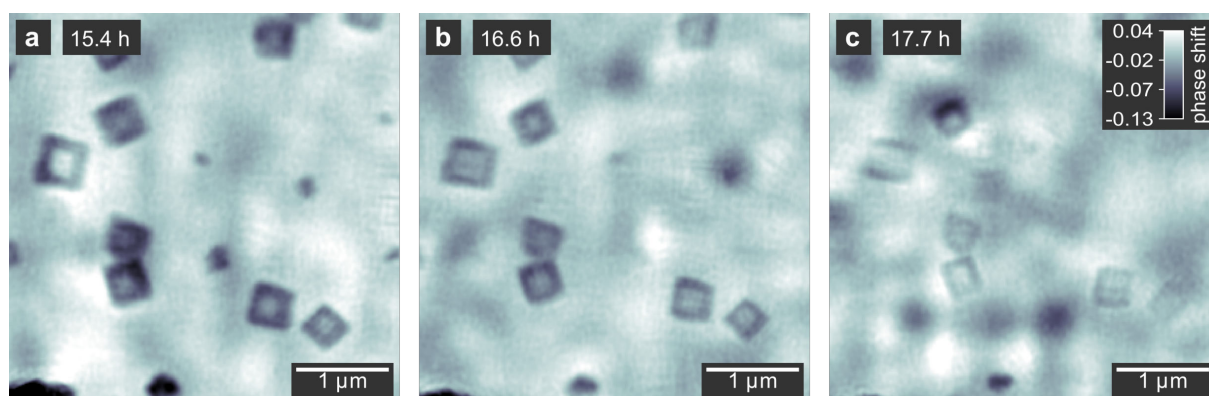
Supplementary Figure 7.14. Histogram of outer dimensions and void sizes of the nanocuboids. Here, we display the same data that is shown in Figure 7.5j, but in the form of a histogram to recognize the size distributions.



Supplementary Figure 7.15. Overview of the in situ imaging experiment at a photon energy of 8.98 keV. The photon energy was set just above the K edge of copper. **a-c** Ptychographic reconstructions of nanocubes overlaid on both windows of the in situ reactor. **d** Ptychographic reconstruction with a larger field of view, highlighting the previously imaged region from **a-c** with a red rectangle. The X-ray beam triggered the nucleation and attachment of nanoparticles at the reactor windows. Almost no particles are found outside the illuminated area after 18 h reaction time. The gray scale indicates the phase shift of the images.



Supplementary Figure 7.16. Beam-induced deviation of the reaction imaged at a photon energy of 8.98 keV. **a** Ptychographic reconstruction and **b** SEM image of the damaged region. Micrometer-sized spherical structures formed under illumination instead of the expected nanocuboids. The gray scale indicates the phase shift of the ptychographic image.



Supplementary Figure 7.17. Hollow metallic Cu nanocuboids vanishing under X-ray exposure at 15.25 keV. **a-c** Ptychographic reconstructions of nanocubes growing on the entrance window of the in situ reactor. We observe that after the end of the void formation, the particles shrink mostly in thickness as evident from the lower phase shift at later reaction times. Also, the outer dimension of the nanocuboids shrink to a lower extent. The gray scale indicates the phase shift of the ptychographic image.

8 Multimodal imaging of cubic Cu₂O@Au nanocage and CuPd alloy nanosphere formation using X-ray ptychography and nano diffraction

A publication containing the results on Cu₂O@Au nanocage formation presented in Sections 8.1-8.8 is in preparation. The manuscript is authored by Lukas Grote, Sarah-Alexandra Hussak, Leif Albers, Karolina Maria Stachnik, Federica Mancini, Martin Seyrich, Olga Vasylieva, Dennis Brückner, Mikhail Lyubomirskiy, Christian G. Schroer, and Dorota Koziej as corresponding author.

Section 8.9 presents a separate in situ imaging experiment on the formation of CuPd alloy nanospheres.

8.1 Abstract

Being able to observe the formation of multi-material nanostructures in situ, simultaneously from a morphological and crystallographic perspective, is a challenging task. Yet, this is essential for the fabrication of nanomaterials with well-controlled composition exposing the most active crystallographic surfaces, as required for highly active catalysts in energy applications. To demonstrate how X-ray ptychography can be combined with scanning nanoprobe diffraction to realize multimodal imaging, we study growing Cu₂O nanocubes and their transformation into Au nanocages. During the growth of nanocubes at a temperature of 138 °C, we measure the crystal structure of an individual nanoparticle and determine the presence of (100) crystallographic facets at its surface. We subsequently visualize the transformation of Cu₂O into Au nanocages by galvanic replacement. The nanocubes interior homogeneously dissolves while smaller Au particles grow on their surface and later coalesce to form porous nanocages. We finally determine the amount of radiation damage making use of the quantitative phase images. We find that both, the total surface dose as well as the dose rate imparted by the X-ray beam trigger additional deposition of Au onto the nanocages. Our multimodal approach can benefit in-solution imaging of multi-material nanostructures in many related fields.

8.2 Introduction

In the chemistry of nanomaterials, the evolution of nanoparticle shape and morphology during the synthesis is equally important as the exposure of the most active crystallographic surfaces in the course of crystallization. This way, nanomaterials with an optimized shape and crystallinity can reach highest performance in catalytic applications, such as (photo)-electrochemical water splitting^{16, 267, 268} and CO₂ reduction.^{269, 270} Since the first discoveries of nanostructured materials,^{4, 6, 7} high-resolution transmission electron microscopy (HR-TEM) has been employed to make a connection between their shape and crystallinity.^{97, 271} Due to its unrivaled spatial resolution, HR-TEM soon uncovered the adaption of the outer shape of nanoparticles to the underlying crystal system, and the exposure of specific low-energy crystallographic planes at the particles' facets soon became evident.²⁷²⁻²⁷⁵ Later, the lattice orientation of individual nanocrystals could be visualized with electron diffraction.²⁷⁶⁻²⁷⁸ However, to gain rational control over a synthesis, in situ visualization of the shape and crystal structure of nanoparticles during formation and transformation processes is a decisive yet difficult task.

The applicability of electron microscopy for in situ monitoring is limited since the liquid environment of a chemical synthesis is often intransparent for electrons. Hard X-rays, on the other hand, can penetrate thick sample environments and are thus an ideal probe for in situ microscopy.²³⁷ To this end, X-ray ptychography is a versatile and convenient method. It is a scanning coherent imaging technique allowing to reconstruct transmission images of a sample from a series of small-angle diffraction patterns.^{77, 79-86} The phase images provide a strong contrast between materials with different densities, which makes the method especially powerful to follow the interactions and individual shape evolutions of different compounds in a multi-material nanostructure. When imaging ex situ with low scattering background, a spatial resolution of 10 nm can be reached.^{202, 241} In our previous work, we showed that hard X-ray ptychography is robust enough to image weakly scattering nanoparticles inside a liquid chemical reactor with a thickness of 1 mm, while still achieving a resolution of 66 nm (c.f. Section 7.3.1). Scanning wide-angle X-ray scattering (WAXS) in the nanofocused X-ray beam complements ptychography by imaging the crystallinity of the nanomaterial.²⁷⁹⁻²⁸³ This way, grain rotation and lattice deformation in AgBr crystals²⁸⁴ as well as the orientation of crystalline domains in a single CsPbBr_3 perovskite nanowire²⁸⁵ were visualized.

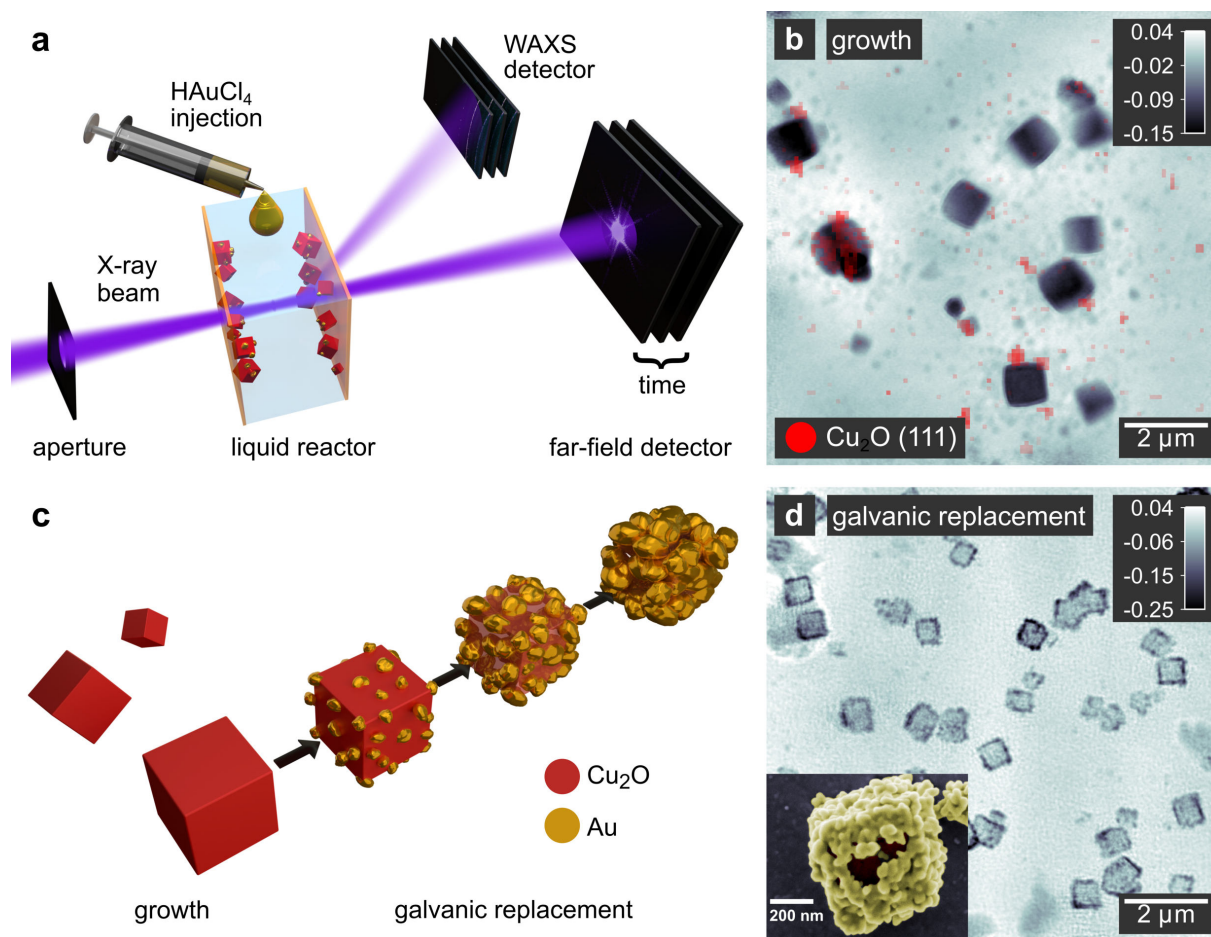


Figure 8.1. Outline of the multimodal in situ imaging experiment on $\text{Cu}_2\text{O}@\text{Au}$ nanocage. **a** Schematic illustration of the experimental setup showing a section of the in situ reactor for simplicity. The nanocubes grow on the inner walls of the reactor. **b** Ptychographic reconstruction of Cu_2O nanocubes growing inside the chemical reactor. The image is overlaid with the spatially resolved diffraction signal (in red), representing diffraction from the Cu_2O (111) crystallographic plane. **c** Illustration of the observed reaction pathway including the growth of Cu_2O nanocubes and their morphological transformation into gold nanocages during the galvanic replacement. **d** In situ ptychographic reconstruction of the nanocubes undergoing an electroless galvanic replacement reaction (GRR) with gold. The gray scale indicates the phase shift in radian. Inset: False-colored scanning electron microscopy (SEM) image of a partly replaced nanocube.

Here, we extend the capabilities of in-solution imaging by combining simultaneously hard X-ray ptychography with scanning nano WAXS during the solvothermal growth of cuprous oxide (Cu_2O) nanocubes (Figure 8.1a). We obtain highly spatially resolved crystallographic information directly overlaid with the morphological characterization in the ptychographic images, allowing us to identify the shape as well as the crystal structure and lattice orientation of a single nanocube in situ (Figure 8.1b). In a second step, we use the Cu_2O nanocubes as a template in a galvanic replacement reaction (GRR) with HAuCl_4 (Figure 8.1c). Galvanic replacement represents a versatile route to a variety of multi-material and hollow nanostructures.^{49, 286} In the case of metal oxide nanoparticles smaller than 100 nm, voids forming in the particle interior during the GRR were observed,^{250, 287} which were accounted to a pinhole corrosion mechanism upon dissolution of the core.^{47, 288, 289} In this study, we combine the material contrast of the ptychographic phase images with WAXS to spot isolated Au nanoparticles nucleating on the surface of the nanocubes while the Cu_2O core is oxidized and dissolves (Figure 8.1d). In the course of the GRR, we observe the Au nanoparticles growing and coalescing into nanocages. Furthermore, the projection images allow us to follow structural changes of the interior of the nanocubes with sizes up to 1 μm .

Finally, the phase shift in the ptychographic images allows to quantify the amount of material.²⁴³ This makes it possible to follow the progress of the chemical transformation, and at the same time to determine the occurrence of radiation damage. We find that the interaction with the X-ray beam triggers additional Au deposition compared to a GRR without exposure to X-rays. We show that a surface dose²⁵² of 2.1 MGy required for a single image does not cause visible radiation damage, however, as the dose of subsequent image acquisitions accumulates, radiation damage becomes significant. An experiment with a more intense X-ray beam shows that a dose rate higher than 18.1 MGy/s in the X-ray focus strongly amplifies the effect.

8.3 Results and Discussion

The reaction of copper(II) acetylacetonate (acac) with benzyl alcohol (BnOH) is a versatile route which enables the synthesis of different Cu and Cu_2O nanoparticle morphologies.^{108, 216} In our previous work, we used X-ray ptychography to follow the growth of Cu_2O nanocubes in a liquid reactor, demonstrating the applicability of X-ray microscopy for in situ observations of the growth of nanomaterials (c.f. Section 7.3). However, the questions about the crystallinity and the exposure of specific crystallographic facets at the surface of the nanocubes remained unanswered. To this end, we designed an advanced experiment and combine ptychographic imaging with simultaneous scanning WAXS. The ptychographic reconstructions can then be overlaid with the additional contrast, resulting in multimodal microscopic images. Here, using the same example of Cu_2O nanocubes, we show an extended microscopy experiment, following the crystallization and the orientation of the crystal lattice of an individual nanocube (Figure 8.2).

8.3.1 Linking crystallization and shape during growth of nanocubes

To synthesize Cu_2O nanocubes,^{136, 216} we fill the in situ reactor with precursor solution and heat it to 138°C for 19 h. Detailed information on the reactor can be found in Chapter 5, as well as in Supplementary Notes 8.1. The nanocubes have a strong affinity to the polyimide walls of the reactor (c.f. Section 7.3.2), thus most of them nucleate and grow on both windows. It takes 26 minutes to acquire a ptychographic image, but the particles remain immobilized at the polyimide even during a series of images.

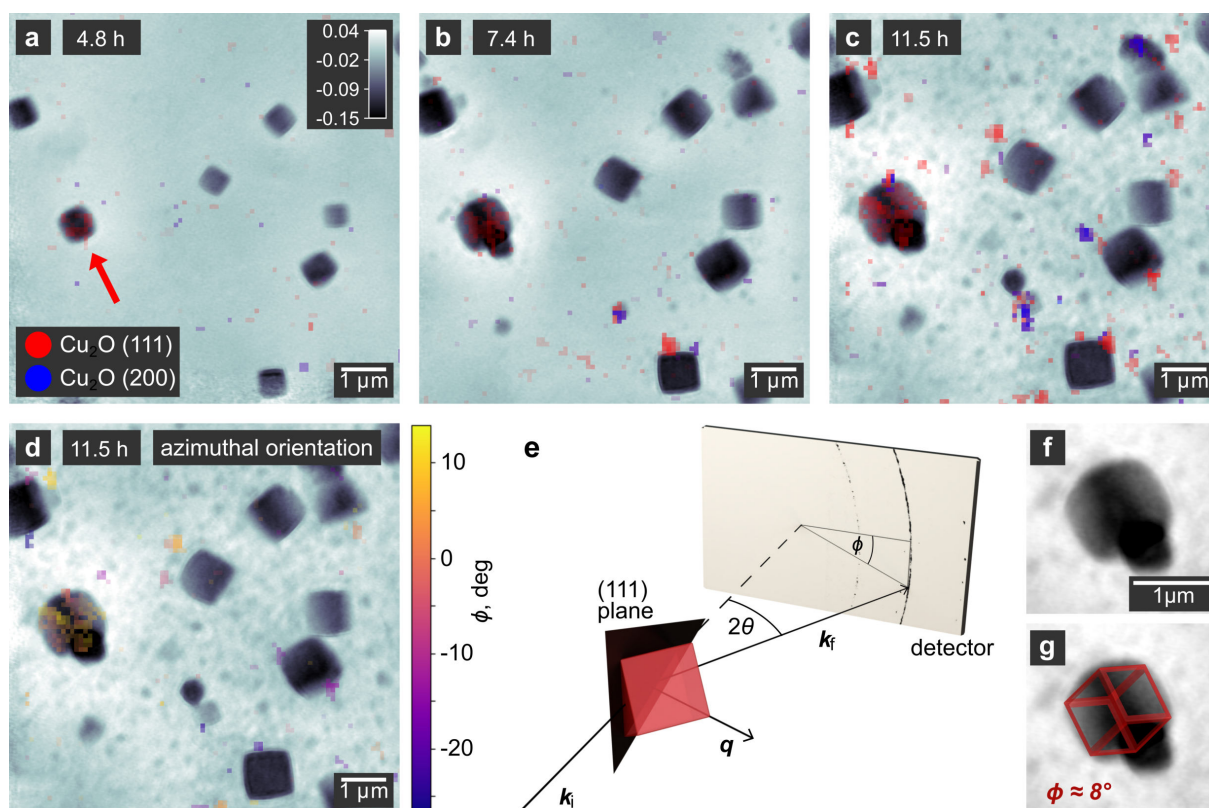


Figure 8.2. Crystallinity of growing Cu_2O nanocubes. **a-c** In situ ptychographic reconstructions during the growth of the Cu_2O nanocubes overlaid with the spatially resolved nano-diffraction signal. The crystallographic orientation is highlighted by color, whereas the gray scale indicates the phase shift of the object in radian as obtained by ptychography. While most of the single-crystalline nanocubes are oriented in a way not fulfilling the Bragg condition, the particle marked with an arrow diffracts at the (111) plane. **d** Same ptychographic reconstruction as in c, but here the overlay indicates the azimuthal orientation of the (111) crystallographic plane. The highlighted particle exhibits an azimuthal rotation of $\phi \approx 8^\circ$. **e** Schematic illustration of the single-particle diffraction geometry showing the incident beam k_i , the diffracted beam k_f and the scattering vector q . It allows to estimate the particle orientation from the position of its (111) reflection. The rotation angle around the normal of the crystallographic plane remains undefined. **f** Magnification of the nanocube highlighted in **a-d**. In **g**, this particle is shown together with a schematic cube representing one possible orientation determined from the diffraction experiment. The orientation of the cubic Cu_2O crystal lattice matches that of the cubic particle.

As the nanocubes grow on both the entrance and the exit windows of the reactor, an X-ray projection image would usually show contributions from these two layers of particles. However, ptychography allows to retrieve several phase images at different positions along the optical axis. This procedure is called multi-slicing,^{87, 91} and we use it to reconstruct separate images of nanocubes on the two windows.²³⁷ Due to a slow deformation of the window material, the distance between them decreased during the time series, which we took into account for the multi-sliced reconstructions (Supplementary Figure 8.2). The distance between the windows also results in a small offset of the scattering angle in the WAXS measurement for the two particle layers, which we use to generate separate WAXS intensity distributions from the two windows (for details, see Section 8.5 and Supplementary Figure 8.3).

Figure 8.2a-c show ptychographic images overlaid with spatially resolved WAXS distributions taken during the growth of the nanocubes. After 11.5 h, the nanocubes reach their final size. While the population of large particles just below 1 μm in size dominates, also smaller nanocubes are visible. Using Fourier ring correlations (FRC),^{217, 218} we find a spatial resolution of about 104 nm for the ptychographic images (Supplementary Figure 8.4). While the spatial resolution in ptychography is independent of the focus size, the latter defines the resolution of the scanning WAXS measurement. As

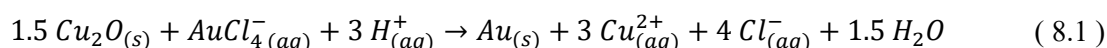
it can be seen from the beam profile in Supplementary Figure 8.5, only the exit window is positioned in the X-ray focus with a size of 135 nm horizontally by 207 nm vertically. Thus, only images taken on the exit window of the reactor have an optimal WAXS resolution.

We focus on the Cu₂O (111) and (100) reflections to study the lattice orientation of individual nanocubes in relation to their shape. The nanocube highlighted with a red arrow in Figure 8.2a exhibits the Cu₂O (111) reflection, confirming the formation of the expected crystal structure. At later growth stages, almost the entire area of this nanocube shows the same reflection, indicating that this nanocube is a single crystal. After 11.5 h (Figure 8.2c), the WAXS image even resembles the cubic shape of the particle visible in ptychography. No other nanocube in the field of view exhibits a clear reflection, thus indicating that none of them has the right orientation to fulfill the diffraction condition. This observation further supports the single-crystalline nature of the particles. In Figure 8.2c-d, we also observe WAXS signal without a corresponding nanocube in the ptychographic images, which we account to an incomplete separation of the WAXS signals from the entrance and exit windows (c.f. Supplementary Figure 8.3), as well as to particles dispersed in the solution.

The orientation of the scattering vector \mathbf{q} with respect to the incident X-ray beam \mathbf{k}_i has a polar component θ corresponding to the diffraction angle, and an azimuthal component ϕ (Figure 8.2e). Figure 8.2d shows the spatial distribution of the azimuthal component. Again, only the highlighted nanocube gives a diffraction signal which is consistent over its entire area. The nanocube has an azimuthal orientation of $\phi \approx 8^\circ$. Together with the known diffraction angle of $2\theta_{111} = 19.73^\circ$, we determine the orientation of the cubic Cu₂O crystal lattice and schematically overlay it with the outer shape of the nanocube (Figure 8.2f-g). Although the lattice orientation orthogonal to \mathbf{q} remains indefinite in this measurement, we find an orientation of the lattice matching the visible orientation of the cubic particle. We can thus conclude that during its entire growth, the nanocube exhibits (100) crystallographic planes at its surfaces.

8.3.2 Cu₂O@Au nanocages: Phase imaging differentiates materials and their respective morphologies

In a next step, we transform the as-prepared Cu₂O nanocubes in an electroless galvanic replacement process with HAuCl₄ into porous Au nanocages. The reaction follows Equation 8.1.²⁸⁹



In the case of polyhedrally shaped Cu₂O templates, previous studies found that corners and edges get covered with Au before the facets.²⁹⁰⁻²⁹² Also, Au preferentially adsorbes to (111) facets first before covering (100) facets in response to the difference in surface energy.²⁹³ However, in the case of cubic templates exhibiting only (100) facets, we can expect a uniform growth of the Au layer. Furthermore, the pH of the reaction medium has a strong effect on the morphology of the resulting Au layer.²⁹⁰ While an acidic medium increases the nucleation efficiency of Au and leads to a smooth layer, a less acidic pH favors particle-like and grainy Au deposition. In our case, to protect the Cu₂O from being etched during the imaging experiment, we use the reactants at neutral pH.

To start the replacement of Cu₂O with Au, we mount one window with nanocubes at the exit position of the reactor together with one empty window and pre-fill the reactor with water. We slowly dose the reaction solution into the reactor and image the gradual replacement during 10 h. The scanning electron microscopy (SEM) images in Figure 8.3 depict the changes in the particle morphology during the GRR. Even though the size of the nanocubes varies between these ex situ experiments, we observe the deposition of individual Au particles with different shapes on their surface. While after 5 h reaction time

(Figure 8.3b), the Cu_2O template underneath the Au deposition is still visible, we observe an Au nanocage with a hollow interior after 10 h (Figure 8.3c). At this stage, a continuous yet porous Au layer resembling the original cubic shape of the template has formed. The energy-dispersive X-ray spectroscopy (EDX) maps in the insets of Figure 8.3 confirm the gradual replacement of Cu_2O by Au. However, in the SEM images, the interior of the particles is not visible and the mechanism underlying the change of the internal shape remains unknown.

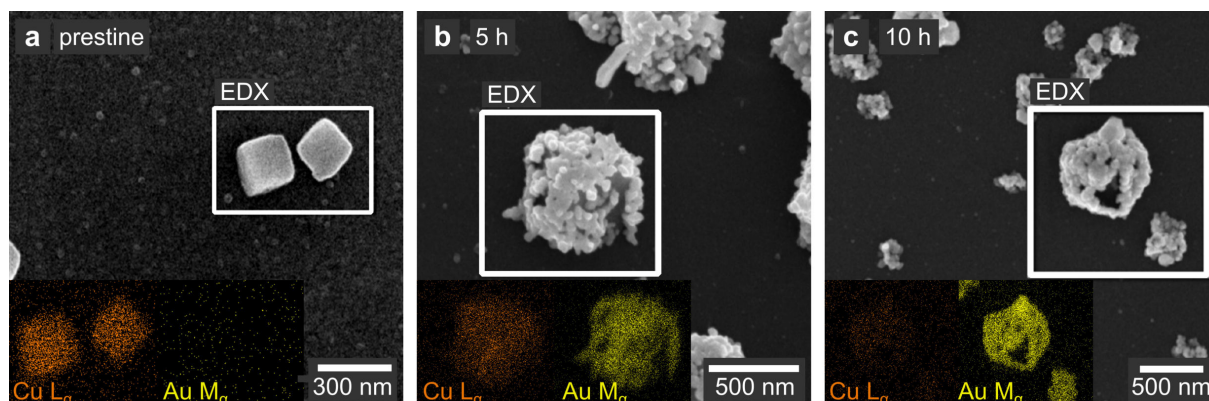


Figure 8.3. Ex situ study of the galvanic replacement of Cu_2O with Au. SEM images and corresponding EDX maps (insets) of **a** pristine and **b-c** Cu_2O nanocubes replaced with HAuCl_4 for 5 and 10 h, respectively. After 5 h (**b**), the GRR is still incomplete, with a grainy layer of Au particles growing at the surface of Cu_2O . After 10 h (**c**), the GRR is complete, yielding hollow Au nanocages.

To follow these structural changes during the process, we exploit the strong material contrast available in ptychographic phase images. Figure 8.4a-h shows an image series taken during the GRR. FRCs indicate a spatial resolution of 82 nm (Supplementary Figure 8.6). We can distinguish the first Au particles on the Cu_2O surface after 2.4 h. There, we observe individual particles on the facets parallel to the image plane, while in the projected view the particles appear as continuous lines along the facets perpendicular to the substrate. As the Au particles grow during the next hours, they start to coalesce and we can distinguish individual, larger Au particles after 3.4 h. The Au particles later form a porous layer covering the entire surface of the template. As exemplarily shown for one of these nanocages in Figure 8.4i, the size of that particle increased from about 625 nm to 1050 nm during the GRR. A similar multi-step Au growth mechanism was observed on silica spheres,²⁹⁴ as well as during the vacuum deposition of Au on polymer²⁹⁵ and silicon²⁹⁶ surfaces. With our experiment, it is feasible to confirm the mechanism in a more challenging liquid environment.

The reactants of the GRR are sensitive to the X-ray beam, thus, to minimize the beam damage we follow the growth of the Au layer with non-spatially resolved WAXS recorded out of focus (Figure 8.4j). For galvanic replacement on metal oxides, both toptactic⁴⁷ and randomly oriented growth^{291, 292, 297} of the shell material were previously observed. In our case the presence of multiple Au reflections indicates that unlike their Cu_2O template the newly formed Au particles have no preferred orientation.

In addition to monitoring the growth of the Au shell, the X-ray images enable us to follow the change of the interior of the nanocubes. Within the resolution of our method, we observe that the dissolution of the Cu_2O template occurs uniformly over the entire volume. The process is illustrated in Figure 8.4k.

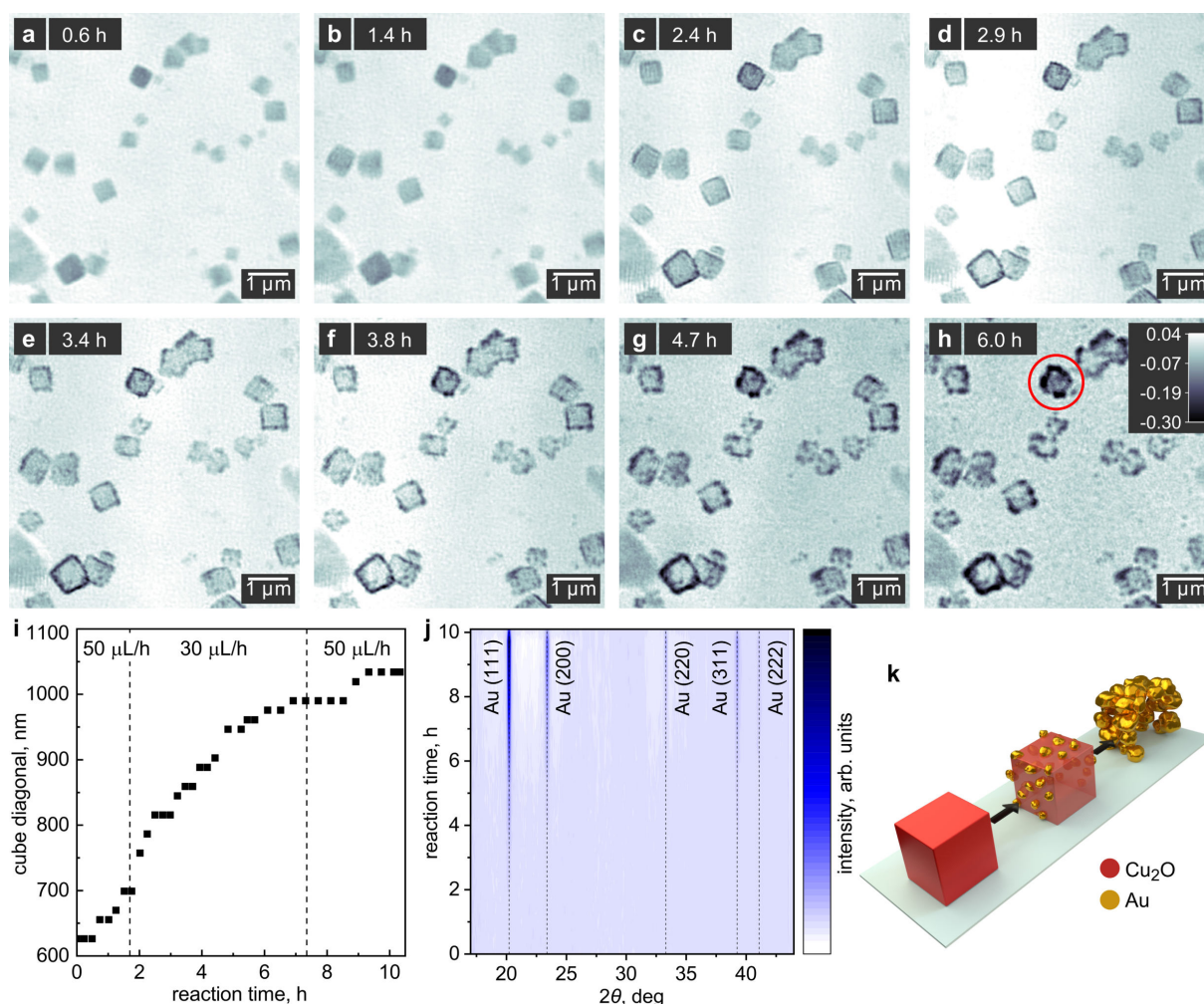


Figure 8.4. In situ ptychographic images of Au nanocage formation. **a-h** Ptychographic images reconstructed after different reaction times while dosing the HAuCl_4 precursor into the reactor. The gray scale indicates the phase shift in radian. **i** Size evolution of the nanocube highlighted with a red circle in **h**. **j** Time-resolved X-ray diffraction (XRD) patterns obtained alongside the ptychographic images. The reflections of Au become stronger as the replacement proceeds. We observe a significant increase in particle size as Au grains grow at its surface. **k** Illustration of the shape evolution during galvanic replacement. While the Cu_2O in the interior of the nanocages homogeneously dissolved upon oxidation, Au particles nucleate and grow at the surface resulting in porous Au nanocages.

8.3.3 Quantification of radiation damage by dose calculation and phase analysis

We observe that repetitive irradiation of the selected field of view leads to X-ray beam-induced deviations from the expected reaction pathway. During the growth as well as during the replacement, additional material deposited onto the substrate at late reaction times (Figure 8.2c-d and Figure 8.4g-h). We parametrize the apparent radiation damage by calculating the surface dose²⁵² imparted by the X-ray beam. Figure 8.5a-c present ptychographic images of GRR recorded under different experimental conditions. The cumulative doses delivered during these measurements are denoted in the lower parts of the images. Figure 8.5a shows a previously unexposed area of the reactor window 6.4 h after the start of the reaction, while the region in Figure 8.5b was continuously imaged over 6.4 h. Both images were recorded using an out-of-focus illumination (c.f. Supplementary Figure 8.7). We observe that a single ptychographic scan with a surface dose of 2.1 MGy (Figure 8.5a) does not cause visible alterations to the particles. In turn, a cumulative dose of 32.7 MGy in Figure 8.5b (for 26 images in total) already results in significantly greater accumulation of Au at the surface of the nanocubes as well as grainy

deposition on initially empty areas of the window (see Supplementary Notes 8.2, Supplementary Table 8.1 and Supplementary Figure 8.8 for experimental parameters and details on dose calculation).

To study the effect of dose rate, we imaged the GRR again with an in-focus illumination as shown in Figure 8.5c. We observe excessive formation of Au shells on the nanocubes and simultaneous Au deposition on the substrate. The effect is far greater than for the out-of-focus measurement in Figure 8.5b. In Figure 8.5c, different exposure settings and the use of an in-focus illumination yield a dose of 31.8 MGy per single image acquisition. We shifted the field of view by $3\ \mu\text{m}$ between subsequent images, resulting in 3 subregions (red dashed lines) with respectively decreasing cumulative dose. Although the rightmost subregion received a comparable cumulative dose to the out-of-focus measurement in Figure 8.5b, yet the particles in Figure 8.5c seem to suffer far more from radiation damage. This may be caused by the almost 50 times greater dose rate per scan point for the measurement in focus (Supplementary Table 8.1), resulting in respectively higher peak intensities that potentially lead to stronger deviations from the expected reaction pathway.

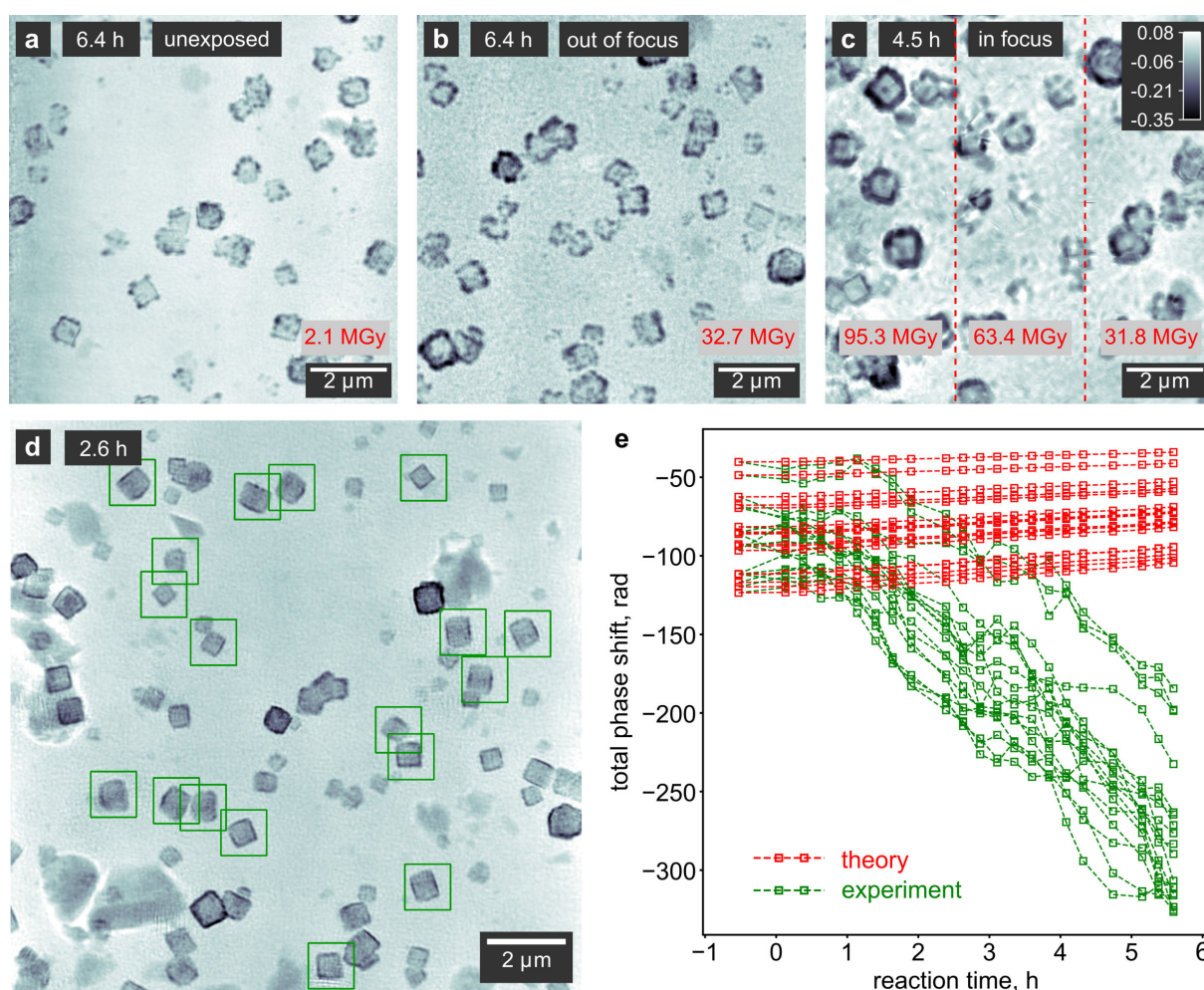


Figure 8.5. Quantification of radiation damage. **a-b** In situ ptychographic reconstructions during the GRR obtained at the same reaction time, showing **a** a region previously unexposed to X-rays and **b** a region continuously exposed for the preceding 6.4 h in the defocus of the X-ray beam. **c** Ptychographic reconstruction of a GRR exposed in the X-ray focus with a shifting field of view. The gray scale indicates the phase shift in radian. **d** Ptychographic reconstruction highlighting a number of areas around individual particles used for the quantitative phase analysis. **e** Expected evolution of the total phase shift of the particles (red) highlighted in **d**, assuming a full conversion from Cu_2O to Au, compared to the measured phase shift (green). We applied a moving average with a window size of 3 data points. A larger negative phase shift indicates more material.

Furthermore, to follow the additional Au deposition by radiation damage in a quantitative way, we select a number of individual particles in the ptychographic images (green rectangles in Figure 8.5d) and plot the total phase shift of each image area vs. reaction time (green data points in Figure 8.5e). We correct for a non-zero phase background by creating histograms of the pixel values in the selected areas. The main peak in the histograms corresponds to the average of the background and is offset to zero. Then, the initial per-particle phase shift of the pristine Cu₂O (first data points in Figure 8.5e) corresponds to nanocubes with an edge length between 300 and 450 nm. These values are in good agreement with the nanocube sizes visible in the images, confirming the robustness of our background subtraction method (for details, see Supplementary Notes 8.3 and Supplementary Figure 8.9-8.10). For each nanocube, we calculate the amount of Cu₂O from the phase shift before the start of the GRR using Equation 8.3. If we assume no radiation damage and a full conversion to Au according to Equation 8.1 at the end of the time series, we can calculate the expected phase shift of the particles in each image (red data points in Figure 8.5e). A comparison with the measured phase shift indicates that the beam causes a reduction of additional Au ions that deposit onto the Cu₂O cubes from approximately 1 h onwards. From Figure 8.4a-b we see that this corresponds to the time when the first visual changes to the nanocubes take place. We can thus conclude that the X-ray beam triggers additional Au deposition onto the nanocubes during the entire GRR. From the difference between the theoretical phase shift values and the measurements, we furthermore find an approximately 3-fold higher amount of Au in the nanocages at the end of the GRR compared to an unexposed reaction.

By imaging a partly unexposed and a partly exposed area within a single ptychographic scan (Supplementary Figure 8.11), it is possible to estimate the amount of Au that additionally deposits onto the substrate towards the end of the GRR. The phase difference between the unexposed and exposed areas of the image (green rectangles in Supplementary Figure 8.11a) indicates an average thickness of the beam-induced Au deposition of 42 nm.

From a chemical point of view the photolysis of the solvent H₂O is known to yield hydrogen peroxide (H₂O₂), molecular hydrogen (H₂) as well as highly reactive radical species including hydroxyl radicals (OH[•]), hydrogen radicals (H[•]) and solvated electrons (e⁻_{aq}).²⁹⁸ Considering the radiolytic yields at pH 7, the predominantly generated species are OH[•], e⁻_{aq} and to a smaller extent H[•].²⁹⁹ Both e⁻_{aq} and H[•] are powerful reducing agents which can reduce Au³⁺ ions present in the aqueous HAuCl₄ solution to elemental Au⁰.³⁰⁰ Under constant irradiation, we can assume that radical species are continuously formed during the experiment. In the absence of Au³⁺ ions radicals undergo back reactions to the molecular products H₂O₂ and H₂.²⁹⁸ As the Au³⁺ concentrations in the reaction solution steadily increases as a consequence of dosing the HAuCl₄ precursor into the reactor, it is plausible that a competition of the radical-induced side reaction to the galvanic replacement on Cu₂O occurs, causing the additional Au deposition.

8.4 Conclusion

We show that multimodal X-ray imaging combining ptychographic phase contrast microscopy with simultaneous scanning diffraction in the nanoprobe is a well-suited tool to observe the formation of nanomaterials directly at the synthesis level in a heated solution. We follow the single-crystalline nature of an individual Cu₂O nanocube throughout its growth, and we identify the orientation of the cubic crystal lattice. By comparing this to the visual orientation of the nanocube, we confirm the presence of (100) crystallographic planes at the nanocube facets. This simultaneous visualization and crystallographic analysis of an individual nanoparticle reflects in part the information accessible with HR-TEM, but measured in a bulk liquid environment. We then track the galvanic replacement of the

nanocubes with HAuCl₄, yielding Au nanoparticles with various shapes on the surface of Cu₂O. The phase contrast images allow to clearly distinguish the newly formed layer of Au particles from the interior of the nanocubes. As the Au particles continue to grow, they coalesce and eventually connect to form a porous nanocage. We could furthermore observe that for the nanocubes under study with sizes up to 1 μm, the dissolution of the interior occurs in a homogeneous way. During both, the growth and the GRR, the interaction with the X-ray beam caused the deposition of additional material within the field of view. At the end of the growth stage, small copper-based particles are visible in the background of the images, while during the GRR, reactive species triggered by the beam presumably lead to the additional reduction of Au³⁺ ions beyond the stoichiometry of the GRR. The excess gold deposited onto the nanocages throughout the entire reaction and again, at later stages, additional particles nucleated on the substrate. The phase analysis allows not only to detect but also to quantify the radiation damage based on the known stoichiometry. We observe an approximately 3-fold higher amount of Au in the nanocages when continuously exposed.

Our work underpins the importance of multimodal X-ray microscopy to the heterogeneous landscape of non-classical formation processes of nanostructures, where many transition pathways from amorphous to crystalline solids remain to be investigated.^{13, 22, 29, 301} In the future, X-ray fluorescence measurements can provide an additional contrast, enabling to track the composition of amorphous building blocks even before crystallization. Moreover, the progress of fourth generation synchrotron sources with improved coherence at high X-ray energies will allow for an improved spatial resolution and reduced radiation damage. This may reveal more complex morphological changes on size scales below 100 nm currently not accessible with in situ ptychography. The generality of our approach further encourages its application in related fields. Studying crystallographic and morphological changes during the lithiation and delithiation of lithium ion battery electrodes in an electrolyte^{75, 302} or the visualization of unwanted phase changes at the active surface of catalysts in an electrochemical device³⁰³ may benefit from multimodal in situ visualization.

8.5 Experimental section

Synthetic procedure

Chemicals: BnOH (>99.8%, anhydrous), Cu(acac)₂ (99.99%) and HAuCl₄·3H₂O (≥99.9% trace metal basis) were purchased from Sigma-Aldrich, and ethanol (absolute) for washing from VWR. Sodium hydroxide (≥99%) was supplied by Carl Roth. All chemicals were used without further purification.

Synthesis of Cu₂O nanocubes: 1.72 mL of BnOH was added to 0.03 mmol Cu(acac)₂ and stirred for 10 min in a glove box under argon atmosphere at room temperature. The solution was transferred to the in situ reactor, sealed, and heated to 138 °C at a rate of 4.5 °C/min. The reaction was stabilized at this temperature, without stirring, for a maximum of 19 h for in situ imaging. All mentioned reaction times are relative to the point when we start heating. For SEM imaging and EDX analysis, the reactor was cooled at a rate of 5.5 °C/min to room temperature. The polyimide windows were rinsed thoroughly with ethanol and dried at 60 °C overnight.

Galvanic replacement: Cu₂O nanocubes prepared in the in situ reactor were used as a starting material. To yield Cu₂O nanocubes with average edge lengths of 500 nm, the reaction time was decreased to 11 h, the amount of Cu(acac)₂ was increased to 0.0764 mmol and the volume of BnOH was reduced to 1.6 mL. Further reaction parameters correspond to the values previously described. An empty window was used in the entrance position of the reactor, while the exit window contained nanocubes. 1.4 mL Milli-Q ultrapure water with a resistivity of 18.2 MΩ·cm at 25 °C was filled into the reactor. At room temperature, a polypropylene cannula was inserted to dose a 20 mmolar HAuCl₄ solution with a syringe pump (PHD Ultra, Harvard Apparatus, USA). The pH of the injection solution was adjusted to 7 by

adding aqueous NaOH and verified with a pH meter (PH20, VWR, Germany). The injection was started at a rate of 50 $\mu\text{L}/\text{h}$. To achieve a close to uniform reaction speed in the un-stirred reactor, the injection rate was decreased to 30 μL after 1.9 h and re-increased to 50 $\mu\text{L}/\text{h}$ after 7.5 h. The reaction time is defined from the start of dosing. After 615 min, the reaction solution was removed to prevent further replacement and the polyimide windows were rinsed thoroughly with Milli-Q ultrapure water and ethanol.

Ex situ characterization

SEM and EDX: Images and maps were measured with a Gemini 1550 SEM (Zeiss, Germany) and an EDX detector Ultim Max 100 (Oxford Instruments, UK) at an acceleration voltage of 10 kV. Samples were coated with 18 nm titanium using a Precision Etching Coating System Model 682 (GATAN, United States) prior to SEM observation and EDX studies.

In situ reactor

We adopted the in situ reactor shown elsewhere (c.f. Chapter 5). Details about changes to the reactor design for the current study and a schematic are given in Supplementary Notes 8.1 and Supplementary Figure 8.1

X-ray ptychography and WAXS measurements

Beamline setup and data acquisition: Measurements were performed at the Ptychographic Nano-analytical Microscope PtyNAMi¹⁸⁴ at the nanoprobe endstation of beamline P06²⁶⁰ at PETRA III at DESY in Hamburg, Germany. Stacks of nanofocusing refractive lenses were used to focus the coherent X-ray beam with a photon energy of 15 keV. To collect small-angle scattering signal for ptychographic imaging, an Eiger X 4M (Dectris AG, Baden-Daettwil, Switzerland) area detector with a pixel size of 75 x 75 μm^2 was placed at the end of an evacuated flight tube 3.370 m behind the sample. The WAXS signal was collected using an Eiger X 500K (Dectris AG, Baden-Daettwil, Switzerland) area detector with the same pixel size. It was placed horizontally to the side of the reactor at a distance of 155 mm, with an angle of 40° between beam axis and detector normal. The resulting azimuthal (φ) and polar (2θ) angle coverages were -27° to 15° and 17° to 45°, respectively. To collect a multimodal data set containing coherent far-field diffraction patterns and spatially resolved WAXS data, the in situ reactor was raster scanned perpendicular to the beam with its exit window in the focus (Supplementary Figure 8.5). For imaging the growth of Cu_2O nanocubes, a field of view of 10 x 10 μm^2 with a step size of 100 nm was used with an exposure time of 0.15 s. Each scan took 26 min. For imaging the GRR, both windows were positioned in front of the focus (Supplementary Figure 8.7). The field of view was set to 15 x 15 μm^2 with a step size of 500 nm and an exposure time of 0.5 s, resulting in 15.5 min per scan. The scanning positions were randomly jittered by up to 50% of the step width to avoid artifacts arising from perfect regular sampling.

Dose calculation: For each ptychographic scan, the surface dose D imparted by the X-ray beam on the specimen was calculated as²⁵²

$$D = \mu' \Phi_0 E \quad (8.2)$$

where μ' is the mass absorption coefficient of the specimen, Φ_0 is the incident photon fluence, and E is the incident photon energy. Mass absorption coefficients were estimated based on the expected mechanism of the GRR, using the mixture rule³⁰⁴ and assuming a linear replacement of Cu_2O by Au according to Equation 8.1. The dose rate per scan point was calculated by substituting the incident fluence Φ_0 in Equation 8.2 with the incident fluence rate per scan point. It does not account for spatial overlap of adjacent scan points and refers to a momentary interaction of X-ray photons with a given region of the specimen within a single exposure. For details on the dose calculation, see Supplementary Notes 8.2.

Ptychographic image reconstruction: The diffraction patterns were cropped to 256 x 256 pixels, resulting in a pixel size in the reconstructed images of 14.51 nm. Image reconstruction was done with the extended ptychographic iterative engine (ePIE).⁸³ The object was initialized as non-absorbing and non-phase-shifting, and the initial probe was set as a Gaussian probe with a full width at half maximum (FWHM) of 1 μm and a phase curvature of 2.2 mm. The images shown in Figure 8.4-8.5 were reconstructed with a virtually enlarged probe.³⁰⁵ We applied multi-slicing to separately reconstruct images of the entrance and exit windows,²³⁷ using the Fresnel nearfield propagator²⁶³ for wave propagation between slices. The image slice corresponding to the entrance window was initialized first, and the exit window slice was activated after 20 iterations. From iteration 100, position refinement was performed every 20 iterations with a maximum displacement of 44 nm.⁸⁹ Reconstructions were run for 1000 iterations. The distance between the slices was initially set to 1 mm. When imaging the growth of nanocubes, it was gradually reduced to adapt to the shrinking distance between the windows of the in situ reactor (for details, see Supplementary Figure 8.2).

WAXS data analysis: The position of the WAXS detector was calibrated from a diffraction measurement of Au formed at the end of the GRR using the pyFAI package.¹⁷¹ Detector images were background-subtracted and azimuthally reshaped with pyFAI, transforming the image data into a cartesian coordinate system of 2θ and φ . Reflections were found by setting a lower threshold to the background-subtracted photon count. Polar-angle histograms of reflection counts showed two distinct peaks corresponding to the offset of the diffraction angle from the two windows (Supplementary Figure 8.3). By setting a threshold of $2\theta = 19.29^\circ$, the data was separated into sub-sets corresponding to either window. WAXS intensities were assigned to a re-binned raster with a pixel size of 100 nm to represent the expected resolution of the scanning experiment. To this end, refined positions from the ptychographic reconstructions were used. Finally, a logarithmic scale normalized to the maximum signal strength was applied for better visualization of the intensity evolution over the course of a reaction.

Image analysis

Fourier ring correlation: Diffraction patterns of one scan were separated into two data sets with equidistant scan points and reconstructed individually using the refined positions from the full data set. The FRC^{217, 218} was calculated from the resulting two images. To account for the lower resolution introduced by separating the data set, we estimated the resolution from the half-bit criterion.

Phase analysis and quantification of beam damage: To quantify the phase shift of a given image area, the background was corrected to a shift of 0 rad using a histogram of all pixel values in that area (see Supplementary Notes 8.3 and Supplementary Figure 8.9-8.10 for details.) The corrected phase shift ϕ_{corr} of an area containing a single particle was then used to calculate the amount of material as

$$n = -\frac{\phi_{\text{corr}}\lambda d^2\rho}{2\pi\delta} \quad (8.3)$$

where λ is the X-ray wavelength, d is the pixel size, ρ is the density of the material and $1 - \delta$ is the real part of the complex refractive index. We used the difference of the refractive index decrement between Cu₂O and Au, respectively, and the surrounding water resulting in⁶⁴

$$\delta_{\text{Cu}_2\text{O}} = 4.1217 \cdot 10^{-6} \text{ and}$$

$$\delta_{\text{Au}} = 1.2126 \cdot 10^{-5}.$$

8.6 Acknowledgements

This work was supported by the Bundesministerium für Bildung und Forschung (BMBF) within the Röntgen-Ångström-Cluster via the project 05K2020 - 2019-06104 XStereoVision (grant no. 05K20GUA), by the European Research Council within the project LINCHPIN (grant no. 818941), and by the Cluster of Excellence “CUI: Advanced Imaging of Matter” of the Deutsche Forschungsgemeinschaft (DFG) - EXC 2056 - project ID 390715994.

We thank Robert Schön for SEM and EDX measurements. Furthermore, we thank Ralph Döhrmann and Stephan Botta for supporting the X-ray measurements.

We acknowledge DESY (Hamburg, Germany), a member of the Helmholtz Association HGF, for the provision of experimental facilities. Parts of this research were carried out at PETRA III and we would like to thank Dr. Gerald Falkenberg and Dr. Jan Garrevoet for assistance in using beamline P06.

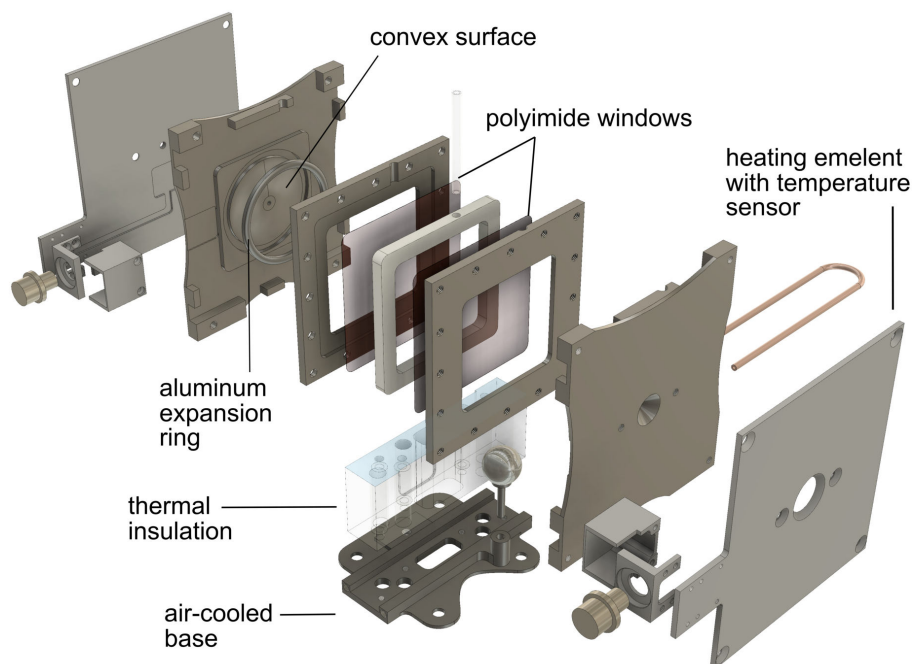
8.7 Author Contributions

D.K., C.G.S. and L.G. conceived the project. S.A.H., F.M. and L.G. prepared the synthetic procedure. L.G., M.S., L.A., S.A.H., K.M.S., O.V., D.B. and M.L. conducted the X-ray ptychography and WAXS experiments. S.A.H. conducted the SEM imaging and EDX measurements and analysed the images. L.G., K.M.S. and M.S. reconstructed the ptychographic images. L.A. analyzed the WAXS data and prepared the WAXS maps. K.M.S. and L.G. calculated the X-ray dose and conducted the phase quantification. All authors contributed to the data interpretation and to the preparation of the manuscript.

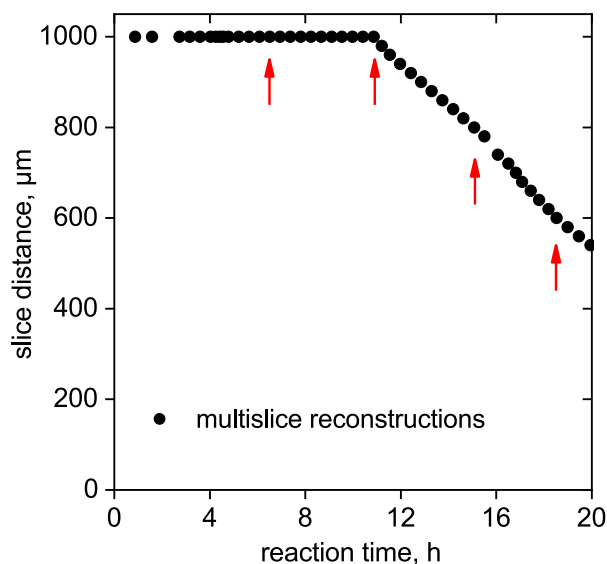
8.8 Supplementary Information

Supplementary Notes 8.1. In situ reactor

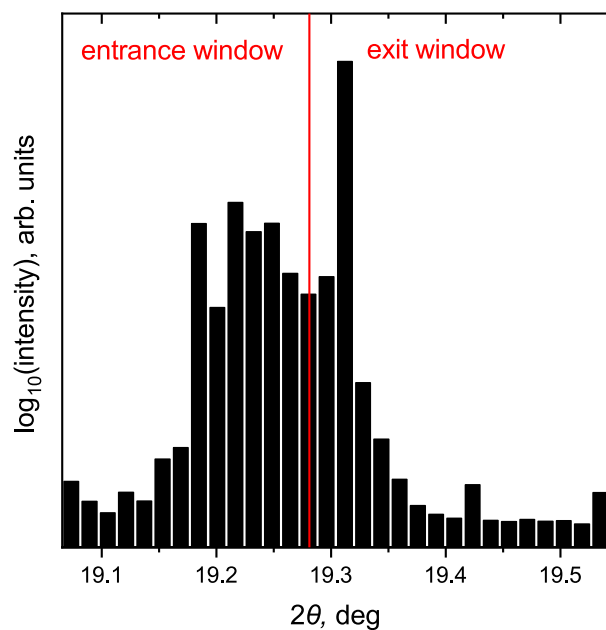
In the present study, we use a modified version of our in situ reactor employed in our previous experiment. Supplementary Figure 8.1 displays an exploded view of the reactor. A major improvement of the current setup comprises temperature sensors built into the heating elements. This way, the position of the temperature sensors is preserved when re-assembling the reactor, ensuring a steady heating characteristic. We furthermore place rings made from aluminum into the convex Invar plates that push onto the polyimide windows. Making use of the higher thermal expansion of aluminum, the rings have the purpose to stretch the polyimide windows when heated and thereby reduce deformation (c.f. Supplementary Figure 8.2).



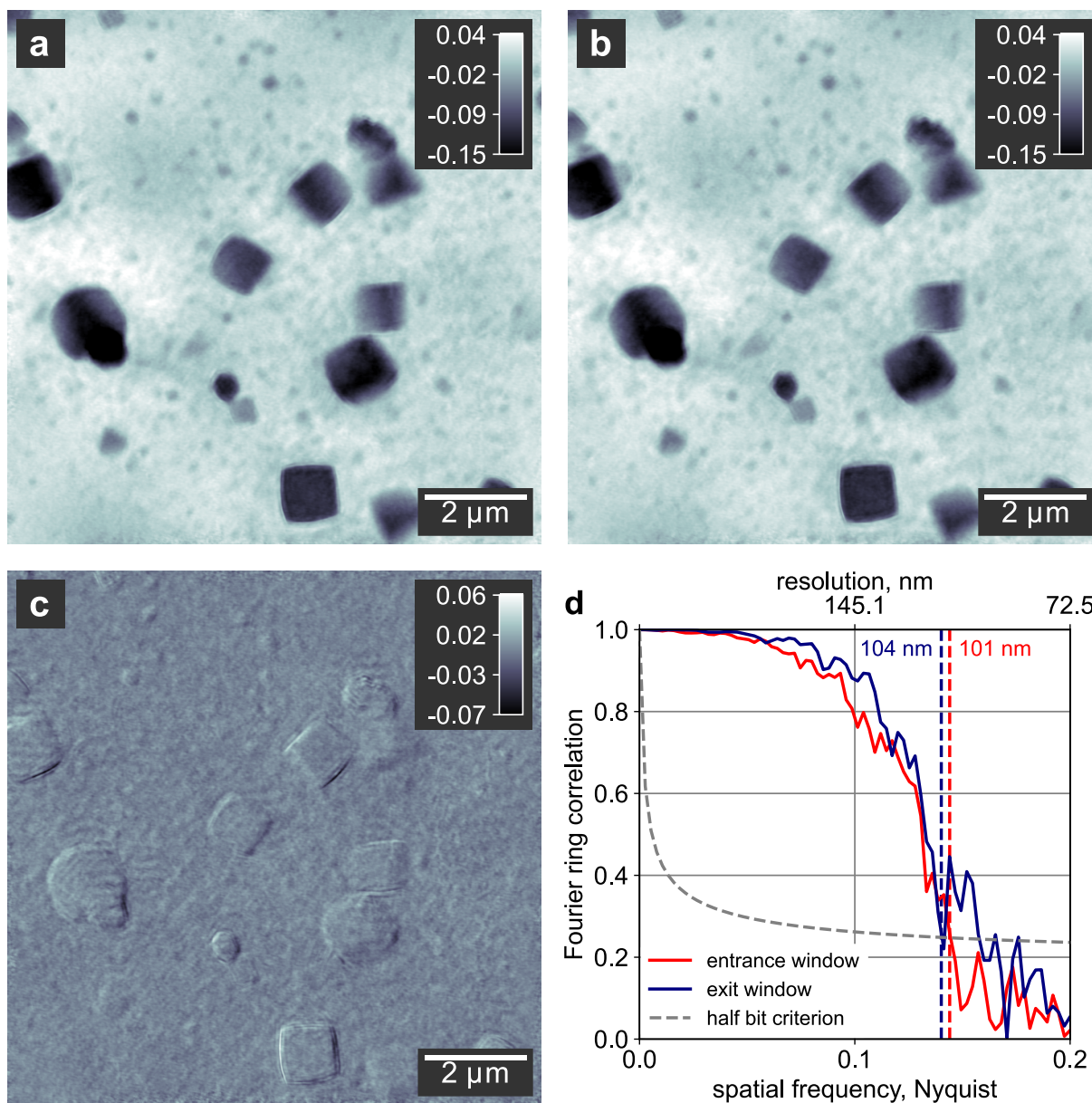
Supplementary Figure 8.1. Schematic illustration of the in situ reactor. A frame made of polytetrafluoroethylene (PTFE) is placed between two polyimide windows and held by two frames made of Invar. The force applied by screwing one of the Invar frames to the other seals the container. A glass capillary allows to fill the container with precursor solution. The container is placed between two Invar plates with a convex surface, reducing the distance between the windows to 1 mm at the center. An expansion ring made of aluminum stretches the polyimide windows when heated. Heat is provided by two flat panel resistive heaters with built-in temperature sensors. A thermal isolation made from Zerodur (Schott Ag, Mainz, Germany) is placed between the heated body and the air-cooled base.



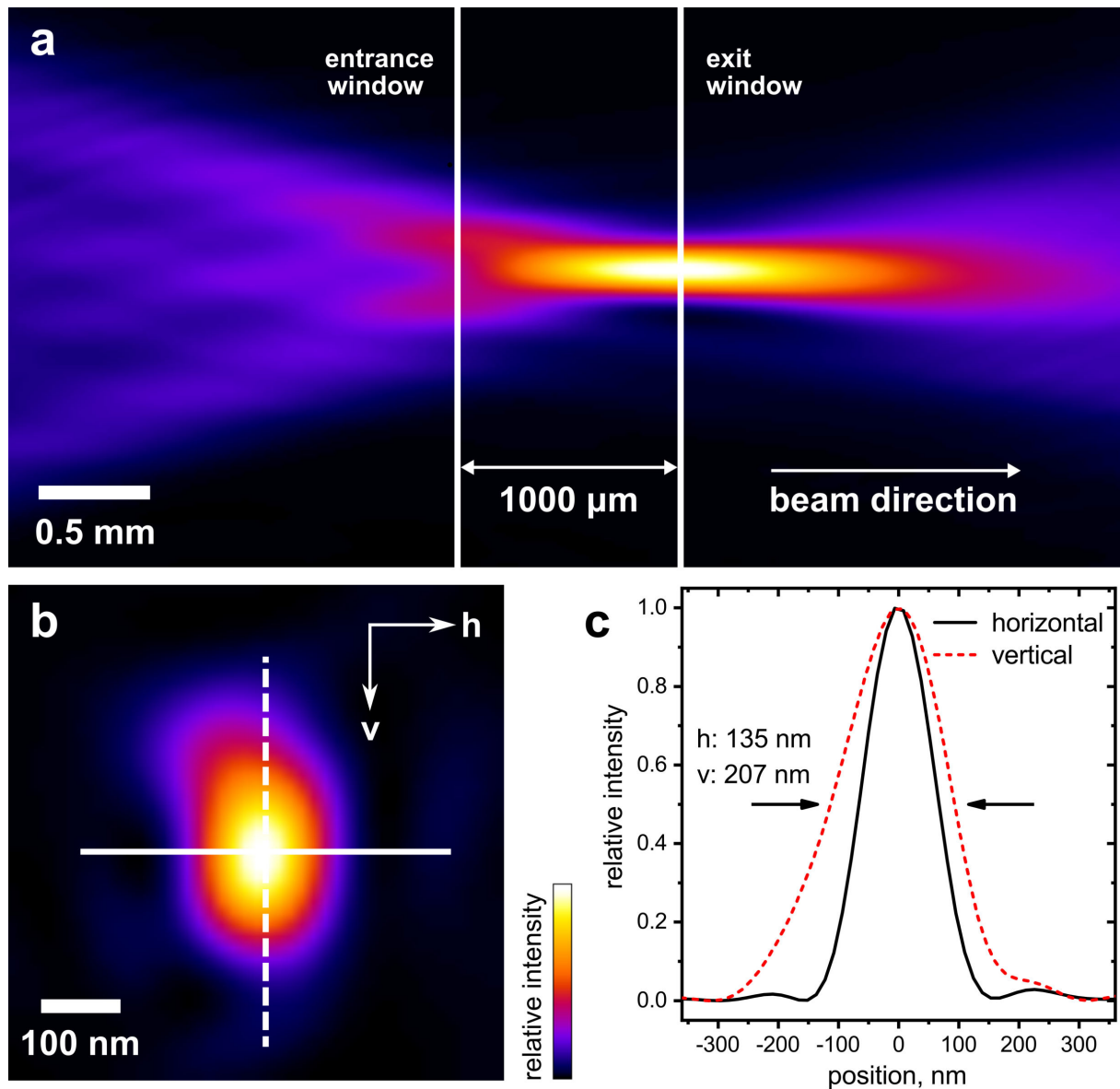
Supplementary Figure 8.2. Gradual decrease of the window distance. During the growth of Cu_2O nanocubes, the polyimide windows of the reactor slightly deformed, leading to a reduction of the distance between them. We already observed this effect in our previous experiments (c.f. Section 7.3.1). The use of aluminum expansion rings in the body of the reactor reduced the effect (c.f. Supplementary Notes 8.1). While in our previous experiment, the distance decreased below 400 μm after about 16 h reaction time, here the distance is significantly higher after the same time. We determine the distance by visual inspection of the multi-sliced ptychographic reconstructions, as a wrong setting of the slice distance results in reconstruction artefacts.



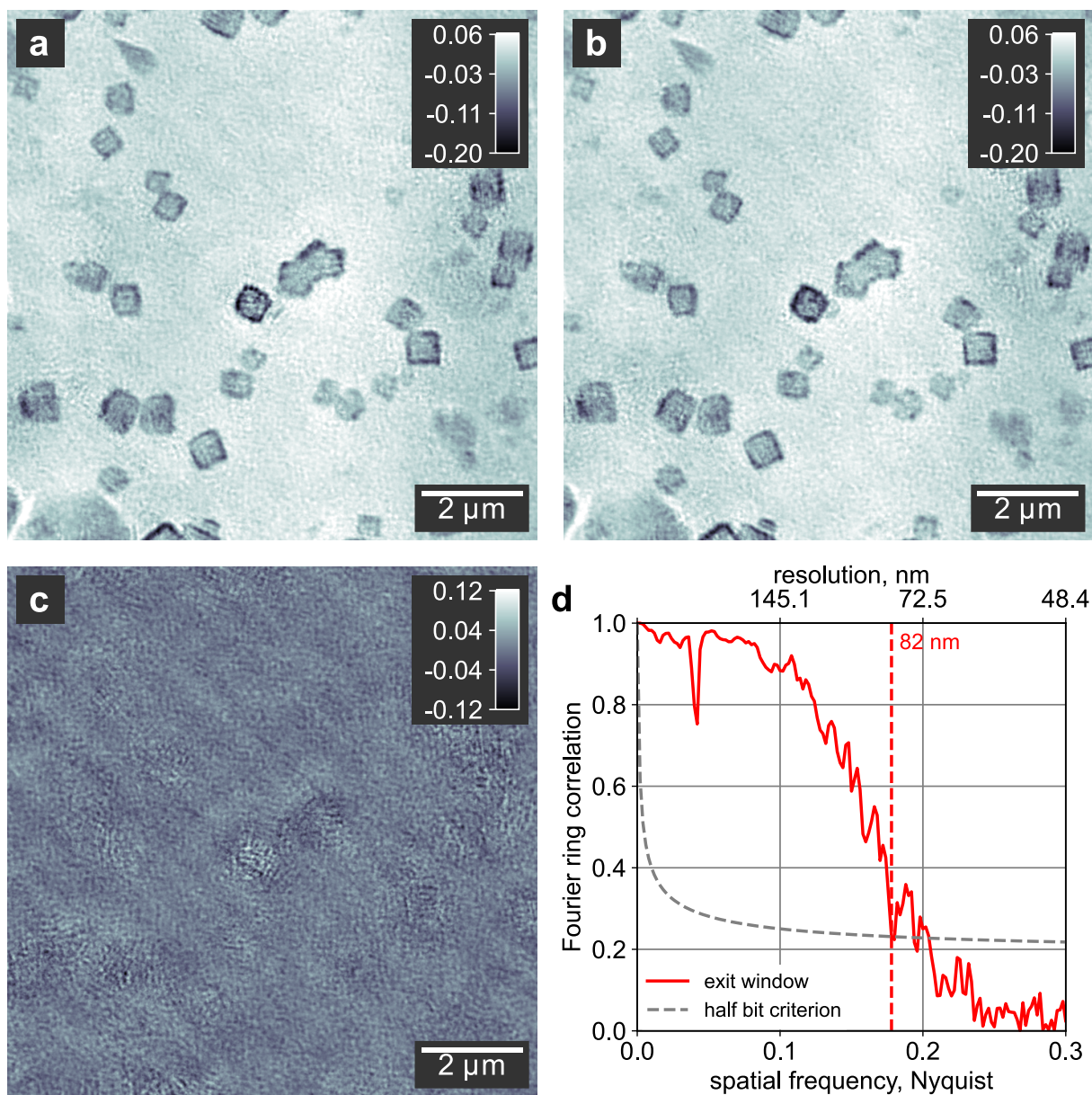
Supplementary Figure 8.3. Polar-angle histogram for WAXS separation. The histogram was obtained from all WAXS intensities of the Cu₂O (111) reflection measured during the growth of nanocubes. Two distinct peaks are visible in the distribution, corresponding to WAXS intensities from the two windows of the reactor. Since these two contributions are not fully separated, WAXS intensities from the respective other window still appear in Figure 8.2.



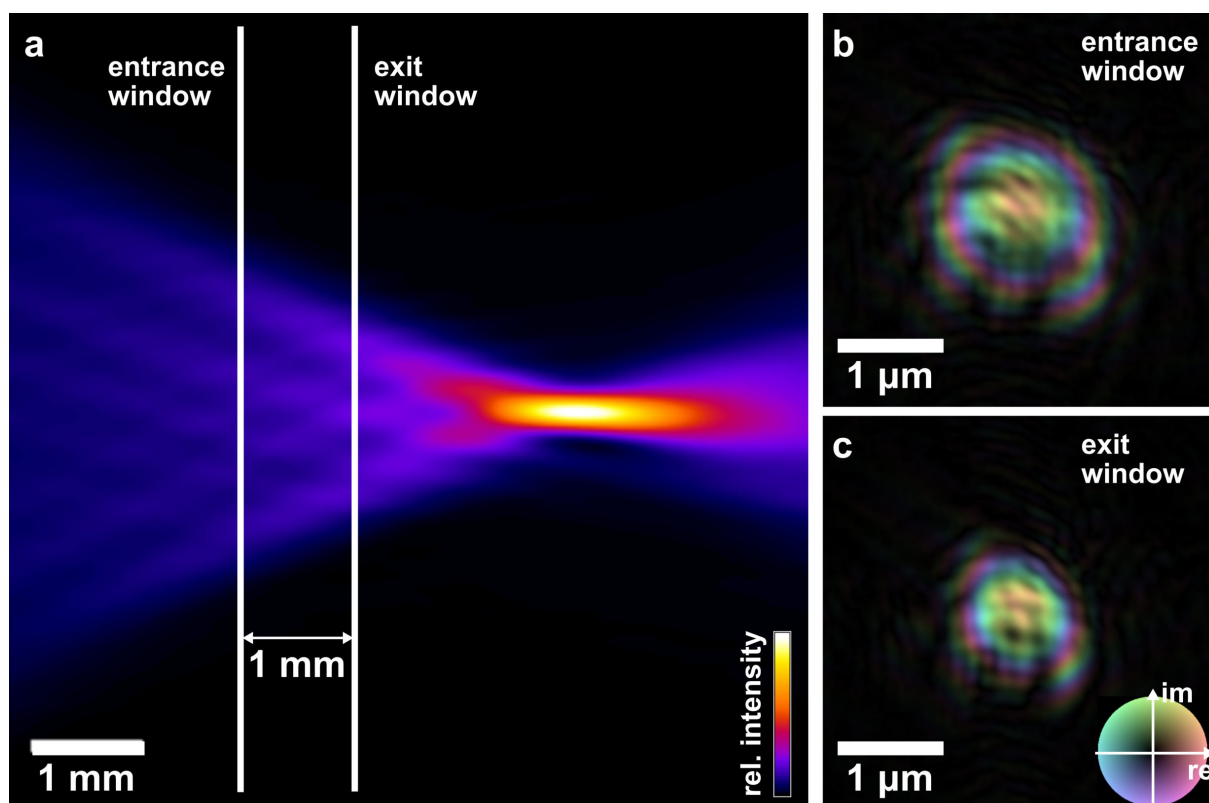
Supplementary Figure 8.4. Spatial resolution of images during nanocube growth. **a-b** Ptychographic reconstructions of Cu_2O nanocubes taken on the exit window of the reactor. Each image was reconstructed using one half of the scan points of the original data set. The gray scale indicates the phase shift in radians. **c** Difference of the images shown in **a-b**. **d** FRCs^{217, 218} of the images shown in **a-b** as well as of respective images taken on the entrance window of the reactor. Using the half-bit criterion, we find a spatial resolutions of 101 nm and 104 nm, respectively.



Supplementary Figure 8.5. Focus characterization and reactor placement for multimodal imaging. **a** Placement of the reactor windows along the caustic of the focused beam for imaging the growth of Cu_2O nanocubes with combined ptychography and WAXS. The figure shows the horizontal intensity profile. The exit window is placed in the focus. **b** Display of the intensity distribution in the focus. **c** Focus characterization on the exit window denoting the FWHM dimensions in horizontal (black) and vertical (red) directions.



Supplementary Figure 8.6. Spatial resolution of images during GRR. **a-b** Ptychographic reconstructions taken on the exit window of the reactor. Each image was reconstructed using one half of the scan points of the original data set. The gray scale indicates the phase shift in radians. **c** Difference of the images shown in **a-b**. **d** FRCs^{217, 218} of the images shown in **a-b**. Here, the half-bit criterion indicates a spatial resolutions of 82 nm.



Supplementary Figure 8.7. Illumination profiles and reactor placement for GRR. **a** Placement of the reactor windows along the caustic of the focused beam for imaging the GRR, displayed as the horizontal intensity. **b-c** Display of the illuminations on the entrance and exit windows, respectively. Brightness represents the amplitude and color represents the phase of the wavefield

Supplementary Notes 8.2. Quantification of surface dose

In this section we provide detailed information on how we obtained the physical quantities in Equation 8.2 required to calculate the surface dose and the surface dose rate of the multi-slicing ptychographic measurements reported in the main text.

Incident photon fluence

To determine the incident photon fluence Φ_0 , we first identified a scan point with no particles in the X-ray beam path and read out the total number of photons measured in the corresponding far-field diffraction pattern. We then derived the incident photon intensity by correcting the detected intensity for a cumulative X-ray transmission factor of all components of the experimental setup between the sample and the detector. For the reported experiment, the cumulative X-ray transmission factor at a photon energy of 15 keV equaled: 87.8% for the upstream sample slice (entrance window) and 95.5% for the downstream sample slice (exit window). Subsequently, we scaled the corresponding reconstructed illumination function with the previously obtained incident intensity (c.f. Supplementary Figure 8.7) and used the scan positions to generate a distribution map of photon intensity accumulated in the scanned area during the measurement. By dividing the total number of photons delivered to the measured region by its surface area, we obtained the incident photon fluence Φ_0 . In this way, we accounted for both the illumination size and the substantial overlap between adjacent scan points.

Incident photon fluence rate

The incident photon fluence rate per scan point was obtained by dividing the transmission-corrected photon intensity measured in the far-field detector by the illumination area (Supplementary Table 8.1). The illumination area was derived from the intensity distribution map of the respective illumination

function, counting all pixels above a threshold of 10% maximum intensity. In this way, we obtain a fluence rate per scan point unaffected by overlap between adjacent scan positions.

Supplementary Table 8.1. Detailed experimental parameters of ptychographic measurements shown in Figure 8.5a-c.

parameter	out of focus (Figure 8.5a,b)	in focus (Figure 8.5c)
incident photon energy	15.0 keV	15.0 keV
exposure time	0.5 s	0.2 s
scan step size	0.5 μm	0.1 μm
illumination area	1.05 μm ²	0.069 μm ²
flux per scan point	2.96 · 10 ⁷ photon/s	10.0 · 10 ⁷ photon/s
fluence rate per scan point	2.26 · 10 ⁷ photon/μm ² /s	108.7 · 10 ⁷ photon/μm ² /s
dose rate per scan point	0.38 MGy/s	18.13MGy/s

Mass absorption coefficient

For each ptychographic image acquired during the reaction time window, coefficients s_i of a stoichiometric mixture of Au _{s_{Au}} Cu _{s_{Cu}} O _{s_O} were calculated,⁵² according to the expected mechanism of the GRR (Equation 8.1). The total atomic mass A of the mixture is then given by:

$$A = \sum_i s_i \cdot A_i, \text{ for } i = \{\text{Au, Cu, O}\} \quad (8.4)$$

and respective weights w_i :

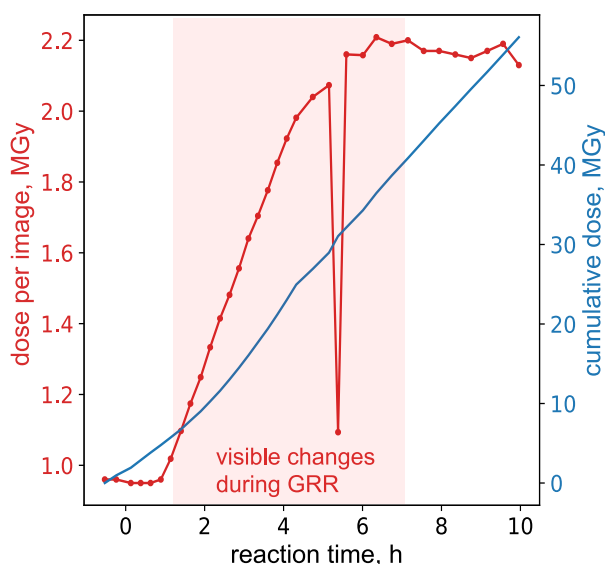
$$w_i = \frac{s_i A_i}{A} \quad (8.5)$$

where A_i is the atomic mass of the i th element constituting the mixture, $i = \{\text{Au, Cu, O}\}$. Subsequently, the weights were used to derive the mass absorption coefficient of the mixture μ'_{mix} :

$$\mu'_{mix} = \sum_i w_i \mu'_i \quad (8.6)$$

where μ'_i is the mass absorption coefficient of the i th element of the mixture.⁶⁴ With an assumption that Au linearly replaces Cu₂O, we utilized this method to calculate mass absorption coefficients for all ptychographic images exhibiting visible structural changes during the reaction. These values were then used to obtain respective surface doses imparted on the sample.

In Supplementary Figure 8.8, the red curve shows the time evolution of the surface dose delivered within a single projection to the imaged region of the out-of-focus measurement in Fig. 5b in the main text. The outlying point corresponds to a measurement acquired with respectively changed scan and exposure parameters. The dose increases as the replacement reaction progresses (area highlighted in red) due to a gradually changing mass absorption coefficient of the Au-decorated Cu₂O nanocubes. The blue curve in Supplementary Figure 8.8 shows in turn the cumulative surface dose delivered to the exposed region of the same measurement as a function of reaction time. The monotonic increase of the cumulative dose is modulated by changing composition of the sample during the replacement reaction.

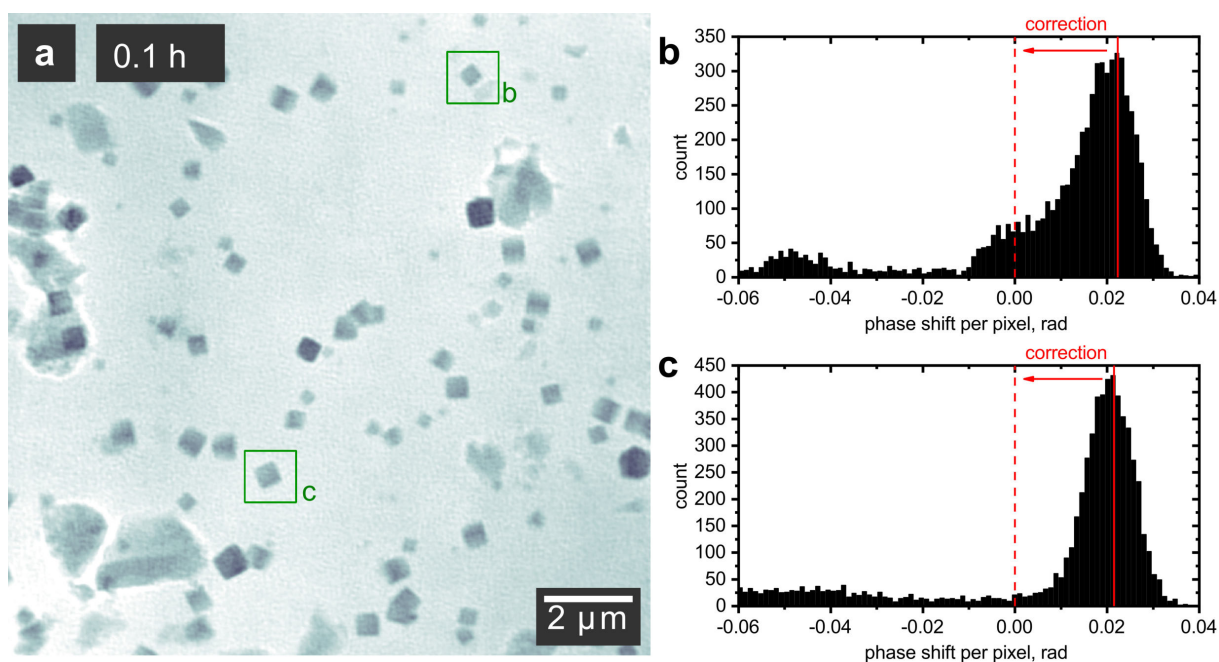


Supplementary Figure 8.8. Dose estimation for imaging the GRR. Surface dose²⁵² absorbed by the sample in the exposed region for each image acquisition (red) and cumulative surface dose (blue). The time frame of visible changes to the nanocubes is highlighted. The outlier in the surface dose values corresponds to the acquisition of an overview image with a shorter exposure and a different scan step size.

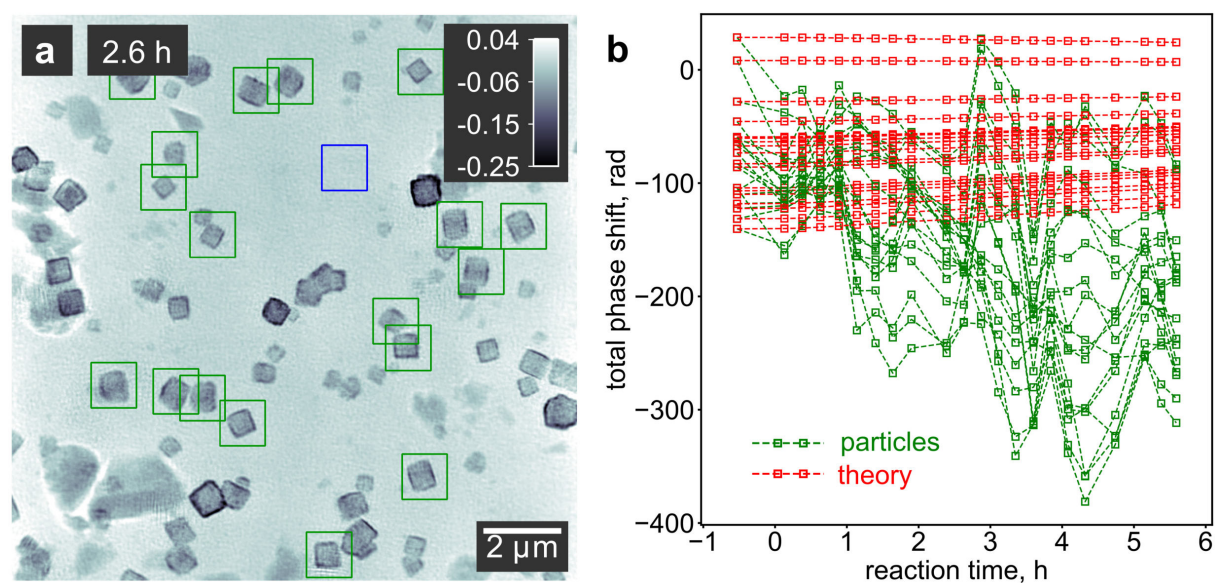
Supplementary Notes 8.3. Background correction for phase quantification

To be able to quantify the amount of Cu_2O contained within an isolated nanocube in a certain area of a ptychographic image, the phase shift of the background must average to zero. For the in situ images, this is however not always the case. We thus correct for the phase background by creating histograms of all pixel values in the selected image area (Supplementary Figure 8.9.). The histograms typically show one main peak corresponding to the background. We identify the maximum of this peak and apply a phase offset to the image area, shifting the maximum to zero.

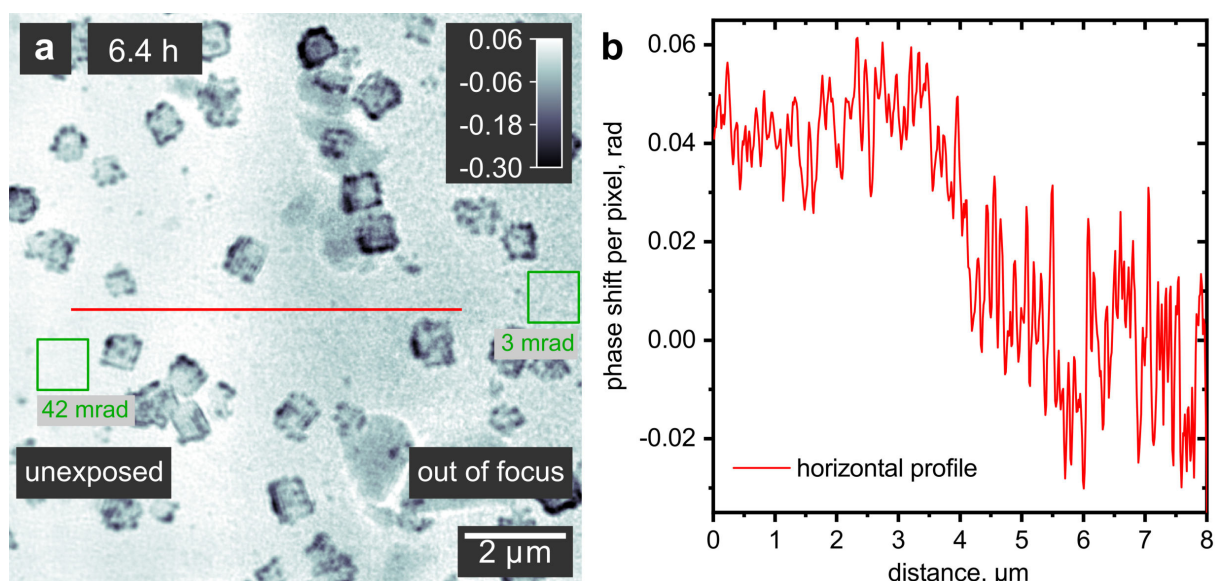
An alternative to this approach would be to select an empty area within the background of an image and subtract the average phase shift of this background from the any image area with a particle. However, this method is not as robust due to the occurrence of non-flat phase backgrounds over the entire image area (phase wedges). Supplementary Figure 8.10. shows a phase analysis of the same particles as selected in Figure 8.5 but using the average background phase shift within the area highlighted in blue for background correction. While we can observe the same trends in Supplementary Figure 8.10.b and Figure 8.5e, the phase analysis using the background subtraction method is less stable.



Supplementary Figure 8.9. Phase background correction. **a** Ptychographic reconstruction of Cu_2O nanocubes before the start of the GRR. **b-c** Histograms of pixel values obtained from the respectively highlighted areas in **a**. Red solid lines mark the maximum of the distribution which is shifted to zero by applying a phase offset.



Supplementary Figure 8.10. Phase analysis with background subtraction method. **a** Ptychographic reconstruction highlighting a number of areas around individual particles used for the quantitative phase analysis. **b** Expected evolution of the total phase shift of the particles (red) highlighted in **a**, assuming a full conversion from Cu_2O to Au , compared to the measured phase shift (green). In contrast to Figure 8.5e, here the measured values were background corrected by subtracting the average phase shift in the area highlighted in blue in **a**. We applied a moving average with a window size of 3 data points.



Supplementary Figure 8.11. Beam-induced Au deposition. **a** Ptychographic reconstruction after 6.4 h of GRR. The left part of the image covers a previously unexposed area, while the right part shows an area continuously exposed during out-of-focus imaging for the entire reaction time. The average phase shift of the two areas highlighted in green is denoted in the image. **b** Phase shift profile along the red line in **a**.

8.9 Imaging the formation of CuPd alloy nanospheres

The synthesis of CuPd nanospheres as well as SEM and EDX imaging were carried out by Federica Mancini. My contribution to this section comprises the acquisition and reconstruction of the ptychographic images.

The solvothermal route in benzyl alcohol,¹³⁶ which we used to synthesize Cu₂O nanocubes (c.f. Section 8.3.1), does not only yield metal oxides, but also metal and alloy nanoparticles.^{306,307} Understanding the formation of alloys is important to tailor their composition and morphology for catalytic applications.³⁰⁸⁻³¹⁰ Due to the strong material contrast of X-ray images, our multimodal imaging approach is a promising way to elucidate the formation mechanism of alloy nanoparticles. If an inhomogeneous distribution of metals is present at an intermediate reaction stage, we should be able to track it with in situ imaging.

We synthesize bimetallic CuPd alloy nanospheres from Cu(acac)₂ and Pd(acac)₂ in BnOH. The molar ratio of the metal precursors is 1:1. Additionally, oleic acid is required as a surfactant to achieve uniform spherical particles. Figure 8.6a shows an SEM image of the CuPd nanospheres on the polyimide substrate. We observe two populations of particles at the end of the reaction. The larger nanospheres reach an average size of 760 nm, while the smaller particles have an average size of 200 nm. The EDX image in Figure 8.6b confirms that the two metals are homogeneously distributed within the nanospheres. We find a molar ratio of 71% Cu and 29% Pd.

In a previous time-resolved powder X-ray diffraction (PXRD) and EDX study of a similar synthesis using Pd(II) acetate instead of acetylacetonate and no oleic acid, it became evident that the reduction of the two metal precursors is not a simultaneous process. At early reaction stages, two different alloys formed, one with high Pd content and another one with high Cu content. As the reaction progressed, the two materials transformed into an alloy with equal contents of Pd and Cu.³⁰⁶ We aim to investigate whether our CuPd nanosphere synthesis also follows these consecutive steps. To this end, we visualize the formation via X-ray ptychography combined with scanning WAXS.

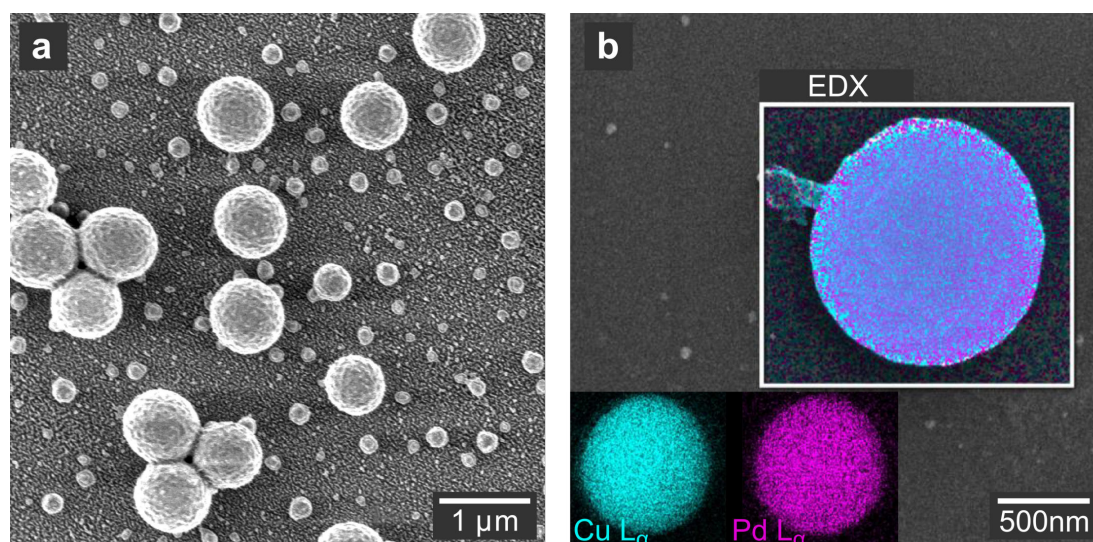


Figure 8.6. **a** SEM image of CuPd nanospheres at the end of the reaction. **b** Elemental distribution of Cu and Pd within a single nanosphere imaged with EDX.

Figure 8.7 shows a series of ptychographic in situ images of the CuPd nanosphere synthesis. We observe that already after 1 h reaction time, a population of small nanospheres is present on the polyimide reactor window and their size does not change visibly during the rest of the reaction. Thermal drifts during the initial heating of the reactor did not allow to acquire images at earlier reaction times. Furthermore, it is visible that the number of small particles decreases towards the end of the reaction, presumably due to detachment from the substrate. The population of large nanospheres exhibits a different behavior. While only one large nanosphere is visible after 1 h, more particles successively attach to the reactor window at later times.

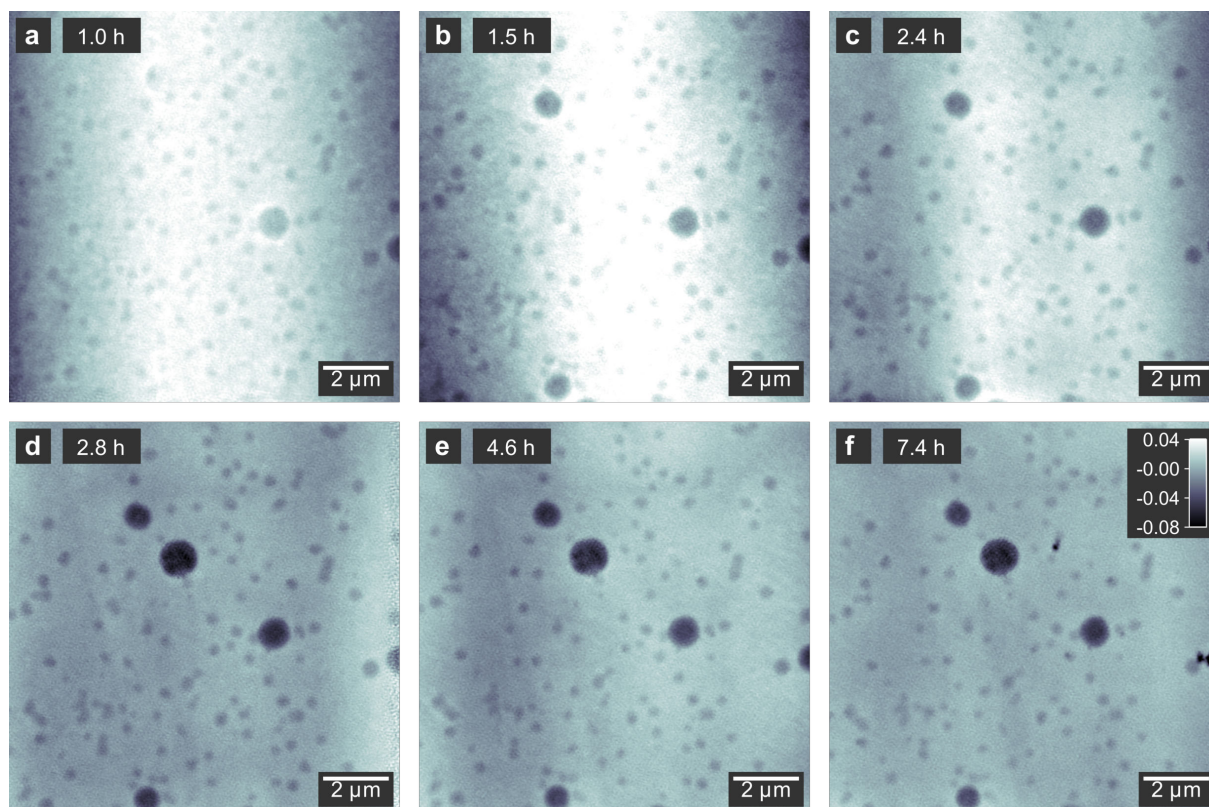


Figure 8.7. **a-f** Ptychographic reconstructions of CuPd nanospheres attached to the entrance window of the in situ reactor. The gray scale indicates the phase shift in radian.

We can hypothesize that the small particles nucleate heterogeneously on the window, while the large ones nucleate homogeneously in the solution and attach to the window as they diffuse through the liquid. Similarly, we identified populations of heterogeneously and homogeneously nucleating Cu₂O nanocubes of different thicknesses in Section 7.3.3. However, the nanospheres do not grow further once they are visible in the images. We do not observe contrast changes that would indicate an evolution of the alloy composition throughout the reaction. Either no inhomogeneities in the alloy composition are present after 1 h reaction time, or they occur on length scales below the current spatial resolution of our method. Moreover, we were not able to collect a meaningful WAXS signal. This could indicate a high degree of polycrystallinity with small crystalline domains, which may have led to weak reflections below the sensitivity of our measurement.

This reaction requires a higher spatial resolution in ptychographic imaging to investigate the possibility of inhomogeneities in the alloy composition at a smaller length scale. Additionally, in a future experiment, the initial thermal expansion of the reactor needs to be reduced to enable imaging at earlier reaction times. This way, it could be possible to arrive at a more detailed conclusion on the formation mechanism of the CuPd alloy nanospheres.

Experimental details

The following experimental details for the synthesis and ptychographic imaging of CuPd nanospheres were different from those described in Section 8.5.

Synthesis: BnOH (>99.8%, anhydrous, Aldrich), Cu(acac)₂ (99.99%, Aldrich), Pd(acac)₂ (99%, Aldrich) and oleic acid (99%, TCI) were used without further purification. Cu(acac)₂ (0,0058 g) and Pd(acac)₂ (0,0029 g) were mixed with BnOH (3.5 mL) and oleic acid (206 μL) in a 4 mL borosilicate glass vial (Labsolute, Th Geyer) inside a glove box under argon atmosphere. The vial was sealed with a screw cap and the solution was stirred for 10 min. 1.72 mL of the solution were transferred to the in situ reactor, sealed, and heated to 110 °C at a rate of 5.5 °C/min. The reaction was stabilized at this temperature for 8 h for in situ imaging. The reactor was cooled to room temperature at a rate of 4.50 °C min⁻¹ and the polyimide windows were rinsed thoroughly with ethanol.

Acquisition of ptychographic data sets: Data sets were recorded in continuous scan mode at a speed of 1 μm/s and an exposure time of 0.1 s.

9 Conclusion and outlook

The X-ray methods utilized in different in situ experiments throughout this thesis are summarized in Figure 9.1. In the study on CoO nanoassemblies (Chapter 4), we combined X-ray spectroscopy and scattering methods to reveal the nonclassical growth and assembly pathway. Each of the analytical techniques elucidated a different aspect of the chemical synthesis. HERFD-XANES in combination with FEFF simulations allowed to follow the rearrangement of the organometallic precursor complex upon chemical reduction of the Co^{3+} precursor. PDFs revealed the lengthening of the Co-O bond during this rearrangement and during the formation of crystalline building-blocks. In the end, SAXS showed that smallest CoO nuclei of 3 nm assembled into superstructures of 20 nm. Crystallization and assembly of building blocks were concomitant processes. There, we concluded that only the combination of analytical methods can bridge the length scales from the atomic level of amorphous precursors to the mesoscopic level of nanoassemblies. Putting together complementary pieces of information enabled to follow all steps of a nonclassical nucleation and growth process. However, one noticeable limitation of SAXS is the fact that we don't visually see what is going on inside the reactor, but instead we must rely on model-based data interpretation.

We could overcome this limitation with in situ X-ray microscopy, which complements the analytical measurements with direct visualizations on the nanoscale. Multi-slicing X-ray ptychography turned out to be a key requirement for imaging inside the newly developed in situ reactor (Chapters 5-6). It allowed

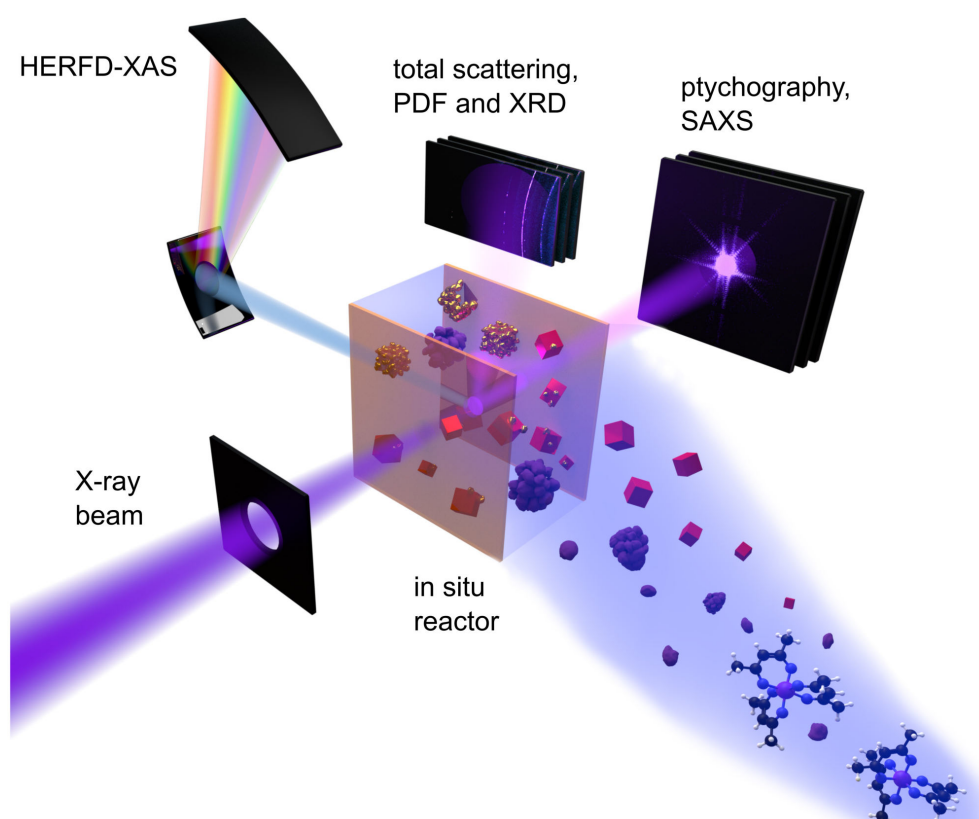


Figure 9.1. Illustration of X-ray analytical and microscopy methods utilized in different in situ experiments on the growth and transformation of nanomaterials in solution.

to separately reconstruct layers of nanoparticles growing on the entrance and exit windows of the reactor at a distance of 1 mm. Reconstructions without multi-slicing would furthermore have reduced the lateral spatial resolution, since the window distance was not lower than the DOF. An in situ imaging experiment on the growth and hollowing of substrate-bound Cu_2O nanocuboids proved the applicability of X-ray ptychography in a heated solution (Chapter 7). The image series at a best achieved resolution of 66 nm and a time resolution of 21.6 min allowed to follow the growth and hollowing of the nanocubes. The measurements furthermore showed that the mechanical and thermal stability of the in situ reactor was sufficient for reproducible in-solution imaging during 20.5 h. The quantitative relation between the reconstructed phase shift and the thickness of Cu_2O enabled modelling the 3D shape of the particles and revealed that the substrate-based growth yielded flat nanocuboids.

Combining in situ ptychographic imaging with complementary XRD contrast using scanning microscopy (Chapter 8) unveiled the crystallographic orientation of a single Cu_2O nanocuboid during growth. The nanocuboid exhibited (100) crystallographic planes at its facets. Moreover, the strong density contrast in X-ray imaging allowed to follow the growth of porous gold shells on the surface of Cu_2O nanocuboids during galvanic replacement. At the same time, the Cu_2O template dissolved in a homogeneous way. We concluded that in situ visualizations featuring crystallographic and material contrasts are key to better understand the morphology-defining mechanisms underlying the emergence of multi-material nanostructures.

We discussed TEM as a complementary method in the field of in situ microscopy (c.f. Section 7.2). The unique penetration power of X-rays makes X-ray microscopy applicable to a much wider range of material systems and sample geometries compared to TEM. It will potentially enable visualizations of nanomaterials under operando conditions, for example in electrochemical devices. Still, the time and spatial resolution achieved with X-ray ptychography is at least one order of magnitude below that of electron micrographs. Further efforts regarding the resolution and imaging speed are required to unlock the full potential of X-ray ptychography for in situ studies in materials science. Increasing the spatial and time resolution in X-ray microscopy certainly is one of the long-sought goals that we expect to reach with fourth generation synchrotron sources. The diffraction limited storage rings feature an increased coherent flux and consequently, they allow for either a faster image acquisition, or a higher photon dose leading to an increased spatial resolution.

However, making full use of the high coherent flux at fourth generation sources cannot be successful without taking radiation damage into account. Both during the hollowing of Cu_2O nanocubes and during their galvanic replacement with gold, interactions between the X-ray beam and the reaction solution induced deviations from the expected synthesis pathway. To cope with the problem of radiation damage, utilizing near-field ptychography is a promising option. The larger illumination that comes with this method allows to use less scanning steps and thus to record a ptychogram in a shorter time. At the same time, the incident X-ray dose is distributed over a much larger area compared to the far-field experiments presented in this thesis. This leads to a reduction of the dose rate which is a key factor for the occurrence of radiation damage (c.f. Section 8.3.3). Moreover, the coherence at higher photon energies available at fourth generation sources and the use of radical scavenging chemicals can potentially help to further reduce radiation damage.

There is still a step to take from imaging of substrate-bound, immobilized nanoparticles to imaging of free-floating nanoparticles in dispersion. To this end, much faster imaging at the time scale of Brownian motion of nanoparticles is required. The short and intense pulses available at X-ray free electron lasers are a promising option for sufficiently fast imaging. A single-shot, full-field imaging method like inline holography can freeze any particle motion.

Imaging the 3D morphology of nanomaterials without the need to rotate the bulky sample environment is a further goal for future experiments. In the present work, we were able to model the 3D shape of Cu_2O nanocuboids (c.f. Section 7.3.3) by making use of a priori knowledge on their composition and orientation. However, 3D imaging of nanomaterials in the general case requires a significant increase in depth resolution, ideally down to the particle size. We can expect a leap in depth resolution from the recently initiated project XStereoVision within the Röntgen-Ångström-cluster. At beamline P06 at PETRA III, an X-ray microscope using two focused nano-beams incident on the sample under different angles is developed. The stereoscopic effect resulting from the two inclined beams substantially increases the effective depth resolution compared to the present experiments with a single beam. It may finally lead to imaging experiments providing the 3D morphology of nanomaterials under in situ conditions.

Bibliography

1. Faraday, M. X. The Bakerian Lecture. - Experimental relations of gold (and other metals) to light. *Phil. Trans. R. Soc.* **147**, 145–181 (1857).
2. Leite, E. R. & Ribeiro, C., Crystallization and Growth of Colloidal Nanocrystals, *Springer*, New York, (2012).
3. Weitz, D. A. & Huang, J. S., in Kinetics of Aggregation and Gelation, eds. F. Family and D. P. Landau, *Elsevier*, (1984).
4. Kreibig, U. & Zacharias, P. Surface plasma resonances in small spherical silver and gold particles. *Z. Physik A* **231**, 128-143 (1970).
5. Granqvist, C. G., Buhrman, R. A., Wyns, J. & Sievers, A. J. Far-infrared absorption in ultrafine Al particles. *Phys. Rev. Lett.* **37**, 625-629 (1976).
6. Alivisatos, A. P. Semiconductor clusters, nanocrystals, and quantum dots. *Science* **271**, 933-937 (1996).
7. Weller, H. Quantized semiconductor particles : A novel state of matter for materials science. *Adv. Mater.* **5**, 88-95 (1993).
8. Colvin, V. L., Schlamp, M. C. & Alivisatos, A. P. Light-emitting diodes made from cadmium selenide nanocrystals and a semiconducting polymer. *Nature* **370**, 354-357 (1994).
9. Alivisatos, A. P. Perspectives on the physical chemistry of semiconductor nanocrystals. *J. Phys. Chem.* **100**, 13226-13239 (1996).
10. Park, J., Kwon, T., Kim, J., Jin, H., Kim, H. Y., Kim, B., Joo, S. H. & Lee, K. Hollow nanoparticles as emerging electrocatalysts for renewable energy conversion reactions. *Chem. Soc. Rev.* **47**, 8173-8202 (2018).
11. Zito, C. A., Perfecto, T. M., Dippel, A. C., Volanti, D. P. & Koziej, D. Low-temperature carbon dioxide gas sensor based on yolk-shell ceria nanospheres. *ACS Appl. Mater. Interf.* **12**, 17745-17751 (2020).
12. Haruta, M. & Delmon, B. Preparation of homodisperse solids. *J. Chim. Phys.* **83** (1986).
13. Jehannin, M., Rao, A. & Cölfen, H. New horizons of nonclassical crystallization. *J. Am. Chem. Soc.* **141**, 10120-10136 (2019).
14. Staniuk, M., Hirsch, O., Kränzlin, N., Böhlen, R., van Beek, W., Abdala, P. M. & Koziej, D. Puzzling mechanism behind a simple synthesis of cobalt and cobalt oxide nanoparticles: In situ synchrotron X-ray absorption and diffraction studies. *Chem. Mater.* **26**, 2086-2094 (2014).
15. Mohammadi Ziarani, G., Malmir, M., Lashgari, N. & Badieli, A. The role of hollow magnetic nanoparticles in drug delivery. *RSC Adv.* **9**, 25094-25106 (2019).
16. Tian, X., Zhao, X., Su, Y.-Q., Wang, L., Wang, H., Dang, D., Chi, B., Liu, H., Hensen, E. J. M., Lou, X. W. & Xia, B. Y. Engineering bunched Pt-Ni alloy nanocages for efficient oxygen reduction in practical fuel cells. *Science* **366**, 850–856 (2019).
17. Zeng, T., He, H., Guan, H., Yuan, R., Liu, X. & Zhang, C. Tunable hollow nanoreactors for in situ synthesis of GeP electrodes towards high-performance sodium ion batteries. *Angew. Chem. Int. Ed. Engl.* **60**, 12103-12108 (2021).
18. Kränzlin, N., van Beek, W., Niederberger, M. & Koziej, D. Mechanistic studies as a tool for the design of copper-based heterostructures. *Adv. Mater. Interf.* **2**, 1500094 (2015).
19. LaMer, V. K. & Dinegar, R. H. Theory, production and mechanism of formation of monodispersed hydrosols. *J. Am. Chem. Soc.* **72**, 4847-4854 (1950).
20. Gibbs, J. W. On the equilibrium of heterogeneous substances. *Transactions of the Connecticut Academy of Arts and Sciences* **3**, 108–248 (1876).
21. Wulff, G. Zur Frage der Geschwindigkeit des Wachstums und der Auflösung der Krystallflagen. *Zeitschrift für Kristallographie und Mineralogie* **34**, 449–530 (1901).
22. Lee, J., Yang, J., Kwon, S. G. & Hyeon, T. Nonclassical nucleation and growth of inorganic nanoparticles. *Nat. Rev. Mater.* **1**, 16034 (2016).

23. Ruiz-Agudo, E., Burgos-Cara, A., Ruiz-Agudo, C., Ibanez-Velasco, A., Colfen, H. & Rodriguez-Navarro, C. A non-classical view on calcium oxalate precipitation and the role of citrate. *Nat. Commun.* **8**, 768 (2017).
24. Gebauer, D. & Wolf, S. E. Designing solid materials from their solute state: A shift in paradigms toward a holistic approach in functional materials chemistry. *J. Am. Chem. Soc.* **141**, 4490-4504 (2019).
25. Gebauer, D., Kellermeier, M., Gale, J. D., Bergstrom, L. & Colfen, H. Pre-nucleation clusters as solute precursors in crystallisation. *Chem. Soc. Rev.* **43**, 2348-2371 (2014).
26. Carcouet, C. C., van de Put, M. W., Mezari, B., Magusin, P. C., Laven, J., Bomans, P. H., Friedrich, H., Esteves, A. C., Sommerdijk, N. A., van Benthem, R. A. & de With, G. Nucleation and growth of monodisperse silica nanoparticles. *Nano Lett.* **14**, 1433-1438 (2014).
27. Gebauer, D., Völkel, A. & Cölfen, H. Stable prenucleation calcium carbonate clusters. *Science* **322**, 1819-1822 (2008).
28. Politi, Y., Metzler, R. A., Abrecht, M., Gilbert, B., Wilt, F. H., Sagi, I., Addadi, L., Weiner, S. & Gilbert, P. U. P. A. Transformation mechanism of amorphous calcium carbonate into calcite in the sea urchin larval spicule. *PNAS* **105**, 17362-17366 (2008).
29. De Yoreo, J. J., Gilbert, P. U., Sommerdijk, N. A., Penn, R. L., Whitlam, S., Joester, D., Zhang, H., Rimer, J. D., Navrotsky, A., Banfield, J. F., Wallace, A. F., Michel, F. M., Meldrum, F. C., Colfen, H. & Dove, P. M. Crystallization by particle attachment in synthetic, biogenic, and geologic environments. *Science* **349**, aaa6760 (2015).
30. Niederberger, M. Multiscale nanoparticle assembly: From particulate precise manufacturing to colloidal processing. *Adv. Funct. Mater.* **27** (2017).
31. Feng, J. & Yin, Y. Self-templating approaches to hollow nanostructures. *Adv. Mater.* **31**, e1802349 (2019).
32. Ostwald, W., Lehrbuch der allgemeinen Chemie, *W. Engelmann*, Leipzig, (1896).
33. Yang, H. G. & Zeng, H. C. Preparation of hollow anatase TiO₂ nanospheres via Ostwald ripening. *J. Phys. Chem. B* **108**, 3492-3495 (2004).
34. Yu, L., Yu, X. Y. & Lou, X. W. D. The design and synthesis of hollow micro-/nanostructures: Present and future trends. *Adv. Mater.* **30**, e1800939 (2018).
35. Yang, X., Fu, J., Jin, C., Chen, J., Liang, C., Wu, M. & Zhou, W. Formation mechanism of CaTiO₃ hollow crystals with different microstructures. *J. Am. Chem. Soc.* **132**, 14279-14287 (2010).
36. Kirkendall, E. O. Diffusion of zinc in alpha brass. *Trans. AIME* **147**, 104-110 (1942).
37. Smigelskas, A. D. & Kirkendall, E. O. Zinc diffusion in alpha brass. *Trans. AIME* **171**, 130-142 (1947).
38. Fan, H. J., Gosele, U. & Zacharias, M. Formation of nanotubes and hollow nanoparticles based on Kirkendall and diffusion processes: a review. *Small* **3**, 1660-1671 (2007).
39. Yin, Y., Rioux, R. M., Erdonmez, C. K., Hughes, S., Somorjai, G. A. & Alivisatos, A. P. Formation of hollow nanocrystals through the nanoscale Kirkendall effect. *Science* **304**, 711-714 (2004).
40. Nakamura, R., Tokozakura, D., Nakajima, H., Lee, J. G. & Mori, H. Hollow oxide formation by oxidation of Al and Cu nanoparticles. *J. Appl. Phys.* **101** (2007).
41. Wang, W., Dahl, M. & Yin, Y. Hollow nanocrystals through the nanoscale Kirkendall effect. *Chem. Mater.* **25**, 1179-1189 (2013).
42. Anderson, B. D. & Tracy, J. B. Nanoparticle conversion chemistry: Kirkendall effect, galvanic exchange, and anion exchange. *Nanoscale* **6**, 12195-12216 (2014).
43. Railsback, J. G., Johnston-Peck, A. C., Wang, J. & Tracy, J. B. Size-dependent nanoscale Kirkendall effect during the oxidation of nickel nanoparticles. *ACS Nano* **4**, 1913-1920 (2010).
44. Hu, Y., Ge, J., Sun, Y., Zhang, T. & Yin, Y. A self-templated approach to TiO₂ microcapsules. *Nano Lett.* **7**, 1832-1836 (2007).
45. Xu, W., Wang, M., Li, Z., Wang, X., Wang, Y., Xing, M. & Yin, Y. Chemical transformation of colloidal nanostructures with morphological preservation by surface-protection with capping ligands. *Nano Lett.* **17**, 2713-2718 (2017).

-
46. Nam, K. M., Shim, J. H., Ki, H., Choi, S. I., Lee, G., Jang, J. K., Jo, Y., Jung, M. H., Song, H. & Park, J. T. Single-crystalline hollow face-centered-cubic cobalt nanoparticles from solid face-centered-cubic cobalt oxide nanoparticles. *Angew. Chem. Int. Ed. Engl.* **47**, 9504-9508 (2008).
 47. Oh, M. H., Yu, T., Yu, S.-H., Lim, B., Ko, K.-T., Willinger, M.-G., Seo, D.-H., Kim, B. H., Cho, M. G., Park, J.-H., Kang, K., Sung, Y.-E., Pinna, N. & Hyeon, T. Galvanic replacement reactions in metal oxide nanocrystals. *Science* **340**, 964-968 (2013).
 48. Chee, S. W., Tan, S. F., Baraissov, Z., Bosman, M. & Mirsaidov, U. Direct observation of the nanoscale Kirkendall effect during galvanic replacement reactions. *Nat. Commun.* **8**, 1224 (2017).
 49. González, E., Arbiol, J. & Puntès, V. F. Carving at the nanoscale: Sequential galvanic exchange and Kirkendall growth at room temperature. *Science* **334**, 1377-1380 (2011).
 50. Als-Nielsen, J. & McMorrow, D., *Elements of modern X-ray physics*, John Wiley & Sons, Chichester, 2 edn., (2011).
 51. Egami, T. & Billinge, S. J. L., *Underneath the Bragg peaks - Structural analysis of complex materials*, Elsevier, Kidlington, 1 edn., (2003).
 52. Jacobsen, C., *X-Ray Microscopy*, Cambridge University Press, Cambridge, (2020).
 53. Joly, Y. & Grenier, S., in *X-Ray absorption and X-Ray emission spectroscopy - theory and applications*, eds. J. A. van Bokhoven and C. Lamberti, John Wiley & Sons, Chichester, (2016), vol. 1.
 54. Kas, J. J., Jorisson, K. & Rehr, J. J., in *X-Ray absorption and X-Ray emission spectroscopy - theory and applications*, eds. J. A. van Bokhoven and C. Lamberti, John Wiley & Sons, Chichester, (2016), vol. 1.
 55. Chen, L. X., in *X-Ray absorption and X-Ray emission spectroscopy - theory and applications*, eds. J. A. van Bokhoven and C. Lamberti, John Wiley & Sons, Chichester, (2016), vol. 1.
 56. Glatzel, P. & Bergmann, U. High resolution 1s core hole X-ray spectroscopy in 3d transition metal complexes—electronic and structural information. *Coordination Chemistry Reviews* **249**, 65-95 (2005).
 57. Swarbrick, J. C., Weng, T. C., Schulte, K., Khlobystov, A. N. & Glatzel, P. Electronic structure changes in cobalt phthalocyanine due to nanotube encapsulation probed using resonant inelastic X-ray scattering. *Phys. Chem. Chem. Phys.* **12**, 9693-9699 (2010).
 58. Glatzel, P., Sikora, M. & Fernández-García, M. Resonant X-ray spectroscopy to study K absorption pre-edges in 3d transition metal compounds. *The European Physical Journal Special Topics* **169**, 207-214 (2009).
 59. Glatzel, P., Alonso-Mori, R. & Sokaras, D., in *X-Ray absorption and X-Ray emission spectroscopy - theory and applications*, eds. J. A. van Bokhoven and C. Lamberti, John Wiley & Sons, Chichester, (2016), vol. 1.
 60. Koziej, D. Revealing complexity of nanoparticle synthesis in solution by in situ hard X-ray spectroscopy - today and beyond. *Chem. Mater.* **28**, 2478-2490 (2016).
 61. Koziej, D. & DeBeer, S. Application of modern X-ray spectroscopy in chemistry—Beyond studying the oxidation state. *Chem. Mater.* **29**, 7051-7053 (2017).
 62. Rehr, J. J., Kas, J. J., Vila, F. D., Prangebc, M. P. & Jorissena, K. Parameter-free calculations of X-ray spectra with FEFF9. *Phys. Chem. Chem. Phys.* **12**, 5503-5513 (2010).
 63. Stribeck, N., in *Applications of synchrotron light to scattering and diffraction in materials and life sciences*, eds. T. A. Ezquerra, M. C. García-Gutiérrez, A. Nogales and M. A. Gómez, Springer, Berlin, (2009).
 64. Henke, B. L., Gullikson, E. M. & Davis, J. C. X-ray interactions: photoabsorption, scattering, transmission, and reflection at E=50-30000 eV, Z=1-92. *Atomic Data and Nuclear Data Tables* **54**, 181-342 (1993).
 65. Billinge, S. J. L. The rise of the X-ray atomic pair distribution function method: a series of fortunate events. *Phil. Trans. A Math. Phys. Eng. Sci.* **377**, 20180413 (2019).
 66. Juhás, P., Davis, T., Farrow, C. L. & Billinge, S. J. L. PDFgetX3: a rapid and highly automatable program for processing powder diffraction data into total scattering pair distribution functions. *J. Appl. Crystallogr.* **46**, 560-566 (2013).
 67. Seeck, O. H., in *X-ray diffraction - Modern experimental techniques*, eds. O. H. Seeck and B. M. Murphy, CRC Press, Boca Raton, (2014), vol. 1.

68. Høydalsvik, K., Fløystad, J. B., Zhao, T., Esmaeili, M., Diaz, A., Andreasen, J. W., Mathiesen, R. H., Rønning, M. & Breiby, D. W. In situ X-ray ptychography imaging of high-temperature CO₂ acceptor particle agglomerates. *Appl. Phys. Lett.* **104**, 241909 (2014).
69. Fam, Y., Sheppard, T. L., Becher, J., Scherhauser, D., Lambach, H., Kulkarni, S., Keller, T. F., Wittstock, A., Wittwer, F., Seyrich, M., Brueckner, D., Kahnt, M., Yang, X., Schropp, A., Stierle, A., Schroer, C. G. & Grunwaldt, J.-D. A versatile nanoreactor for complementary in situ X-ray and electron microscopy studies in catalysis and materials science. *J. Synchrotron Radiat.* **26**, 1769-1781 (2019).
70. Baier, S., Wittstock, A., Damsgaard, C. D., Diaz, A., Reinhardt, J., Benzi, F., Shi, J., Scherer, T., Wang, D., Kübel, C., Schroer, C. G. & Grunwaldt, J.-D. Influence of gas atmospheres and ceria on the stability of nanoporous gold studied by environmental electron microscopy and in situ ptychography. *RSC Adv.* **6**, 83031-83043 (2016).
71. Baier, S., Damsgaard, C. D., Scholz, M., Benzi, F., Rochet, A., Hoppe, R., Scherer, T., Shi, J., Wittstock, A., Weinhausen, B., Wagner, J. B., Schroer, C. G. & Grunwaldt, J. D. In situ ptychography of heterogeneous catalysts using hard X-rays: High resolution imaging at ambient pressure and elevated temperature. *Microsc. Microanal.* **22**, 178-188 (2016).
72. Ishiguro, N., Higashino, T., Hirose, M. & Takahashi, Y. Nanoscale visualization of phase transition in melting of Sn-Bi particles by in situ hard X-ray ptychographic coherent diffraction imaging. *Microsc. Microanal.* **26**, 878-885 (2020).
73. Weber, S., Diaz, A., Holler, M., Schropp, A., Lyubomirskiy, M., Abel, K. L., Kahnt, M., Jeromin, A., Kulkarni, S., Keller, T. F., Glaser, R. & Sheppard, T. L. Evolution of hierarchically porous nickel alumina catalysts studied by X-ray ptychography. *Adv. Sci.* **9**, e2105432 (2022).
74. Donnelly, C., Finizio, S., Gliga, S., Holler, M., Hrabec, A., Odstrcil, M., Mayr, S., Scagnoli, V., Heyderman, L. J., Guizar-Sicairos, M. & Raabe, J. Time-resolved imaging of three-dimensional nanoscale magnetization dynamics. *Nat. Nanotechnol.* **15**, 356-360 (2020).
75. Weker, J. N., Liu, N., Misra, S., Andrews, J. C., Cui, Y. & Toney, M. F. In situ nanotomography and operando transmission X-ray microscopy of micron-sized Ge particles. *Energy Environ. Sci.* **7**, 2771-2777 (2014).
76. Hoppe, R., Reinhardt, J., Hofmann, G., Patommel, J., Grunwaldt, J.-D., Damsgaard, C. D., Wellenreuther, G., Falkenberg, G. & Schroer, C. G. High-resolution chemical imaging of gold nanoparticles using hard x-ray ptychography. *Appl. Phys. Lett.* **102** (2013).
77. Pfeiffer, F. X-ray ptychography. *Nat. Photonics* **12**, 9-17 (2018).
78. Rodenburg, J. & Maiden, A., in *Springer Handbook of Microscopy*, eds. P. W. Hawkes and J. C. H. Spence, Springer International Publishing, Cham, (2019), DOI: 10.1007/978-3-030-00069-1_17.
79. Hoppe, W. Beugung im Inhomogenen Primärstrahlwellenfeld. III. Amplituden- und Phasenbestimmung bei unperiodischen Objekten. *Act. Cryst.* **A25** (1969).
80. Hegerl, R. & Hoppe, W. Dynamische theorie der kristallstrukturanalyse durch elektronenbeugung im inhomogenen primärstrahlwellenfeld. *Berich. Bunsen. Phys. Chem.* **74**, 1148-1154 (1970).
81. Rodenburg, J. M., Hurst, A. C., Cullis, A. G., Dobson, B. R., Pfeiffer, F., Bunk, O., David, C., Jefimovs, K. & Johnson, I. Hard-x-ray lensless imaging of extended objects. *Phys. Rev. Lett.* **98**, 034801 (2007).
82. Thibault, P., Dierolf, M., Bunk, O., Menzel, A. & Pfeiffer, F. Probe retrieval in ptychographic coherent diffractive imaging. *Ultramicrosc.* **109**, 338-343 (2009).
83. Maiden, A. M. & Rodenburg, J. M. An improved ptychographical phase retrieval algorithm for diffractive imaging. *Ultramicrosc.* **109**, 1256-1262 (2009).
84. Thibault, P., Dierolf, M., Menzel, A., Bunk, O., David, C. & Pfeiffer, F. High-resolution scanning X-ray diffraction microscopy. *Science* **321**, 379-382 (2008).
85. Rodenburg, J. M., Hurst, A. C. & Cullis, A. G. Transmission microscopy without lenses for objects of unlimited size. *Ultramicrosc.* **107**, 227-231 (2007).
86. Rodenburg, J. M. & Faulkner, H. M. L. A phase retrieval algorithm for shifting illumination. *Appl. Phys. Lett.* **85** (2004).
87. Maiden, A. M., Humphry, M. J. & Rodenburg, J. M. Ptychographic transmission microscopy in three dimensions using a multi-slice approach. *J. Opt. Soc. Am. A* **29**, 1606-1614 (2012).

-
88. Abbe, E. Beiträge zur Theorie des Mikroskops und der mikroskopischen Wahrnehmung. *Archiv für Mikroskopische Anatomie* **9**, 413–468 (1873).
 89. Maiden, A. M., Humphry, M. J., Sarahan, M. C., Kraus, B. & Rodenburg, J. M. An annealing algorithm to correct positioning errors in ptychography. *Ultramicrosc.* **120**, 64-72 (2012).
 90. Rodenburg, J. M. & Bates, R. H. T. The theory of super-resolution electron microscopy via Wigner-distribution deconvolution. *Phil. Trans. R. Soc. Lond. A* **339**, 521-553 (1992).
 91. Tsai, E. H. R., Usov, I., Diaz, A., Menzel, A. & Guizar-Sicairos, M. X-ray ptychography with extended depth of field. *Opt. Expr.* **24**, 29089-29108 (2016).
 92. Seyrich, K. M., High-resolution and in-solution hard X-ray ptychography at the ptychographic nano-analytical microscope PtyNAMi. PhD thesis, *University of Hamburg*, 2021.
 93. Hessel, C. M., Pattani, V. P., Rasch, M., Panthani, M. G., Koo, B., Tunnell, J. W. & Korgel, B. A. Copper selenide nanocrystals for photothermal therapy. *Nano Lett.* **11**, 2560-2566 (2011).
 94. Talapin, D. V., Lee, J.-S., Kovalenko, M. V. & Shevchenko, E. V. Prospects of colloidal nanocrystals for electronic and optoelectronic applications. *Chem. Rev.* **110**, 389–458 (2010).
 95. Barbosa, S., Agrawal, A., Rodriguez-Lorenzo, L., Pastoriza-Santos, I., Alvarez-Puebla, R. A., Kornowski, A., Weller, H. & Liz-Marzan, L. M. Tuning size and sensing properties in colloidal gold nanostars. *Langmuir* **26**, 14943-14950 (2010).
 96. Kovalenko, M. V., Scheele, M. & Talapin, D. V. Colloidal nanocrystals with molecular metal chalcogenide surface ligands. *Science* **324**, 1417-1420 (2009).
 97. Peng, X., Manna, L., Yang, W., Wickham, J., Scher, E., Kadavanich, A. & Alivisatos, A. P. Shape control of CdSe nanocrystals. *Nature* **404**, 59-61 (2000).
 98. Holmes, J. D., Johnston, K. P., Doty, R. C. & Korgel, B. A. Control of thickness and orientation of solution-grown silicon nanowires. *Science* **287**, 1471-1473 (2000).
 99. Niederberger, M., Garnweitner, G., Ba, J., Polleux, J. & Pinna, N. Nonaqueous synthesis, assembly and formation mechanisms of metal oxide nanocrystals. *Int. J. Nanotechnol.* **4**, 263-272 (2007).
 100. Shevchenko, E. V., Talapin, D. V., Rogach, A. L., Kornowski, A., Haase, M. & Weller, H. Colloidal synthesis and self-assembly of CoPt₃ nanocrystals. *J. Am. Chem. Soc.* **124**, 11480-11485 (2002).
 101. Schliehe, C., Juarez, b. H., Pelletier, M., Jander, S., Greshnykh, D., Nagel, M., Meyer, A., Foerster, S., Kornowski, A., Klinke, C. & Weller, H. Ultrathin PbS sheets by two-dimensional oriented attachment. *Science* **329**, 550-553 (2010).
 102. Yang, J., Son, J. S., Yu, J. H., Joo, J. & Hyeon, T. Advances in the colloidal synthesis of two-dimensional semiconductor nanoribbons. *Chem. Mater.* **25**, 1190-1198 (2013).
 103. Bai, J., Han, S. H., Peng, R. L., Zeng, J. H., Jiang, J. X. & Chen, Y. Ultrathin rhodium oxide nanosheet nanoassemblies: Synthesis, morphological stability, and electrocatalytic application. *ACS Appl. Mater. Interf.* **9**, 17195-17200 (2017).
 104. Litwinowicz, A.-A., Takami, S., Hojo, D., Aoki, N. & Adschiri, T. Hydrothermal synthesis of cerium oxide nanoassemblies through coordination programming with amino acids. *Chem. Lett.* **43**, 1343-1345 (2014).
 105. Barick, K. C., Aslam, M., Prasad, P. V., Dravid, V. P. & Bahadur, D. Nanoscale assembly of amine functionalized colloidal iron oxide. *Journal of Magnetism and Magnetic Materials* **321**, 1529-1532 (2009).
 106. He, X., Song, X., Qiao, W., Li, Z., Zhang, X., Yan, S., Zhong, W. & Du, Y. Phase- and size-dependent optical and magnetic properties of CoO nanoparticles. *J. Phys. Chem. C* **119**, 9550-9559 (2015).
 107. Lagunas, A., Mairata i Payeras, A., Jimeno, C., Puentes, V. F. & Pericàs, M. A. Low-temperature synthesis of CoO nanoparticles via chemically assisted oxidative decarbonylation. *Chem. Mater.* **20**, 92-100 (2008).
 108. Staniuk, M., Zindel, D., van Beek, W., Hirsch, O., Kränzlin, N., Niederberger, M. & Koziej, D. Matching the organic and inorganic counterparts during nucleation and growth of copper-based nanoparticles – in situ spectroscopic studies. *CrystEngComm* **17**, 6962-6971 (2015).
 109. Kränzlin, N., Staniuk, M., Heiligt, F. J., Luo, L., Emerich, H., van Beek, W., Niederberger, M. & Koziej, D. Rationale for the crystallization of titania polymorphs in solution. *Nanoscale* **6**, 14716-14723 (2014).

110. Hirsch, O., Zeng, G., Luo, L., Staniuk, M., Abdala, P. M., van Beek, W., Rechberger, F., Süess, M. J., Niederberger, M. & Koziej, D. Aliovalent Ni in MoO₂ lattice - probing the structure and valence of Ni and its implication on the electrochemical performance. *Chem. Mater.* **26**, 4505-4513 (2014).
111. Koziej, D., Rossell, M. D., Ludi, B., Hintennach, A., Novak, P., Grunwaldt, J. D. & Niederberger, M. Interplay between size and crystal structure of molybdenum dioxide nanoparticles--synthesis, growth mechanism, and electrochemical performance. *Small* **7**, 377-387 (2011).
112. Hubner, M., Koziej, D., Bauer, M., Barsan, N., Kvashnina, K., Rossell, M. D., Weimar, U. & Grunwaldt, J. D. The structure and behavior of platinum in SnO₂-based sensors under working conditions. *Angew. Chem. Intl. Ed. Engl.* **50**, 2841-2844 (2011).
113. Strach, M., Mantella, V., Pankhurst, J. R., Iyengar, P., Loiudice, A., Das, S., Corminboeuf, C., van Beek, W. & Buonsanti, R. Insights into reaction intermediates to predict synthetic pathways for shape-controlled metal nanocrystals. *J. Am. Chem. Soc.* **141**, 16312-16322 (2019).
114. Hutchings, G. S., Zhang, Y., Li, J., Yonemoto, B. T., Zhou, X., Zhu, K. & Jiao, F. In situ formation of cobalt oxide nanocubanes as efficient oxygen evolution catalysts. *J. Am. Chem. Soc.* **137**, 4223-4229 (2015).
115. Kvashnina, K. O., Romanchuk, A. Y., Pidchenko, I., Amidani, L., Gerber, E., Trigub, A., Rossberg, A., Weiss, S., Popa, K., Walter, O., Caciuffo, R., Scheinost, A. C., Butorin, S. M. & Kalmykov, S. N. A novel metastable pentavalent plutonium solid phase on the pathway from aqueous plutonium(VI) to PuO₂ nanoparticles. *Angew. Chem. Intl. Ed. Engl.* **58**, 17558-17562 (2019).
116. Hirsch, O., Kvashnina, K. O., Luo, L., Süess, M. J., Glatzel, P. & Koziej, D. High-energy resolution X-ray absorption and emission spectroscopy reveals insight into unique selectivity of La-based nanoparticles for CO(2). *PNAS* **112**, 15803-15808 (2015).
117. Glatzel, P., Singh, J., Kvashnina, K. O. & Bokhoven, J. A. V. In situ characterization of the 5d density of states of Pt nanoparticles upon adsorption of CO. *J. Am. Chem. Soc.* **132**, 2555-2557 (2010).
118. Kuciakowski, J., Kmita, A., Lachowicz, D., Wytrwal-Sarna, M., Pitala, K., Lafuerza, S., Koziej, D., Juhin, A. & Sikora, M. Selective magnetometry of superparamagnetic iron oxide nanoparticles in liquids. *Nanoscale* **12**, 16420-16426 (2020).
119. Saha, D., Bøjesen, E. D., Mamakhel, A. H., Bremholm, M. & Iversen, B. B. In situ PDF study of the nucleation and growth of intermetallic PtPb nanocrystals. *ChemNanoMat* **3**, 472-478 (2017).
120. Tyrsted, C., Lock, N., Jensen, K. M. Ø., Christensen, M., Bøjesen, E. D., Emerich, H., Vaughan, G., Billinge, S. J. L. & Iversen, B. B. Evolution of atomic structure during nanoparticle formation. *IUCrJ* **1**, 165-171 (2014).
121. Jensen, K. M., Christensen, M., Juhas, P., Tyrsted, C., Bøjesen, E. D., Lock, N., Billinge, S. J. & Iversen, B. B. Revealing the mechanisms behind SnO₂ nanoparticle formation and growth during hydrothermal synthesis: an in situ total scattering study. *J. Am. Chem. Soc.* **134**, 6785-6792 (2012).
122. Zobel, M., Neder, R. B. & Kimber, S. A. J. Universal solvent restructuring induced by colloidal nanoparticles. *Science* **347**, 292-294 (2015).
123. Narayanan, T., Wacklin, H., Kononov, O. & Lund, R. Recent applications of synchrotron radiation and neutrons in the study of soft matter. *Cryst. Rev.* **23**, 160-226 (2017).
124. Ingham, B. X-ray scattering characterisation of nanoparticles. *Cryst. Rev.* **21**, 229-303 (2015).
125. Montanarella, F., Geuchies, J. J., Dasgupta, T., Prins, P. T., van Overbeek, C., Dattani, R., Baesjou, P., Dijkstra, M., Petukhov, A. V., van Blaaderen, A. & Vanmaekelbergh, D. Crystallization of nanocrystals in spherical confinement probed by in situ X-ray scattering. *Nano Lett.* **18**, 3675-3681 (2018).
126. Zheng, X., Shen, G., Li, Y., Duan, H., Yang, X., Huang, S., Wang, H., Wang, C., Deng, Z. & Su, B.-L. Self-templated synthesis of microporous CoO nanoparticles with highly enhanced performance for both photocatalysis and lithium-ion batteries. *J. Mater. Chem. A* **1**, 1394-1400 (2013).

-
127. Qi, Y., Zhang, H., Du, N. & Yang, D. Highly loaded CoO/graphene nanocomposites as lithium-ion anodes with superior reversible capacity. *J. Mater. Chem. A* **1**, 2337 (2013).
128. Sun, B., Liu, H., Munroe, P., Ahn, H. & Wang, G. Nanocomposites of CoO and a mesoporous carbon (CMK-3) as a high performance cathode catalyst for lithium-oxygen batteries. *Nano Res.* **5**, 460-469 (2012).
129. Jiang, Z. J. & Jiang, Z. Interaction induced high catalytic activities of CoO nanoparticles grown on nitrogen-doped hollow graphene microspheres for oxygen reduction and evolution reactions. *Sci. Rep.* **6**, 27081 (2016).
130. Guo, S., Zhang, S., Wu, L. & Sun, S. Co/CoO nanoparticles assembled on graphene for electrochemical reduction of oxygen. *Angew. Chem. Intl. Ed. Engl.* **51**, 11770-11773 (2012).
131. Liao, L., Zhang, Q., Su, Z., Zhao, Z., Wang, Y., Li, Y., Lu, X., Wei, D., Feng, G., Yu, Q., Cai, X., Zhao, J., Ren, Z., Fang, H., Robles-Hernandez, F., Baldelli, S. & Bao, J. Efficient solar water-splitting using a nanocrystalline CoO photocatalyst. *Nat. Nanotechnol.* **9**, 69-73 (2014).
132. Park, K.-W. & Kolpak, A. M. Understanding photocatalytic overall water splitting on CoO nanoparticles: Effects of facets, surface stoichiometry, and the CoO/water interface. *J. Cat.* **365**, 115-124 (2018).
133. Li, Y., Zhang, J., Liu, Z., Liu, M., Lin, H. & Che, R. Morphology-dominant microwave absorption enhancement and electron tomography characterization of CoO self-assembly 3D nano-flowers. *J. Mater. Chem. C* **2**, 5216 (2014).
134. Rai, A. K., Anh, L. T., Gim, J. & Kim, J. One-step synthesis of CoO anode material for rechargeable lithium-ion batteries. *Ceramics International* **39**, 9325-9330 (2013).
135. Chen, Z., Xu, A., Zhang, Y. & Gu, N. Preparation of NiO and CoO nanoparticles using M₂+oleate (M=Ni, Co) as precursor. *Curr. Appl. Phys.* **10**, 967-970 (2010).
136. Niederberger, M. Nonaqueous sol-gel routes to metal oxide nanoparticles. *Acc. Chem. Res.* **40**, 793-800 (2007).
137. Papaefthimiou, V., Dintzer, T., Hillion, A., Teschner, D., Dupuis, V., Hävecker, M., Tamion, A., Knop-Gericke, A., Schlögl, R., Tournus, F. & Zafeirotos, S. Nontrivial redox behavior of nanosized cobalt: New insights from ambient pressure X-ray photoelectron and absorption spectroscopies. *ACS Nano* **5**, 2182-2190 (2011).
138. de Groot, F., Vanko, G. & Glatzel, P. The 1s x-ray absorption pre-edge structures in transition metal oxides. *J. Phys.: Cond. Mat.* **21**, 104207 (2009).
139. Choi, H. C., Lee, S. Y., Kim, S. B., Kim, M. G., Lee, M. K., Shin, H. J. & Lee, J. S. Local structural characterization for electrochemical insertion-extraction of lithium into CoO with X-ray absorption spectroscopy. *J. Phys. Chem. B* **106**, 9252-9260 (2002).
140. Sankar, G., Sarode, P. R. & Rao, C. N. R. A XANES study of mixed-valence transition-metal oxides and rare-earth alloys. *Chem. Phys.* **76**, 435-442 (1983).
141. Andonova, S., de Ávila, C. N., Arishtirova, K., Bueno, J. M. C. & Damyanova, S. Structure and redox properties of Co promoted Ni/Al₂O₃ catalysts for oxidative steam reforming of ethanol. *Applied Catalysis B* **105**, 346-360 (2011).
142. de Juan, A., Jaumot, J. & Tauler, R. Multivariate Curve Resolution (MCR). Solving the mixture analysis problem. *Analytical Methods* **6**, 4964-4976 (2014).
143. Jaumot, J., Gargallo, R., de Juan, A. & Tauler, R. A graphical user-friendly interface for MCR-ALS: a new tool for multivariate curve resolution in MATLAB. *Chemometrics and Intelligent Laboratory Systems* **76**, 101-110 (2005).
144. Radón, M., Srebro, M. & Broclawik, E. Conformational stability and spin states of cobalt(II) acetylacetonate: CASPT2 and DFT study. *Journal of Chemical Theory and Computation* **5**, 1237-1244 (2009).
145. von Chrzanowski, L. S., Lutz, M. & Spek, A. L. alpha-Tris(2,4-pentanedionato-kappa(2)O,O')cobalt(III) at 240, 210, 180, 150 and 110 K. *Act. Crystallogr. C* **63**, m283-m228 (2007).
146. Niwa, H., Higashiyama, K., Amaha, K., Kobayashi, W., Ishii, K. & Moritomo, Y. High-energy-resolution XANES of layered oxides for sodium-ion battery. *Appl. Phys. Expr.* **12**, 052005 (2019).
147. Sano, M. XANES study at the Co K absorption edge in a series of cobalt(III) complexes. *Inorg. Chem.* **27**, 4249-4253 (1988).

148. Saib, A. M., Borgna, A., van de Lossdrecht, J., van Berge, P. J. & Niemantsverdriet, J. W. XANES study of the susceptibility of nano-sized cobalt crystallites to oxidation during realistic Fischer-Tropsch synthesis. *Applied Catalysis A* **312**, 12-19 (2006).
149. Vråstad, T., Øye, G., Rønning, M., Glomm, W. R., Stöcker, M. & Sjöblom, J. Interfacial chemistry of cobalt(II) during sol-gel synthesis of cobalt-containing mesoporous materials. *Microporous and Mesoporous Materials* **80**, 291-300 (2005).
150. Choy, J. H., Jung, H. & Yoon, J. B. Co K-edge XAS study on a new cobalt-doped-SiO₂ pillared clay. *J. Synchrotron Radiat.* **8**, 599-601 (2001).
151. Booth, C. H. & Bridges, F. Improved self-absorption correction for fluorescence measurements of extended x-ray absorption fine-structure. *Physica Scripta* **T115**, 202-204 (2005).
152. Vreshch, V. D., Yang, J. H., Zhang, H., Filatov, A. S. & Dikarev, E. V. Monomeric square-planar cobalt(II) acetylacetonate: mystery or mistake? *Inorg. Chem.* **49**, 8430-8434 (2010).
153. Cotton, F. A. & Elder, R. C. Crystal structure of tetrameric cobalt(II) acetylacetonate. *Inorg. Chem.* **4**, 1145-1151 (1965).
154. Ludi, B., Suess, M. J., Werner, I. A. & Niederberger, M. Mechanistic aspects of molecular formation and crystallization of zinc oxide nanoparticles in benzyl alcohol. *Nanoscale* **4**, 1982-1995 (2012).
155. Bilecka, I., Elser, P. & Niederberger, M. Kinetic and thermodynamic aspects in the microwave-assisted synthesis of ZnO nanoparticles in benzyl alcohol. *ACS Nano* **3**, 467-477 (2009).
156. Burgess, J., Fawcett, J. & Russell, D. R. Bis(2,4-pentanedionato)cobalt(II). *Act. Crystallogr. C* **67**, e13-e13 (2000).
157. Sasaki, S., Fujino, K. & Tacéuchi, Y. X-ray determination of electron density distributions in oxides, MgO, MnO, CoO, and NiO, and atomic scattering factors of their constituent atoms. *Proceedings of the Japan Academy B* **55**, 43-48 (1979).
158. Momma, K. & Izumi, F. VESTA 3for three-dimensional visualization of crystal, volumetric and morphology data. *J. Appl. Crystallogr.* **44**, 1272-1276 (2011).
159. Mildner, D. F. R. & Hall, P. L. Small-angle scattering from porous solids with fractal geometry. *J. Phys. D: Appl. Phys.* **19**, 1535-1545 (1986).
160. Glatter, O. & Kratky, O., Small angle X-ray scattering, *Academic Press*, (1982).
161. Kapuscinski, M., Agthe, M., Lv, Z. P., Liu, Y., Segad, M. & Bergstrom, L. Temporal evolution of superlattice contraction and defect-induced strain anisotropy in mesocrystals during nanocube self-assembly. *ACS Nano* **14**, 5337-5347 (2020).
162. Lv, Z. P., Kapuscinski, M. & Bergstrom, L. Tunable assembly of truncated nanocubes by evaporation-driven poor-solvent enrichment. *Nat. Commun.* **10**, 4228 (2019).
163. Josten, E., Wetterskog, E., Glavic, A., Boesecke, P., Feoktystov, A., Brauweiler-Reuters, E., Rucker, U., Salazar-Alvarez, G., Bruckel, T. & Bergstrom, L. Superlattice growth and rearrangement during evaporation-induced nanoparticle self-assembly. *Sci. Rep.* **7**, 2802 (2017).
164. Tiede, D. M., Kwon, G., He, X., Mulfort, K. L. & Martinson, A. B. F. Characterizing electronic and atomic structures for amorphous and molecular metal oxide catalysts at functional interfaces by combining soft X-ray spectroscopy and high-energy X-ray scattering. *Nanoscale* **12**, 13276-13296 (2020).
165. Kvashnina, K. O. & Scheinost, A. C. A Johann-type X-ray emission spectrometer at the Rossendorf beamline. *J. Synchrotron Radiat.* **23**, 836-841 (2016).
166. Buffet, A., Rothkirch, A., Dohrmann, R., Korstgens, V., Abul Kashem, M. M., Perlich, J., Herzog, G., Schwartzkopf, M., Gehrke, R., Muller-Buschbaum, P. & Roth, S. V. P03, the microfocus and nanofocus X-ray scattering (MiNaXS) beamline of the PETRA III storage ring: the microfocus endstation. *J. Synchrotron Radiat.* **19**, 647-653 (2012).
167. Bruetzel, L. K., Fischer, S., Salditt, A., Sedlak, S. M., Nickel, B. & Lipfert, J. A Mo-anode-based in-house source for small-angle X-ray scattering measurements of biological macromolecules. *Rev. Sci. Instrum.* **87**, 025103 (2016).
168. Solé, V. A., Papillon, E., Cotte, M., Walter, P. & Susini, J. A multiplatform code for the analysis of energy-dispersive X-ray fluorescence spectra. *Spectrochimica Acta Part B: Atomic Spectroscopy* **62**, 63-68 (2007).
169. Ravel, B. & Newville, M. ATHENA, ARTEMIS, HEPHAESTUS: data analysis for X-ray absorption spectroscopy using IFEFFIT. *J. Synchrotron Radiat.* **12**, 537-541 (2005).

-
170. Jaumot, J., de Juan, A. & Tauler, R. MCR-ALS GUI 2.0: New features and applications. *Chemometrics and Intelligent Laboratory Systems* **140**, 1-12 (2015).
171. Ashiotis, G., Deschildre, A., Nawaz, Z., Wright, J. P., Karkoulis, D., Picca, F. E. & Kieffer, J. The fast azimuthal integration Python library: pyFAI. *J. Appl. Crystallogr.* **48**, 510-519 (2015).
172. Yang, X., Juhás, P., Farrow, C. L. & Billinge, S. J. L. xPDFsuite: an end-to-end software solution for high throughput pair distribution function transformation, visualization and analysis. *ArXiv*, 1402.3163 (2014).
173. Farrow, C. L., Juhas, P., Liu, J. W., Bryndin, D., Bozin, E. S., Bloch, J., Proffen, T. & Billinge, S. J. PDFfit2 and PDFgui: computer programs for studying nanostructure in crystals. *J. Phys.: Cond. Mat.* **19**, 335219 (2007).
174. Ilavsky, J. Nika: software for two-dimensional data reduction. *J. Appl. Crystallogr.* **45**, 324-328 (2012).
175. Grote, L., Zito, C. A., Frank, K., Dippel, A.-C., Reisbeck, P., Pitala, K., Kvashnina, K. O., Bauters, S., Detlefs, B., Ivashko, O., Pandit, P., Rebber, M., Harouna-Mayer, S. Y., Nickel, B. & Koziej, D. Raw data for "X-ray studies bridge the molecular and macro length scales during the emergence of CoO assemblies". zenodo. doi:10.5281/zenodo.4746349 (2021).
176. Windig, W. & Stephenson, D. A. Self-modeling mixture analysis of second-derivative near-infrared spectral data using the simplisma approach. *Analytical Chemistry* **64**, 2735-2742 (1992).
177. Chen, L., Mashimo, T., Iwamoto, C., Okudera, H., Omurzak, E., Ganapathy, H. S., Ihara, H., Zhang, J., Abdullaeva, Z., Takebe, S. & Yoshiasa, A. Synthesis of novel CoCx@C nanoparticles. *Nanotechnol.* **24**, 045602 (2013).
178. Kotlarchyk, M., Stephens, R. B. & Huang, J. S. Study of Schultz distribution to model polydispersity of microemulsion droplets. *J. Phys. Chem. C* **92**, 1533-1538 (1988).
179. Saloga, P. E. J. & Thunemann, A. F. Microwave-assisted synthesis of ultrasmall zinc oxide nanoparticles. *Langmuir* **35**, 12469-12482 (2019).
180. Hargreaves, J. S. J. Some considerations related to the use of the Scherrer equation in powder X-ray diffraction as applied to heterogeneous catalysts. *Catalysis, Structure & Reactivity* **2**, 33-37 (2016).
181. Ruland, W. The integral width of the convolution of a Gaussian and a Cauchy distribution. *Act. Crystallogr. C* **19**, 581 (1965).
182. Guérin, T., Dolgushev, M., Bénichou, O. & Voituriez, R. Universal kinetics of imperfect reactions in confinement. *Commun. Chem.* **4** (2021).
183. Benichou, O., Chevalier, C., Klafter, J., Meyer, B. & Voituriez, R. Geometry-controlled kinetics. *Nat. Chem.* **2**, 472-477 (2010).
184. Schropp, A., Döhrmann, R., Botta, S., Brückner, D., Kahnt, M., Lyubomirskiy, M., Ossig, C., Scholz, M., Seyrich, M., Stükelberger, M. E., Wiljes, P., Wittwer, F., Garrevoet, J., Falkenberg, G., Fam, Y., Sheppard, T. L., Grunwaldt, J.-D. & Schroer, C. G. PtyNAMi: ptychographic nano-analytical microscope. *J. Appl. Crystallogr.* **53**, 957-971 (2020).
185. Schroer, C. G., Baumbach, C., Döhrmann, R., Klare, S., Hoppe, R., Kahnt, M., Patommel, J., Reinhardt, J., Ritter, S., Samberg, D., Scholz, M., Schropp, A., Seiboth, F., Seyrich, M., Wittwer, F. & Falkenberg, G. Hard x-ray nanoprobe of beamline P06 at PETRA III. *AIP Conf. Proc.* **1741**, 030007-030007 (2016).
186. Hübschmann, U. & Links, E., Tabellen zur Chemie: Grundlagen für das chemische Rechnen in Ausbildung und Beruf, *Handwerk und Technik*, Hamburg, (1991).
187. van Schilfgaarde, M., Abrikosov, I. A. & Johansson, B. Origin of the Invar effect in iron-nickel alloys. *Nature* **400**, 46-49 (1999).
188. Lide, D. R., ed., CRC handbook of chemistry and physics, CRC Press, London (1998).
189. Zhu, C., Liang, S., Song, E., Zhou, Y., Wang, W., Shan, F., Shi, Y., Hao, C., Yin, K., Zhang, T., Liu, J., Zheng, H. & Sun, L. In-situ liquid cell transmission electron microscopy investigation on oriented attachment of gold nanoparticles. *Nat. Commun.* **9**, 421 (2018).
190. Grunwaldt, J.-D., Hannemann, S., Schroer, C. G. & Baiker, A. 2D-mapping of the catalyst structure inside a catalytic microreactor at work: Partial oxidation of methane over Rh/Al₂O₃. *J. Phys. Chem. B* **110**, 8674-8680 (2006).

191. Kodur, M., Kumar, R. E., Luo, Y., Cakan, D. N., Li, X., Stuckelberger, M. & Fenning, D. P. X-ray microscopy of halide perovskites: Techniques, applications, and prospects. *Adv. Ener. Mater.* **10**, 1903170-1903170 (2020).
192. Meyer, Q., Zeng, Y. & Zhao, C. In situ and operando characterization of proton exchange membrane fuel cells. *Adv. Mater.* **31**, 1901900-1901900 (2019).
193. Baier, S., Damsgaard, C. D., Klumpp, M., Reinhardt, J., Sheppard, T., Balogh, Z., Kasama, T., Benzi, F., Wagner, J. B., Schwieger, W., Schroer, C. G. & Grunwaldt, J.-D. Stability of a bifunctional Cu-based core at zeolite shell catalyst for dimethyl ether synthesis under redox conditions studied by environmental transmission electron microscopy and in situ X-ray ptychography. *Microsc. Microanal.* **23**, 501–512 (2017).
194. Ulvestad, A., Singer, A., Clark, J. N., Cho, H. M., Kim, J. W., Harder, R., Maser, J., Meng, Y. S. & Shpyrko, O. G. Topological defect dynamics in operando battery nanoparticles. *Science* **348**, 1344-1347 (2015).
195. Nelson Weker, J. & Toney, M. F. Emerging in situ and operando nanoscale X-ray imaging techniques for energy storage materials. *Adv. Funct. Mater.* **25**, 1622-1637 (2015).
196. Li, L., Chen-Wiegart, Y.-c. K., Wang, J., Gao, P., Ding, Q., Yu, Y.-S., Wang, F., Cabana, J., Wang, J. & Jin, S. Visualization of electrochemically driven solid-state phase transformations using operando hard X-ray spectro-imaging. *Nat. Commun.* **6**, 6883-6883 (2015).
197. Grunwaldt, J.-D. & Schroer, C. G. Hard and soft X-ray microscopy and tomography in catalysis: Bridging the different time and length scales. *Chem. Soc. Rev.* **39**, 4741-4741 (2010).
198. Bozzini, B., Kourousias, G., Gianoncelli, A., Jones, M. W. M., Riessen, G. V. & Kiskinova, M. Soft X-ray ptychography as a tool for in operando morphochemical studies of electrodeposition processes with nanometric lateral resolution. *J. Electron Spectros. Relat. Phenomena* **220**, 147-155 (2017).
199. Tavares, P. F., Al-Dmour, E., Andersson, Å., Cullinan, F., Jensen, B. N., Olsson, D., Olsson, D. K., Sjöström, M., Tarawneh, H., Thorin, S. & Vorozhtsov, A. Commissioning and first-year operational results of the MAX IV 3 GeV ring. *J. Synchrotron Radiat.* **25**, 1291-1316 (2018).
200. Schroer, C. G., Agapov, I., Brefeld, W., Brinkmann, R., Chae, Y.-C., Chao, H.-C., Eriksson, M., Keil, J., Gavalda, X. N., Röhlberger, R., Seeck, O. H., Sprung, M., Tischer, M., Wanzenberg, R. & Weckert, E. PETRA IV: The ultra-low emittance source project at DESY. *J. Synchrotron Radiat.* **25**, 1277-1290 (2018).
201. Raimondi, P. ESRF-EBS: The extremely brilliant source project. *Synchr. Rad. News* **29**, 8-15 (2016).
202. Reinhardt, J., Hoppe, R., Hofmann, G., Damsgaard, C. D., Patommel, J., Baumbach, C., Baier, S., Rochet, A., Grunwaldt, J.-D., Falkenberg, G. & Schroer, C. G. Beamstop-based low-background ptychography to image weakly scattering objects. *Ultramicrosc.* **173**, 52-57 (2017).
203. Schropp, A., Hoppe, R., Patommel, J., Samberg, D., Seiboth, F., Stephan, S., Wellenreuther, G., Falkenberg, G. & Schroer, C. G. Hard x-ray scanning microscopy with coherent radiation: Beyond the resolution of conventional x-ray microscopes. *Appl. Phys. Lett.* **100**, 253112-253112 (2012).
204. Becher, J., Sheppard, T. L., Fam, Y., Baier, S., Wang, W., Wang, D., Kulkarni, S., Keller, T. F., Lyubomirskiy, M., Brueckner, D., Kahnt, M., Schropp, A., Schroer, C. G. & Grunwaldt, J.-D. Mapping the pore architecture of structured catalyst monoliths from nanometer to centimeter scale with electron and X-ray tomographies. *J. Phys. Chem. C* **123**, 25197-25208 (2019).
205. Wang, D., Li, B., Rong, L., Tan, F., Healy, J. J., Zhao, J. & Wang, Y. Multi-layered full-field phase imaging using continuous-wave terahertz ptychography. *Opt. Lett.* **45**, 1391-1394 (2020).
206. Huang, X., Yan, H., He, Y., Ge, M., Öztürk, H., Fang, Y.-L. L., Ha, S., Lin, M., Lu, M., Nazaretski, E., Robinson, I. K. & Chu, Y. S. Resolving 500 nm axial separation by multi-slice X-ray ptychography. *Acta Crystallogr. A* **75**, 336-341 (2019).
207. Shimomura, K., Hirose, M. & Takahashi, Y. Multislice imaging of integrated circuits by precession X-ray ptychography. *Acta Crystallogr. A* **74**, 66-70 (2018).
208. Öztürk, H., Yan, H., He, Y., Ge, M., Dong, Z., Lin, M., Nazaretski, E., Robinson, I. K., Chu, Y. S. & Huang, X. Multi-slice ptychography with large numerical aperture multilayer Laue lenses. *Optica* **5**, 601-607 (2018).

-
209. Tsai, E. H. R., Odstrcil, M., Usov, I., Holler, M., Diaz, A., Bosgra, J., Menzel, A. & Guizar-Sicairos, M., presented at Imaging and Applied Optics, *Optical Society of America* (2017).
210. Shimomura, K., Suzuki, A., Hirose, M. & Takahashi, Y. Precession x-ray ptychography with multislice approach. *Phys. Rev. B* **91**, 214114-214114 (2015).
211. Suzuki, A., Furutaku, S., Shimomura, K., Yamauchi, K., Kohmura, Y., Ishikawa, T. & Takahashi, Y. High-resolution multislice X-ray ptychography of extended thick objects. *Phys. Rev. Lett.* **112**, 053903-053903 (2014).
212. Godden, T. M., Suman, R., Humphry, M. J., Rodenburg, J. M. & Maiden, A. M. Ptychographic microscope for three-dimensional imaging. *Opt. Expr.* **22**, 12513-12523 (2014).
213. Blender - a 3D modelling and rendering package, <http://www.blender.org>.
214. Hunter, J. D. Matplotlib: A 2D graphics environment. *Comp. Sci. & Eng.* **9**, 90-95 (2007).
215. Niederberger, M., Bartl, M. H. & Stucky, G. D. Benzyl alcohol and titanium tetrachloride - A versatile reaction system for the nonaqueous and low-temperature preparation of crystalline and luminescent titania nanoparticles. *Chem. Mater.* **14**, 4364-4370 (2002).
216. Kränzlin, N., Ellenbroek, S., Duran-Martin, D. & Niederberger, M. Liquid-phase deposition of freestanding copper foils and supported copper thin films and their structuring into conducting line patterns. *Angew. Chem. Int. Ed. Engl.* **51**, 4743-4746 (2012).
217. Banterle, N., Bui, K. H., Lemke, E. A. & Beck, M. Fourier ring correlation as a resolution criterion for super-resolution microscopy. *J. Struct. Biol.* **183**, 363-367 (2013).
218. van Heel, M. & Schatz, M. Fourier shell correlation threshold criteria. *J. Struct. Biol.* **151**, 250-262 (2005).
219. Lima, E., Diaz, A., Guizar-Sicairos, M., Gorelick, S., Pernot, P., Schleier, T. & Menzel, A. Cryo-scanning x-ray diffraction microscopy of frozen-hydrated yeast. *J. Microsc.* **249**, 1-7 (2013).
220. Schroer, C. G., Brack, F.-E., Brendler, R., Höning, S., Hoppe, R., Patommel, J., Ritter, S., Scholz, M., Schropp, A., Seiboth, F., Nilsson, D., Rahomäki, J., Uhlén, F., Vogt, U., Reinhardt, J. & Falkenberg, G., presented at Advances in X-Ray/EUV Optics and Components VIII, *SPIE* (2013).
221. Schroer, C. G., Seyrich, M., Schropp, A., Döhrmann, R., Botta, S., Wiljes, P., Brückner, D., Kahnt, M., Wittwer, F., Grote, L., Koziej, D., Garrevoet, J. & Falkenberg, G. Ptychographic nano-analytical microscope (PtyNAMi) at PETRA III: signal-to-background optimization for imaging with high sensitivity. *Proc. SPIE* **11112**, 111120D (2019).
222. Schroer, C. G., Seyrich, M., Kahnt, M., Botta, S., Döhrmann, R., Falkenberg, G., Garrevoet, J., Lyubomirskiy, M., Scholz, M., Schropp, A. & Wittwer, F. PtyNAMi: ptychographic nano-analytical microscope at PETRA III: interferometrically tracking positions for 3D x-ray scanning microscopy using a ball-lens retroreflector. *Proc. SPIE* **10389**, 103890E (2017).
223. Loetgering, L., Du, M., Eikema, K. S. E. & Witte, S. zPIE: an autofocusing algorithm for ptychography. *Opt. Lett.* **45**, 2030-2033 (2020).
224. Kahnt, M., Grote, L., Brückner, D., Seyrich, M., Wittwer, F., Koziej, D. & Schroer, C. G. Raw data for "Multi-slice ptychography enables high-resolution in situ measurements in extended chemical reactors". DOI: 10.5281/zenodo.3978334 (2020).
225. Xia, Y., Zhao, T., Zhu, X., Zhao, Y., He, H., Hung, C. T., Zhang, X., Chen, Y., Tang, X., Wang, J., Li, W. & Zhao, D. Inorganic-organic competitive coating strategy derived uniform hollow gradient-structured ferroferric oxide-carbon nanospheres for ultra-fast and long-term lithium-ion battery. *Nat. Commun.* **12**, 2973 (2021).
226. Wei Seh, Z., Li, W., Cha, J. J., Zheng, G., Yang, Y., McDowell, M. T., Hsu, P. C. & Cui, Y. Sulphur-TiO₂ yolk-shell nanoarchitecture with internal void space for long-cycle lithium-sulphur batteries. *Nat. Commun.* **4**, 1331 (2013).
227. Xiao, J., Cheng, K., Xie, X., Wang, M., Xing, S., Liu, Y., Hartman, T., Fu, D., Bossers, K., van Huis, M. A., van Blaaderen, A., Wang, Y. & Weckhuysen, B. M. Tandem catalysis with double-shelled hollow spheres. *Nat. Mater.*, DOI: 10.1038/s41563-021-01183-0 (2022).
228. Sun, J., Zhang, J., Zhang, M., Antonietti, M., Fu, X. & Wang, X. Bioinspired hollow semiconductor nanospheres as photosynthetic nanoparticles. *Nat. Commun.* **3**, 1139 (2012).

229. Perfecto, T. M., Zito, C. A. & Volanti, D. P. Effect of NiS nanosheets on the butanone sensing performance of ZnO hollow spheres under humidity conditions. *Sensors and Actuators B: Chemical* **334** (2021).
230. Toe, C. Y., Zheng, Z., Wu, H., Scott, J., Amal, R. & Ng, Y. H. Transformation of cuprous oxide into hollow copper sulfide cubes for photocatalytic hydrogen generation. *J. Phys. Chem. C* **122**, 14072–14081 (2018).
231. Banner, D. J., Firlar, E., Rehak, P., Phakatkar, A. H., Foroozan, T., Osborn, J. K., Sorokina, L. V., Narayanan, S., Tahseen, T., Baggia, Y., Král, P., Shokuhfar, T. & Shahbazian-Yassar, R. In situ liquid-cell TEM observation of multiphase classical and nonclassical nucleation of calcium oxalate. *Adv. Funct. Mater.* **31**, 2007736 (2021).
232. Hutzler, A., Fritsch, B., Jank, M. P. M., Branscheid, R., Martens, R. C., Spiecker, E. & März, M. In situ liquid cell TEM studies on etching and growth mechanisms of gold nanoparticles at a solid–liquid–gas interface. *Adv. Mater. Interf.* **6**, 1901027 (2019).
233. Nielsen, M. H., Li, D., Zhang, H., Aloni, S., Han, T. Y., Frandsen, C., Seto, J., Banfield, J. F., Colfen, H. & De Yoreo, J. J. Investigating processes of nanocrystal formation and transformation via liquid cell TEM. *Microsc. Microanal.* **20**, 425–436 (2014).
234. Evans, J. E., Jungjohann, K. L., Browning, N. D. & Arslan, I. Controlled growth of nanoparticles from solution with in situ liquid transmission electron microscopy. *Nano Lett.* **11**, 2809–2813 (2011).
235. Ma, X., Lin, F., Chen, X. & Jin, C. Unveiling growth pathways of multiply twinned gold nanoparticles by in situ liquid cell transmission electron microscopy. *ACS Nano* **14**, 9594–9604 (2020).
236. Tan, S. F., Bisht, G., Anand, U., Bosman, M., Yong, X. E. & Mirsaidov, U. In situ kinetic and thermodynamic growth control of Au-Pd core-shell nanoparticles. *J. Am. Chem. Soc.* **140**, 11680–11685 (2018).
237. Kahnt, M., Grote, L., Bruckner, D., Seyrich, M., Wittwer, F., Koziej, D. & Schroer, C. G. Multi-slice ptychography enables high-resolution measurements in extended chemical reactors. *Sci. Rep.* **11**, 1500 (2021).
238. Madi, K., Staines, K. A., Bay, B. K., Javaheri, B., Geng, H., Bodey, A. J., Cartmell, S., Pitsillides, A. A. & Lee, P. D. In situ characterization of nanoscale strains in loaded whole joints via synchrotron X-ray tomography. *Nat. Biomed. Eng.* **4**, 343–354 (2020).
239. Leung, C. L. A., Marussi, S., Atwood, R. C., Towrie, M., Withers, P. J. & Lee, P. D. In situ X-ray imaging of defect and molten pool dynamics in laser additive manufacturing. *Nat. Commun.* **9**, 1355 (2018).
240. de Smit, E., Swart, I., Creemer, J. F., Hoveling, G. H., Gilles, M. K., Tyliczszak, T., Kooyman, P. J., Zandbergen, H. W., Morin, C., Weckhuysen, B. M. & de Groot, F. M. Nanoscale chemical imaging of a working catalyst by scanning transmission X-ray microscopy. *Nature* **456**, 222–225 (2008).
241. Deng, J., Preissner, C., Klug, J. A., Mashrafi, S., Roehrig, C., Jiang, Y., Yao, Y., Wojcik, M., Wyman, M. D., Vine, D., Yue, K., Chen, S., Mooney, T., Wang, M., Feng, Z., Jin, D., Cai, Z., Lai, B. & Vogt, S. The Velociprobe: An ultrafast hard X-ray nanoprobe for high-resolution ptychographic imaging. *Rev. Sci. Instrum.* **90**, 083701 (2019).
242. Miao, J., Charalambous, P., Kirz, J. & Sayre, D. Extending the methodology of X-ray crystallography to allow imaging of micrometre-sized non-crystalline specimens. *Nature* **400**, 342–344 (1999).
243. Reinhardt, J. & Schroer, C. G. Quantitative ptychographic reconstruction by applying a probe constraint. *J. Instrum.* **13**, C04016–C04016 (2018).
244. Chapman, H. N. & Nugent, K. A. Coherent lensless X-ray imaging. *Nat. Photonics* **4**, 833–839 (2010).
245. Bø Fløystad, J., Skjønsvell, E. T. B., Guizar-Sicairos, M., Høydalsvik, K., He, J., Andreasen, J. W., Zhang, Z. & Breiby, D. W. Quantitative 3D X-ray imaging of densification, delamination and fracture in a micro-composite under compression. *Adv. Eng. Mater.* **17**, 545–553 (2015).
246. Schropp, A., Hoppe, R., Meier, V., Patommel, J., Seiboth, F., Lee, H. J., Nagler, B., Galtier, E. C., Arnold, B., Zastrau, U., Hastings, J. B., Nilsson, D., Uhlen, F., Vogt, U., Hertz, H. M. &

-
- Schroer, C. G. Full spatial characterization of a nanofocused x-ray free-electron laser beam by ptychographic imaging. *Sci. Rep.* **3**, 1633 (2013).
247. Bradski, G. The OpenCV library. *Dr Dobb's J. Software Tools* **25**, 120-125 (2000).
248. Tianou, H., Wang, W., Yang, X., Cao, Z., Kuang, Q., Wang, Z., Shan, Z., Jin, M. & Yin, Y. Inflating hollow nanocrystals through a repeated Kirkendall cavitation process. *Nat. Commun.* **8**, 1261 (2017).
249. Wang, X., Feng, J., Bai, Y., Zhang, Q. & Yin, Y. Synthesis, properties, and applications of hollow micro-/nanostructures. *Chem. Rev.* **116**, 10983-11060 (2016).
250. Sutter, E. A. & Sutter, P. W. In situ liquid cell electron microscopy of Ag-Au galvanic replacement reactions. *Nanoscale* **9**, 1271-1278 (2017).
251. de Groot, F. M., de Smit, E., van Schooneveld, M. M., Aramburo, L. R. & Weckhuysen, B. M. In-situ scanning transmission X-ray microscopy of catalytic solids and related nanomaterials. *ChemPhysChem* **11**, 951-962 (2010).
252. Howells, M. R., Beetz, T., Chapman, H. N., Cui, C., Holton, J. M., Jacobsen, C. J., Kirz, J., Lima, E., Marchesini, S., Miao, H., Sayre, D., Shapiro, D. A., Spence, J. C. & Starodub, D. An assessment of the resolution limitation due to radiation-damage in x-ray diffraction microscopy. *J. Electron Spectros. Relat. Phenomena* **170**, 4-12 (2009).
253. Chantler, C. T. Detailed tabulation of atomic form factors, photoelectric absorption and scattering cross section, and mass attenuation coefficients in the vicinity of absorption edges in the soft X-ray ($Z=30-36$, $Z=60-89$, $E=0.1$ keV–10 keV), addressing convergence issues of earlier work. *J. Phys. Chem. Ref. Dat.* **29**, 597-1056 (2000).
254. Olliges-Stadler, I., Rossell, M. D., Suess, M. J., Ludi, B., Bunk, O., Pedersen, J. S., Birkedal, H. & Niederberger, M. A comprehensive study of the crystallization mechanism involved in the nonaqueous formation of tungstite. *Nanoscale* **5**, 8517-8525 (2013).
255. Yang, T., Chen, H., Jia, Z., Deng, Z., Chen, L., Peterman, E. M., Weaver, J. C. & Li, L. A damage-tolerant, dual-scale, single-crystalline microlattice in the knobby starfish, *Protoreaster nodosus*. *Science* **375**, 647–652 (2022).
256. Couasnon, T., Alloyeau, D., Ménez, B., Guyot, F., Ghigo, J.-M. & Gélabert, A. In situ monitoring of exopolymer-dependent Mn mineralization on bacterial surfaces. *Sci. Adv.* **6**, eaaz3125 (2020).
257. Bahn, S. Y., Jo, B. H., Choi, Y. S. & Cha, H. J. Control of nacre biomineralization by Pif80 in pearl oyster. *Sci. Adv.* **3**, e1700765 (2017).
258. Jiang, W., Qu, Z.-B., Kumar, P., Vecchio, D., Wang, Y., Ma, Y., Bahng, J. H., Bernardino, K., Gomes, W. R., Colombari, F. M., Lozada-Blanco, A., Veksler, M., Marino, E., Simon, A., Murray, C., Muniz, S. R., de Moura, A. F. & Kotov, N. A. Emergence of complexity in hierarchically organized chiral particles. *Science* **368**, 642–648 (2020).
259. Jang, D., Meza, L. R., Greer, F. & Greer, J. R. Fabrication and deformation of three-dimensional hollow ceramic nanostructures. *Nat. Mater.* **12**, 893-898 (2013).
260. Schroer, C. G., Boye, P., Feldkamp, J. M., Patommel, J., Samberg, D., Schropp, A., Schwab, A., Stephan, S., Falkenberg, G., Wellenreuther, G. & Reimers, N. Hard X-ray nanoprobe at beamline P06 at PETRA III. *Nuclear Instrumentation and Methods in Physics Research Section A: Accelerators, Spectrometers, Detectors and Associated Equipment* **616**, 93-97 (2010).
261. Wakonig, K., Stadler, H. C., Odstrcil, M., Tsai, E. H. R., Diaz, A., Holler, M., Usov, I., Raabe, J., Menzel, A. & Guizar-Sicairos, M. PtychoShelves, a versatile high-level framework for high-performance analysis of ptychographic data. *J. Appl. Crystallogr.* **53**, 574-586 (2020).
262. Odstrcil, M., Menzel, A. & Guizar-Sicairos, M. Iterative least-squares solver for generalized maximum-likelihood ptychography. *Opt. Expr.* **26**, 3108-3123 (2018).
263. Goodman, J. W., Introduction to Fourier optics, *Roberts and Company Publishers*, Englewood, 3 edn., (2005).
264. Lowe, D. G. Distinctive image features from scale-invariant keypoints. *Int. J. Comp. Vis.* **60**, 91-110 (2004).
265. Schneider, C. A., Rasband, W. S. & Eliceiri, K. W. NIH Image to ImageJ: 25 years of image analysis. *Nat. Methods* **9**, 671-675 (2012).
266. Grote, L., Seyrich, M., Döhrmann, R., Harouna-Mayer, S. Y., Mancini, F., Kaziukenas, E., Fernandez-Cuesta, I., Zito, C. A., Vasylieva, O., Wittwer, F., Kronenberg, M., Mogos, N.,

- Landmann, M., Schroer, C. G. & Koziej, D. Raw data for "Imaging Cu₂O nanocube hollowing in solution by quantitative in situ X-ray ptychography". zenodo. doi:10.5281/zenodo.4746349 (2022).
267. Wang, S., Liu, G. & Wang, L. Crystal facet engineering of photoelectrodes for photoelectrochemical water splitting. *Chem. Rev.* **119**, 5192-5247 (2019).
268. Kim, C. W., Yeob, S. J., Cheng, H.-M. & Kang, Y. S. A selectively exposed crystal facet-engineered TiO₂ thin film photoanode for the higher performance of the photoelectrochemical water splitting reaction. *Energy Environ. Sci.* **8**, 3646-3653 (2015).
269. De Gregorio, G. L., Burdyny, T., Loiudice, A., Iyengar, P., Smith, W. A. & Buonsanti, R. Facet-dependent selectivity of Cu catalysts in electrochemical CO₂ reduction at commercially viable current densities. *ACS Catal.* **10**, 4854-4862 (2020).
270. Lee, H.-E., Yang, K. D., Yoon, S. M., Ahn, H.-Y., Lee, Y. Y., Chang, H., Jeong, D. H., Lee, Y.-S., Kim, M. Y. & Nam, K. T. Concave rhombic dodecahedral Au nanocatalyst with multiple high-index facets for CO₂ reduction. *ACS Nano* **9**, 8384-8393 (2015).
271. Cozzoli, P. D., Kornowski, A. & Weller, H. Low-temperature synthesis of soluble and processable organic-capped anatase TiO₂ nanorods. *J. Am. Chem. Soc.* **125**, 14539-14548 (2003).
272. Grzelczak, M., Perez-Juste, J., Mulvaney, P. & Liz-Marzan, L. M. Shape control in gold nanoparticle synthesis. *Chem. Soc. Rev.* **37**, 1783-1791 (2008).
273. Song, H., Kim, F., Connor, S., Somorjai, G. A. & Yang, P. Pt nanocrystals: Shape control and Langmuir-Blodgett monolayer formation. *J. Phys. Chem. B* **109**, 188-193 (2005).
274. Liu, M. & Guyot-Sionnest, P. Mechanism of silver(I)-assisted growth of gold nanorods and bipyramids. *J. Phys. Chem. B* **109**, 22192-22200 (2005).
275. Manna, L., Milliron, D. J., Meisel, A., Scher, E. C. & Alivisatos, A. P. Controlled growth of tetrapod-branched inorganic nanocrystals. *Nat. Mater.* **2**, 382-385 (2003).
276. Ophus, C. Four-dimensional scanning transmission electron microscopy (4D-STEM): From scanning nanodiffraction to ptychography and beyond. *Microsc. Microanal.* **25**, 563-582 (2019).
277. Brunetti, G., Robert, D., Bayle-Guillemaud, P., Rouvière, J. L., Rauch, E. F., Martin, J. F., Colin, J. F., Bertin, F. & Cayron, C. Confirmation of the domino-cascade model by LiFePO₄/FePO₄ precession electron diffraction. *Chem. Mater.* **23**, 4515-4524 (2011).
278. Ferrer Orri, J., Doherty, T. A. S., Johnstone, D., Collins, S. M., Simons, H., Midgley, P. A., Ducati, C. & Stranks, S. D. Unveiling the interaction mechanisms of electron and X-ray radiation with halide perovskite semiconductors using scanning nanoprobe diffraction. *Adv. Mater.*, DOI: 10.1002/adma.202200383, 2200383 (2022).
279. Zhang, Y., Garrevoet, J., Wang, Y., Roeh, J. T., Terrill, N. J., Falkenberg, G., Dong, Y. & Gupta, H. S. Molecular to macroscale energy absorption mechanisms in biological body armour illuminated by scanning X-ray diffraction with in situ compression. *ACS Nano* **14**, 16535-16546 (2020).
280. Bhowmik, A., Lee, J., Britton, T. B., Liu, W., Jun, T.-S., Sernicola, G., Karimpour, M., Balint, D. S. & Giuliani, F. Deformation behaviour of [001] oriented MgO using combined in-situ nano-indentation and micro-Laue diffraction. *Act. Mater.* **145**, 516-531 (2018).
281. Hrauda, N., Zhang, J., Wintersberger, E., Etselstorfer, T., Mandl, B., Stangl, J., Carbone, D., Holy, V., Jovanovic, V., Biasotto, C., Nanver, L. K., Moers, J., Grutzmacher, D. & Bauer, G. X-ray nanodiffraction on a single SiGe quantum dot inside a functioning field-effect transistor. *Nano Lett.* **11**, 2875-2880 (2011).
282. Dubslaff, M., Hanke, M., Schöder, S., Burghammer, M., Boeck, T. & Patommel, J. X-ray nanodiffraction at individual SiGe/Si(001) dot molecules and its numerical description based on kinematical scattering theory. *Appl. Phys. Lett.* **96** (2010).
283. Wallentin, J., Jacobsson, D., Osterhoff, M., Borgstrom, M. T. & Salditt, T. Bending and twisting lattice tilt in strained core-shell nanowires revealed by nanofocused X-ray diffraction. *Nano Lett.* **17**, 4143-4150 (2017).
284. Huang, Z., Bartels, M., Xu, R., Osterhoff, M., Kalbfleisch, S., Sprung, M., Suzuki, A., Takahashi, Y., Blanton, T. N., Salditt, T. & Miao, J. Grain rotation and lattice deformation

- during photoinduced chemical reactions revealed by in situ X-ray nanodiffraction. *Nat. Mater.* **14**, 691-695 (2015).
285. Marcal, L. A. B., Oksenberg, E., Dzhigaev, D., Hammarberg, S., Rothman, A., Bjorling, A., Unger, E., Mikkelsen, A., Joselevich, E. & Wallentin, J. In situ imaging of ferroelastic domain dynamics in CsPbBr₃ perovskite nanowires by nanofocused scanning X-ray diffraction. *ACS Nano* **14**, 15973-15982 (2020).
286. Liu, X. Cu₂O microcrystals: a versatile class of self-templates for the synthesis of porous Au nanocages with various morphologies. *RSC Adv.* **1** (2011).
287. Sutter, E., Jungjohann, K., Bliznakov, S., Courty, A., Maisonhaute, E., Tenney, S. & Sutter, P. In situ liquid-cell electron microscopy of silver-palladium galvanic replacement reactions on silver nanoparticles. *Nat. Commun.* **5**, 4946 (2014).
288. Xiong, L., Li, S., Zhang, B., Du, Y., Miao, P., Ma, Y., Han, Y., Zhao, H. & Xu, P. Galvanic replacement-mediated synthesis of hollow Cu₂O–Au nanocomposites and Au nanocages for catalytic and SERS applications. *RSC Adv.* **5**, 76101-76106 (2015).
289. Lowe, James M. & Coridan, R. H. Mechanistic control of a galvanic replacement reaction on cuprous oxide. *Nanoscale Adv.* **1**, 1343-1350 (2019).
290. Susman, M. D., Popovitz-Biro, R., Vaskevich, A. & Rubinstein, I. pH-dependent galvanic replacement of supported and colloidal Cu₂O nanocrystals with gold and palladium. *Small* **11**, 3942-3953 (2015).
291. Zhu, H., Du, M., Yu, D., Wang, Y., Wang, L., Zou, M., Zhang, M. & Fu, Y. A new strategy for the surface-free-energy-distribution induced selective growth and controlled formation of Cu₂O–Au hierarchical heterostructures with a series of morphological evolutions. *J. Mater. Chem. A* **1**, 919-929 (2013).
292. Zhu, H., Du, M., Yu, D., Wang, Y., Zou, M., Xu, C. & Fu, Y. Selective growth of Au nanograins on specific positions (tips, edges and facets) of Cu₂O octahedrons to form Cu₂O–Au hierarchical heterostructures. *Dalton Trans* **41**, 13795-13799 (2012).
293. Liu, X. W. Selective growth of Au nanoparticles on (111) facets of Cu₂O microcrystals with an enhanced electrocatalytic property. *Langmuir* **27**, 9100-9104 (2011).
294. Preston, T. C. & Signorell, R. Growth and optical properties of gold nanoshells prior to the formation of a continuous metallic layer. *ACS Nano* **3** (2009).
295. Kaune, G., Ruderer, M. A., Metwalli, E., Wang, W., Couet, S., Schlage, K., Röhlberger, R., Roth, S. V. & Müller-Buschbaum, P. In situ GISAXS study of gold film growth on conducting polymer films. *ACS Appl. Mater. Interf.* **1**, 353–360 (2009).
296. Schwartzkopf, M., Buffet, A., Korstgens, V., Metwalli, E., Schlage, K., Benecke, G., Perlich, J., Rawolle, M., Rothkirch, A., Heidmann, B., Herzog, G., Müller-Buschbaum, P., Röhlberger, R., Gehrke, R., Striebeck, N. & Roth, S. V. From atoms to layers: in situ gold cluster growth kinetics during sputter deposition. *Nanoscale* **5**, 5053-5062 (2013).
297. Qin, Y., Che, R., Liang, C., Zhang, J. & Wen, Z. Synthesis of Au and Au–CuO cubic microcages via an in situ sacrificial template approach. *J. Mater. Chem. A* **21** (2011).
298. Ward, J. F., in *Progress in Nucleic Acid Research and Molecular Biology*, eds. W. E. Cohn and K. Moldave, (1988), vol. 35.
299. Gachard, E., Remita, H., Khatouri, J., Keita, B., Nadjo, L. & Belloni, J. Radiation-induced and chemical formation of gold clusters. *New J. Chem.*, 1257-1265 (1998).
300. Long, N. N., Vu, L. V., Kiem, C. D., Doanh, S. C., Nguyet, C. T., Hang, P. T., Thien, N. D. & Quynh, L. M. Synthesis and optical properties of colloidal gold nanoparticles. *J. Phys.: Conf. Series* **187** (2009).
301. Grote, L., Zito, C. A., Frank, K., Dippel, A. C., Reisbeck, P., Pitala, K., Kvashnina, K. O., Bauters, S., Detlefs, B., Ivashko, O., Pandit, P., Rebber, M., Harouna-Mayer, S. Y., Nickel, B. & Koziej, D. X-ray studies bridge the molecular and macro length scales during the emergence of CoO assemblies. *Nat. Commun.* **12**, 4429 (2021).
302. Li, Y., Sun, H., Cheng, X., Zhang, Y. & Zhao, K. In-situ TEM experiments and first-principles studies on the electrochemical and mechanical behaviors of α -MoO₃ in Li-ion batteries. *Nano Energy* **27**, 95-102 (2016).
303. Mao, H., Fu, Y., Yang, H., Deng, Z. Z., Sun, Y., Liu, D., Wu, Q., Ma, T. & Song, X. M. Ultrathin 1T-MoS₂ nanoplates induced by quaternary ammonium-type ionic liquids on

-
- polypyrrole/graphene oxide nanosheets and its irreversible crystal phase transition during electrocatalytic nitrogen reduction. *ACS Appl. Mater. Interf.* **12**, 25189-25199 (2020).
304. Jackson, D. F. & Hawkes, D. J. X-ray attenuation coefficients of elements and mixtures. *Phys. Rep.* **70**, 169—233 (1981).
305. Wittwer, F., Hoppe, R., Seiboth, F., Reinhardt, J., Scholz, M. & Schroer, C. G. Ptychography with a virtually enlarged illumination. *Microsc. Microanal.* **24**, 48-49 (2018).
306. Staniuk, M., Rechberger, F., Tervoort, E. & Niederberger, M. Adapting the concepts of nonaqueous sol–gel chemistry to metals: synthesis and formation mechanism of palladium and palladium–copper nanoparticles in benzyl alcohol. *Journal of Sol-Gel Science and Technology* **95**, 573-586 (2020).
307. Staniuk, M. M., Puzzling mechanism of nanoparticle formation - In situ studies of non-aqueous sol-gel syntheses. PhD thesis, *ETH Zurich*, 2016.
308. Zhang, L., Hou, F. & Tan, Y. Shape-tailoring of CuPd nanocrystals for enhancement of electrocatalytic activity in oxygen reduction reaction. *Chem. Commun.* **48**, 7152-7154 (2012).
309. Yamauchi, M., Abe, R., Tsukuda, T., Kato, K. & Takata, M. Highly selective ammonia synthesis from nitrate with photocatalytically generated hydrogen on CuPd/TiO₂. *J. Am. Chem. Soc.* **133**, 1150-1152 (2011).
310. Xu, C., Zhang, Y., Wang, L., Xu, L., Bian, X., Ma, H. & Ding, Y. Nanotubular mesoporous PdCu bimetallic electrocatalysts toward oxygen reduction reaction. *Chem. Mater.* **21**, 3110-3116 (2009).

List of abbreviations

2D	two-dimensional
3D	three-dimensional
3PIE	three-dimensional iterative ptychographic engine
acac	acetylacetonate
BnOH	benzyl alcohol
CS	central stop
DC	direct current
DCM	double crystal monochromator
DFT	density functional theory
DOF	depth of field
DOS	density of states
ED	electron diffraction
EDX	energy-dispersive X-ray spectroscopy
ePIE	extended iterative ptychographic engine
EXAFS	extended X-ray absorption fine structure
FEM	finite element method
FIB	focused ion beam
FRC	Fourier ring correlation
FT	Fourier transform
FWHM	full width at half maximum
FZP	Fresnel zone plate
GRR	galvanic replacement reaction
HERFD	high energy-resolution fluorescence-detected
HR-TEM	high-resolution transmission electron microscopy
ICSD	inorganic crystal structure database
MCR-ALS	multivariate curve resolution by alternating least squares
NA	numerical aperture
NFL	nano-focusing lenses
OSA	order sorting aperture
PCB	printed circuit board
PDF	pair distribution function
PEEK	polyether ether ketone
PID	proportional–integral–derivative
PTFE	polytetrafluoroethylene
PtyNAMi	ptychographic nano-analytical microscopy
PXRD	powder X-ray diffraction
RIXS	resonant inelastic X-ray scattering
SAXS	small-angle X-ray scattering
SEM	scanning electron microscopy
SIFT	scale-invariant feature transform
STXM	scanning transmission X-ray microscopy
SVD	singular value decomposition

WAXS	wide-angle X-ray scattering
XANES	X-ray absorption near-edge structure
XAS	X-ray absorption spectroscopy
XRD	X-ray diffraction

List of figures

Figure 1.1. Example materials showing nonclassical crystallization and shape transformation.	12
Figure 2.1. Plots of the Gibbs free energy for classical and nonclassical nucleation and growth.	15
Figure 2.2. Schematic illustration of classical and nonclassical crystallization pathways.	16
Figure 2.3. Overview of self-templating hollowing mechanisms of nanoparticles.	18
Figure 2.4. Hollowing of TiO ₂ spheres via Ostwald ripening.	18
Figure 2.5. Hollowing through the nanoscale Kirkendall effect.	19
Figure 2.6. Schematic of the surface protected conversion mechanism.	20
Figure 2.7. Schematic of the GRR of Mn ₃ O ₄ with Fe ²⁺ via pinhole corrosion mechanism.	21
Figure 3.1. HERFD-XAS of CoO at the K edge and corresponding energy diagram.	24
Figure 3.2. Illustration of the photon-in/photon-out process and HERFD-XAS.	25
Figure 3.3. Illustration of the pair distribution function.	28
Figure 3.4. Acquisition scheme of a ptychographic data set.	34
Figure 3.5. The 3PIE reconstruction algorithm on the example of a 2-sliced object.	35
Figure 4.1. SEM and TEM images of CoO assemblies at the end of the reaction.	41
Figure 4.2. Determination of chemical constituents from the in situ HERFD-XANES study.	42
Figure 4.3. Structure determination of the reaction intermediate Co(acac) ₂	43
Figure 4.4. Following the rearrangement of the Co complex and the crystallization of CoO.	45
Figure 4.5. Results of the sequential PDF refinement on the CoO synthesis.	47
Figure 4.6. SAXS data modelling to follow the assembly of CoO nanocrystals.	48
Figure 4.7. Overview of the emergence of nanoassemblies of CoO in BnOH.	50
Figure 5.1. Schematic illustration of the in situ reactor for imaging.	78
Figure 5.2. Liquid container of the in situ reactor.	79
Figure 5.3. Photograph of the in situ reactor mounted at PtyNAMi at beamline P06.	79
Figure 5.4. Display of a flat heating element of the reactor.	81
Figure 5.5. Reactor temperature control and stability.	81
Figure 5.6. Thermal simulation of the reactor.	82
Figure 6.1. Schemes of the ptychographic measurements on the polyimide foil and in the reactor.	84
Figure 6.2. SEM images of two regions of a polyimide foil covered with Cu ₂ O nanocubes.	86
Figure 6.3. Phases of the reconstructed objects from the single polyimide foil experiment.	87
Figure 6.4. Estimated resolutions of the single polyimide foil experiment using FRC.	88
Figure 6.5. Comparison of two multi-slice reconstructions of the same dataset.	89
Figure 6.6. Phase reconstructions of the experiment using the chemical reactor.	90
Figure 7.1. Overview of the in situ imaging experiment on Cu ₂ O nanocubes.	99
Figure 7.2. Quality estimation of in situ imaging in solution.	100
Figure 7.3. Analysis of the growth process of Cu ₂ O nanocubes from a 2D perspective.	102
Figure 7.4. Analysis of the growth process of Cu ₂ O nanocubes from a 3D perspective.	103
Figure 7.5. Hollowing process of the Cu ₂ O nanocuboids.	104
Figure 7.6. Beam-induced damage to the Cu ₂ O nanocuboids.	106
Figure 8.1. Outline of the multimodal in situ imaging experiment on Cu ₂ O@Au nanocages.	126
Figure 8.2. Crystallinity of growing Cu ₂ O nanocubes from in situ ptychography and WAXS.	128
Figure 8.3. Ex situ study of the galvanic replacement of Cu ₂ O with Au.	130
Figure 8.4. In situ ptychographic images of Au nanocage formation.	131
Figure 8.5. Quantification of radiation damage during the galvanic replacement of Cu ₂ O with Au.	132

Figure 8.6. SEM and EDX images of CuPd nanospheres.	148
Figure 8.7. In situ ptychographic images of CuPd nanospheres.....	148
Figure 9.1. Illustration of X-ray methods utilized in different in situ experiments.	151
Supplementary Figure 4.1. Schematics of the reactor used for in situ HERFD-XANES and PDF. ..	54
Supplementary Figure 4.2. TEM images of CoO nanocrystallite assemblies at high magnification..	55
Supplementary Figure 4.3. TEM images of CoO nanocrystallite assemblies at low magnification. .	56
Supplementary Figure 4.4. Size evolution of polyhedral CoO crystallites and assemblies.	56
Supplementary Figure 4.5. TEM images before and just after the onset of crystallization of CoO. .	57
Supplementary Figure 4.6. In situ Co 1s2p HERFD-XANES spectra during the synthesis of CoO..	58
Supplementary Figure 4.7 SVD results of the in situ HERFD-XANES data set.	59
Supplementary Figure 4.8. Co 1s2p HERFD-XANES spectrum of a CoO powder reference.	61
Supplementary Figure 4.9. Rel. concentrations of the precursor and the intermediate towards CoO.	62
Supplementary Figure 4.10. Calculated Co K-edge XANES spectra of precursor and CoO product.	62
Supplementary Figure 4.11. Structure determination of the intermediate Co(acac) ₂	64
Supplementary Figure 4.12. In situ total scattering data for the synthesis of CoO at 160 °C.	65
Supplementary Figure 4.13. Background correction of the in situ total scattering data.....	65
Supplementary Figure 4.14. Ex situ PDFs for the synthesis of CoO at 160 °C.	66
Supplementary Figure 4.15. PDF refinement results for the synthesis of CoO at 160 °C.	67
Supplementary Figure 4.16. PDF refinement with higher <i>r</i> range for the synthesis of CoO.....	68
Supplementary Figure 4.17. Fit of experimental and calculated PDF using the cubic CoO phase. ...	68
Supplementary Figure 4.18. In situ total scattering data for the synthesis of CoO at 140 °C.	69
Supplementary Figure 4.19. Additional refined PDF parameters for the CoO synthesis at 140 °C. .	70
Supplementary Figure 4.20. Laboratory SAXS data of CoO assemblies after 20 and 90 min.....	72
Supplementary Figure 4.21. PXRD data of dried CoO particles and Co(acac) ₃ precursor.	74
Supplementary Figure 4.22. TEM image of CoO particles after 90 min reaction time.	75
Supplementary Figure 4.23. Overview of the emergence of CoO nanoassemblies.	75
Supplementary Figure 7.1 Schematic representation of the imaging in situ reactor.	111
Supplementary Figure 7.2. Thermal simulations on the imaging in situ reactor.....	112
Supplementary Figure 7.3. Growth and hollowing of Cu ₂ O nanocubes on the exit window.....	113
Supplementary Figure 7.4. Ptychographic reconstructions from split data set for FRC.	114
Supplementary Figure 7.5. Effect of position refinement during reconstruction.	114
Supplementary Figure 7.6. Reactor position and illumination profiles for in situ ptychography. ...	115
Supplementary Figure 7.7. Finding the distance between the reactor windows.	116
Supplementary Figure 7.8. Effect of incomplete slice separation on ptychogr. reconstruction.	117
Supplementary Figure 7.9. Detailed view of the growth phase of Cu ₂ O nanocubes.....	118
Supplementary Figure 7.10. Overview of the image processing steps used to track nanocubes.....	119
Supplementary Figure 7.11. Background selection for thickness calculation of Cu ₂ O nanocubes..	119
Supplementary Figure 7.12. Evolution of the aspect ratio of tracked Cu ₂ O nanocubes.....	120
Supplementary Figure 7.13. Confirmation of void formation in Cu ₂ O nanocubes without beam. ..	121
Supplementary Figure 7.14. Histogram of outer dimensions and void sizes of Cu ₂ O nanocuboids.	121
Supplementary Figure 7.15. In situ imaging of Cu ₂ O nanocube growth at 8.98 keV.	122
Supplementary Figure 7.16. Radiation damage during imaging at 8.98 keV.....	123
Supplementary Figure 7.17. Cu nanocuboids vanishing under X-ray exposure at 15.25 keV.....	123
Supplementary Figure 8.1. Schematic illustration of the imaging in situ reactor.	138
Supplementary Figure 8.2. Gradual decrease of the window distance during in situ imaging.....	138
Supplementary Figure 8.3. Polar-angle histogram for WAXS separation.	139
Supplementary Figure 8.4. Spatial resolution of in situ images during Cu ₂ O nanocube growth.	140

Supplementary Figure 8.5. Focus characterization and reactor position for multimodal imaging...	141
Supplementary Figure 8.6. Spatial resolution of in situ images during GRR.	142
Supplementary Figure 8.7. Illumination profiles and reactor position for GRR.	143
Supplementary Figure 8.8. Dose estimation for imaging the GRR.....	145
Supplementary Figure 8.9. Phase background correction for material quantification.	146
Supplementary Figure 8.10. Quantitative phase analysis with background subtraction method.	146
Supplementary Figure 8.11. Beam-induced Au deposition during GRR.	147

List of publications

- Lukas Grote, Martin Seyrich, Ralph Döhrmann, Sani Y. Harouna-Mayer, Federica Mancini, Emilis Kaziukenas, Irene Fernandez-Cuesta, Cecilia A. Zito, Olga Vasylieva, Felix Wittwer, Michal Kronenberg, Natnael Mogos, Mirko Landmann, Christian G. Schroer, and Dorota Koziej, “Imaging Cu₂O nanocube hollowing in solution by quantitative in situ X-ray ptychography”, *Nature Communications* (*accepted*)
- Lukas Grote, Cecilia A. Zito, Kilian Frank, Ann-Christin Dippel, Patrick Reisbeck, Krzysztof Pitala, Kristina O. Kvashnina, Stephen Bauters, Blanka Detlefs, Oleh Ivashko, Pallavi Pandit, Matthias Rebber, Sani Y. Harouna-Mayer, Bert Nickel, and Dorota Koziej, “X-ray studies bridge the molecular and macro length scales during the emergence of CoO assemblies”, *Nature Communications* **12**, 4429 (2021)
DOI: 10.1038/s41467-021-24557-z
- Maik Kahnt, Lukas Grote, Dennis Brückner, Martin Seyrich, Felix Wittwer, Dorota Koziej, and Christian G. Schroer, “Multi-slice ptychography enables high-resolution measurements in extended chemical reactors”, *Scientific Reports* **11**, 1500 (2021)
DOI: 10.1038/s41598-020-80926-6
- Tomke E. Glier, Lewis Akinsinde, Malwin Paufler, Ferdinand Otto, Maryam Hashemi, Lukas Grote, Lukas Daams, Gerd Neuber, Benjamin Grimm-Lebsanft, Florian Biebl, Dieter Rukser, Milena Lippmann, Wiebke Ohm, Matthias Schwartzkopf, Calvin J. Brett, Toru Matsuyama, Stephan V. Roth, and Michael Rübhausen, “Functional printing of conductive silver-nanowire photopolymer composites”, *Scientific Reports* **9**, 6465 (2019)
DOI: 10.1038/s41598-019-42841-3
- Christian G. Schroer, Martin Seyrich, Andreas Schropp, Ralph Döhrmann, Stephan Botta, Patrik Wiljes, Dennis Brückner, Maik Kahnt, Felix Wittwer, Lukas Grote, Dorota Koziej, Jan Garrevoet, and Gerald Falkenberg, “Ptychographic Nano-Analytical Microscope (PtyNAMi) at PETRA III: signal-to-background optimization for imaging with high sensitivity”, *Proc. SPIE* **11112**, X-Ray Nanoimaging: Instruments and Methods IV, 111120D (9. September 2019)
DOI: 10.1117/12.2529096

Curriculum vitae

Personal information

Name	Lukas Grote
Date of birth	31 st of August, 1993
Place of birth	Haselünne, Germany
Citizenship	German

Education

02/2018 – 08/2022	Dissertation in Physics Hybrid Nanostructures Laboratory Department of Physics, University of Hamburg, Germany
10/2015 – 11/2017	M.Sc. in Nanoscience Department of Physics, University of Hamburg, Germany Thesis: “X-ray fluorescence nanotomography on an integrated circuit”
10/2012 – 09/2015	B.Sc. in Nanoscience Department of Physics, University of Hamburg, Germany Thesis: “Nanocomposites for 3D printing: Characterization and improvement of a polymer nanoparticle composite regarding printing resolution and conductivity”
08/2004 – 07/2012	Abitur Gymnasium Leoninum Handrup, Handrup

Acknowledgements

The accomplishment of this Ph.D. work would not have been possible without the help of my colleagues. I would like to express my sincere gratitude to everyone who contributed to the completion of this project, in one way or another, by fruitful discussions, helpfulness, and a pleasant working atmosphere.

First, I would like to thank Prof. Dr. Dorota Koziej for giving me the opportunity to work on this exciting and interdisciplinary project, as well as for supervising and supporting my work with great expertise and commitment. I furthermore thank Dorota for allowing me to work on this project with a lot of freedom and the possibility to outline many aspects myself. Dorota's door was always open to discuss any issue with my work, and I thank her for motivating me and offering many insights and new perspectives.

Further, I would like to express my gratitude to Prof. Dr. Christian Schroer for co-supervising this project and for giving valuable insights and comments during the preparation of the manuscripts. I thank Christian for introducing me to the world of X-ray microscopy already during my M.Sc., and my experiences during that time helped me significantly to complete this Ph.D. project.

I would like to thank the members of the examination committee, Prof. Dr. Arwen Pearson, Prof. Dr. Gabriel Bester, and PD Dr. Thomas Keller, for their interest in my work and for their efforts.

I appreciate the pleasant, supportive, and cooperative working atmosphere in the Hybrid Nanostructures Group at CHyN, and I would like to thank all present and former members for interesting discussions, many nice moments, and for being kind office mates. It was my pleasure to work with Cecilia Zito on our joint project on the nanoassemblies. I appreciate her expertise and kindness that made this work a very valuable experience. Sarah-Alexandra Hussak supported me with her positive attitude and friendliness. I thank her for untiringly coping with the difficulties of synthesizing nanocubes in the reactor. I also thank Federica Mancini for her great efforts in the lab. Leif Albers advanced the tricky data analysis with a pragmatic way of coding. I would like to thank him for working with me on this project. Natnael Mogos joined this project in the very beginning of my Ph.D. studies when we still needed to figure out some synthetic details. I thank him for his patience and support to finally obtain cubic nanoparticles. Moreover, I would like to thank Karolina Stachnik, Sina Röper, and Jonas Voss for continuing with the in situ imaging project and taking it to the next level. It is good to know the future experiments in their skilled hands.

Martin Seyrich contributed to the in situ imaging experiments with great proficiency. I would like to thank him for the fruitful and friendly collaboration on this project and for his patient support. Furthermore, his passion for photography yielded nice photographs of the in situ reactor and many permanent impressions from the numerous beamtimes. I would further like to acknowledge Maik Kahnt for his work on multi-slicing ptychography to support the in situ experiments. Moreover, I express my sincere gratitude to Kilian Frank for a very enjoyable collaboration on the nanoassembly project.

I thank Prof. Dr. Kristina Kvashnina for introducing me to the FEFF method and helping me out patiently with simulations. Furthermore, I would like to thank Ralph Döhrmann for his support during the design of the reactor and for helping me out with Invar when I ran short. I further thank Mirko Landmann for explaining me the subtleties of FEM simulations. Moreover, I express my gratitude to Andreas Schropp, Dennis Brückner, and Felix Wittwer, Olga Vasylieva and Matthias Rebber for doing shifts at the beamline and supporting the experiments with their expertise.

I would like to thank the people working at the P06, P07, P21.1, ID26 and cSAXS beamlines, as well as the members of our mechanical workshop. Without their great work, none of the results presented in this work could have been accomplished.

Finally, I thank my family for their support. Especially, I would like to thank Anna for always being at my side. I am very grateful to her for encouraging and supporting me during the whole duration of my doctoral studies.

Parts of this thesis were proofread by Dorota Koziej, Karolina Stachnik,
Jagadesh Kopula Kesavan, Matthias Rebber, and Cecilia Zito.

Eidesstattliche Versicherung / Declaration on oath

Hiermit versichere ich an Eides statt, die vorliegende Dissertationsschrift selbst verfasst und keine anderen als die angegebenen Hilfsmittel und Quellen benutzt zu haben.

Ich versichere, dass das gebundene Exemplar der Dissertation und das in elektronischer Form eingereichte Dissertationsexemplar (über den Docata-Upload) und das bei der Fakultät (zuständiges Studienbüro bzw. Promotionsbüro Physik) zur Archivierung eingereichte gedruckte gebundene Exemplar der Dissertationsschrift identisch sind.

I hereby declare upon oath that I have written the present dissertation independently and have not used further resources and aids than those stated in the dissertation.

I, the undersigned, declare that the bound copy of the dissertation and the dissertation submitted in electronic form (via the Docata upload) and the printed bound copy of the dissertation submitted to the faculty (responsible Academic Office or the Doctoral Office Physics) for archiving are identical.

Hamburg, 04.07.2022

Lukas Grote